

**Spectral And Timing Properties Of Black Holes And
Neutron Stars In X-Ray Binaries Using Two-Component
Advective Flow Solution**

**Thesis submitted for the Degree of
Doctor of Philosophy (Science)
in
Physics (Theoretical)**

**by
Ayan Bhattacharjee**

**Department of Physics
University of Calcutta
2019**

Dedicated to,

*Those who almost gave up;
But, didn't.*

ABSTRACT

Accretion flow around a black hole (BH) or a neutron star (NS) emits high energy radiations with varying spectral and temporal properties. Observed temporal variations point to the existence of a mechanism, dictated by the flow dynamics and not by the stellar surface or magnetic fields, that is common in both types of compact objects. Spectral energy distributions of multiple sources indicate that the Comptonization process, the dominant mechanism for changing states in X-ray, takes place inside the flow which has similar physical properties in both the objects. The two-component advective flows (TCAF), hitherto applicable only for black holes, satisfy an array of such required properties. This prompted us towards the search for a generalized solution applicable to accretion disks around both BHs and NSs.

In Chapters 2 and 3, we discuss previous models of the accretion flows around BHs and NSs, respectively.

Chapters 4 and 5 show our successful implementation of TCAF solution for BHs where it explains spectral and timing properties self-consistently and provided a well-constrained estimate of the mass of the central compact object in each system.

In Chapter 6, we show that TCAF, combined with a normal boundary layer (NBOL), explains the spectral features of NSs due to thermal Comptonization. State transition properties are addressed and the origin of the geometry of some phenomenological models are suggested. In Chapter 7, we investigate the inviscid flows with cooling to show that, for wind dominated systems, such as Cir X-1, our solutions are capable of reproducing the observational frequencies of Low-Frequency, hecto-Hz and kilo-Hz QPOs. In Chapter 8, we show the formation of boundary layers and viscous disks from a sub-Keplerian flow when the viscosity is high. Along with Chapter 3, these findings prove the applicability of TCAF formalism to NSs.

In Chapter 9, we show the formation of TCAF Around NS (TANS). We construct a new spectral model based on the TCAF, TANS, which requires 3 additional physical parameters (based on the inferences of the previous chapters) to produce different types of observed spectra for NSs. This suggests that TANS can be treated as a generalized physical model for BHs and NSs.

Sometimes I lie awake at night, and I ask,
“Where have I gone wrong?”
Then a voice says to me,
“This is going to take more than one night.”
-Charles M. Schulz

When I was drafting the first version of the thesis, I decided to write the introduction at the very end, knowing that it would be the toughest part. The rest of the chapters were based on the work conducted in the last five years, based on the factual findings, based on the articles that were published. So, it was, in its own way, easy to pen down. The summary was also something that transpired very recently but had a well-constrained framework. But, the introduction demanded something more, a connection with broader aspects within the discipline and a look-back on the ever-changing motivations. And, I thought that was going to be tough.

Clearly, I was wrong!

It was nothing compared to the task at hand: acknowledging the people, events and ideas that shaped the thesis, as it stands today.

To begin with, I would like to acknowledge the constant support and motivation provided by Prof. Sandip K. Chakrabarti. The work we have been doing for the past three years on the numerical simulation of spectral and timing properties of accreting neutron stars was inspired by his work in the domain of stellar-mass and supermassive black holes; conceived by him for the cases of neutron stars due to his unparalleled physical insight into the subject and flexibility to adapt in the face of new observations; implemented by his steadfast approach in supervising our work. I would personally like to thank him for tolerating and answering any and all of my academic questions, irrespective of time or place, for the past 5 years, I have worked under his supervision.

I would like to thank Dr Ramkrishna Das for his support as the Officiating Supervisor, since December 2018. Dr Das has always been patient with me and helped me whenever needed. He also organized Departmental Seminars which gave me the scope to interact more within the Department and work on my speaking skills in front of a broader group of people.

The academic staff of SNBNCBS has been more than helpful during my tenure here. I would especially like to thank Chandrakana Chatterjee, Rupam Porel, and Moumita Banik, as they have been assisting us with administrative works since 2012. I would also like to acknowledge the efforts made by the Deputy Registrar, Ms Nibedita Konar, for handling the academic processes through her hard-working attitude and promptness in solving any unforeseen issues. The erstwhile Deputy Registrar, Dr Sunish Kumar Deb, has always been cordial and helpful and he still continues to be so whenever we meet. The computational facilities provided by SNBNCBS have been utilized for the Thesis. The System Administrator, Dr. Sanjay Chowdhury, has been and continues to be, extremely helpful in assisting with technical issues relating to the Clusters. I would also like to thank the Computer Service Cell, especially, Bijay Pramanik, Abhijit Ghosh and Sagar De, for keeping the facilities running 24×7 , without which the simulations would not have been possible.

I would like to acknowledge the academic and personal support I got from the students and faculties of the Indian Centre for Space Physics. They have been more than hospitable to us during our academic visits. I would like to acknowledge the support I got from my collaborators Dr Dipak Debnath and Dr Indrani Banerjee for the past three years. Because of them, the work has progressed smoothly and I learned a lot from them.

On the personal front, none of this would ever be possible without the thousands of sacrifices made by my parents: Mr. Naru Gopal Bhattacharjee and Mrs. Arati Bhattacharjee. These two self-less heroes of mine have done whatever it takes to ensure that I had a prosperous childhood; had a continued education; instilled moral values; and taught work-ethics by being exemplary parents and the best family one could ask for.

The next person is the one who is always next to me, through thick and thin of life and had been there through the ups-and-downs of the PhD tenure. I had always loved my work, my family, my friends. In fact, I tried so much in

being what I needed to be that I forgot an important part of it all: myself. Ruchi, you are the reason, why I finally felt that I deserved love and care. You are the one who made me feel confident under my skin, made me realize my potential and worth. In our journey together through the past five years, you have taught me many things, which would have otherwise alluded me. You are one of the most dedicated, passionate, creative and resourceful persons I have met. I truly believe that you would become a great researcher someday, going by your exponential learning curve.

To Tukun 'di', my best(est!) senior in SNB, you are a one-of-a-kind person who is unfazed at the face of grief, despair, stress, and the biggest problem of all: my constant whining about everything. You had been my one true friend through all the emotions, the ear to all K-drama-like stories, and the sensei to the foodie in me. I am forever thankful to you for being my friend in every need, work and personal. If you ever need anything, even when it hasn't been your day, your week, your month, or even your year, but I'll be there for you! 'Always'.

In a similar spirit, I would like to acknowledge the support of my longest-running friend, Anuvab Banerjee, who is also my colleague and group-mate. He has seen me through most of my life, going through life having ups-and-(mostly-)downs. We have been friends since Kindergarten and apart from the two years in Master's course, have studied in the same Institutes as well. This really helped me in discussing any and all topic with him at any point in time, many of which have had a great impact on the work. As there is no need for any prelude, which is true of any long-running friendship, much time is saved while discussing work. I would like to thank Anuvab and Riddhi, one of the hardest working scholars I have seen, for their extensive support during the culmination of the Thesis. Both of them have gone out of their way to help me in finishing the draft in time. I could not thank you enough.

I would especially like to thank Shreeram Nagarkoti and Dr Sudipta Sasmal for being the level-headed confidants that they have been since I met them. They have inspired me to go the extra mile at work while also being a family man. Their dedication to their research and family are commendable and I wish them and family happiness and prosperity for the days to come. During the editorial process of the Festschrift, I realized the resourcefulness of Dr Sasmal (now, Sudipta 'da') when he went through all the papers again and again to sort out all the issues. His suggestions helped me back then and continues to do so now, both personally and on academic front (read, last-moment-panic-of-printing-the-Thesis!).

I would like to acknowledge the academic discussions I had with Sumanta Kundu, Arindam Ghosh and Biplab Bhattacharjee, during the seven years of being at SNBNCBS. Their insight into their corresponding fields and technical expertise has always been a great help to me.

I would also like to acknowledge the faculty members, viz., Dr Punyabrata Pradhan, Prof Amitabha Lahiri and Prof Arup Kumar Roychoudhury, whose lectures in the Master's course and projects and helped me in gaining the essential technical and temperamental skill-sets needed for the PhD course.

Contents

| | |
|--|-----------|
| Dedication | i |
| Abstract | ii |
| Acknowledgements | iii |
| List of Publication | viii |
| Abbreviations, Acronyms and Initialisms | ix |
| List of commands | xi |
| 1 Introduction | 1 |
| 2 Modelling of accretion flows around Black Holes | 8 |
| 2.1 Major observational and theoretical results before TCAF | 9 |
| 2.1.1 1950s | 9 |
| 2.1.2 1960s | 10 |
| 2.1.3 1970s | 11 |
| 2.1.4 1980s | 15 |
| 2.2 Development of TCAF paradigm | 18 |
| 2.3 Application of TCAF for BHs | 24 |
| 3 Modelling of accretion flows around Neutron Stars | 26 |
| 3.1 Major observational results and models | 27 |
| 3.1.1 Evolution of theories: Timing Properties | 27 |
| 3.1.2 Evolution of theories: Spectral Properties | 30 |
| 3.2 Prospect of TCAF as the generalized flow around NS | 32 |
| 4 Fitting the data of Black Hole transient H1743-322 by TCAF solution | 34 |
| 4.1 Introduction | 35 |
| 4.2 Method of Analysis | 37 |
| 4.2.1 Two Component Advective Flow (TCAF) Solution | 37 |
| 4.2.2 Propagatory Oscillatory Shock (POS) model | 40 |
| 4.3 Observation and Data Analysis | 41 |
| 4.4 Results | 45 |
| 4.4.1 Spectral Data Fitted by TCAF model | 45 |
| 4.4.2 Correlating spectral and timing properties | 47 |
| 4.4.3 Mass estimation using TCAF and POS model fits | 48 |
| 4.5 Discussions and Conclusions | 48 |

| | | |
|-----------|--|------------|
| 5 | TCAF paradigm applied to persistent BHC: Cyg X-1 | 55 |
| 5.1 | Introduction | 56 |
| 5.2 | Observation and Data Analysis | 58 |
| 5.3 | Results | 60 |
| 5.3.1 | Spectral Data Fitted by TCAF model during hard phase (phase II of the source activity) | 60 |
| 5.3.2 | Spectral Data Fitted by TCAF model during the flaring phase (phase III of the source activity) | 62 |
| 5.4 | Conclusions | 67 |
| 6 | Comptonized spectra of a weakly magnetized neutron star (NS) | 69 |
| 6.1 | Simulation Setup | 70 |
| 6.2 | Scattering Process | 77 |
| 6.2.1 | Radiative processes | 77 |
| 6.2.2 | Photoelectric absorption | 79 |
| 6.2.3 | Effects of cooling | 79 |
| 6.3 | Results | 81 |
| 6.4 | Thermal reprocessing in the disc | 83 |
| 6.5 | Discussions and Conclusions | 90 |
| 7 | Simulation of Inviscid flows around NS which include Shock Waves | 93 |
| 7.1 | Method | 94 |
| 7.1.1 | Model Equations | 95 |
| 7.1.2 | SPH: Implementation of the cooling law | 96 |
| 7.1.3 | Conservation of angular momentum | 98 |
| 7.1.4 | Boundary Conditions | 99 |
| 7.1.5 | Coalescing of Particles | 99 |
| 7.1.6 | Timing Analysis | 100 |
| 7.2 | Results | 101 |
| 7.3 | Conclusions | 104 |
| 8 | Simulation of Viscous flows around NS | 108 |
| 8.1 | Method | 109 |
| 8.2 | Results | 109 |
| 8.3 | Conclusions | 111 |
| 9 | Generalized flows around neutron stars | 114 |
| 9.1 | Flow configuration with a vertical viscosity gradient and strong cooling | 115 |
| 9.2 | A unified spectral model for BHs and NSs | 115 |
| 10 | Summary | 121 |
| 10.1 | Fulfillment of objectives | 121 |
| 10.2 | Future Plans | 123 |
| 10.2.1 | Study of X-ray Binaries | 123 |
| 10.2.2 | Numerical Simulation | 123 |
| 10.2.3 | Model Development | 124 |
| | Bibliography | 125 |

| | | |
|----------|---|------------|
| A | Geometrical Aspects of a Black Hole | 136 |
| A.1 | General relativistic form | 136 |
| A.2 | Pseudo-Newtonian form | 137 |
| B | Fluid dynamical aspects of an accretion flow | 138 |
| B.1 | Governing equations | 138 |
| B.1.1 | Conservation of Mass | 138 |
| B.1.2 | Conservation of Momentum | 138 |
| B.1.3 | Conservation of Energy | 138 |
| B.1.4 | Shocks | 139 |
| C | Radiative Processes | 140 |
| C.1 | Thermal Emission | 140 |
| C.2 | Non-thermal Emission | 142 |
| D | Numerical and visualization tools | 144 |
| D.1 | Data visualization techniques | 144 |
| D.1.1 | SuperMongo | 144 |
| D.1.2 | GnuPlot | 144 |
| D.1.3 | XmGrace | 145 |
| D.1.4 | ROOT | 145 |
| D.1.5 | MATHEMATICA | 145 |
| D.2 | Computational setups and techniques | 145 |
| D.2.1 | Code testing platforms | 146 |
| D.2.2 | Performance statistics | 146 |
| D.2.3 | Usage of clusters | 146 |

List of Publications

Publications Toward Thesis

1. *The 2004 outburst of BHC H1743-322: analysis of spectral and timing properties using the TCAF solution*, by **Ayan Bhattacharjee**, Indrani Banerjee, Anuvab Banerjee, Dipak Debnath, Sandip K Chakrabarti in **Monthly Notices of the Royal Astronomical Society**, **466**, 1372-1381 (2016), [DOI:10.1093/mnras/stw3117](https://doi.org/10.1093/mnras/stw3117)
2. *Constraining Mass of Cygnus X-1 from Analysis of the Hard State Spectral Data using TCAF Solution*, by Indrani Banerjee, **Ayan Bhattacharjee**, Anuvab Banerjee, Dipak Debnath, & Sandip K. Chakrabarti, 2019 (submitted to **Monthly Notices of the Royal Astronomical Society Letters**), [arXiv:1904.11644](https://arxiv.org/abs/1904.11644)
3. *Monte Carlo Simulations of Thermal Comptonization Process in a Two Component Advective Flow around a Neutron Star.*, by **Ayan Bhattacharjee**, Sandip K. Chakrabarti, in **Monthly Notices of the Royal Astronomical Society**, **472**, 1361-1371 (2017), [DOI:10.1093/mnras/stx1867](https://doi.org/10.1093/mnras/stx1867)
4. *Timing Properties of Shocked Accretion Flows around Neutron Stars in presence of cooling*, by **Ayan Bhattacharjee**, Sandip K. Chakrabarti, in **The Astrophysical Journal**, **873**, 119 (2019), [DOI:10.3847/1538-4357/ab074a](https://doi.org/10.3847/1538-4357/ab074a)
5. *Timing Properties of Shocked Accretion Flows around Neutron Stars in presence of cooling. II. Viscous Disks and Boundary Layers*, by **Ayan Bhattacharjee**, Sandip K. Chakrabarti, 2019, Submitted to **The Astrophysical Journal**
6. *Possible Mechanism of Spectral State Transitions of Z and Atoll sources in Accreting Neutron Stars*, by **Ayan Bhattacharjee**, Sandip K. Chakrabarti, 2019, Submitted to **Nature Communications**

Book Publications

7. *Generalized Flows Around Neutron Stars.*, by **Ayan Bhattacharjee**, in Mukhopadhyay B., Sasmal S. (eds) **Exploring the Universe: From Near Space to Extra-Galactic**, Astrophysics and Space Science Proceedings, vol 53. Springer, Cham (2018)

Other Publications

8. *Spectral Analysis of χ Class Data of GRS 1915+105 Using TCAF Solution.*, by Anuvab Banerjee, **Ayan Bhattacharjee**, and Sandip K. Chakrabarti, Submitted to **Monthly Notices of the Royal Astronomical Society Letters**.

List of Abbreviations, Acronyms and Initialisms

| | |
|------------------|--|
| AGN: | Active Galactic Nuclei |
| ARR: | Accretion Rate Ratio |
| ARRID: | Accretion Rate Ratio Intensity Diagram |
| ASM: | All Sky Monitor |
| BH: | Black Hole |
| BHC: | Black Hole Candidate |
| CENBOL: | CENtrifugal pressure dominated BOundary Layer |
| Cir: | Circinus |
| DEC: | Declination |
| eV: | electron Volt |
| EXOSAT: | European X-ray Observatory Satellite |
| FB: | Flaring Branch |
| FITS: | Flexible Image Transport System |
| GTI: | Good Time Interval |
| HB: | Horizontal Branch |
| HEAO: | High Energy Astronomical Observatory |
| HEASARC: | High Energy Astrophysics Research Archive Center |
| HEASOFT: | High Energy Astrophysics Software |
| HEXTE: | High-Energy X-ray Timing Experiment |
| HFQPO: | High-Frequency Quasi-Periodic Oscillation |
| hHz QPO: | hecto-Hertz Quasi-Periodic Oscillation |
| HIMS: | Hard Intermediate State |
| HMXB: | High-Mass X-Ray Binary |
| HS: | Hard State |
| IC: | Inner Cloud |
| INTEGRAL: | INTErnational Gamma-Ray Astrophysics Laboratory |
| IS: | Island State |
| ISM: | Interstellar Medium |
| KD: | Keplerian Disk |
| keV: | kilo electron Volt |
| kHz QPO: | kilo-Hertz Quasi-Periodic Oscillation |
| kPc: | kilo Parsec |
| LB: | Lower Banana state |
| LFQPO: | Low-Frequency Quasi-Periodic Oscillation |
| LLB: | Lower Left Banana state |
| LLC: | Linked List Chain |
| LMXB: | Low-Mass X-Ray Binary |
| MC: | Monte Carlo |
| MJD: | Modified Julian Date |
| NB: | Normal Branch |
| NBOL: | Normal BOundary Layer |
| NS: | Neutron Star |

OC: Outer Cloud
PCA: Proportional Counter Array
Pc: Parsec
PCU: Proportional Counter Unit
QPO: Quasi-Periodic Oscillation
RAKED: RAdiative KEplerian Disk
RA: Right Ascension
RXTE: Rossi X-ray Timing Explorer
SAA: South Atlantic Anomaly
Sco: Scorpius
SED: Spectral Energy Distribution
SIMS: Soft Intermediate State
SMBH: Super-Massive Black Hole
SPH: Smoothed Particle Hydrodynamics
SS: Soft State
TANS: TCAF Around Neutron Stars
TCAF: Two-Component Advective Flow
TVD: Total Variation Diminishing
UB: Upper Banana state
WD: White Dwarf
XRB: X-Ray Binary

List of useful commands

- gFTP:** gFTP is a free/open-source multithreaded File Transfer Protocol client program. A text-user-interface is also available which is named 'sFTP'.
- makegti:** Creation of Good Time Interval file, specifics of time-window, intended PCUs, offsets can be mentioned.
- powspec:** Creation of Power Density Spectra from a Light Curve.
- rbnpha:** Rebinning of unbinned background spectral data.
- rddescr:** Channel descriptor creator.
- runpcabackest:** Creation of background spectral estimate file for both bright and faint sources.
- saextrct:** Extraction of Array Mode Science data.
- sefilter:** Useful for extraction of event mode data.
- wget:** GNU Wget is a computer program that retrieves content from web servers.

Chapter 1

Introduction

The scientific method of studying nature comprises of the following steps: 1. systematic observation, 2. measurement, and experiment, and 3. the formulation, testing, and modification of hypotheses (Def. Oxford English Dictionary). This method has been used since the 17th Century to make sense of nature and formulate the laws of nature. One of the most remarkable achievements of this method is that it allows skepticism (in the form of peer-review) which is still at the core of any progress made in the field of science. The institutionalized dis-confirmation amongst scientists filters the conjectures which do not reflect the reality and only propagates the bare minimum facts. This is the reason why the cumulative knowledge gathered since the introduction of the method has lead to solid theoretical basis of physics. In simpler terms, the intended property of the system of interest is observed systematically and independently, multiple times. The measurements are taken, independent of each other. If the study does not have a pre-assigned theory, a hypothesis is proposed empirically. Then, further repeated experiments are carried out to test the hypothesis, either leading to solidification of the theory or a modification of it.

In the last 70 years or so, the advancement of technology and theories went hand in hand, which has lead to an exponential boom in the field of physical sciences. The field of astrophysics is one of the key areas where this progress has been monumental. But, what sets this field of study apart, is the the lack of the second part of the second step: (controlled) experiments. In most cases of astrophysical studies no table-top experiments are possible as the objects being studied show extreme variations of physical condition (density, temperature, magnetic fields etc.) which can not be replicated at Earth. This made the study of astrophysical systems extremely difficult. The only information about the systems available to us are the observed data. As detectors developed in leaps and bounds after the invention of semi-conductors, it helped in the design of better, accurate instruments, covering a broader range of the electromagnetic spectrum. The acquired data shed light on previous theories: some held true, some did not. New data also lead to newer questions and models for their explanations. The lack of tuning capabilities for the systems did not stop the progress; rather propagated the surveys and cataloging of observed results. This catalogues and surveys were and are still useful in making initial estimates of the systems and curate the observations. At its present from, study of astrophysical systems are carried out at vast number of observatories: ground based, satellites or even using the Earth as a whole (e.g. Event Horizon Telescope). The systems are studied using km waves to gamma rays, to probe different regions of the system which emits in different wavelengths. Data archiving and analysis have also become robust, systematic and easy with passing years.

Given this setup, the design of the thesis was done keeping observations as the test of the works carried out. The information associated with photons detected are: energy, time of arrival

(and polarization, if possible). The binning of photons w.r.t energy generates spectra, binning with time generates lightcurves. So, the spectral and temporal properties are the ways we can peek into any astrophysical system. In this regard, one such class of objects which show significant spectral and temporal variations, which makes them optimal for studying, is compact X-ray binaries. The compact objects in the universe are those which are not disrupted by the gravitational pull of other nearby objects. The strong gravity of these objects are attributed to the genesis of their compactness. The compact objects are born after the “death” of a star, i.e, when a star has burnt up all it’s nuclear fuel to succumb to its self-gravity, it settles into a compact object. Depending on the initial mass, the stars end up into one of the different types of objects, broadly classified as White Dwarfs (WD), Neutron Stars (NS) and Black Holes (BH). After the nuclear fuel at the core of a star burns up, the generation of thermal energy and hence, thermal pressure, comes to a halt. The core collapses as a consequence of this. The degree of collapse depends on the balancing forces which are present. For white dwarfs, the electron degeneracy pressure supports the gravitational pull. In case of a neutron star, the support is provided by neutron degeneracy pressure. If, the mass of the dying star is above a certain limit, these pressures are unable to balance the gravitational pull of the core and the star collapses completely onto a singularity (see, appendix A for a detailed discussion), forming a black hole. These X-ray binaries are active in the soft and hard X-rays (0.1 to 300 keV) during accretion of matter onto them. This high energy radiation is generated due to the release of gravitational energy from deep within the gravitational potential (appendix A).

Out of these 3 types of objects, stellar mass black holes and neutron stars show many similarities in their spectral (Fig. 1.2a and 1.3) and temporal features (Fig. 1.4a). This is due to their closeness of mass and size, and the similarities of their companion stars which supply matter through accretion. In comparison, the spectra of a supermassive black, peaks at a different energy range and has other radiation mechanism which dominate the features (see, Fig. 1.2b). However, the spectra of NS shows multiple peaks and power-laws (Fig. 1.3), and requires more components to fits phenomenologically. A one-to-one correspondance between 3 types of QPOs in BHs and NSs can be found in low frequencies (Fig 1.4a), but multiple kHz QPOs are also seen in the power density spectra of the NS sources, which are not seen for BHs (Fig. 1.4b). These similarities and differences are explored in detail in the next two Chapters.

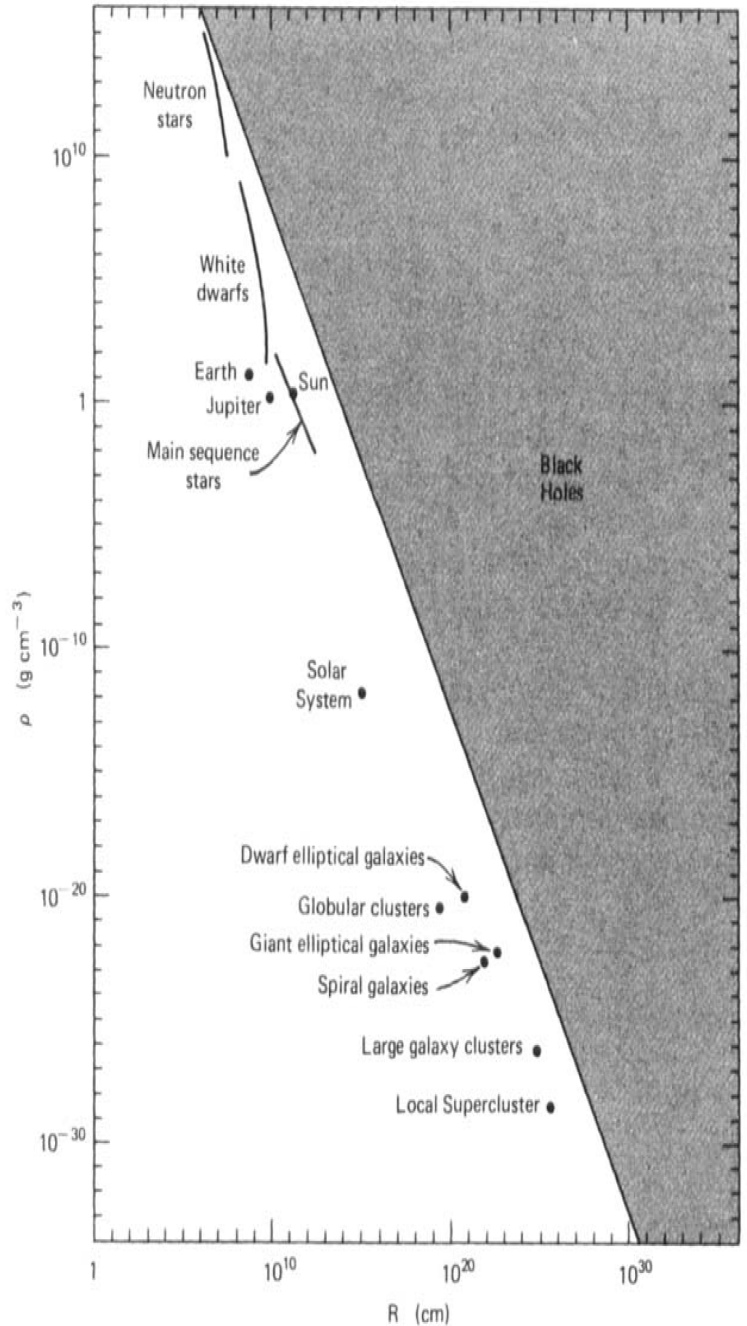


Figure 1.1: The average density and radii of different astrophysical objects (Shapiro and Teukolsky 1983). White dwarfs and neutron stars occupy the high density and low size domain, along with the stellar mass black holes. However, as the average volume of a black hole increases more rapidly with mass, the average density of a black hole decrease with increase of mass.

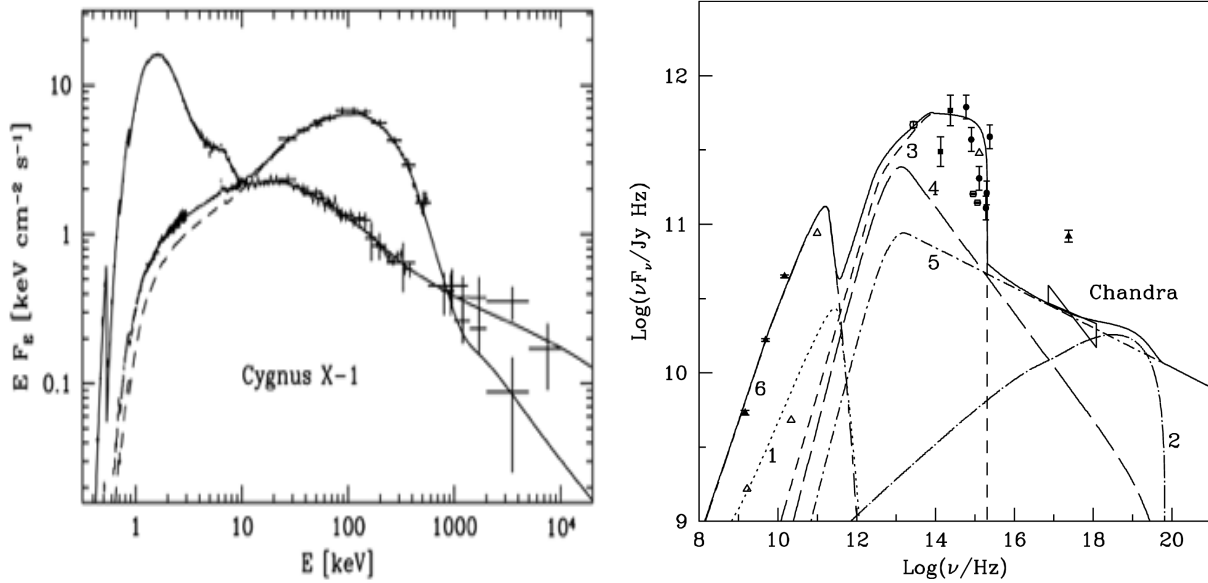


Figure 1.2: Panel 1: Spectra of Cygnus X-1 in hard (peak $\sim 100\text{keV}$) and soft state (peak $\sim 1\text{keV}$) from Gilfanov 2010. Panel 2: Spectra of super-massive black hole M87, from Mandal and Chakrabarti (2008). Contributions from 6 different radiation mechanisms are shown.

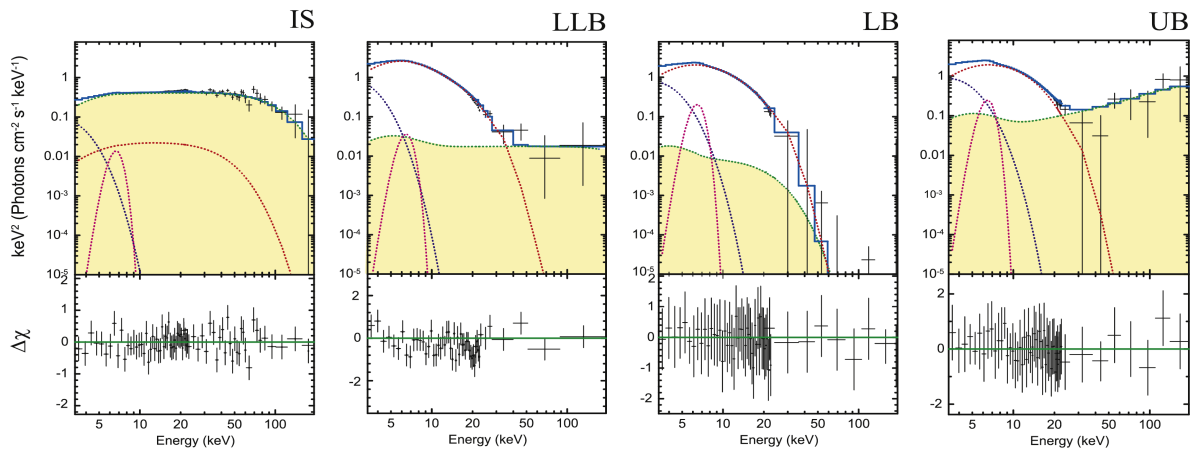


Figure 1.3: Spectral variation of Atoll NS LMXB 4U 1705-44, from Seifina et al. 2015. Four spectral types: 1. Island State, 2. Lower-Left Banana, 3. Lower Banana, and 4. Upper Banana, are shown here. These classifications are based on the position on the colour-colour diagram, following van der Klis 1989. Here, the fits were obtained using two COMPTB components, a blackbody for the lower energy, for the continuum and a Gaussian for the line emission at around 6.5 keV.

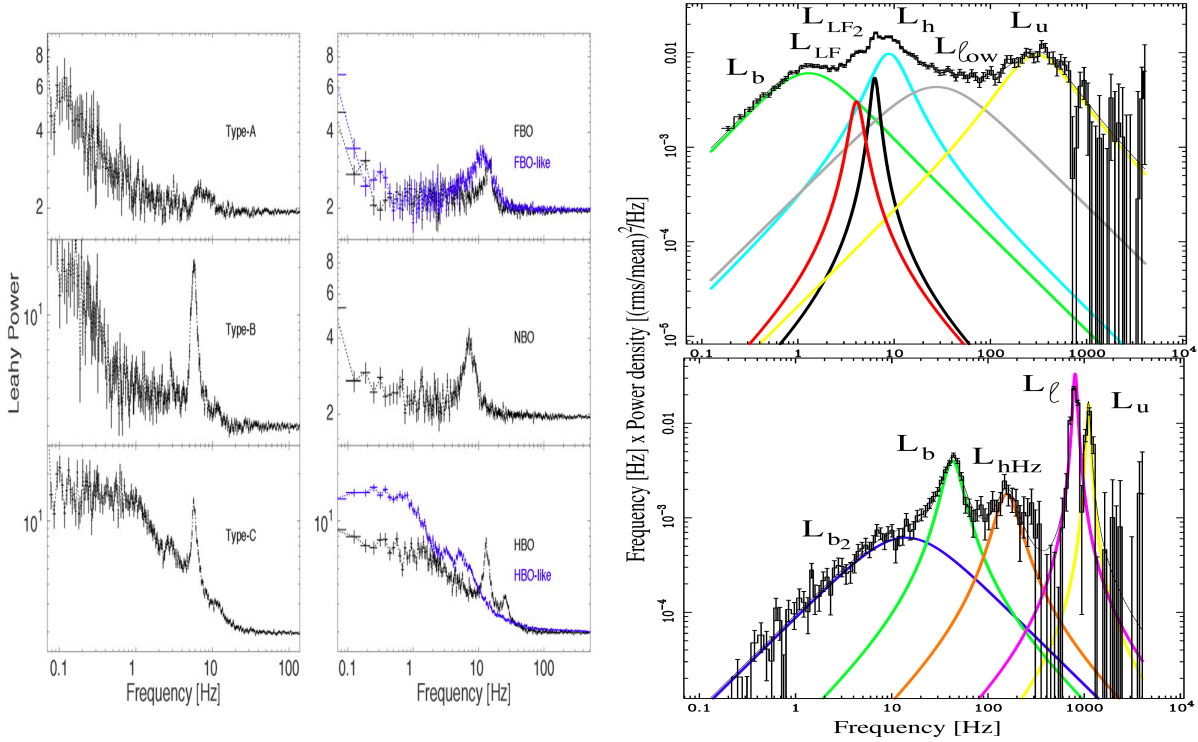


Figure 1.4: Column 1: Similarities of LFQPOs of black holes and neutron stars. The A, B and C type QPOs have a one-to-one correspondence with the FBO, NBO and HBOs. Examples of QPOs from BH LMXBs. From top to bottom, QPOs are taken from XTE J1859+226, GX 339-4 and again GX 339-4. Column 2: Examples of QPOs from NS LMXBs. From top to bottom, QPOs are taken from GX 17+2 and 4U 1705-44 (FBO and FBO-like QPOs, respectively), GX 17+2, and Cyg X-2 and 4U 1728-34 (HBO and HBO-like QPOs, respectively). Credit: Motta et al. (2017). Column 3: Different frequencies present in the PDS of a neutron star. The PDS also shows the presence of strong kHz QPOs (detailed discussion on the meaning of different components is present in Chapter 3). Credit: van Doesburgh and van der Klis (2017).

The main questions we wanted to address in the thesis are:

1. Is there a steady state configuration of accreting matter for black hole candidates?
2. Is there a solution which can simultaneously explain spectral and timing properties?
3. Is there a formalism which answers the above questions which can also be applied to neutron stars?
4. Can there be a generalised solution for black holes and neutron stars?

In the next two Chapters, we discuss observational results and theoretical models of accretion around black holes and neutron stars, especially in light of the Two-Component Advective Flow (TCAF) solution (question 1). In Chapters 4 and 5, we discuss the works on spectral and temporal data analysis of two black hole candidates (BHCs) with the TCAF solution (question 2). In Chapters 6, we highlight the key results of our work on the spectral properties of neutron stars with TCAF (question 3). In Chapter 7, the timing properties of shocked accretion flows around neutron stars are discussed (question 3). In Chapter 8, the effects of viscosity in forming discs and boundary layers are discussed (question 3). In Chapter 9, we discuss the formation of TCAF around neutron stars, suggesting TCAF is at the core of a generalized solution for black holes and neutron stars (question 4). We also construct a spectral model, for black holes and neutron stars, based on TCAF and the findings of previous chapters (question 4). We summarize the results in Chapter 10.

In this thesis, we took a minimalist approach in what is kept in detail, what is discussed at somewhat lengthy manner, what is briefly mentioned and what is kept out. We went in detailed analysis of the specific works which are integral part of the thesis and the overall theme of it. This is the reason why the chapters have the individual methods and conclusion sections, to discuss the essential scientific processes used and most important conclusions, all within the same chapter. We do this with the hope that each chapter can be read, understood up to a sufficient degree and be interpreted independently. To complement each chapter and avoid redefining terms, two separate sections are included before the text: “Abbreviations, Acronyms and Initialisms” and “List of commands”. Independent of where these have been used, the list can be used for further assistance.

In order to keep the thesis compact and to avoid repetition of standard and/or oft-used topics, which are covered in an in-depth manner in books, papers or theses of previous works related to this one, we strictly avoid restating those topics, unless it is done so in a new light. Whenever such a situation arose, which it does quite often, we refer to the books that have been followed, the theses of those, which discuss the implementation of such schemes, and we use those schemes as-is. We have used four separate techniques for simulation and data analysis. Efforts have been made to maintain brevity and originality of the text. It is also believed that the works that have been published and/or submitted for review contain the best possible versions of the work, largely due to the extensive peer reviews, and in parts due to sticking to a clear goal. Thus, only those results, which are integral to the theme, are included rather than all the simulations, analysis which were carried out during the last five years. This reduced digressions and increased the efficiency of stringing the chapters together. For the same reason, equation of theoretical models, solutions are also not included unless they are directly used. For completeness, the references for those texts are given for anyone who is interested. Three separate appendices have been added for basic theoretical concepts which underline the broader subject of the thesis. These were kept out of the

main text as a more specific case or form of these equations or laws have been used in the work and are discussed in relevant chapters. We traded a lengthy paragraph or a sequence of equations for a diagram, plot or image wherever applicable. We also refrain from using the summary as a restatement of the conclusions of the previous chapters, rather we briefly discuss how each chapter, successfully or otherwise, fit within the theme and serve their purpose in fulfilling the objectives of the thesis. This also leads to a smoother transition towards the future plans which are, although related, fall outside the plan and context of the thesis.

Chapter 2

Modelling of accretion flows around Black Holes

ABSTRACT

In this Chapter, we first go through observational and theoretical developments on the accretion processes around BHs before the TCAF solution was conceived. We do so in a somewhat chronological way to highlight how observations shaped the way theories were constructed, how some models failed to explain newly observed data and how a common thread can be found which pointed to the TCAF being at the core of the accretion flow process around BHs. We loosely follow the review article by Chakrabarti 2002. We summarize the cases most relevant to the thesis. For a detailed and broader outlook refer to Chakrabarti (1996; 2002; 2015; 2017). We also show gradual development of the TCAF paradigm starting from Chakrabarti 1989 to Chakrabarti 1997. Applications of TCAF around BHs, from 1997 to 2019 have been mentioned as well.

In order to give an idea of the chronological developments of accretion flows around black holes, we start with the first studies of accretion process, rather than the theoretical predictions or the observational evidence of black holes.

Major observational and theoretical results before TCAF

1950s

The problem of how much matter would a star gather while moving through the interstellar medium was first studied by Hoyle and Lyttleton in 1939. They ignored the effects of pressure to study the axisymmetric particle accretion through a shock front. The pressure effects were taken into account by Sir Hermann Bondi in 1952 when he computed the mass accretion rate onto a star at rest within an infinite cloud of gas. The results clearly showed that matter, that was subsonic at a large distance, can become supersonic at the star surface. Bondi's results also indicated in which direction the study of accretion would proceed in the following decades. The heat, generated from geometric compression alone, may be lost and the required pressure at the inner edge may be diminished allowing a much larger inflow rate. The polytropic index γ would become close to unity near the star due to this non-adiabaticity. The results also pointed out that a correct understanding might require a time-dependant solution. The reproduced results of the Bondi flow, as per the method mentioned by Chakrabarti in the *Theory of Transonic Astrophysical Flows* in 1990, are given below.

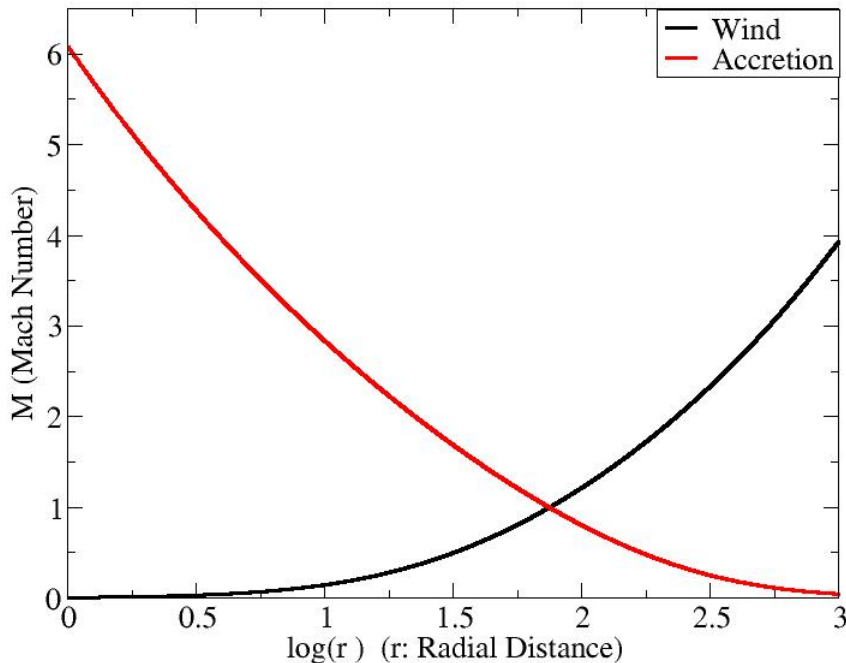


Figure 2.1: Transonic solutions of the ‘Bondi Flow’ around a spherically symmetric object, reproduced with the prescription by Chakrabarti 1990. The sonic point is at $r_c = 75$.

Important results from solar physics influenced the study of accretion in the following years. Biermann's suggestion of explaining the behaviour of cometary tails by assuming outflows from a solar surface (1951; 1952) was explained by Parker (1958). His solution in 1958 was similar to Bondi-flow solution apart from the fact that it generated at a smaller radius and went to infinity. The flow was driven by thermal pressure and resulted in one of the subsonic branches crossing the sonic point to become supersonic. This not only explained the velocity of solar winds at Earth's orbit but also proved to be important in the subject of solar and stellar winds, and for astrophysical jets, in general.

On the observational front, the ground based instruments came up with some pioneering results. The first of the double radio sources was discovered when Jennison and Das Gupta (1953) first resolved the two radio blobs of Cygnus A in 1953. The train of optical knots seen emitting from M87 were termed as 'jets' by Baade and Minkowski in 1954, who proclaimed that these must be ejected from the nucleus of a galaxy. The study of cosmic radio jets began with this discovery. This emission of powerful radio jets were indirect evidence of the presence of massive black holes at the centers of active galaxies.

1960s

The instrumental advancements set in due to post-war scenario, lead to increased observations in radio frequency. They became popular and lead to many new discoveries in this decade. Solar wind observations were much easier compared to those of radio jets of galactic nuclei which lead to the advancements made in improving the wind solution (of Bondi flow) by additional physics. However, the Bondi solution was satisfying enough to prompt workers to apply this model to explain various know observations of star-gas interactions. The very first Quasi Stellar Object (QSO), 3C272 was discovered in 1963. Hazard, Mackay and Shimmins (1963) observed the object by the radio occultations of it's moon with Parkes 210 feet radio telescope. They found two distinct radio sources and located their positions. M. Schmidt (1963), obtained the redshift of Hydrogen emission lines by optical measurements. This clearly showed the need of exchanging data and results, at early developing stage of the subject. In the Texas symposium, held in the same year, various explanations were proposed which converged to the idea that the vast amount of energy released from the QSOs must be gravitational in nature. Salpeter, in 1964, used the Schwarzschild solution of 1916 and interpreted that the luminosity could be due to Bondi accretion on a very massive compact object with mass $> 10^7 M_{\odot}$. He also concluded that for a galaxy such as ours where the mass of the central object is around $10^6 M_{\odot}$, and where heavy dust grains are present in the interstellar medium, the time scale of such a collapse exceeds well beyond $10^8 years$ due to radiation effects alone. These objects were termed as 'collapsed matter' or 'collapsers' as the term 'black holes' was still not coined. The term 'black hole' was first used by J. Wheeler in 1967. For a reasonable set of parameters, the luminosity was computed to be $10^{47} ergs sec^{-1}$. Whether the QSOs were local objects or they were cosmological in nature, the confusion persisted.

In 1966, Zeldovich and Guseynov remarked on the existence of such 'unseen' compact objects. There were several binary systems in which the the companion was an 'unseen' yet massive compact object which indicated that a 'collapsed star' should exist in these systems. The typical luminosities of such quasars is about $10^{44-47} ergs sec^{-1}$ (or in terms of mass, a destruction of $\sim 0.002 - 2 M_{\odot} yr^{-1}$ completely at each quasar). This tremendous activity was thought to be caused by accretion close to Eddington rate, on super-massive black holes, as strongly argued by Lynden-bell in 1969.

The major breakthrough in the theoretical front was the vacuum solution of Einstein equation

for a rotating compact object, which was derived by Roy P. Kerr in 1963. This introduced a new metric where the mass and spin of the black holes were the parameters that decided the gravitational field around a spinning object. Most of the black hole candidates detected so far, are Kerr black holes with different values of spins.

Further observations on Active Galactic Nuclei revealed that QSOs were only a special case of such objects. Many forms were identified: line-less BL Lacs, fainter Seyfert galaxies, Blazars, Quasars, Optically Violent Variables, Liners etc. Modern day observations lead to a unification of such objects. Supermassive black holes, when viewed from different inclination angle, appear as different ‘objects’ in various phases of it’s activity. Observations also revealed the existence of pulsars and X-ray sources. Towards the end of 1967, Hewish discovered the regular pulses of Radio waves. Two of the interesting models were by Ostriker (1968), who proposed that these were due to emission from the hot spots of a rotating compact object, and by Barnothy and Barnothy (1968), which proposed that the occulting binary companion amplified the radiation of the other Neutron star.

The atmospheric absorption hindered the ground based observations in X-ray. The development of rocket technology lead to observation up to smaller X-ray energies. The Aerobee rocket, mostly used for high atmospheric and cosmic ray research in the 1950s, were used to detect X-ray sources. Giacconi used these to discover X-ray sources in 1962. During 1962-1966, the positions of sources such as Cygnus region, Scorpius X-1 and Crab Nebula were determined. The first black hole candidate, Cyg X-1, was also discovered in this attempt (Giacconi et al. 1962; 1965; Gursky et al. 1966). The existence of an unseen companion was also seen from simple binary accretion models. The Palomar plates, a catalogue of observations, were also used to carry out optical measurements. Axford and Newman (1967) included viscosity and thermal conduction to find the modified solutions of Bondi flows and winds, simultaneously. The solutions included weak shocks for both the branches. Further work with complex interactions were also carried out in this decade which lead to the formation of bow shocks.

1970s

Whereas the discovery of black holes, from Radio and X-ray observations, prompted many to device simple models of accretion flows and theory of black holes in the 60s, the 70s saw the competition to come up with “working model”. Diverse, simplistic yet bold, models were proposed. The advent of better satellite observations and the competition to conjure a realistic model lead to confusion in many fronts. The spherical accretion was not radiatively efficient enough to explain the observed spectra of QSOs and it ignored the angular momentum of inflowing matter. The lack of any hard surface of black holes, also raised the point that outflows or jets observed must originate from the accretion flow itself. Thus came forward many models which tried to address these issues.

One of the key signatures of a rotating (Kerr) Black hole, was the presence of double-horn pattern (due to Doppler Shift) of line emission from accreting flow. Many researchers (e.g., Wyller 1970) identified this property and were investigating objects in this respect. Bardeen (1970) made the suggestion that by the time the mass of the accreting matter is more than 50% of the initially non-rotating black hole, the black hole is more likely to become an extremal Kerr black hole for which the spin parameter $a \sim 1$. Although it was remarked that the radiation effects would slow it down to $a = 0.998$ (Thorne 1974).

In 1972, Pringle and Rees, discussed at length about accretion onto a black hole or a neutron star when the matter possesses angular momentum. The cases in presence of magnetic field for a

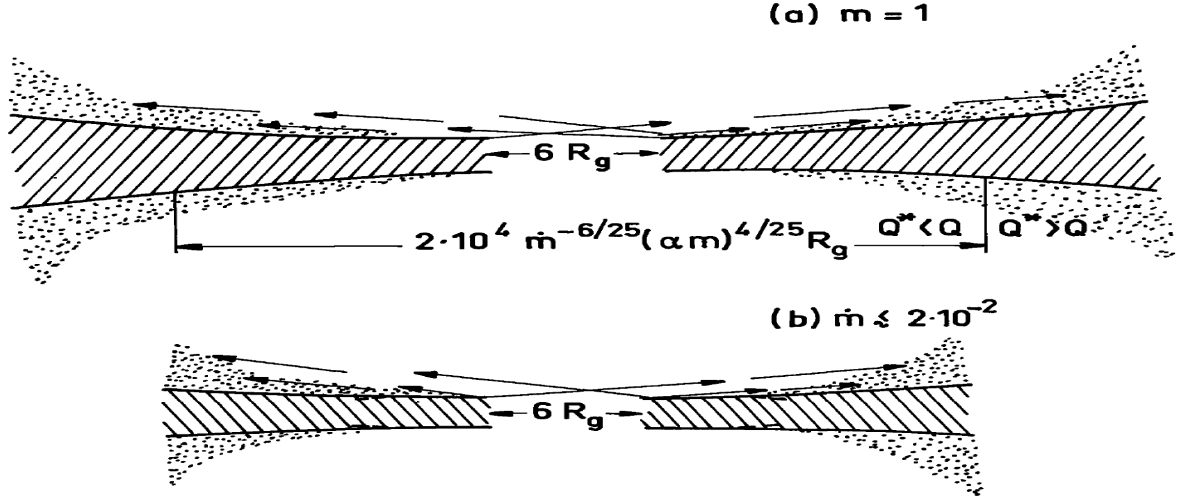


Figure 2.2: The optically thick and geometrically thin ‘standard-disc’ by Shakura and Sunyaev (1973). Bondi flows had low densities to produce the observed luminosity of black holes. This was tackled in this scenario by rotating Keplerian disc which emitted a multi-colour blackbody spectrum. This disc, however, had no advective motion and was assumed to be static.

neutron star was also discussed. This gave a quantitative idea about the spectra emerging from the accretion, which were compared with the observed results of the black hole source Cygnus X-1 and neutron star Centaurus X-3. The flaring up of the inner edge which due to 1. low accretion rate leading to low efficiency of radiation and 2. high accretion rate leading to high radiation pressure. These were clearly the precursors of radiation pressure supported thick disc and ion pressure supported tori, which became well used models in the later decades. In 1973, Shakura and Sunyaev wrote a paper on accretion where they assumed the disc to have Keplerian angular momentum distribution, throughout. The disc was truncated at $3r_g = 6GM/c^2$, where r_g is the Schwarzschild radii of the black hole, for stability reasons. The viscosity was assumed to be responsible for the redistribution of angular momentum which settled into a Keplerian one. The heat generated from the viscous effects were assumed to dissipate instantaneously from each radial point. Due to the thin structure, assumed, the only significant component in the viscous stress tensor was the $\omega_{r\phi}$ component and it was taken proportional to the local gas pressure due to thermal motion, i.e., $\omega_{r\phi} = \alpha\rho v_s^2$. Here, α is the proportionality constant, ρ is the density and v_s is the isothermal sound speed. (The name α viscosity came from this). The assumed vertical equilibrium helped in calculating the vertical height at any point and it came out to be very small compared to the radial distance (hence, the name thin disc). It was later in 1993, when Chakrabarti and Molteni corrected the viscous term for a motion with high radial velocity, when they added the ram pressure to the gas pressure and the expression became $\omega_{r\phi} = \alpha\rho(v_s^2 + v_r^2)$, where v_r is the radial component of velocity of matter.

Standard disc model: The model had two key assumptions:

1. Matter rotates in circular Keplerian orbits around the compact object.
2. The disc is thin, i.e., half thickness of disc at a radius r , ($H(r)$) is very small compared to the radial distance.

$$H(r) \ll r.$$

The case with Newtonian geometry was studied by Shakura & Sunyaev (1973). The general

relativistic effects were included in the study of Novikov & Thorne (1973). In these models, viscosity served in carrying out the angular momentum from one layer to another layer of Keplerian orbit. This makes the matter spiral inward. The loss of gravitational energy as the matter moves inward, partially increases the kinetic energy and partially converts to thermal energy and is radiated away from the disc surface. The accretion rate (\dot{m}) and viscosity parameter controls the structure of the disc and spectrum of radiation.

For the steady state disc, the radiation energy flux radiated from the disc surface at radius r is given by Shapiro and Teukolsky, in 1983.

$$F(r) = 5 \times 10^{26} M_{bh}^2 \dot{m}_{17} (2r^{-3}) (1 - \sqrt{\frac{3}{r}}), \quad (2.1)$$

where, M_{bh} is the mass of the black hole, \dot{m}_{17} is the mass accretion rate in the units of $10^{17} g s^{-1}$ and r is in $2GM_{bh}/c^2$ unit.

Since the Shakura-Sunyaev disc is optically thick (optical depth $\tau > 1$), the photons interact enough number of times with the gas particles to produce a black body radiation spectrum at each element of the disc-face with surface temperature $T_s(r)$ obtained by equating the dissipation rate to the blackbody flux, and hence, the local effective temperature is given by Shapiro and Teukolsky (1983),

$$T_s(r) = \left(\frac{F(r)}{\sigma}\right)^{1/4} = 5 \times 10^7 M_{bh}^{-1/2} \dot{m}_{17}^{1/4} 2r^{-3/4} (1 - \sqrt{\frac{3}{r}})^{1/4}. \quad (2.2)$$

where, σ is the Stefan-Boltzmann constant. In case of accretion around a stellar mass black hole, the effective temperature peaks around $1keV$, whereas for supermassive black holes, the radiation emitted from such a disc is in the ultra-violet region and is widely known as the big-blue bump (e.g., Malkan & Sargent 1982; Malkan 1983; Sun & Malkan 1989; Chakrabarti 2010). For $\dot{m} \sim 10^{17} - 10^{18} g s^{-1}$, the radiation from the standard thin disc around a $10M_{\odot}$ black hole generally extends up to $1 - 10 keV$.

The UHURU satellite, intended for astrophysical observations, was launched on December 1970. This opened up the front of more observations on black hole candidates such as Cygnus X-1. Schreier et al. (1972) reported the 73ms variability of this source, which was confirmed only recently in 1994 to be Quasi-Periodic Oscillations by Vikhlinin (1994).

In the succeeding year of the publication of standard disc model, Lightman and Eardley (1974) pointed out that the constant value of viscosity, as assumed in the model, would lead to inconsistency in a radiation pressure dominated region, leading to breaking down of the disc into thin rings. Thorne and Price, in 1975, pointed out that the spectrum of Cygnus X-1 could not be explained by the Shakura-Sunyaev disc. To address this problem, Lightman and Shapiro (1975) came up with their version of a single component disc with two temperatures, which flared up near the inner edge. Although, it was reasonably fitting the X-Ray data of Cyg X-1, the disc was proven to be thermally unstable, by Pringle (1976).

Similar X-Ray observations (Katz 1976) carried out on several black hole candidates revealed that the spectrum had two components, the X-Ray bump was explained by a multicolour black-body and the relatively harder power law component was explained by the Comptonization of soft photons by the ‘magnetized corona’. The geometry considered was Newtonian and thus, had an improper inner boundary condition. The two components were thought to be of two different states of the system, the ‘soft state’ with the multicolour blackbody and the ‘hard state’ with the

power law. The nomenclature is still used in the literature. In 1977, Ichimaru, came up with the notion of two distinct solutions of the same disc, which corresponded to the two different spectrum. The inner part was puffed up in both the cases. Depending on the outer boundary conditions, the flow at a distance, one of the branches became optically thin which emitted the hard X-Ray and the other settled into the optically thick branch which emitted the soft X-rays. The optically thin solution with the imposed condition of self-similarity (i.e., the lack of any length scale) lead to the Advection Dominated Flow (or ADAF; Narayan and Yi, 1994). Hoshi and Inoue (1988), found similar transition from optically thin to optically thick solution when they considered X-ray irradiated discs. It was understood that the bimodal behaviour holds the key to explaining the two states of the spectra.

Incorporating general relativity in the accretion disc picture, seemed like the next logical step. Bardeen and Patterson (1975) tried explaining the behaviour of matter at large distance ($100GM/c^2$ to $10^4GM/c^2$) on a tilted disc. Wilson (1974) earlier showed how Kerr metric played a role in changing the axis of axisymmetric flow from the normal to binary plane to other direction. Further and detailed work with Kerr geometry was carried out by Cunningham in 1975. The first significant work in visualizing such a accretion disc was done by Luminet in 1979. He showed how the bending of light would make the disc look warped towards the edges. The bottom half (w.r.t., the viewing direction) would also be visible due the photon bending. The effect of Doppler shift was also shown through numerical simulation, where the matter moving towards the viewer would appear blue shifted and the matter spinning away from the viewer would appear red shifted.

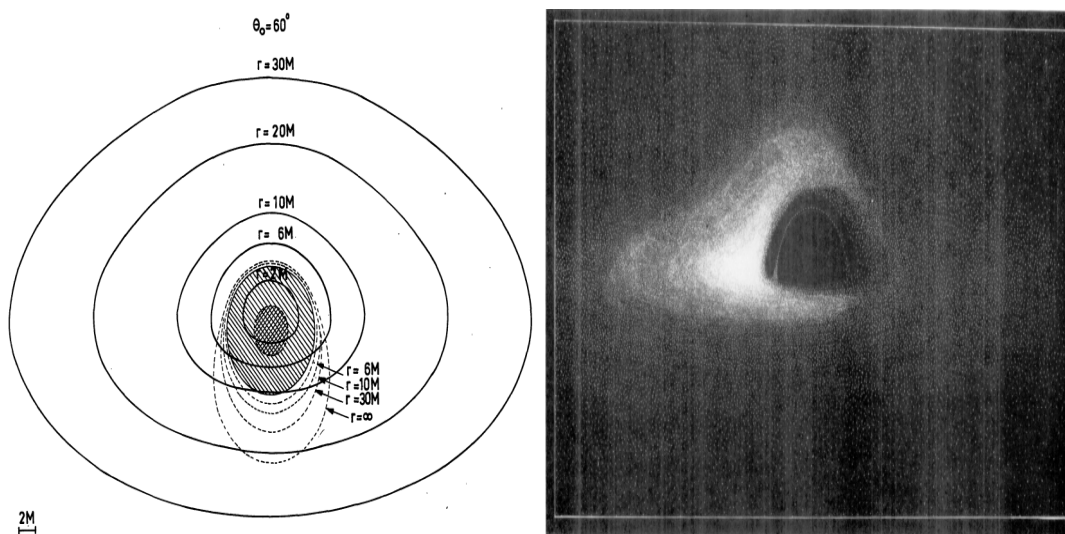


Figure 2.3: Panel 1: Isoradial curves representing rays emitted at constant radius from the hole, as seen by an observer at 30° above the disc's plane. Full line: direct images; dashed lines: secondary images. Image from Luminet (1979). Panel 2: The diagram shows the simulated image of an accretion disc on equatorial plane around a rotating black hole. The Doppler shift makes one side appear brighter than the other. Image from Luminet (1979).

Heating and cooling effects were added to Bondi flow to study the spherical accretion in further details. Michel extended the work on the adiabatic flow in a fully general relativistic form, in 1972. Effects of tangled magnetic fields, pre-heating on the luminosity of the accreting flow were carried

out. The limiting value of accretion rate was investigated in presence of such effects and were found to be less than the Eddington limit for black holes, by Shapiro in 1973. The spherical Bondi flow was carried out for a neutron star as well where the inner boundary condition was different. Matter settled down on the surface of a neutron star with zero velocity and the region with such a behaviour was termed as the boundary layer. It was realized that it was a part of the flow itself (Shapiro and Salpeter 1975). Although black holes lack hard surfaces, the presence of angular momentum creates a similar boundary layer for black holes as well, which will be mentioned later in greater detail. Another way of looking into analyzing the spectrum was to take a steady distribution of density and velocity profiles, with different cooling and heating mechanisms. The study by Meszaros, in 1975, included bremsstrahlung and synchrotron radiation for an isolated black hole accreting from the interstellar media and for a black hole with a binary companion. He assumed the plasma to have a single temperature and attained the variation of that with radial distance. A similar study for Keplerian disc with two temperatures was carried out by Eardley and Lightman in 1975. A supersonic flow must have a shock transition if the fluid pressure is finite in the upstream direction. That means, accretion onto a neutron star, or winds propagating supersonically to a medium of finite pressure must have a shock. Blumenthal and Matthews (1976) studied the general relativistic solutions of the spherically symmetric adiabatic flow. They came up with shock solutions for the case of a neutron star. A previous work by Holzer and Axford, in 1970, in the context of solar wind, showed similar results of formation of shock. As the black holes do not have a hard surface, radially falling matter with a single sonic point between infinity and horizon would have a shock free solution.

Time-dependant numerical simulations started during this decades with the pioneering works by Wilson (1972). He studied the accretion of rotating matter around a Kerr black hole and found evidence of propagating shocks if the angular momentum is high. In his work he kept the angular momentum constant. Further works were done by including pressure terms and effects due to heating and cooling on the Keplerian disc framework. Maraschi, Reina and Treves (1976) drew important conclusions when they included radiation pressure. It showed that the accretion rate can go beyond the Eddington rate without being unstable. This was an important result which contradicted the prior notion of small rate of accretion. The general relativistic case with constant angular momentum, pressure term was studied by Lynden-Bell in 1978. The results showed that the flow would develop giant vortices due to the centrifugal force which would stop matter from reaching the axis.

The realization that matter would flare up towards the inner edge of the disc, be it for the centrifugal force or the thermal instabilities, lead to the arrival of ‘thick discs’. The discs ignored radial motion and in order to explain the origin of jets and outflows, the concepts of ‘vortices’ and ‘funnels’ were brought in. The angular momentum distributions were also assumed in an ad-hoc manner, hence they were not self-consistent.

1980s

The theoretical developments that started in the 70s, were carried forward and cemented in the 80s. Numerical simulations of accretion discs also saw some progress in this decade. Begelman (1978) studied the spherical accretion in Schwarzschild metric for a polytropic equation of state and found one critical point. A similar work was done with a relativistic equation of state by Moncrief (1980), whereas some others worked on non-adiabatic flows as well. When magnetic dissipative heating was added, the sound speed increases enough to reduce the Bondi flow to a subsonic one, hence producing shock waves or non-steady flows. This work was done by Scharleman in 1981.

The effect of $e^- - e^+$ pair production on the emergent spectrum for a spherical Bondi flow was studied by Yahel in Brinkman in 1981, where they found that the $\gamma - \gamma$ interaction pushes the cut-off of the power law to 1 MeV. Thorne and his collaborators (1981), worked in detail on the general relativistic photo-hydrodynamical spherical accretion in the optically thick regime in 1981. The nature of critical points in presence of radiative transfer was studied by Flammang in 1982. Ipser and Price worked on Schwarzschild geometry with synchrotron emission and identified different regions on basis of whether they are important for synchrotron self-absorption or not. The nature of emitted spectrum from a converging optically thick flow, in Newtonian geometry was done by Payne and Blandford in 1981. The spectral index α , where $F \sim \nu^\alpha$, was close to 2. For a general relativistic case, the value was shown to be near 1.5. This is one of the key signatures of a black hole where the bulk motion Comptonization produces such a steep power law dependance (Chakrabarti 1995; 1997; Chakrabarti and Titarchuk 1995). Colpi, Maraschi and Treves came up with the more generalized single temperature solution for Newtonian geometry, in 1984, that showed the Quasar luminosities can be a few percent of the Eddington luminosity. The two temperature models showed the variation of electron and proton temperatures w.r.t. radial distance in the backdrop of a flow distribution. This also indicated that cooling effects would be different for electrons and protons and would lead to them having different temperatures. In presence of Compton cooling, Coulomb coupling and bremsstrahlung and synchrotron emission, the temperature difference can be such that $T_p \sim 1000T_e$. Although these were not able to explain the excess luminosities of, the Keplerian disc formalism with its multi colour black body was there to explain the excess (Sun and Malkan 1989). Wandel and Petrosian (1988) showed that two parameters alone, the mass of the black hole and the accretion rate determine the nature of the spectrum. They found the mass of the Quasar in the range $10^8 - 10^{9.5}M_\odot$ and for Seyferts, it is in the range $10^{7.5} - 10^{8.5}M_\odot$. The line emissions from the active galactic nuclei, are found to be always Doppler shifted. This was proposed to be due to the rapidly rotating cloud around the galactic center, which surrounded the disc from both sides. The variation of Doppler velocity with distance from the center calculated from reverberation mapping (Blandford and McKee 1982) technique. This technique is often used to determine the mass of the AGNs. The greater the motion of clouds, the greater is the Doppler broadening. Any variation in the continuum spectra of AGNs is seen in the line emissions with some time delay. The delay time can be used to measure the distance of broad line emission regions. The masses of NGC 5548 ($8.8 \times 10^7 M_\odot$) and NGC 3227 ($3.8 \times 10^7 M_\odot$) have been determined in this manner.

As the study of accretion physics became more understandable, more and more astrophysicists joined in from across different branches. As a result, they brought in their expertise and shortcomings to the subject. In 1981, Cox tried to explain the quasi-periodic oscillations in accretion discs around dwarf novae. This work was extended in relativistic domain by Nowak and Wagoner (1991) in the next decade and disco-seismology was initiated. Whereas some proposed that trapped photons oscillated to produce the QPOs (Kato 1978; Kato, Honma and Matsumoto 1988), some others believed that it was the shock oscillation in accretion columns that lead to the QPOs.

The most significant breakthrough came, when Paczyński and Wiita (1980) came up with a reduced potential which mimicked the effects of general relativity fairly. They presented the following form of potential:

$$\Phi = -\frac{GM}{r - \frac{2GM}{c^2}}.$$

where, G is the gravitational constant, M is the mass of black hole and c is the velocity of light in vacuum. The details of this potential has already been discussed in the Chapter where we talked

about the geometry around black holes. A similar potential, which captured the essence of general relativity, was devised for Kerr metric by Chakrabarti and Khanna (1992). It was perfected by Chakrabarti and Lu in 1995. The effective potential is written as:

$$\Phi(r, \theta) = 1 - \frac{1}{r - r_0} + \frac{r_1 a l}{r^3} + \frac{(1 - 2/r) l^2}{2r^2 \sin^2 \theta}.$$

where the added θ component extends the description to motion away from the equatorial plane. It was realized (Chakrabarti and Mondal 2006; 2007), that beyond the marginally stable orbit ($r = r_{ms}$), the flow velocity increases to meet the inner boundary conditions and the disc cannot remain Keplerian in that domain. It was thought that either the thick disc was a valid picture near the black hole or a sub-Keplerian component is generated from the Keplerian flow of the standard disc near the black hole.

Thick disc: The assumptions of modeling this disc were:

1. The disc is geometrically thick, i.e,

$$H(r) \sim r.$$

2. The pressure gradient term in Euler equation cannot be neglected and thus, the angular momentum does not remain Keplerian (Rees 1984; Chakrabarti 1996).

The disc becomes thick as the pressure effects are significant. The sound speed $a \sim (GM_{bh}/r)^{1/2}$ (Rees 1984; Chakrabarti 1996). Pressure can become significant for either of the two reasons, giving rise to two different models.

1. Radiation pressure dominated thick discs are formed when accretion rates onto the central object is super-Eddington i.e., when $\dot{m} > \dot{m}_{Edd}$. For such accretion rates, luminosity of accretion disc becomes comparable to or exceeds the Eddington luminosity. Radiation pressure causes the accreting flow to be sub-Keplerian and puffs up the disc geometrically. Structure of such disc becomes that of a torus and a funnel wall is produced around the rotation axis of the matter (Rees 1984; Chakrabarti 1996; 2010). Radiation escapes through this funnel (Rees 1984; Chakrabarti 1996).

2. Ion pressure dominated thick discs are formed when accretion rate is very small and the flow cannot cool because of inefficient radiation process (Rees 1984; Chakrabarti 1996). In such cases, internal energy is stored inside the disc which increases its temperature comparable to the virial temperature. The disc puffs up because of this (Rees 1984; Chakrabarti 1996).

However, in these thick discs, the advection terms has not been taken into account and thus, these are not transonic and it is not a complete solution from infinity to the horizon.

Slim disc: Assumptions of the slim disc, proposed by Abramowicz et al. in 1988, were:

1. Contribution from both advective term and pressure gradient term.
2. Moderate super-Eddington accretion rate, i.e., $\dot{m} \approx \dot{m}_{Edd}$.
3. Geometrical structure is neither thick, nor thin ($H(r) < r$).

However, this type of disc model is not fully self-consistent (Ryu 1998, Chakrabarti 2002). For instance, Abramowicz et al. (1988) gave examples of a disc with 50 times critical rate (800 times the Eddington rate) and the angular momentum sometimes decreased outward. Such a distribution would be unstable and not seen in nature.

More general solution were found by Chen and Taam (1993) in the next decade where they pointed out that most of the viscous heat is advected towards the black hole.

Next, we discuss one of the most successful models which is based on the earlier theoretical solutions of Chakrabarti (1990), namely, two-component advective flow (TCAF) model, proposed

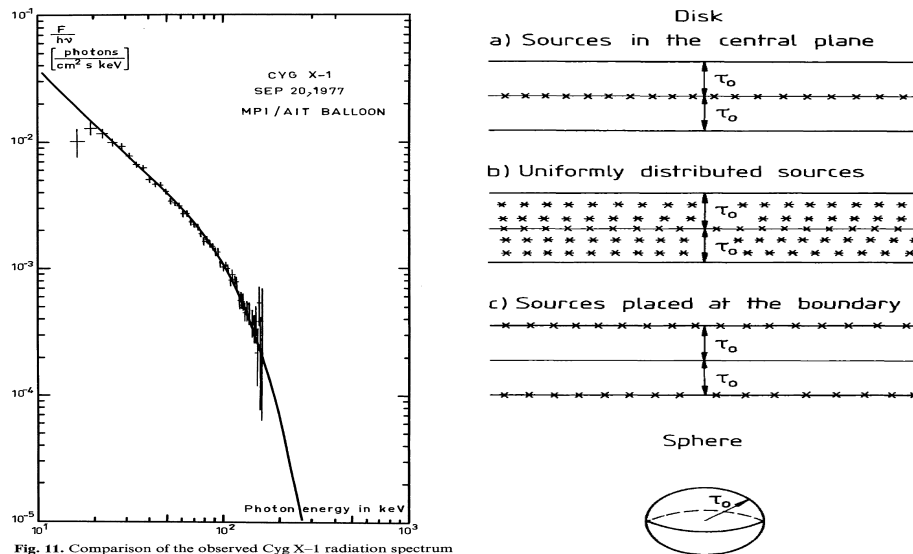


Fig. 11. Comparison of the observed Cyg X-1 radiation spectrum (Voges et al., 1979) with the spectrum resulting from Comptonization of low frequency photons in the plasma cloud with $\tau_0 = 5$ and $kT_e = 27$ keV

Figure 2.4: The additional power-law component, which was required to fit observed spectra, was proposed to be a result of Compton scattering of disc photons in a cloud near the disc by Sunyaev and Titarchuk (1980; 1985). The fit of Cygnus X-1 with their Comptonized spectral component is shown in panel 1 [from Sunyaev and Titarchuk (1980)]. In panel 2, the geometries are listed, for which analytical results were obtained [from Sunyaev and Titarchuk (1985)].

by Chakrabarti (1995, 1996), which explains the spectral and timing properties of the accretion disc quite satisfactorily [e.g., Chakrabarti & Manickam (2000); Nandi, Manickam, Rao & Chakrabarti (2001); Chakrabarti et al. (2002; 2003; 2005; 2008; 2009); Dutta et al. (2010); Debnath et al. (2010); Pal et al. (2011); Nandi et al. (2012)].

Sunyaev and Titarchuk (1980; 1985) showed the variation of spectra of hard photons with some geometric structure of Comptonizing clouds, which intercepted soft photons from a standard disc and re-radiated them.

Development of TCAF paradigm

The 90s saw a clear shift from Keplerian Disc paradigm, which dealt with matter of high angular momentum and low advection velocity, towards the advective disc paradigm, which took the radial motion into account and tried to solve the accretion problem self-consistently. It was done to explain observations under the paradigm of a single framework, rather than relying on different models for different observational results.

The goal of unifying all the possible scenarios, including every possible physical process, viz., heating, cooling, pair production etc. in a time dependant manner in a totally general relativistic framework, was not fulfilled, but some significant progress were made in this decade.

The most significant breakthrough in this field came in 1989. Chakrabarti derived the hydrodynamical solution for flow in vertical equilibrium, on the equatorial plane. It was done for an inviscid flow, by solving the mass and momentum conservation equations. In 1990, the solution for viscous flows considering the energy conservation equations were done. The introduction of shock conditions (adiabatic, isothermal or isentropic) in the astrophysical transonic flows showed that matter can only enter the black hole following certain topologies, when the specific angular

momentum and energy are specified. All possible solution topologies are found w.r.t. the variations of specific angular momentum (λ) and energy (\mathcal{E}) of system. The modification of solutions were studied in detail w.r.t. variation of viscosity. Existence of shocks in the accretion and wind branches came as a natural consequence of solving the conservation equations and the variation of the shock location and strengths were studied w.r.t. variation of α viscosity. The stability of shocks were studied for both the wind branch and the accretion branch.

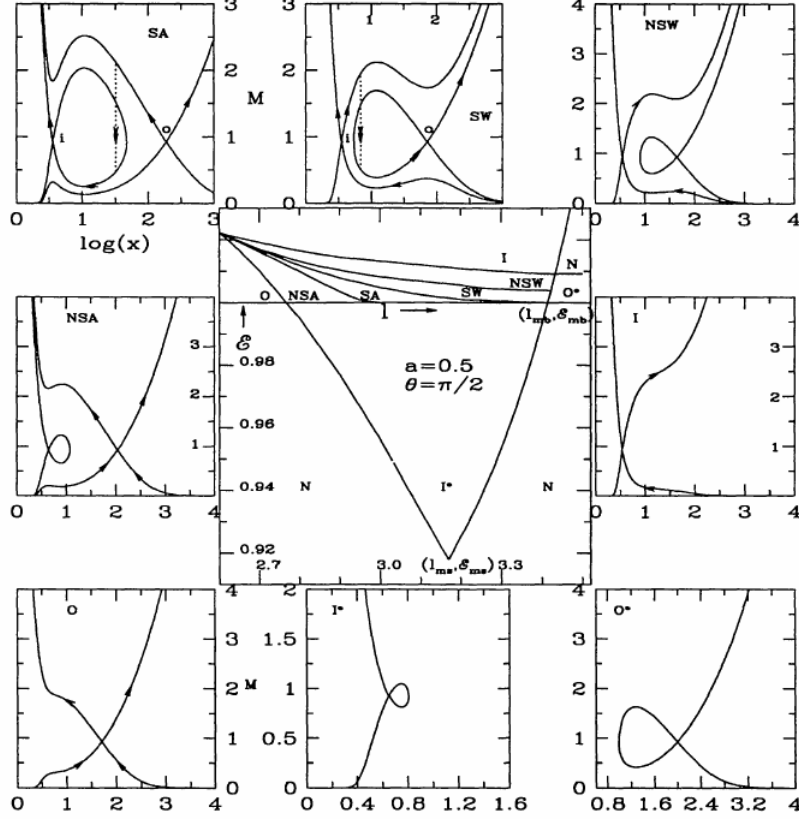


Figure 2.5: The classification of the entire parameter space for a Kerr black hole. Taken from Chakrabarti (1996).

Numerical evidence of formation of shocks using Smoothed Particle Hydrodynamics was found by Chakrabarti and Molteni in 1993, for a flow of constant height. The results for accretion and wind branches are shown in the Fig. 2.6. The mechanism assumes a set of conservation laws which are written w.r.t, a co-moving frame. The pseudo particles have a radius up to which they average or smooth out all the neighbouring interactions. The value of the radius is time dependant at each position and changes according to the resolution needed to deal with the forces present at that location. In Chakrabarti and Molteni (1993), the theoretical shock locations are determined for two sets of parameters, (a) $\mathcal{E} = 0.01095$, $\lambda = 1.90$ and (b) $\mathcal{E} = 0.05571$, $\lambda = 1.75$. The relevant shock locations are $X_{s2} = 2.6$, $X_{s3} = 23.6$ and $X_{s2} = 4.4$, $X_{s3} = 6.04$.

The wind branches are also investigated in this paper. The outer shock location was found to be stable for the accretion branch and the inner shock location was stable for the wind branch.

Chakrabarti, Molteni and Lanzafame in 1994 simulated a 2D flow in vertical equilibrium. Evidence of outflow being generated by the post shock region was also found. The work was done in comparison with hybrid model (Chakrabarti 1990), which assumed the flow to be in vertical equilibrium at radial point. The vertically averaged quantities are used instead of 1D

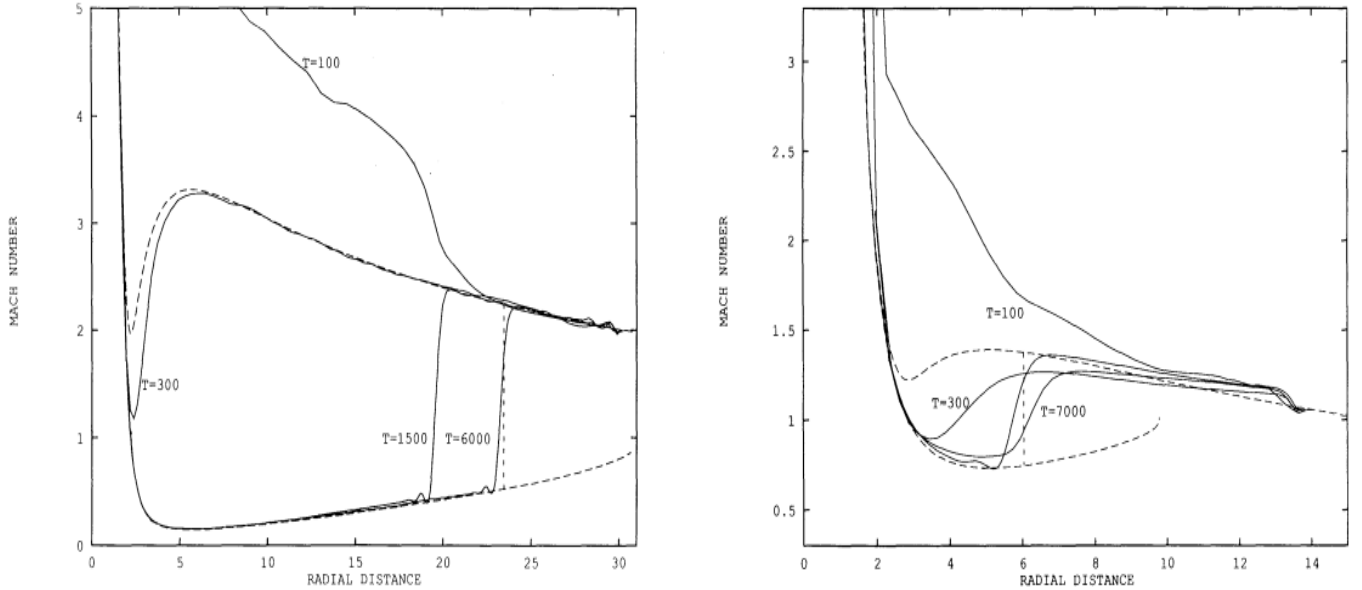


Figure 2.6: Results of numerical simulation for accretion flows from Chakrabarti and Molteni (1993). The parameters specific energy and angular momentum, are denoted as \mathcal{E} and λ , respectively. For panel 1, $\mathcal{E} = 0.01095$, $\lambda = 1.90$. For panel 2, $\mathcal{E} = 0.05571$, $\lambda = 1.75$. The dashed curve shows the analytical pre-shock and post shock branches. Simulated flow, initially unperturbed, lie on the supersonic branch. When the flow is perturbed, shocks are produced, which evolved until they reached the analytical location at X_{s3} (solid curves). Some intermediate evolutionary phases are marked with time since the beginning of the simulation. Vertical dashed lines show the theoretical shock location. In (b), final shock locations with higher (marked with $T = 7000$) and lower viscosities are shown for comparison.

equations. The modified shock conditions are attained. The flow is generated via Smoothed Particle Hydrodynamics (SPH) simulation.

Two Component Advective Flow (TCAF; Chakrabarti 1995; 1997) TCAF model (Chakrabarti 1995; 1997) is based on the physics of shock formation in a sub-Keplerian (low angular momentum) flow (transonic hybrid model). Unlike the Keplerian disc, this flow has a higher radial velocity which can reach up to the velocity of light c at the horizon of the black hole and becomes supersonic (Mach number $M = \frac{v_r}{a_r} > 1$, where, v_r and a_r are the radial velocity and the sound speed, respectively). However, far away from the black holes, the matter is subsonic since its radial velocity $v_r \sim 0$ while $a_r > 0$. Thus, a black hole accretion is always transonic in nature (Chakrabarti 1990). It can be easily shown that a transonic flow is necessarily sub-Keplerian at the sonic point(s) (Chakrabarti 1990). The accreted matter advects the mass, entropy, energy etc. along with it. As the sub-Keplerian flow approaches the black hole, at a certain radius $r = r_s$, the angular momentum becomes comparable to the local Keplerian angular momentum and the matter slows down due to centrifugal barrier. As a result, a shock is formed (Chakrabarti 1989; 1990; 1996). However, the formation of the shock depends on parameters like the specific energy and specific angular momentum of the flow, the heating and cooling mechanisms, and the viscosity present in the flow etc. Because of this shock, the kinetic energy of the incoming flow is converted into thermal energy and the matter is heated up. Therefore a CENTrifugal pressure dominated BOundary Layer (CENBOL) forms around the black hole (Chakrabarti 1995; 1997). Inside the

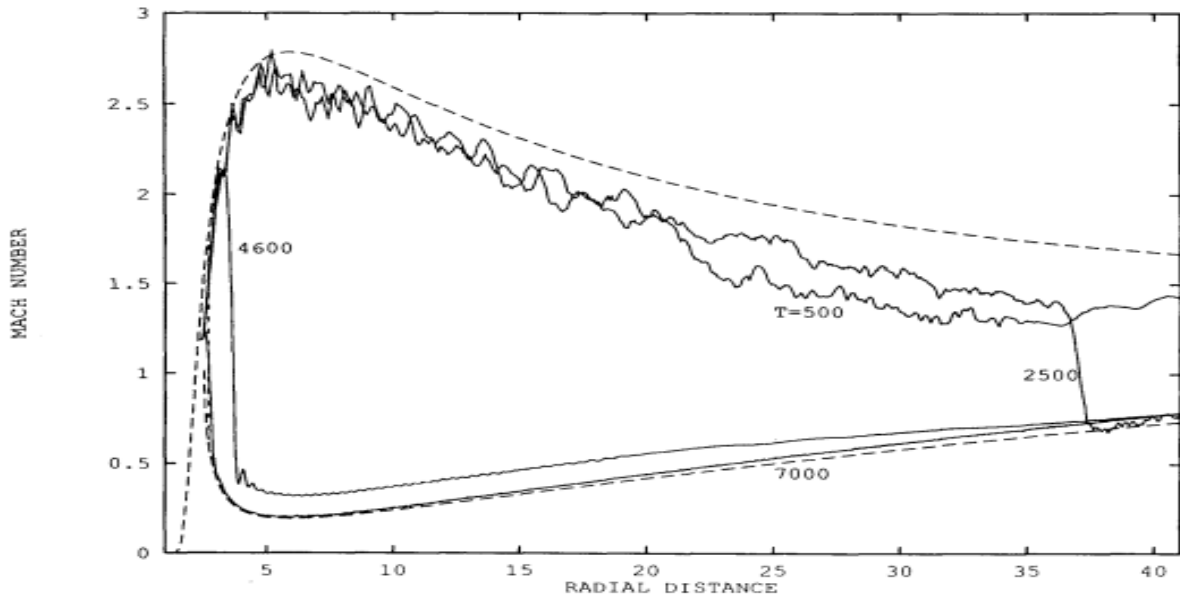


Figure 2.7: Results of numerical simulation of shock formation in winds close to a black hole from Chakrabarti and Molteni (1993). The parameters are $\mathcal{E} = 0.01725$, $\lambda = 1.90$. The dashed curve shows the analytical pre-shock and post shock branches and vertical dashed lines show the theoretical shock location at $X_{s2} = 2.7$. Taken from Chakrabarti and Molteni (1993).

CENBOL, the density of matter also increases. Subsequently, the flow continues its journey to the black holes and accretes onto the black hole supersonically.

TCAF consists of two major disc components, namely, a high viscosity, standard Keplerian disc component and a low viscosity sub-Keplerian halo component (Chakrabarti 1995; 1997). The Keplerian disc resides on the equatorial plane and it is flanked by the sub-Keplerian flow.

In the region $r < r_s$, the Keplerian disc is assumed to be evaporated because of heating. The Keplerian matter mixes up with the sub-Keplerian halo inside the CENBOL and form a single component (Chakrabarti 1995; 1997). The outflows and jets are believed to be produced from the CENBOL region (Chakrabarti 1995; 1997; 1999). A part of the low energy, blackbody photons (soft photons) that are emitted from the Keplerian disc, is intercepted by the hot electrons in the CENBOL. These photons are energized by the inverse-Compton scattering with these electrons and emerge as hard radiations. Thus, the radiated spectra are produced from both the components and are a function of accretion rates (Chakrabarti 1995; 1997). The relative importance of the accretion rates of these two components determine whether the spectrum is going to become hard or soft. The transition from the hard to soft state is found to be smoothly initiated by the mass accretion rates of the disc (Chakrabarti 1995; 1997). The fast variability of the photon counts are explained by the time variation of the flow dynamics. If the shock moves back and forth then the hard radiations are expected to be modulated at the frequency of this oscillations since they are mainly produced in the post-shock region (Chakrabarti and Manickam 2000; Chakrabarti 2005). This way an important observed feature of several black hole candidates, namely, the quasi-periodic oscillation (QPO) is explained. According to the TCAF solution, different length scales of the flow are responsible for the different QPO frequencies (Chakrabarti 2005).

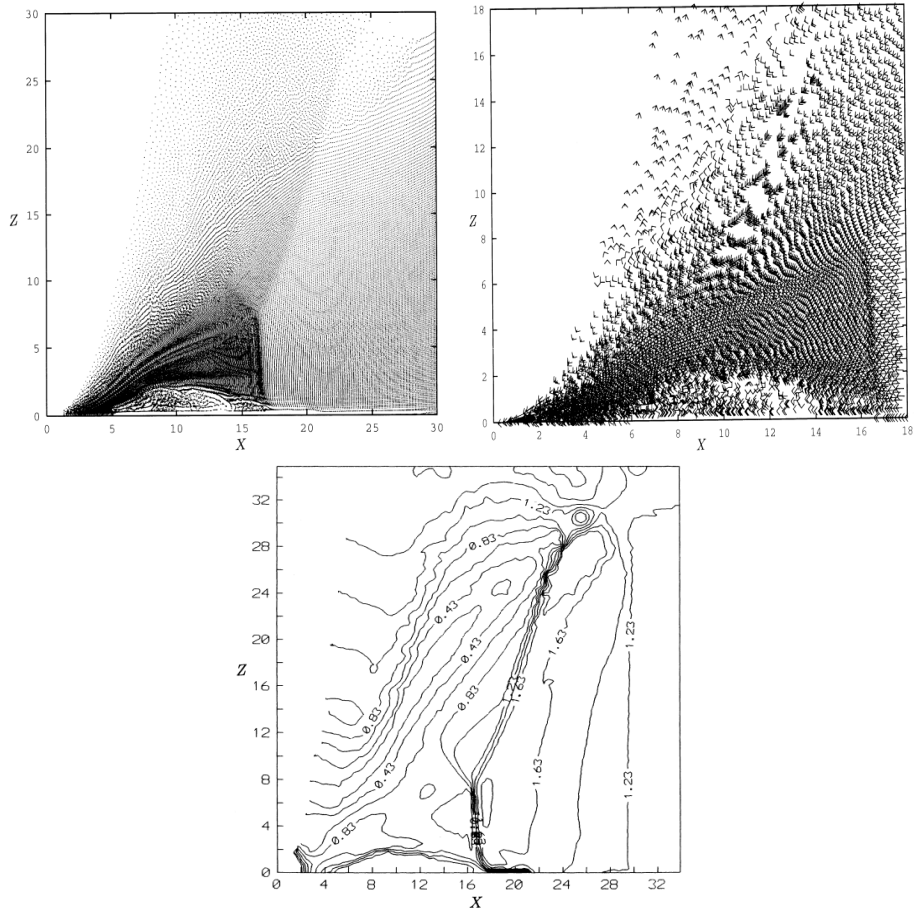


Figure 2.8: Results of simulation of thick accretion discs with shocks (seen here at $x \sim 16.6$) in which matter is injected with angular momentum $\lambda = 1.65$ and energy $\mathcal{E} = 0.006$, from Molteni, Lanzafame and Chakrabarti (1994). Total number of particles are 60,000. Panel 1: X-Z coordinates of the particles, Panel 2: Mach number fields of the flow close to the shock, and Panel 3: Contours of constant Mach number. Taken from Molteni, Lanzafame and Chakrabarti (1994).

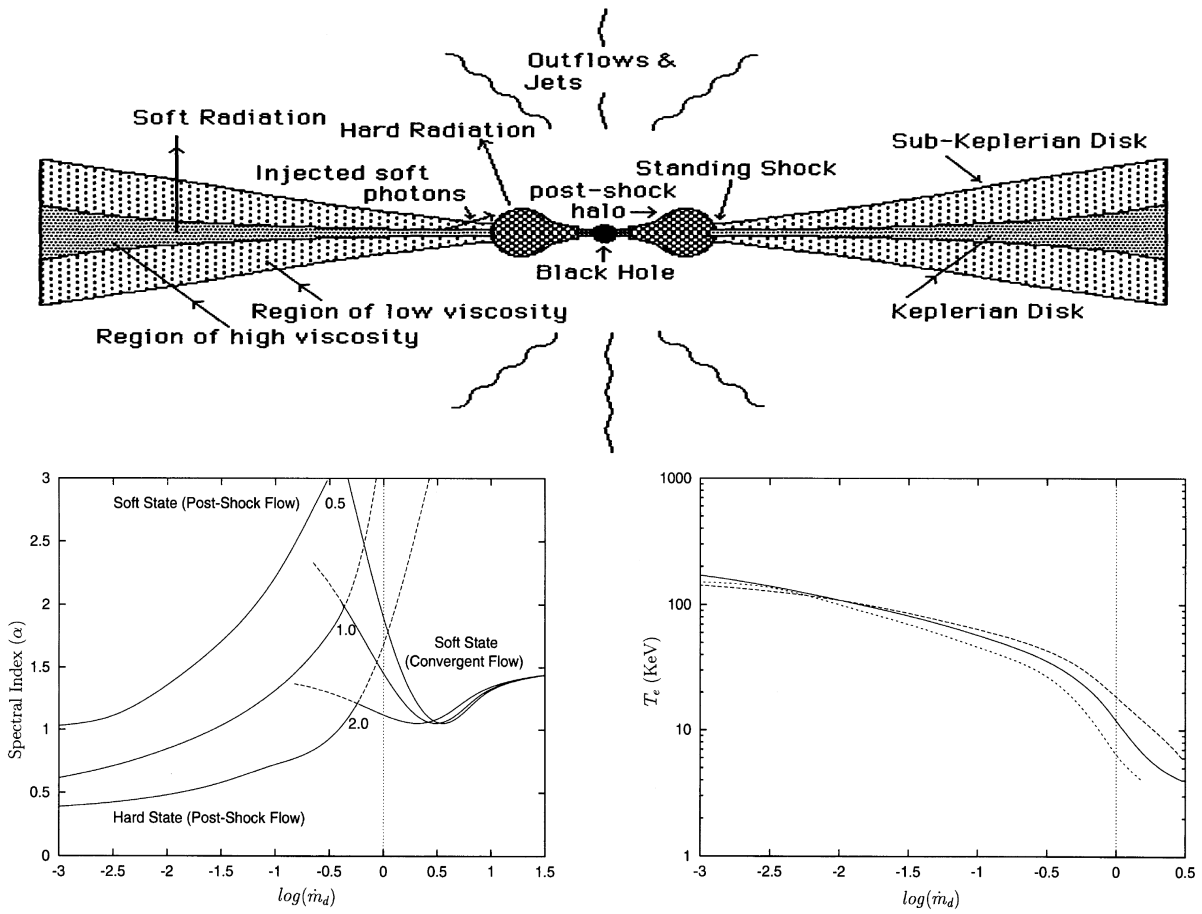


Figure 2.9: The Two-Component Advective Flow solution (Chakarabarti 1989; 1995; 1997) geometry is shown in panel 1 (from Chakrabarti and Titarchuk 1995). The variation of power-law (spectral) index and temperature of cloud with the accretion rate is shown in bottom panels 2 and 3, respectively [Chakrabarti and Titarchuk (1995)].

In 1996, Chakrabarti included viscous heating and a generalized cooling to give the grand unification of solutions for viscous transonic flows in the equatorial plane.

It was also concluded in 1997, by Chakrabarti, that even without the formation of shock, the centrifugal barrier is strong enough puff the disc up to create the Comptonizing cloud which effectively behaves like the CENBOL and produces the inverse-Comptonized spectra.

In 1997 Ryu, Chakrabarti and Molteni, used Total Variation Diminishing schemes to reproduce the results of SPH simulation with sharper shocks. The TVD scheme allowed the provision of including radiative transfer processes and Monte Carlo randomization technique.

Application of TCAF for BHs

Problems successfully addressed with the advective disc paradigm:

Sub-Keplerian motion on a large scale: Supersonic flows are proven to be sub-Keplerian in nature. So, a formation of shock in flow, which is the abrupt transition from a supersonic state to subsonic state, would imply that matter had a sub-Keplerian distribution of angular momentum before the shock. Thus, the presence of shock in any disc around a black hole would mean the flow is sub-Keplerian. These flows have higher radial and lower rotational velocity, hence the Doppler shift observed in line emissions from these regions would be smaller compared to Keplerian flow, when the mass of black hole is same. In other words, for the same Doppler shift, the mass of the central object has to be more. Chakrabarti (1995) pointed out that the disc of M87 contained spiral shocks, meaning the flows is sub-Keplerian and therefore mass of central object would be higher ($4 \times 10^9 M_\odot$) than the value predicted ($2 \times 10^9 M_\odot$) by assuming a Keplerian disc. Recent works by Dopita et al in 1997 also stresses the fact that shock ionization is the cause of emission process in M87.

Sub-Keplerian motion on a small scale: Starting from the introduction of Shakura-Sunyaev disc in 1973, it became a norm of sorts to assume the Keplerian disc up to the marginally stable orbit, $r_{ms} = 3R_g$. Chakrabarti pointed out, in the context of advective discs, that the inner edge could at most extend up to $\sim 10 - 20R_g$, where the CENBOL should be formed. Di Mattio and his coworkers studied the QPOs for objects during the hard-to-soft state transitions and found the inner edge of the disc goes in to about $6 - 25R_g$, which is closer than the value predicted by Chakrabarti (Meszaros 1975; Kozłowski et al. 1978). The spectral analysis carried out by Nowak and Wagoner (1991), also revealed a similar length scale.

Power-law hard radiation in very high states: When the accretion rate is high enough, the sub-Keplerian and Keplerian region of the Two Component Advective Flow, becomes seemingly indistinguishable, as pointed out by Chakrabarti (1995; 1997). However, near the black hole horizon, due to the inner boundary condition, matter has to become supersonic and thus the flow starts gaining velocity near the black hole. The radial velocity becomes dominant compared to the diffusive motion of the electron plasma. This bulk motion Comptonizes the trapped photons to a very high energy by dumping its radial momentum onto them. The flow is mostly advected inwards, and the escaped radiation produced a power law. This power law spectrum has a definite slope which is seen as the hall-mark in all black hole candidates (Borozdin et al. 1999). The TCAF solution is based on the transonic solution which respect the inner boundary condition for black holes, which is independent of the history of the in falling matter.

Quasi-Periodic Oscillations from black hole candidates: Similar to the cases of neutron stars, the X-ray received from galactic black hole candidates often show oscillations which remain persistent over a period of time. The advective disc solutions by Chakrabarti allows the formation of

shocks and oscillation of the post shock region would lead such an oscillation in X-rays. During a state transition, the observation of such QPOs only strengthens the theory. The oscillations occurs in hard X-rays only which was proved by Chakrabarti and Manickam (2000). It indicated that the origin of QPOs lie in the shock oscillation process, as the post shock region acts as the Comptonizing cloud.

Outflows and their effects on the spectral properties: Observational evidences suggested that the outflows and jets emitted from the M87, are generated from a few tens of Schwarzschild radii of the horizon. This readily nullifies the scale free solutions of ADAF or any of it's variants. The TCAF solution clearly brings in the CENBOL as the region which acts as the base of emitting jets and outflows. Das and Chakrabarti (2000) have shown the variation of outflow rates w.r.t. inflow rates when the shock strength (i.e. the compression ratio at the shock) is varied. The outflows created a feedback effect in the spectrum. The softening of hard state and the hardening of soft state was predicted and observed in the case of GRS 1915+105.

Relationship of outflows and the black hole states: The variation of outflow to inflow ratio peaks at a moderate value of shock strength (R). For a very high shock strength, the hard state, small outflows are seen. For a very soft state, low shock strength, there is virtually no outflow. The observational evidence by Aharonian and *Völk* (2001) confirms the results.

Formation of TCAF from simulation: In 2013, time dependant numerical simulation (Giri and Chakrabarti, 2013) of viscous transonic flows showed TCAF to be a stable configuration given the α , energy and λ parameters are in the same domain as Chakrabarti 1990. They also showed that the disc only forms beyond a critical value of α . This strengthened the fact that only the advective components are present during the hard spectral states. During an outburst, a sudden rise of viscosity can trigger disc formation which leads to spectral softening.

Variation of QPOs from simulation: A Monte-Carlo code for Comptonization is also coupled with the TVD code to incorporate the non-local cooling process. This has successfully reproduced the spectra of black holes. It was found that the variation of QPO frequencies can be attributed to the variation of the two accretion rates (Giri, Garain and Chakrabarti 2015). With increasing disc accretion rate, the Compton cooling quenches the CENBOL and the shock oscillation occurs at a smaller and smaller radius. This in turn increases the QPO frequency.

Explanation of hysteresis during outburst from simulation: The rise and decline time of an outburst is not the same for the transient sources. In fact it takes a much longer time to make the soft-to-hard transition after an outburst. A time-dependent viscosity was used by Roy and Chakrabarti (2017) to show that the flux variation profile of an outbursting black hole follows the profile of average specific angular momentum of the system. This again showed that onset of viscosity triggers the outbursts.

Collimation of outflows from simulation: In 2017, Deb and Chakrabarti showed that even the introduction of small toroidal magnetic flux tubes in the accretion can collimate the outflows coming out of the post-shock region of the CENBOL.

Chapter 3

Modelling of accretion flows around Neutron Stars

ABSTRACT

In this Chapter, we first go through the observational and theoretical developments on the accretion processes around NSs before the TCAF solution was conceived. We do so in a somewhat chronological way to highlight how observations shaped the way theories were constructed, how some models failed to explain newly discovered data and how a common thread can be found which pointed to the TCAF being at the core of the accretion flow process around NSs. We follow the review article by Bhattacharjee 2018 for the cases NSs. Finally, we highlight the instances where TCAF was applied to NSs, previously and how we have applied so in our work, to showcase the position of these findings on a larger scale.

The modelling of accreting neutron stars were largely prompted by significant observational findings in the last 50 years. Although many of the models are of great phenomenological importance, it is impossible to cover all of those and their modified versions, in this text. We take a separate approach to address the evolution of such theories: we point to the observational evidence that either proved the validity of a theory, prompted a modification or refuted a theory in light of new results. This approach lets us to touch upon the relevant models as well as compare them in terms of predictions of observational results.

Major observational results and models

Evolution of theories: Timing Properties

The temporal variations of accreting NSs (both magnetic and weakly-magnetic) are reflected in the Power Density Spectra (PDS) of the lightcurves at different energies. The presence and evolution of Quasi-Periodic Oscillations (QPOs) reveal significant details about both the hydrodynamic and radiative transfer processes. In order to discuss the chronological developments in timing studies, we briefly define (Wang 2016) different classes of QPOs and their observed properties.

- **Low-Frequency QPOs (LFQPO):** Low-frequency QPOs are observed in the range of 5 - 60 Hz, with Quality Factor $Q \geq 2$, and amplitudes of 1% – 10%. The Horizontal-, Normal-, and Flaring Branch Oscillations all lie in this domain and are respectively abbreviated as HBO, NBO and FBO.
- **hecto-Hz QPOs (hHz QPO):** The hecto-hertz (hHz) QPO is usually a peaked noise. If the peak is coherent enough to have a quality factor $Q > 2$, it is classified as a QPO. The frequency ν_{hHz} is seen in the range of 100 – 200 Hz. It has rms amplitude between 2% and 20%.
- **Kilo Hz QPOs (kHz QPO):** These are defined as the QPOs in the range $200 Hz < \nu_{kHz} < 1300 Hz$.

The first detailed study of a magnetic neutron star, with almost radial accretion, was carried out by Elsner & Lamb (1977). They studied the formation of magnetosphere, its scale and structure, the stability of its boundary and the plasma flow into the magnetosphere and Alfvén surface. Ghosh, Lamb & Pethick (1977) studied the spin-up and spin-down mechanism of the star due to this. Ghosh & Lamb (1979a, 1979b) focused on the radial and vertical structures of the transition region and the changing of period of the pulsating stars. Van der Klis et al. (1985) studied the power density spectra of the source GX 5-1, and found intensity dependence of the centroid frequency, width and power of the observed QPOs (20 Hz and 40 Hz) and low-frequency noises ($< 15 Hz$). Lamb et al. (1985) found QPOs in 5-50 Hz range for Sco X-1. They proposed that a clumpy disc, whilst interacting with a weak magnetosphere, produced the modulation in accretion rate and oscillations in X-ray flux. Priedhorsky et al. (1986) found a bimodal behaviour in the response of QPO frequency with intensity. The 6 Hz QPO, in the quiescent state, was anti-correlated with intensity. The QPO in the active state, however, was correlated with intensity and varied from 10-20 Hz. Two modes of spectral behaviours were also identified for Sco X-1. Paczynski (1987) suggested the luminosity variations of the boundary might be a result of unsteady flow with low viscosity. Van der Klis et al. (1990) studied the atoll source 4U 1636-53. Correlation between spectral shape, fast variability, burst duration and temperature with accretion rate \dot{M}

hinted that the source state is determined by the accretion rate \dot{M} . The persistent intensity varied independent of other characteristics, indicating that intensity was not probably a good measure of accretion rate. Strohmayer et al. (1996) studied the burst and quiescent states of the LMXB 4U 1728-34 to find pulsations of 363 Hz and twin QPOs, respectively. The twin kHz QPOs varied between 650-1100 Hz, with count rate till reaching a maximum, while maintaining a constant separation of 363 Hz. The magnetospheric beat frequency model was used to explain the X-ray variability. Van der Klis et al. (1997) found the twin kHz QPO frequency separation is not constant, rather varied from 310 to 230 Hz, for Sco X-1. It was concluded that any beat frequency model or photon bubble model was unlikely to explain the origin of these peaks. Authors also found HBOs near 45 Hz and 90 Hz, both of which increased with accretion rate. In Méndez et al. 1997, the energy-dependent study of twin kHz QPO and band-limited noise revealed different behaviours, suggesting the two processes are originated at two different radii. It was remarked that the kHz QPOs were due to oscillations of the boundary layer, very close to the surface and the broad noise was generated from near the inner edge of a disc. It was also mentioned that QPO frequency and the noise cut-off frequencies tracked \dot{M} better than the count rate. Wijnands et al. (1997) found the coexistence of HBOs and kHz QPOs for GX 17+2. This suggested that the magnetospheric beat frequency model could not address both the phenomena simultaneously. The rms and FWHM of the upper kHz QPO varied with the change in frequency, whereas the similar quantities remained almost constant for lower kHz QPO with the change of frequency. Wijnands et al. (1998) found both kHz QPOs and HBOs for the Z-source Cyg X-2. Jonker et al. (1998) showed that the twin kHz QPO frequencies moved to higher values with the increase of accretion rate for the Z-source GX 340+0. However, the rms and FWHM of lower QPO remained consistently constant, whereas the ones corresponding to upper kHz QPO decreased. Simultaneous HBO was also detected along with its second harmonic between 20 to 50 Hz and 38 Hz and 69 Hz. It was also concluded from the study of FWHM of HBOs with states, that something other than \dot{M} determined the timing properties. Wijnands et al. (1998) found very similar results for the object GX 5-1, where simultaneous kHz QPOs and HBOs were observed.

In Titarchuk et al. (1998, hereafter TLM98) a super-Keplerian transition layer was invoked to explain the kHz QPOs (a detailed discussion to be followed in the next section). Méndez et al. (1998) showed that the LMXB 4U 1608-522 had twin kHz QPOs and the frequency separation is not constant with the change of centroid frequencies, contradicting a simple beat-frequency interpretation. The authors compared different models for the accretion onto this atoll source having 10% average luminosity of Sco X-1, a Z-source showing similar features, and concluded that neither the photon-bubble model, the transition layer model nor any modified beat frequency model was able to explain the phenomena. Méndez & van der Klis (1999) found simultaneous existence of burst oscillations and twin kHz QPOs for the source 4U 1728-34. The frequency separation always remained smaller than the burst frequency, for varying accretion rates. For the same object, Titarchuk & Osherovich (1999) used the transition layer model to identify the low-Lorentzian frequency to be due to radial oscillation in viscous time-scale and the break frequency to be associated with radial diffusion time-scale. Psaltis et al. (1999) studied many non-pulsating NSs and black holes (BHs) of varying luminosities and source types. A correlation between 1)the NS: kHz QPOs and HBOs, 2)BH: QPOs and noises, of the same type but varying 3 orders of magnitude in frequency and coherence was found. This suggested that the variations are systematic and related by similar processes in the two types of sources, further constraining the theoretical models of these phenomena. Titarchuk et al. (1999) added the effects of Coriolis forces and interaction of the magnetosphere with the flow to explain the different modes of QPOs

observed for 4U 1728-34. Dieters et al. (2000) remarked that the position on the Z-track or the spectral state was not the only parameter that governs the behaviour of Sco X-1. Jonker et al. (2000) discovered a new broad component in the PDS of GX 340+0 between 9 Hz to 14 Hz. Yu et al. (2001) studied the source Sco X-1 and found that the upper kHz QPO frequency and the ratio of lower to upper kHz QPO amplitude were anti-correlated with the count rate that varied in the NBO timescale (6-8 Hz). This suggested that some of the NBO flux was generated from inside the inner disc radius and the radiative stress modulated the NBO frequency. Munro et al. (2000) did a long term study of a total of 13 Z and atoll sources to remark that the atoll sources trace out the colour-colour diagram over a larger range of luminosity, on a much longer timescale and have harder spectra when they are faint as compared to the Z-sources. But, both types trace out similar three-branched colour-colour patterns, suggesting a similarity, which was previously not recorded because of incomplete sampling.

Belloni et al. (2002) conducted a detailed analysis of PDS of multiple BHCs and NSs, by decomposing the PDS onto 4 primary Lorentzian functions. They showed that this not only provides better statistics, but also yields a better phenomenology which tracked the evolution of different QPO frequencies with spectral states. It was found that a one-to-one correspondence can be found between different QPOs in NSs and BHs, which obey similar correlations. This suggested that, apart from the mass dependence of the dynamical timescale, the physical processes governing the phenomena could be the same and the high-frequency components might not require the NS surface as black holes also show similar features with weaker amplitude. Mauche (2002) drew a similar conclusion by studying the correlations between two QPOs in BHCs, NSs, and White Dwarfs (WDs) which showed that the correlated nature can be extended another two orders of magnitude with WDs. The author discussed several models in light of the observed QPOs and dwarf-nova oscillations (DNOs). All models that relied on the presence of strong magnetic fields or a stellar surface to explain the high-frequency oscillations were ruled out. The only one which produced the observed frequencies was the TL model where Keplerian orbital frequencies are suggested as the origin of QPOs.

Wijnands et al. (2003) studied multiple accreting neutron stars which had burst oscillations. It was found that any simple beat frequency model or any model which relied on general relativistic effects very close to the rotating star is unlikely to explain the phenomena. The authors stated that the QPOs can be understood in terms of resonances at privileged radii in an accretion disc, but pointed towards general relativistic epicyclic motions to be the cause of such resonance. Barret et al. (2005) studied the Q factor and coherence time variation of both the kHz QPOs to reveal that the Q factors follow different patterns in the two. From their analysis of the LMXB 4U 1608-52, that any model involving clumps orbiting within or above the accretion disc was ruled out, and disc/shock oscillations were suggested as the more likely mechanism. Belloni et al. (2005) showed that the ratio of upper and lower kHz QPO frequencies was found to be 3/2 only because of biased sampling. A simple resonance model of a Keplerian disc, thus, is unlikely to address the kHz QPOs. Cassella et al. (2006) studied the continuous transition from FBO to NBO in $\sim 100s$ timescale, for Sco X-1. From the one-to-one correspondence between the LFQPOs in BHs and NSs, it was inferred that the physical mechanisms that determine these oscillations, which are present in both, are in favour of a disc origin of oscillation and rules out models involving interaction with the surface or magnetosphere.

Méndez (2006) studied, for multiple NSs, the maximum Q factor and rms power associated with upper and lower kHz QPOs. For the lower one, Q_{max} increased at first and decreased exponentially with increasing luminosity. For the upper one, the Q value remained almost independent of the

luminosity of the sources. The author suggested that one possible mechanism of generation of kHz QPOs would be that the mass accretion rate sets the size of the inner radius of the disc which determines the QPO frequency as well as the relative contribution of the high-energy part of the spectrum to the total luminosity. Boutloukos et al. (2006) also pointed towards high radial accretion instead of a Keplerian disc, to explain the relatively lower value of kHz QPO frequencies found in the source Cir X-1. Wang et al. (2012) studied the energy dependence of the low-frequency NBOs for Sco X-1. They concluded that in near Eddington luminosities, the oscillations in the TL, the region between the inner edge of disc and neutron star, might be responsible for the NBOs. It was noted that the centroid frequency varied non-monotonically with energy indicating a radial oscillation.

Evolution of theories: Spectral Properties

The explanation of soft state spectra of NSs demanded the presence of a blackbody emission from the boundary layer of a neutron star (Mitsuda et al. 1984). For the harder states with a power-law tail in the energy spectrum, the need of Compton scattering became evident (White et al. 1986, Mitsuda et al. 1989). The difference between these two models was that while the former assumed a cooler boundary layer, the latter assumed a hotter one, compared to the accretion disc. Sunyaev and his collaborators (Inogamov and Sunyaev, 1999; Popham and Sunyaev, 2001; Gilfanov and Sunyaev, 2014) assume that the Keplerian disc reaches all the way to the NS and is connected with the boundary layer where the thickness increases due to higher temperature. Most of these studies were done to address the soft state spectra of neutron stars. The state transition of neutron stars in LMXBs presented another problem. The fact that disc accretion rate was not the single factor that controlled the size or temperature of the Compton cloud, used to model the hard state spectra, lead to the conclusion that some unknown parameter, related to the truncation radius of the disc, is responsible for the hard X-ray tail (Barret 2001, Barret et al. 2002, Di Salvo and Stella 2002). Paizis et al. (2006) found a systematic positive correlation between the hard X-ray tail and the radio luminosity, inferring that the Compton cloud might serve as the base of radio jets (which is same as proposed for black holes by Chakrabarti and his group. See Chakrabarti, 2017 and references therein for a review). Recent phenomenological works place a TL or Compton cloud between the Keplerian disc and the boundary layer (Farinelli et al. 2008; Titarchuk et al. 2014, hereafter TSS14). It has been argued in the past (Chakrabarti, 1989; Chakrabarti, 1996; Chakrabarti & Sahu, 1997) that while in black hole accretion, passing of the flow through the inner sonic point ensures that the flow becomes sub-Keplerian just outside the horizon, in the case of NSs, the Keplerian flow velocity must slow down to match with the sub-Keplerian surface velocity. Numerical simulations clearly showed that jumping from a Keplerian disc to a sub-Keplerian disc is mediated by a super-Keplerian region (Chakrabarti & Molteni, 1995). In TSS14 the TL was expanded several-fold to explain the spectral properties.

Monte-Carlo simulations are essential in generating and understanding spectra emergent from highly non-local processes such as Comptonization. Toy models were made of spherical Compton clouds of constant temperature and optical depth, surrounding a weakly magnetic neutron star to generate hard X-ray tails (Seon et al. 1994). In case of neutron stars with strong magnetic fields ($B \sim 10^{10-12}$ Gauss), matter lands at the poles through the accretion column and the use of such a geometry leads to the successful explanation of spectral properties (Odaka et al. 2013, Odaka et al. 2014) in certain cases. Although these studies provide some answers, so far, the spectral fitting carried out were based on phenomenological models which used arbitrarily placed Compton cloud. Since 1995, the entire community of black holes and neutron stars have started

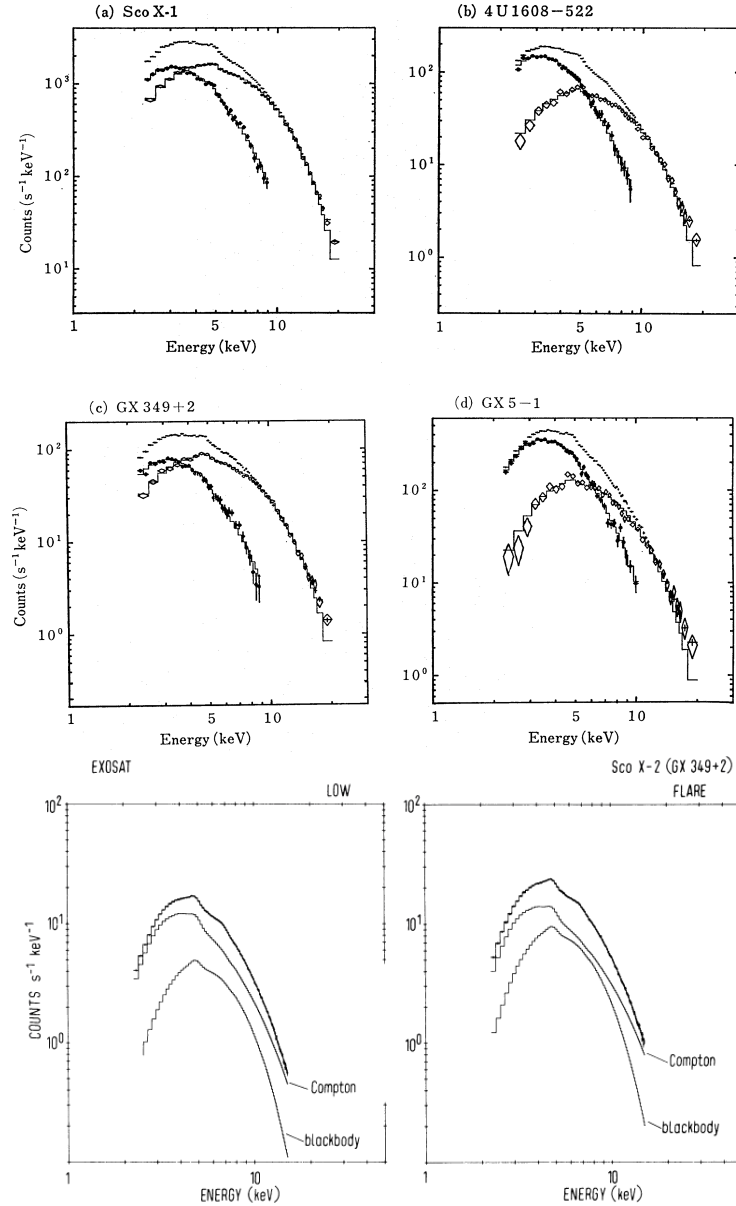


Figure 3.1: Panel 1-4: For multiple NSs, the spectral fitting in soft states required two components: (diskbb + blackbody), taken from Mitsuda et al. (1984). This suggested that a thermal emission is coming from the boundary layer of the star. Panel 5-6: In the harder states, an additional Comptonized component was needed for spectral fitting (White et al. 1986).

to use cartoon models of the flow inspired by the solution of CT95, both for the explanation of spectral and the explanation of QPOs.

An extended TL was used to explain spectra using COMPTT and COMPTB models. Out of the two COMPTB components used, the one corresponding to Comptonization of NS surface photons, showed a saturation in COMPTB models spectral index (Farinelli and Titarchuk 2011). Many NS LMXBs are studied using this framework, such as 4U 1728-34 (Seifina et al. 2011), GX 3+1 (Seifina and Titarchuk 2012), GX 339+0 (Seifina et al. 2013), 4U 1820-30 (Titarchuk et al. 2013), Scorpius X-1 (TSS14), 4U 1705-44 (Seifina et al. 2015) etc. Recently, the HMXB 4U 1700-37 has also been examined using the same model (Seifina et al. 2016).

Prospect of TCAF as the generalized flow around NS

We list some properties of a ‘generalized’ flow around NS which are present in the TCAF:

- ν_{LF} bimodal behaviour: Two separate accretion rates control the intensity. One reduces the oscillation radius, another increases it.
- Correlated QPOs seen in BHs, NSs and WDs: The generalized model should not require the presence of a stellar surface or magnetosphere.
- Similar ν_{kHz} in sources of varying intensity: QPOs are controlled by more than one accretion rates.
- Long coherence time of kHz QPOs: Clumpy disc models with azimuthal asymmetry to generate QPOs in Keplerian orbital time-scale are unlikely. Radial and vertical oscillation would be preferred.
- A ‘mass’ accretion rate which controls both the inner edge of the disc that generates kHz QPOs also decides the relative contribution to high energy part of the spectrum.
- The Compton cloud acts as the base of the jet.
- The state transition is not controlled by a single accretion rate.
- Low ν_{kHz} in some NSs: Radial accretion (advective flow) is preferred over a Keplerian disc.

In fact, Chakrabarti and Sahu (1997) pointed out how the Bondi flow would be modified around a neutron star and showed the formation of shock at the surface. This possibility was earlier discussed in Chakrabarti 1996 where a generalized solution for BHs and NSs were formalized. This has also been reflected in Chakrabarti 2017, where a detailed review of TCAF is presented along with the similarities of flow configuration around BHs and NSs. How the influence of magnetic fields for NSs can change the structure is also discussed there.

We, therefore, investigate the applicability of TCAF around neutron stars and make the needed modifications along the way. We, first use X-ray data to verify the TCAF around BHs with the example of a transient and a persistent black hole. Then, we use multiple methods (details in individual chapters) to simulate the spectral and timing properties of TCAF around an NS. In Chapter 6, we look at the thermal Comptonization processes in the TCAF geometry and compare the spectra with observed cases. In Chapter 7, we solve time-dependent hydrodynamic equations to simulate the accretion flows around NSs and analyze the timing properties, in comparison with

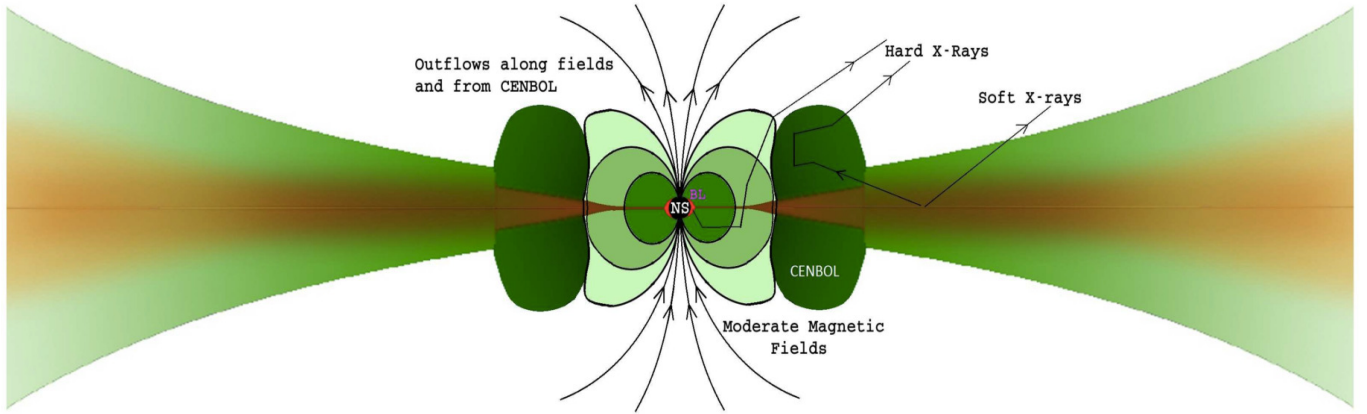


Figure 3.2: A schematic diagram of accretion dynamics and radiation processes in a Two-Component Advective Flow solution with a centrifugal barrier supported shock front close to a neutron star with a moderate magnetic field. The Normal Boundary Layer (NBOL) on the star surface (denoted by BL, here) as a result of a shock and a secondary Compton cloud in the magnetosphere apart from the possible presence of CENBOL makes the spectra complex (from Chakrabarti 2017).

the observed features. This study is carried forward in Chapter 8 for viscous flows where the formation of NBOL is shown, around the star. In Chapter 9, we show the formation of TCAF from advective flows and also construct a spectral model for the weakly magnetic neutron stars, based on TCAF. The new model comprises of the TCAF parameters and three new physical parameters, introduced based on the findings of Chapters 6-8.

Chapter 4

Fitting the data of Black Hole transient H1743-322 by TCAF solution

ABSTRACT

The black hole transient H1743-322 exhibited several outbursts with temporal and spectral variability since its discovery in 1977. These outbursts occur at a quasi-regular recurrence period of around 0.5 – 2 years, since its rediscovery in March 2003. We investigate accretion flow dynamics around the Low Mass X-ray Binary H1743-322 during its 2004 outburst using the RXTE/PCA archival data. We use Two Component Advective Flow (TCAF) solution to analyze the spectral data. From the fits with TCAF solution, we obtain day to day variation of physical accretion rates of Keplerian and sub-Keplerian components, size of the Compton cloud and its other properties. Analysis of the spectral properties of the 2004 outburst by keeping fitted normalization to be in a narrow range and its timing properties in terms of the presence and absence of QPOs, enable us to constrain the mass of the black hole in a range of $10.31M_{\odot} - 14.07M_{\odot}$ which is consistent with other estimates reported in the literature. This findings were reported in Bhattacharjee et al. (2017). Figures 4.1, 4.2, 4.5, 4.7-4.9 have been taken from there.

Introduction

The advent of X-ray astronomy and the launch of Rossi X-Ray Timing Explorer (RXTE) in 1995 have significantly enhanced our understanding about the accretion processes around compact sources, such as black holes (BHs) and neutron stars (NSs). Most of these compact sources are in binaries, with the NS or the BH as the primary which accretes matter from the companion star (secondary) either by Roche-lobe overflow or by capturing the mass lost from the secondary in the form of winds. Due to the presence of turbulent viscosity, a part of the gravitational potential energy lost by the accreting matter is emitted in the form of radiations, chiefly in the soft X-ray domain. Even when significant viscosity is absent, stored thermal energy is lost in X-ray domain by inverse Comptonization. An outbursting Black Hole Candidate (BHC) primarily exhibits four different spectral states, namely, hard state (HS), hard-intermediate state (HIMS), soft-intermediate state (SIMS), and soft state (SS) (e.g., McClintock & Remillard, 2006; Nandi et al., 2012; Debnath et al., 2013). Simultaneous analysis of the timing properties of these BHCs reveal that low frequency Quasi-Periodic Oscillations (QPOs) are also evident in the power density spectra (PDS) of these objects (e.g., Remillard & McClintock, 2006). Evolution of spectral and temporal characteristics of several BHCs during their outbursts have been extensively studied (e.g., McClintock & Remillard, 2006; Nandi et al., 2012). It has been noted that the various spectral states can be related to different branches of the hardness intensity diagram (HID; Belloni et al., 2005 and Debnath et al., 2008) or, in a more physical hysteresis diagram using accretion rate ratio and X-ray intensity (ARRID; Mondal et al., 2014; Jana et al., 2016). The HID or the ARRID shows the objects in different spectral states, generally, in the sequence: HS \rightarrow HIMS \rightarrow SIMS \rightarrow SS \rightarrow SIMS \rightarrow HIMS \rightarrow HS. It is well established that in order to interpret majority of black hole spectra two types of spectral components, namely, a multi-colour blackbody component and a powerlaw component are needed. The multi-colour blackbody component seems to originate from an optically thick, geometrically thin Keplerian flow (Shakura & Sunyaev, 1973) while the powerlaw tail of the spectrum is believed to be emanated from a ‘‘Compton’’ cloud (Sunyaev & Titarchuk, 1980, 1985). Several theoretical and phenomenological models ranging from a magnetic corona (Galeev et al., 1979) to a hot gas corona over the disc (Haardt & Maraschi, 1993; Zdziarski et al., 2003) to a two component advective flow (TCAF) solution (Chkrabarti, 1995, 1997; Chakrabarti & Titarchuk, 1995; hereafter CT95) exist in the literature which attempts to explain the spectrum and expound the nature and origin of this ‘‘Compton’’ cloud. In this Chapter, we use TCAF solution to investigate the spectral and timing properties of the source during its 2004 outburst.

The Galactic transient low mass BHXB H1743-322 is located at R.A. = $17^{\text{h}}46^{\text{m}}15^{\text{s}}.61$ and Dec = $-32^{\circ}14'00''.6$ (Gursky et al., 1978). The discovery of this source goes back to August-September 1977, when Kaluziński & Holt (1977) reported its first X-ray activity with the Ariel V All Sky Monitor. This was subsequently followed by observations from the HEAO I satellite (Doxsey et al., 1977). Further activities of the source in the X-ray band 12-180 keV were observed during the 1977-78 outbursts with the HEAO I satellite (Cooke et al., 1984). Based on the colour-colour diagram, obtained from the spectral data of the HEAO I satellite, White & Marshall (1984) classified the source to be a potential BHC. Since its first detection, it remained in the quiescent state till 1984 when EXOSAT observations reported X-ray activities (Raynolds, 1999) which was subsequently followed by detection of activities by TTM/COMIS instruments on board MirKvant in 1996 (Emelyanov et al., 2000). On March 21, 2003, the INTEGRAL satellite detected a bright source named IGR J17464-3213 (Revnivtsev et al., 2003) which displayed X-ray activities and later, RXTE confirmed the presence of such an activity from the same region in the sky (Markwardt

& Swank, 2003) validating the source to be H1743-322. Since 2003, it exhibited several X-ray activities with quasi-regular intervals of about one to two years. In order to investigate multi-wavelength properties of the source, it was comprehensively monitored in X-rays (Parmar et al., 2003; Remillard et al., 2006; McClintock et al., 2009), IR (Steeeghs et al., 2003), and in radio bands (Rupen et al., 2003) during its 2003 outburst. McClintock et al. (2009) and Miller-Jones et al. (2012) eventually followed up further investigations of the source in the multi-wavelength during its 2003 and 2009 outbursts respectively.

The mass of the BHC in H1743-322 has not yet been dynamically measured, although several attempts have been made to predict the mass of the BH. Analyzing 2003 outburst data, Shaposhnikov & Titarchuk (2009, ST09) calculated mass of this black hole candidate to be $13.3 \pm 3.2 M_{\odot}$ using their QPO frequency-Photon Index correlation method. McClintock et al. (2009) estimated its mass to be $\sim 11M_{\odot}$ using their high frequency QPO correlation method. From the model of high frequency QPOs based on the mass-angular momentum (i.e., spin of the black hole), Pétri (2008) predicted that its mass should lie in the range of $9 - 13M_{\odot}$. Based on its spectral and timing properties using two recent outbursts (Molla et al. 2016a, hereafter M16a) estimated the mass of the BHC to be $M_{BH} = 11.21_{-1.96}^{+1.65}$. These authors also used the method of ST09 and narrowed down the range to $11.65 \pm 0.67M_{\odot}$. The source is reported to be at a distance of 8.5 ± 0.8 kpc with the inclination angle of $\theta \sim 75^{\circ} \pm 3^{\circ}$. Steiner et al. (2012) also constrains to the spin a of the source, $-0.3 < a < 0.7$ with a 90% confidence level.

Recent outbursts of H1743-322 in 2010 and 2011 again showed the characteristic state transitions (Shaposhnikov and Tomsick, 2010; Shaposhnikov, 2010) as observed in other outburst sources (Nandi et al., 2012). It was pointed out by Debnath et al. (2010) that depending upon the outburst light curve profiles, there are mainly two types of outbursting BHCs: the ‘fast-rise slow-decay’ (FRSD) type and the ‘slow-rise slow-decay’ (SRSD) type. The source H1743-322 belongs to the first category. Debnath et al. (2013) investigated the average temporal and spectral properties of the object using combined disc black body (DBB) and power law (PL) model using data of 2010 and 2011 outbursts. Mondal et al. (2014) analyzed the RXTE/PCA data during its 2010 outburst using the TCAF solution allowing the normalization N of the TCAF model to vary in order to get the best fit (see Fig. 4.6). On the other hand, M16a analyzed the data of H1743-322 using TCAF solution during its 2010 and 2011 outbursts, restricting the normalization N within a narrow range to estimate the mass of the central object. Here, we follow the same procedure of M16a and M16b to analyse the 2004 outburst of H1743-322 which not only enables us to understand the underlying accretion flow dynamics but also allows us to give a fresh estimate to the mass of the BHC H1743-322. We first determine the average value of normalization by keeping it free within a narrow range. The constant, averaged value of the normalization is then used to refit the spectral data and estimate the mass of the BHC. The 2008b outburst was a ‘failed outburst’ and hence was not analyzed. The 2005 outburst could not be analyzed due to lack of data (Coriat et al. 2011). The anomalous outburst of 2003, which showed significant activity in radio well, has been studied in detail by Chakrabarti, Nagarkoti and Debnath (2019). From the rest of the cases, 2004 outburst was the most prominent one, in terms of total flux and duration. Hence, we selected this 117 day long 2004 outburst for our analysis.

Since several outbursts have already been studied one could surmise that analysis of yet another outburst would be of limited use. If one observed the sequence of outbursts, the one in 2003 took place after about twenty years and after that there are quasi-regular outbursts, some very small and some moderate. The one in 2003 is very anomalous (Chakrabarti et al. 2019) in the sense that its intensity was more than five times larger than the next prominent ones, such as those in

2004, 2010, 2011 etc. and at least 10 to 15 times stronger than several others. This is probably an indication that 2003 outburst could have been triggered by a non-linear instability and the system is slowly settling and relaxing after subsequent outbursts, probably before going to a long quiescence state again. It is thus no surprise that ST09 estimation of mass of 2003 outburst had a huge error margin while M16a estimate using the same method but 2010 and 2011 data shows a narrower margin. Assuming 2003 outburst is truly anomalous, the first stereotypical outburst is in 2004 and it is important to study this. While fitting the spectra we find that it is highly soft in much of the time where a standard disc is enough to fit the data. The region where both spectral components are seen prominently, and both the flow components are important is in the declining state. So we concentrate only on the declining state of 2004 data.

Judging from the fact that in initial outbursts, the source was going to very bright soft states and then more relative times have been spent in harder states, every outburst can be thought to be separately important and combination of the evolution of physical parameters may lead to the understanding of the long term behaviour of the system. Furthermore, from the light curves it is easy to see that decay time scales and peak fluxes are different and both of these parameters are governed by viscosity in the Keplerian flow. The pattern of mass accretion rate variations are also found to be different from one outburst to the other. Even the accuracy of the estimated mass is vastly different for the same method (M16a). Thus it is essential that every outburst be studied as accurately as possible.

We organize the Chapter in the following way: In §2 we discuss the salient features of the TCAF solution and the Propagatory Oscillatory Shock (POS) model. In §3, we discuss observation and methods of data analysis implementing HEASARC's HEASoft software package. In §4, we present the results obtained from the spectral analysis using the TCAF solution and the POS model. Finally, in §5 we conclude with a brief discussion summarizing our main findings with some remarks for future work.

Method of Analysis

Two Component Advective Flow (TCAF) Solution

Prior to the launch of RXTE, Chakrabarti & Titarchuk (CT95) explored the well-established solution of a transonic flow (see, Chakrabarti, 1990, Chakrabarti 1996, hereafter C96) and proposed that the accretion flow generally exhibits a two-component behavior, namely, a viscous Keplerian flow sandwiched by a weakly viscous sub-Keplerian flow (Fig. 4.1). This solution, popularly known as the Two-Component Advective Flow (TCAF) solution in the literature enunciates that the sub-Keplerian halo component, envelops the Keplerian disc and since it requires negligible viscosity to accrete, falls into the BH with a much higher radial velocity (Soria et al., 2001; Smith et al., 2002; Wu et al., 2002; Cambier & Smith, 2013; Tomsick et al., 2014). The sub-Keplerian flow is advective, can reach supersonic speeds and has angular momentum less than that of a Keplerian distribution. Hence, it undergoes a centrifugal pressure supported shock transition to become subsonic in between the two sonic points. The complete solutions are worked out in detail in Chakrabarti, 1989 (hereafter C89), and C96. The centrifugal pressure impedes the flow and as a result a standing or oscillating shock is formed depending on whether the Rankine-Hugoniot conditions are satisfied (C89, C96). Thus, the flow puffs up in the vertical direction, and forms the CENTrifugal pressure dominated BOundary Layer (CENBOL). This CENBOL acts as the Comptonizing cloud which up-scatters the seed black body photons coming from the Keplerian disc. In the natural hard state of a BHC, this is the only component that is present. The com-

ponent near the equatorial plane has a viscosity higher than the critical value and is Keplerian in nature having the characteristics of a standard disc. This component is not always present close to the black hole. When the outburst is triggered by increase of matter and viscosity, this disc formation is initiated from outside and it moves in on a daily basis, increasing the supply of Keplerian matter as well as soft seed photons which are intercepted by the CENBOL and are inverse-Comptonized through repeated scattering. A typical route of the photon emerging from the Keplerian disc to the observer via CENBOL is shown in Fig. 4.1. Initially the hard state is formed when the rates were still low and shock front was hundreds of Schwarzschild radii away and the advective (halo) component rate increases first due to its short infall time. Subsequently, the Keplerian rate starts to increase since its angular momentum is high and it is to be transported by viscosity. Here the object goes to hard intermediate states. The rate continues to rise and the cooling time scale inside CENBOL starts to be smaller compared to the infall time scale when the condition of oscillation of the shock front is violated and the QPO seen thus far, becomes sporadic and state becomes soft-intermediate. Finally, if Keplerian matter supply is really high, and the viscosity can transport angular momentum very efficiently, soft photons overwhelmingly cools the CENBOL removing it altogether and the soft state is produced. This gradual transformation of the size and shape of the CENBOL is clearly depicted in Fig. 4.2. When the companion turns off the active phase, the process is reversed albeit in a different time scale. Thus, by giving a clear theoretical origin of the Compton cloud (CENBOL) and self-consistently amalgamating the synergy and the inter-conversion of the two components through viscosity, the TCAF solution provides a clear picture of the entire outburst process and obviates the need of phenomenological models in the subject.

For the calculations, all the equations are reduced to their dimensionless forms. The important references can be found in Chakrabarti 1989 (hydrodynamical equations), CT95 (spectral, radiative transfer equations), Debnath et al. (2015a). The last one is the first papers after inclusion of TCAF in XSPEC, where important equations (eq. no. 1 to 5) of TCAF solutions are summarized.

Lengths are measured in units of $r_s = 2GM_{BH}/c^2$ (G and c being gravitational constant and the velocity of light), and the accretion rates are measured in units of Eddington rate (also a function of the black hole mass M_{BH}). The disc accretion rate (\dot{m}_d), the halo accretion rate (\dot{m}_h), the shock location (X_s), the shock compression ratio (R) and the mass of the BHC (M_{BH}) are taken as input parameters and a resulting spectrum is generated. The first four parameters are dependent on the flow properties. Hence, their time-variation reveals the accretion flow dynamics around the object during an outburst. Numerical simulations (Giri & Chakrabarti 2013) and spectral studies (Ghosh et. al. 2011) of BHCs reveal that the TCAF solution is the most general solution for accreting matter onto a black hole. Self-consistency and stability check of the transonic solution by Giri & Chakrabarti (2013) and Mondal & Chakrabarti (2013) corroborates that an advective flow will eventually give rise to a TCAF solution (CT95) when viscous stress near the equatorial plane is substantial. This solution therefore invokes two types of energy extraction processes into a single coherent framework: i) viscous dissipation in the Keplerian component to produce soft X-rays and ii) Inverse Comptonization of these soft photons to produce hard photons by stored thermal energy in the weakly viscous CENBOL.

After obtaining the shape of the overall spectra, suitable model normalization N is used to raise or lower it to match the observed spectra. In diskbb plus powerlaw model, the normalization comes only from the disc integrated photon number which is used to obtain the inner edge of the truncated disc. In TCAF fits, one cannot separate the black body and powerlaw components since the disc radiation and its Comptonized spectrum are summed up along with the reflected

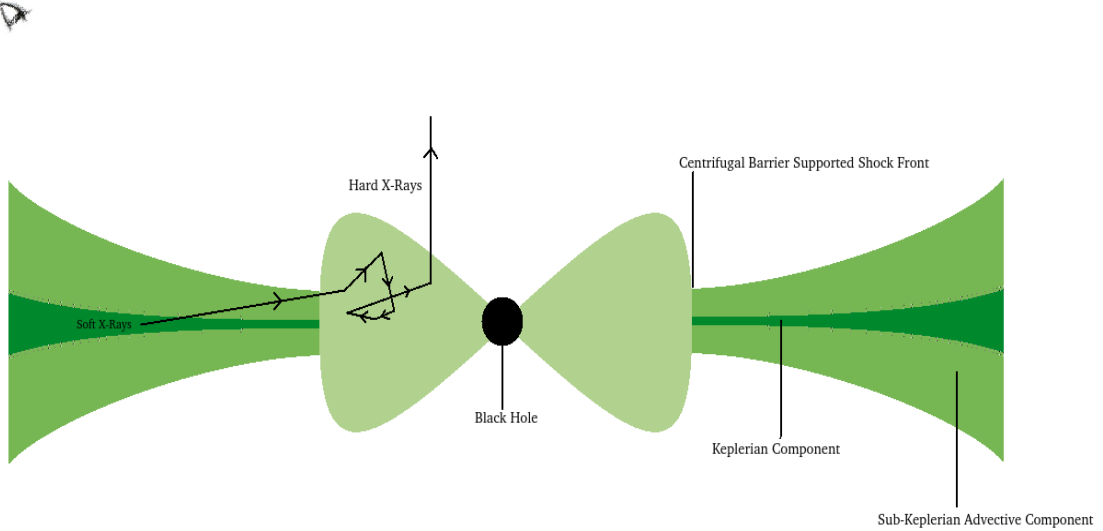


Figure 4.1: A schematic diagram of the accretion flow dynamics and radiation processes in a Two Component Advective Flow (TCAF) solution. Adapted from CT95 and taken from Bhattacharjee et al. (2017).

components in the fits file. The information about the inner edge of the truncated disc is in determining the shock location which is also the outer edge of the Compton cloud (CENBOL). Since these information are already fed into the grid of the fits file, we only require a constant normalization which is primarily mass (M_{BH}), distance (D in units of 10 kpc) and inclination angle (i) dependent through a functional relation $N \sim [r_S^2/4\pi D^2] \sin(i)$ (Molla et al. 2016b, hereafter M16b). Error in mass determination would give rise to error in normalization. Ideally if the CENBOL was lying in a plane, the inclination angle would be globally constant, unless the disc is precessing (which we do not assume here). Also, M_{BH} should not vary over the time scales of observation. Since $M_{BH} \sim T^4$, and the spectral fits are sensitive to the temperature T , a small error in determination of T gives rise to a significant error in M_{BH} . This in turn is reflected in the normalization. Moreover, there can be changes in the peak flux with spectral states when the CENBOL changes its shape and size self-consistently. The variation of flux is due to the variation of accretion rates (\dot{m}_d and \dot{m}_h), shock location (X_s) and compression ratio (R). In any case, our result is independent of the exact value of normalization, and our requirement is that it may remain in a narrow range so that we are certain the fitting routine stays in the same global minimum. The average value, for statistical reasons, is taken as the constant value of normalization for the outburst and the entire study is repeated with this constant normalization. Under this assumption, if the M_{BH} fluctuates, D and i have to adjust to ensure a constant N , though that does not affect our analysis. For all practical purposes, this N is ‘fixed’ from one outburst to the other as it should be when precession of the disc is absent.

Recently, the TCAF model (CT95; Chakrabarti, 1997) has been successfully incorporated in HEASARC’s spectral analysis software package XSPEC (Arnaud, 1996) as a local additive table model (Debnath, Chakrabarti & Mondal 2014; Mondal, Debnath & Chakrabarti 2014; Debnath, Mondal & Chakrabarti 2015a; Debnath, Molla, Chakrabarti & Mondal 2015b; Jana et al. 2016; Chatterjee et al. 2016; Mondal, Chakrabarti & Debnath 2016; M16b). It accomplishes fitting of the spectral data of several transient BHCs (e.g., H 1743-322, GX 339-4, MAXI J1659-152, MAXI J1836-194), during their X-ray outbursts which in turn enables us to get a much clearer picture

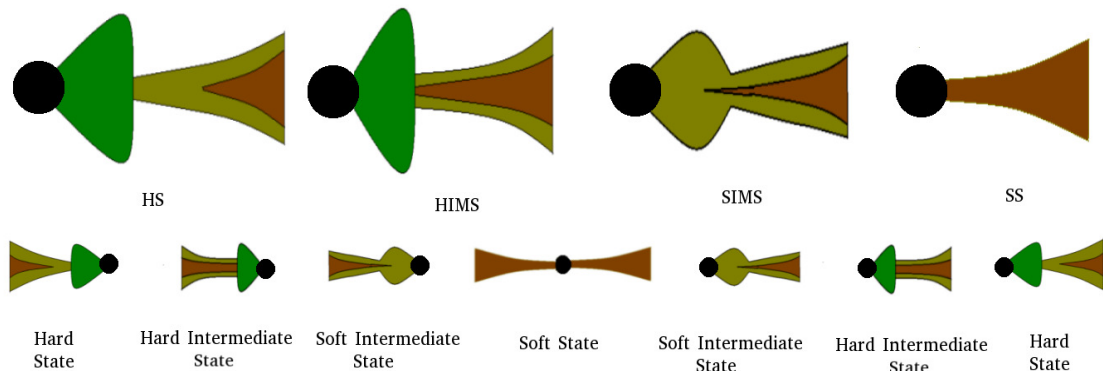


Figure 4.2: A schematic diagram showing the evolution of the CENBOL and the Keplerian disc in a Two Component Advective Flow (TCAF) solution. At the onset of an outburst, the halo is dominant and the shock front is far away (hard state: HS). The Keplerian component moves inward, cooling the CENBOL and making it smaller (hard intermediate:HIMS). For high disc accretion rate, first the CENBOL cools and QPOs became sporadic (soft Intermediate state: SIMS) and finally the halo component is cooled down totally (soft state: SS). The reverse sequence follows when the supply at the outer edge halted. Adapted from Chakrabarti (2016), and taken from Bhattacharjee et al. (2017).

of the accretion flow dynamics in terms of the disc and halo mass accretion rates, the location and size of the Comptonizing cloud (here, CENBOL) and the strength of the shock, which in conjunction with the size and halo rate gives an idea of the optical depth.

Propagatory Oscillatory Shock (POS) model

Once the Keplerian disc is formed, the CENBOL is cooled down gradually. If the cooling timescale of the CENBOL lies within $\sim 50\%$ of the infall time scale from the shock front to the black hole, a resonance occurs when the shock or the outer edge of the Compton cloud starts to oscillate (Molteni, Sponholz & Chakrabarti, 1996; Chakrabarti & Manickam, 2000; Chakrabarti et al. 2015). The oscillation of the shock front leads to the generation of low frequency quasi-periodic oscillations (QPOs) in the power density spectra of the light curves. Due to variation of shock conditions with the changes in disc and halo accretion rates, the average shock location moves inward (outward) for the rising (declining) phase of the outburst (Fig. 4.2). Simultaneously, the QPO frequencies evolve as well.

The frequency of oscillation of the shock front, which in turn is related to the QPO frequency (ν_{qpo}) is obtained from the inverse of the infall time (t_{infall}). If, c is the speed of light, G is the gravitational constant and M_{BH} is the mass of the black hole, then the unit of frequency is given by, $\nu_{s0} = \frac{c^3}{2GM_{BH}}$. The QPO frequency is then written as,

$$\nu_{qpo} = \nu_{s0}/t_{infall} = \frac{c^3}{2GM_{BH}} \frac{1}{[RX_s(X_s-1)^{1/2}]}$$

where, R is the shock compression ratio and X_s is the shock location in units of r_S (Chakrabarti et al. 2008; Chakrabarti et al. 2009; Debnath et al. 2010; Nandi et al. 2012; Debnath et al.

2013).

According to the POS model, the shock location varies with time as,

$$X_s(t) = X_s(0) \pm tv_0/r_S,$$

where v_0 and $X_s(0)$ are the initial location and velocity of the shock. The plus (minus) sign is associated with the shock front for declining (rising) phase. This can, in turn, be used to determine the mean radial velocity of the shock front during the outburst which further enables us to study the evolution of X_s and hence the evolution of the QPO frequencies. The POS model has a parametric dependence on the mass M_{BH} . Hence, if QPOs are observed in a series of consecutive days, then the POS model can be used to fit the variation of the QPO frequency with time. The value of mass which gives the best fit to the data will be the mass of the BH.

Observation and Data Analysis

RXTE/PCA covered the 2004 outburst of H1743-322 spanning from July 11, 2004 (MJD=53197.287) to November 5, 2004 (MJD=53314.749). 42 observations were recorded by RXTE during the aforementioned period with an average gap of ~ 3 days between consecutive observations. The data was acquired using the process described in Fig. 4.3. We use HEASARC's software package HEASoft, version HEADAS 6.18 and XSPEC version 12.9.0 to carry out our data analysis procedure (see Fig. 4.4). In order to generate the source and the background ".pha" files and fit the spectrum exploiting the TCAF solution we follow the procedure adopted by Debnath et al. (2013, 2014). For spectral analysis, the Standard2 mode Science Data of PCA (FS4a*.gz) were used. Spectra from all the Xenon layers of PCU2 consisting of 128 channels (without any binning/grouping of the channels) were extracted for all the observational IDs. Dead-time and pca breakdown correction were incorporated in our analysis. We extracted the PCA background by applying the command "runpcabackest" and by using the latest bright-source background model. In order to take care of the South Atlantic Anomaly (SAA) data we incorporated the pca saa history file. The task "pcarsp" was used to create the response files. For preparing the power density spectra (PDS) all active PCUs were used for a broad energy binned between 0-35 channel data. The 2.5 - 25 keV PCA spectra of these observation IDs with appropriate background subtraction were fitted with TCAF solution based additive model fits file. To accomplish the best fit, a Gaussian line was used to model the iron line emission. Throughout the outburst, the hydrogen column density (N_H) was kept fixed at 1.6×10^{22} atoms cm^{-2} (Capitanio et al. 2009) for absorption model *wabs*. A systematic instrumental error of 1% was assumed. We used "err" command to find out 90% confidence error values in model fitted parameters.

Here we initially fit the entire 117 day long outburst using *wabs*(diskbb+PL)* model. Next, we fit the last 27 days of the outburst (declining phase) by keeping \dot{m}_d , \dot{m}_h , X_s , and M_{BH} free and normalization within the range $10 < N < 20$ as in Molla et al. (M16a). Next, using the POS model, the velocity of the shock front was found out using the parameters as obtained from the previous analysis. The same process of spectral fits using the TCAF model was repeated using the average value of normalization obtained from the previous analysis. For this purpose, the model fits file (TCAF.fits) was used which uses the theoretical spectra-generating software by varying the five basic input parameters in the suitably upgraded CT95 code and is then incorporated in the XSPEC as a local additive model. The version of TCAF used for fitting the spectra in the present work is TCAFv0.1.R3.fits used in Debnath et al. (2015a) and references therein.

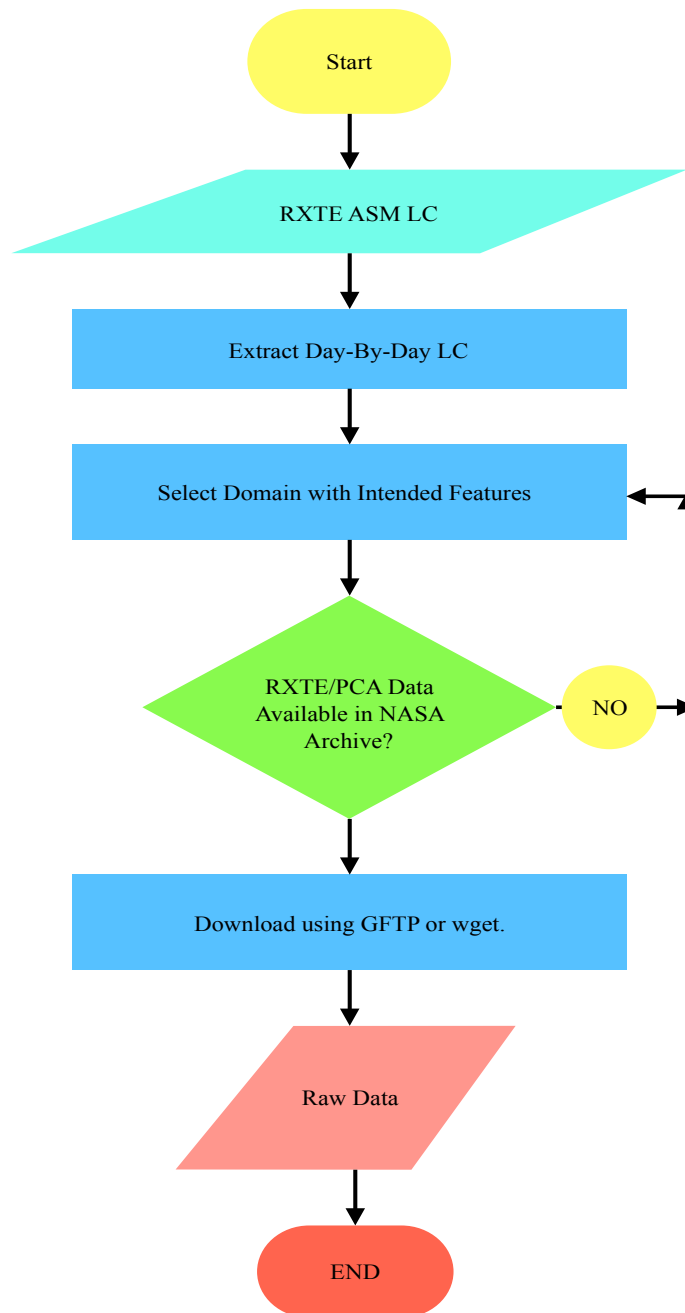


Figure 4.3: A working flowchart of the NASA archival data acquisition process. As we mainly worked with the RXTE/PCA data, only that has been mentioned here. For HEXTE similar mechanism can be applied.

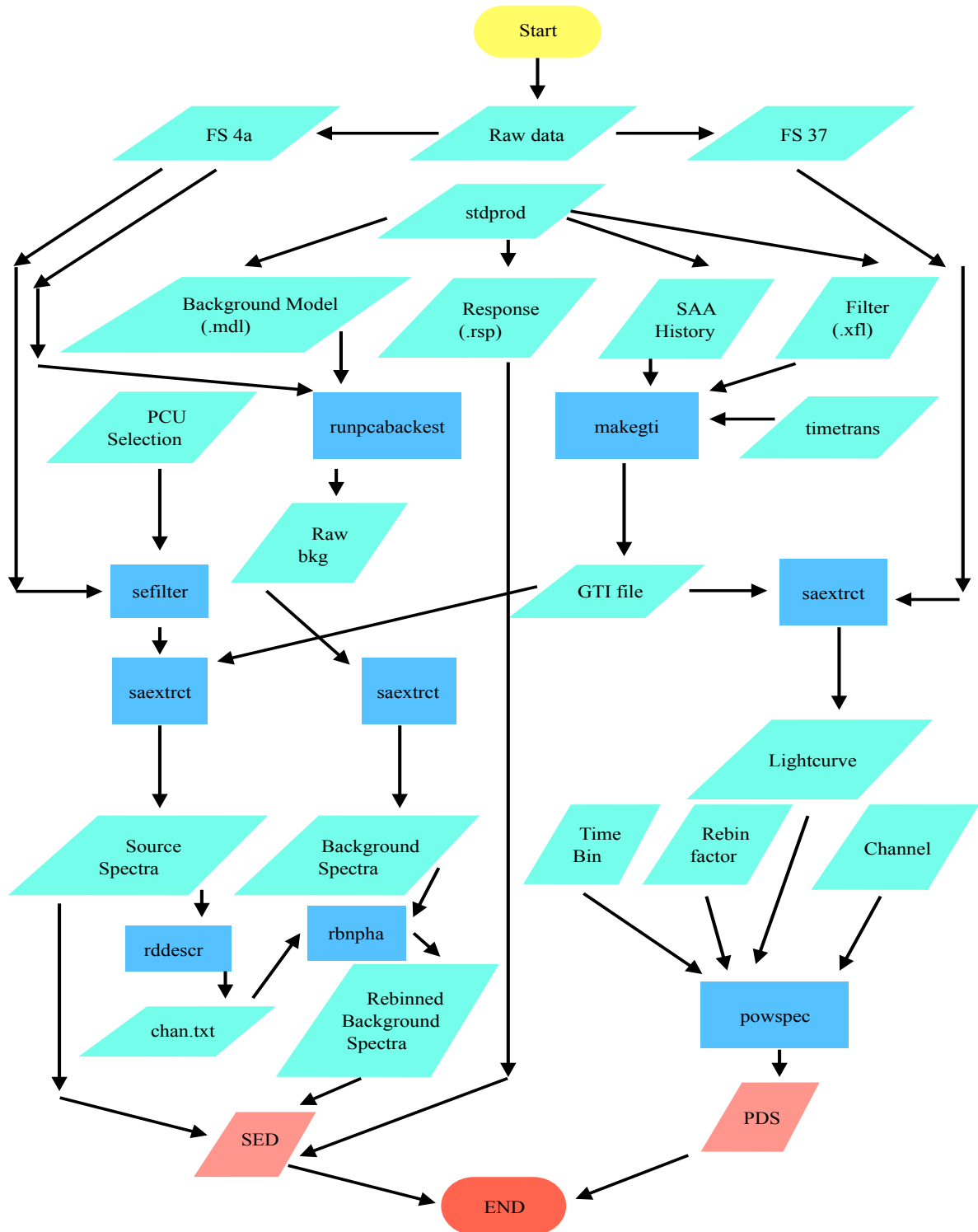


Figure 4.4: A working flowchart of the data reduction process [following Debnath et al. (2013; 2014)]. Only the important steps in reducing the raw data into spectrum and lightcurve, are represented. NASA’s HEASARC tool, HEASOFT version 6.18 and 6.21 have been used for different datasets of this work. For the commands, check the list of commands.

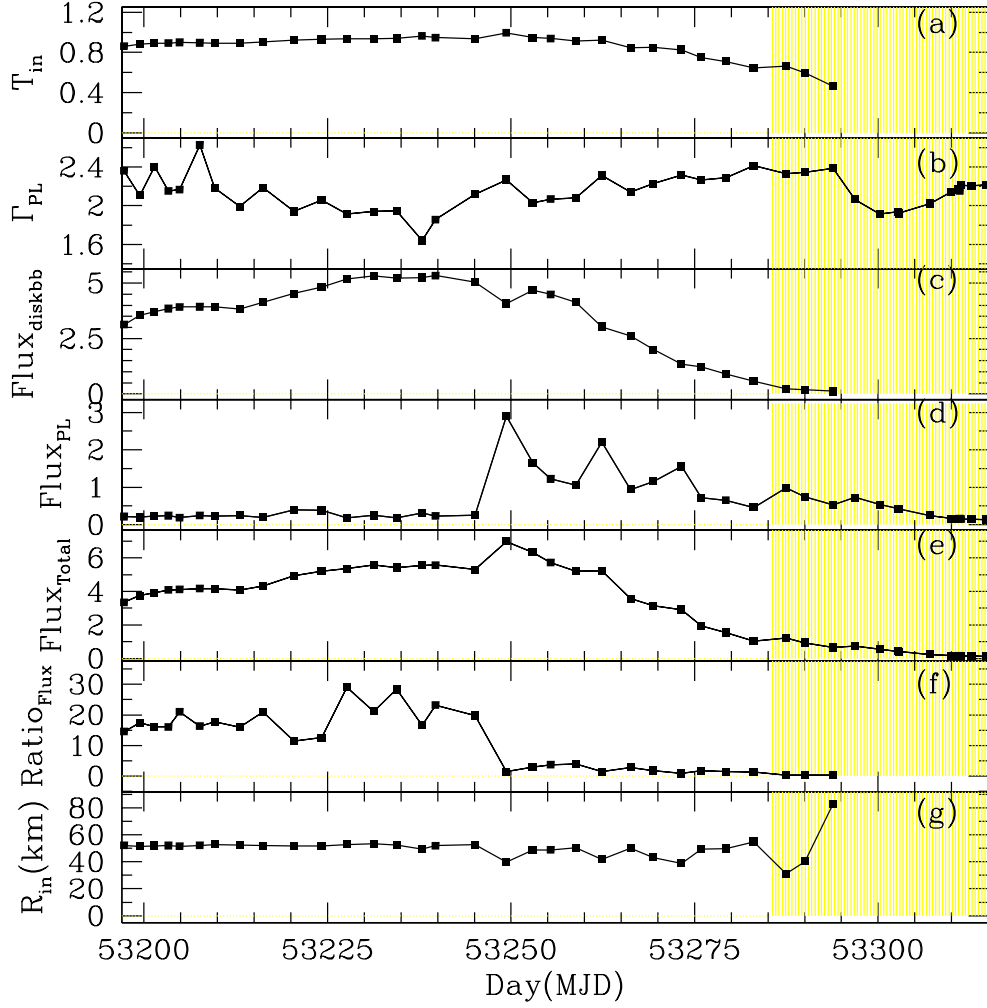


Figure 4.5: Variation of (a) the *diskbb* Temperature (T_{in}) in units of keV, (b) the *power law* photon index (Γ), (c) the *diskbb* flux ($\text{Flux}_{\text{diskbb}}$) in units of 10^{-9} ergs $\text{cm}^{-2}\text{s}^{-1}$, (d) the *powerlaw* flux (Flux_{PL}) in units of 10^{-9} ergs $\text{cm}^{-2}\text{s}^{-1}$, (e) the total flux ($\text{Flux}_{\text{Total}}$) in units of 10^{-9} ergs $\text{cm}^{-2}\text{s}^{-1}$, (f) the ratio of *diskbb* flux ($\text{Flux}_{\text{diskbb}}$) and *powerlaw* flux (Flux_{PL}), $\text{Ratio}_{\text{flux}}$, and (g) the inner edge of the disc (R_{in}) in units of km, given by the *diskbb* normalization with MJD (days). All the above variations are in the 2.5-25.0 keV energy band. The declining phase, that was fitted with TCAF solution, is shaded with yellow. Taken from Bhattacharjee et al. (2017).

Results

Here, we present the results obtained from the analysis of the data of H1743-322 during the 2004 outburst by the TCAF fits.

A comparison of RXTE/ASM light curves of H1743-322 between 2003 and 2009 shows that the source predominantly resided in the softer states during the 2004 outburst, namely, soft-state (SS) and soft-intermediate state (SIMS), and only towards the end of the outburst the source entered in the hard-intermediate state (HIMS) and hard-state (HS) (Fig. 4.5(e)). Capitanio et. al (2005) also reports a similar behavior of the source during this outburst.

Figures 4.5(a) and 4.5(b), illustrate variation of *diskbb* temperature T_{in} and the *powerlaw* photon index Γ with MJD. Figures 4.5(c) and 4.5(d) show the variation of the flux contributed by *diskbb* and *powerlaw* models respectively, while Fig. 4.5(e) shows the variation of the total spectral flux. The ratio of *diskbb* flux ($Flux_{diskbb}$) and *powerlaw* flux ($Flux_{PL}$), ($Ratio_{flux}$) is shown in Panel 4.5(f). The variation of the inner edge of the disc (R_{in}), given by the *diskbb* normalization with MJD is shown in Fig. 4.5(g). We calculated the individual flux contributions for the *diskbb* and the *powerlaw* components by using the convolution model “cflux” once for the *diskbb* and then for the *powerlaw*, to fit the spectra in the 2.5-25 keV energy band. The analysis with *wabs*(diskbb+powerlaw)* model also reveals that the data for the rising phase was only obtained well after the object settled into Soft-Intermediate state. Subsequently, during the rising phase, the peak and the initial part of the declining phase of the outburst the underlying accretion flow was primarily governed by a single component, i.e., the Keplerian flow. As a result, its spectrum is principally fitted by *diskbb* and the additional advective component is not needed. Since in TCAF we are interested to study the interplay between the two components, we concentrate on the declining phase during MJD=53287.484 - MJD=53314.749 period.

Spectral Data Fitted by TCAF model

Table 4.1 illustrates the variation of the physical parameters, namely, the disc accretion rate (\dot{m}_d), the halo rate (\dot{m}_h), the shock location (X_s) which gives an indication of the size of the Compton cloud and the strength of the shock (R) with days (MJD) in the 2.5-25 keV (3-53 channels) energy band during the declining phase of the outburst. To explicitly show that the rates are independent, we also plot the ratio $ARR(=\dot{m}_h/\dot{m}_d)$. The model normalization (N) is kept in the range 10 – 20. The average value of N (N_{avg}) is determined and the same procedure is repeated for the constant value of $N = N_{avg} = 13.65$, which we think is a good estimate of the normalization. If we ignore possible precession in the system, contribution from jets which have not been introduced in TCAF, and the possible change in shape with states, this can be treated as true normalization for the system. The spectral evolution of the rest of the parameters are shown in Table 4.2. The trends of variation of the flow parameters were found to be similar in both cases. Hence, we only discuss the spectral evolution for N in the range 10 – 20.

Spectral Evolution of the Declining Phase and Corresponding TCAF Parameters:

(i) *Hard-Intermediate State (HIMS)*: For a period of ~ 13 days, MJD=53287.484 to 53300.208, the object seems to have remained in the Hard-Intermediate state (HIMS) which is evident from Table 4.1 and Fig. 4.7. During this period the PCA flux consistently decreases as long as \dot{m}_d is greater than \dot{m}_h , from MJD=53287.484 to MJD=53293.882 and then remains roughly constant (Fig. 4.7 a). On MJD=53296.834, \dot{m}_h becomes greater than \dot{m}_d and shock suddenly moves outward from $X_s = 27.803r_S$ to $X_s = 75.662r_S$. During the HIMS to HS transition, on MJD=53296.834 and MJD=53300.208, QPOs were observed in the power density spectra (PDS). A typical spectra

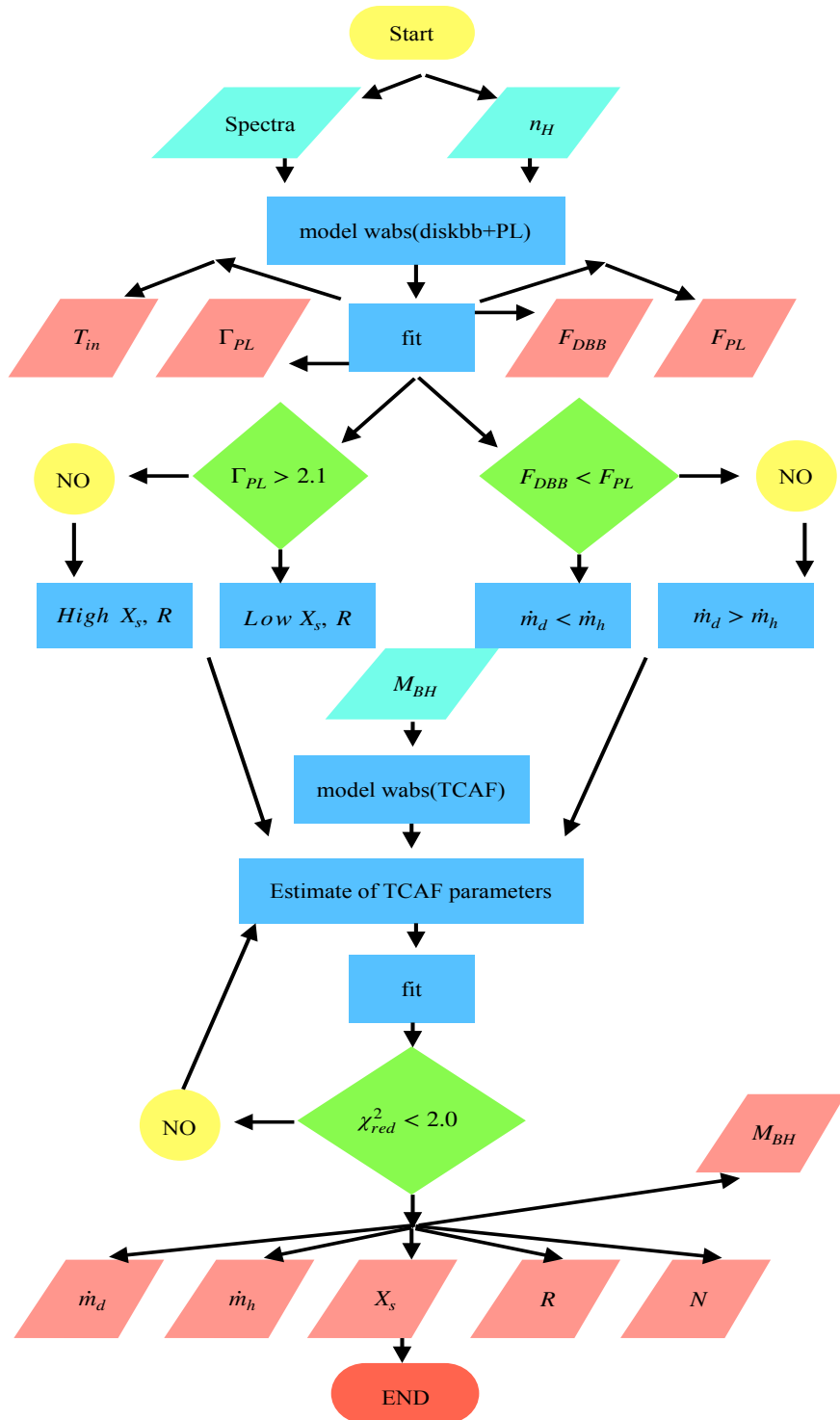


Figure 4.6: A rough scheme of how spectral data is fitted with the TCAF spectral code. As the fitting is achieved with an additive local model, using a fits file, the initial guesses of the parameters are important in obtaining quicker fits or avoiding local minima or extrema. Here, F_{DBB} , and F_{PL} denote the diskbb and power-law fluxes, respectively. Rest of the notations are based on the text.

of this state, along with the unfolded models and residue is shown in Fig. 4.8(a).

(ii) *Hard-state (HS)*: From the data in Table 4.1 it seems after MJD=53300.208 the source entered in the Hard-State (HS) and remained there till the end of the observation. A typical spectra of this state, along with the unfolded models and residue is shown in Fig. 4.8b. The PCA flux also went down from this day and remained low till the end of the observation which is characteristic of the Hard State. This is evident from Fig. 4.7a. No QPOs were observed in the power-density spectrum of the source during these days. The disc accretion rate which had fallen towards the end of the Hard Intermediate State (HIMS) remains low (~ 0.022) while the halo rate remains comparatively higher (~ 0.13). The shock front moves further and further outward with time, from $\sim 75 r_S$ to $\sim 171 r_S$, in a period of ~ 14 days. The propagation of the shock front not only gives the clear picture as promised by the TCAF spectral fits, but also helps us to use another method of verifying the mass of the object by an independent method, namely, by the use of Propagatory Oscillatory Shock (POS) model (Chakrabarti et al., 2005, 2008; Debnath et al. 2010, 2013; Nandi et al. 2012). The spectral analysis restrict both mass and normalization in a narrow domain. We investigate below to check whether the same mass range is obtained from the timing analysis or not.

The mass was determined to be $\langle M_{BH} \rangle = 12.36 \pm 1.73 M_\odot$, with an average $\langle \chi_{red}^2 \rangle = 0.82 \pm 0.20$, and the average normalization is found to be $N_{avg} = 13.65 \pm 2.49$. The same process, when repeated by using a fixed $N = N_{avg} = 13.65$, yielded similar results. These are shown in Fig. 4.9. The mass was determined to be $\langle M_{BH} \rangle = 12.19 \pm 1.88 M_\odot$, with an average $\langle \chi_{red}^2 \rangle = 0.79 \pm 0.19$. The peak of the Gaussian line profile was close to the same value as that of the previous case.

Correlating spectral and timing properties

Timing analysis was limited by the lack of observation of low-frequency QPOs in the declining phase of the outburst. Out of the 14 data IDs, only 2 days showed prominent QPOs. We use this to determine the mass of the object separately. We use the POS model in determining the QPO frequencies from the spectral fit parameters, and use the same equations to obtain the value of mass, for which the deviation between the theoretical and observational QPO frequencies are minimum. We also determine inward velocity of the shock front for the first day of QPO observation to compare our results with previous works (Chakrabarti & Manickam, 2000; Chakrabarti et al. 2009; Debnath et al. 2013).

Each PDS was analysed with a Lorentzian fit using the `ftools` commands. The values of the centroid frequency, full-width at half-maxima and peak power are obtained with 90% confidence. From the values of X_s , R , M_{BH} , the oscillation frequency of the shock front which is directly related to the frequency of the QPOs can be derived and compared to the frequency obtained independently from the analysis of the power density spectrum, ν_{QPO}^{PDS} .

The QPO frequencies obtained from the POS model using the corresponding values of the TCAF parameters taken from Table 4.1, along with their respective systematic errors are given in Table 4.3, and is denoted by ν_{qpo}^{POS} . The same calculation is repeated for the case with constant normalization, using the respective parameters from Table 4.2 and is reported in Table 4.4. We found that these two values agree with each other within the error bars.

Next, on MJD=53296.834 and MJD=53300.208, when QPOs were observed, we used the corresponding fit parameters X_s and R and varied the mass from 9 to 15 M_\odot to calculate the corresponding QPO frequencies, ν_{QPO} . The chi-square of the distribution is calculated using ν_{QPO}^{PDS} . The value of the mass for which the chi-square is minimum corresponds to M_{BH}^{POS} which is quite close to the value of the mass obtained from the TCAF fits, M_{BH} , on each of the days.

We calculated the velocity of the shock front for the first day (MJD=53296) of QPO observation. The velocity of the shock front is $v_0 = 107.0_{-18.083}^{+18.083} \text{ cm s}^{-1}$, which is of the order of values found by Debnath et al. (2013). For the constant normalization case, it came out to be $v_0 = 31.6_{-16.146}^{+16.146} \text{ cm s}^{-1}$. This is in the same ball park for all the outburst sources GRO J1655-40 (Chakrabarti et al., 2005, 2008), XTE J1550-564 (Chakrabarti et al., 2009), GX 339-4 (Debnath et al., 2010; Nandi et al., 2012), H 1743-322 (Debnath et al., 2013) and IGR J17091-3624 (Iyer et al., 2015) and is generally thought to be due to the change of pressure in CENBOL due to Compton cooling which drives the shock radially (Mondal et al. 2015). The deviation between these two approaches may be due to the fact that POS had only two points to fit the evolution of QPOs. With constant normalization, the position of the shock front does not change much during the two consecutive days which gives rise to a large systematic error in its measurement which is responsible for the discrepancy between the shock velocities in the two cases.

Mass estimation using TCAF and POS model fits

The three different methods used in determining the mass of the black hole, yield masses in the same range, up to the corresponding error-bars. We obtain the average value of mass to be $\langle M_{BH} \rangle = 12.36 \pm 1.73 M_{\odot}$, for spectral fits with free normalization. The average value of mass is found to be $12.19 \pm 1.88 M_{\odot}$, when the normalization is kept constant at $N = N_{avg} = 13.65$. The POS model was applied to both the scenarios for both the observation IDs. In the first case, the masses obtained were $14.011 M_{\odot}$ and $10.479 M_{\odot}$ respectively. For the second case, the masses were $12.156 M_{\odot}$ and $11.125 M_{\odot}$ respectively. All four of these values lie within the range estimated by the spectral fits with constant normalization ($10.31 M_{\odot} - 14.07 M_{\odot}$). Incidentally, Molla et al. (M16a) also obtained the average value of normalization $N \sim 15.55$ which lies within the range predicted by us. Our result conforms with the previous predictions of Shaposhnikov & Titarchuk (2009) and McClintock et al. (2009). However, both these methods use mass of other BHC as a reference to calculate mass of an unknown BH, but our method gives an independent method, where mass can be estimated even from one spectral fit using TCAF solution. We do not require to know the mass of other BHCs to estimate mass of an unknown BHC. In Shaposhnikov & Titarchuk 2009, mass only can be predicted if there are sufficient observations in the transition and saturation branches of their QPO frequency-Photon Index correlation plot. Similarly, in high frequency correlation method (used in McClintock et al. 2009), mass of those unknown BHCs can be predicted, which have shown signature of HFQPOs (so far only 7 BHCs). These sources have shown multiple set (2:3) of HFQPOs.

The iron line emission profile was found to be peaked at around 6.5 keV for all the fits, with an average of $6.57 \pm 0.13 \text{ keV}$. Fig. 4.7 shows variations of all the TCAF parameters with MJD. Thus, we find that the normalization N of the TCAF model does not change over a period of seven years i.e., from 2004-2011 indicating that probably the accretion disc is not precessing with significant amplitude.

Discussions and Conclusions

In this Chapter, we investigated evolution of spectral properties of the Galactic BHC H1743-322 during the declining phase of the 2004 outburst to study the accretion flow dynamics and to extract the mass of the BH independently from each observation. This was the first ‘normal’ outburst after about 20 years. However, data during hard and hard-intermediate states in the rising phase is missing and since then it was mostly in soft states except towards the end of the

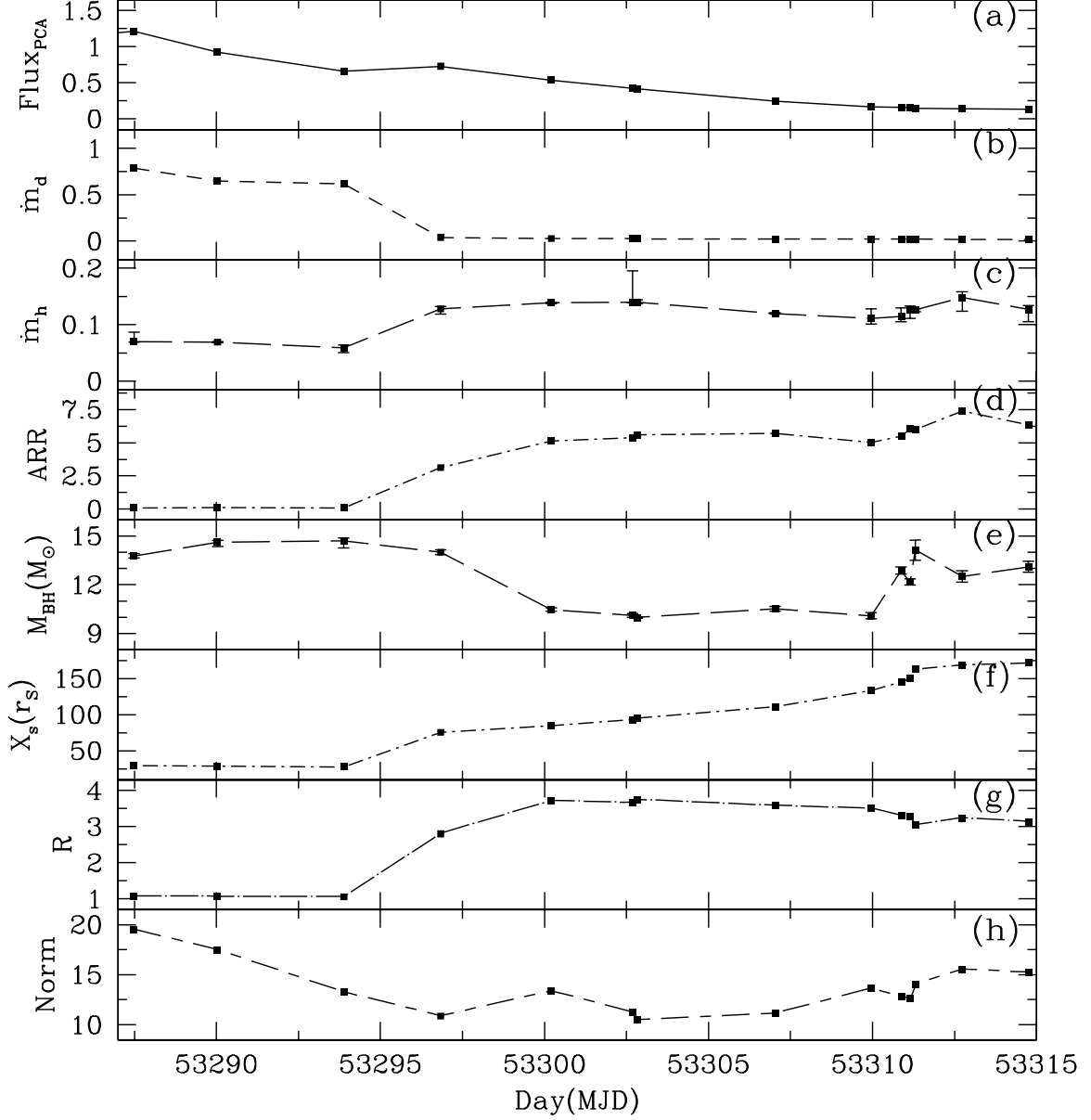


Figure 4.7: Variation of (a) the total PCA flux (in units of 10^{-9} ergs $\text{cm}^{-2}\text{s}^{-1}$), (b) the disc accretion rate \dot{m}_d (in Eddington units), (c) the sub-Keplerian halo accretion rate \dot{m}_h (in Eddington units), (d) the accretion rate ratio, $\text{ARR}(= \dot{m}_h/\dot{m}_d)$, (e) the mass of the black hole (in units of M_\odot), (f) the shock location X_s (in units of r_s), (g) the shock strength R , and (h) the normalization of the TCAF model, with day (MJD). Note that the normalization is restricted between 10 – 20 in the above fits. Variation of all the aforementioned quantities are studied in the 2.5-25.0 keV energy band. We have added error-bars corresponding to Fig. 4.7(c) and Fig. 4.7(e). The remaining error-bars are too inconspicuous to be marked. Taken from Bhattacharjee et al. (2017).

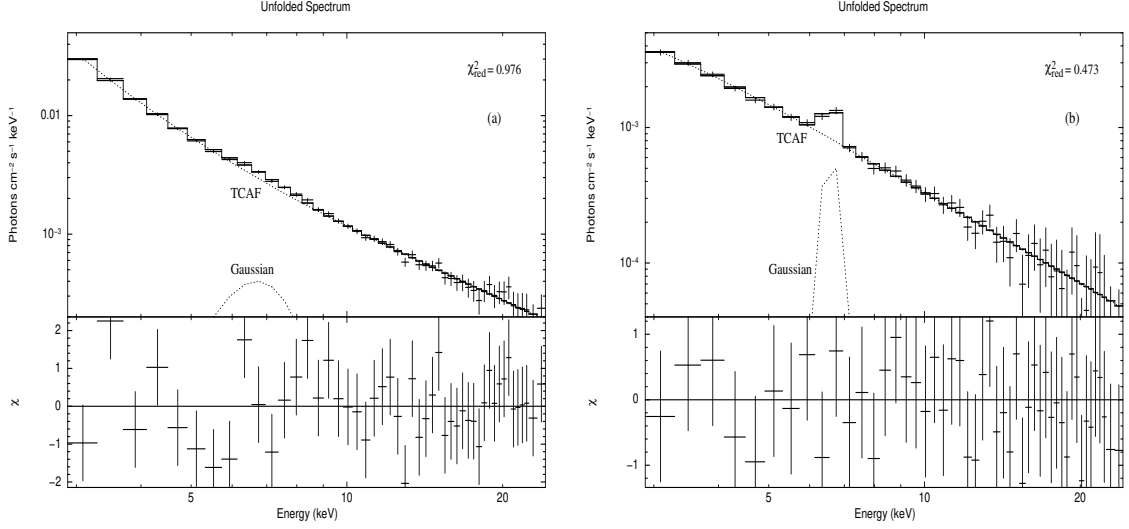


Figure 4.8: Unfolded spectra with residue of two observations (ID: 90115-01-03-00 (a) and 90115-01-06-00 (b)) for energy 2.5-25.0 keV, fitted with $wabs(TCAF+Gaussian)$ models, taken from Bhattacharjee et al. (2017).

Table 4.1

Table 4.1: TCAF Model Fitted Parameters in 2.5-25 keV energy band for normalization in the range 10 – 20. Here, we list the variations of disc accretion rate (\dot{m}_d) and halo accretion rate (\dot{m}_h) in Eddington units, shock location (X_s) in Schwarzschild radius, shock compression ratio (R), mass of the BHC (M_{BH}) in M_\odot and model normalization (N) with MJD along with their errors. The reduced (χ^2) values for each case is also shown in the last column. Taken from Bhattacharjee et al. (2017).

| Obs. | Id. | MJD | $\dot{m}_d (M_{Edd})$ | $\dot{m}_h (M_{Edd})$ | $X_s (r_S)$ | R | $M_{BH} (M_\odot)$ | N | χ^2/dof |
|------|---------|-----------|----------------------------|---------------------------|-----------------------------|---------------------------|----------------------------|----------------------------|--------------|
| 1 | X-02-00 | 53287.484 | $0.785^{+0.108}_{-0.028}$ | $0.070^{+0.017}_{-0.001}$ | $29.790^{+0.019}_{-0.019}$ | $1.070^{+0.001}_{-0.001}$ | $13.774^{+0.143}_{-0.141}$ | $19.496^{+0.165}_{-0.164}$ | 37.41/40 |
| 2 | X-02-01 | 53290.036 | $0.649^{+0.007}_{-0.007}$ | $0.064^{+0.001}_{-0.001}$ | $28.862^{+0.023}_{-0.023}$ | $1.063^{+0.002}_{-0.001}$ | $14.611^{+0.127}_{-1.253}$ | $17.481^{+0.304}_{-0.303}$ | 44.00/40 |
| 3 | X-03-00 | 53293.882 | $0.617^{+0.055}_{-0.021}$ | $0.059^{+0.005}_{-0.008}$ | $27.803^{+0.032}_{-0.032}$ | $1.055^{+0.001}_{-0.001}$ | $14.700^{+0.176}_{-0.438}$ | $13.242^{+0.120}_{-0.120}$ | 39.04/40 |
| 4 | X-03-10 | 53296.834 | $0.041^{+0.004}_{-0.004}$ | $0.128^{+0.004}_{-0.009}$ | $75.662^{+0.704}_{-0.699}$ | $2.804^{+0.010}_{-0.010}$ | $13.995^{+0.151}_{-0.149}$ | $10.856^{+0.102}_{-0.102}$ | 40.92/40 |
| 5 | X-04-00 | 53300.208 | $0.027^{+0.001}_{-0.0003}$ | $0.139^{+0.001}_{-0.002}$ | $84.784^{+1.265}_{-1.249}$ | $3.717^{+0.046}_{-0.046}$ | $10.476^{+0.091}_{-0.090}$ | $13.355^{+0.156}_{-0.155}$ | 41.69/40 |
| 6 | X-04-10 | 53302.689 | $0.026^{+0.0003}_{-0.005}$ | $0.140^{+0.055}_{-0.001}$ | $93.115^{+1.528}_{-1.506}$ | $3.660^{+0.158}_{-0.134}$ | $10.112^{+0.106}_{-0.105}$ | $11.228^{+0.171}_{-0.171}$ | 35.92/40 |
| 7 | X-04-20 | 53302.829 | $0.025^{+0.007}_{-0.003}$ | $0.140^{+0.004}_{-0.003}$ | $95.118^{+0.657}_{-0.654}$ | $3.745^{+0.022}_{-0.021}$ | $9.981^{+0.044}_{-0.044}$ | $10.480^{+0.072}_{-0.071}$ | 31.09/40 |
| 8 | X-05-00 | 53307.032 | $0.021^{+0.005}_{-0.003}$ | $0.120^{+0.001}_{-0.001}$ | $114.867^{+0.737}_{-0.733}$ | $3.519^{+0.024}_{-0.028}$ | $10.517^{+0.150}_{-0.140}$ | $11.121^{+0.250}_{-0.249}$ | 31.58/40 |
| 9 | X-05-01 | 53309.956 | $0.022^{+0.004}_{-0.004}$ | $0.111^{+0.017}_{-0.010}$ | $133.474^{+1.572}_{-1.556}$ | $3.505^{+0.032}_{-0.032}$ | $10.094^{+0.204}_{-0.200}$ | $13.625^{+0.238}_{-0.238}$ | 17.51/40 |
| 10 | X-05-03 | 53310.876 | $0.021^{+0.004}_{-0.003}$ | $0.115^{+0.015}_{-0.010}$ | $145.277^{+1.281}_{-1.273}$ | $3.309^{+0.023}_{-0.023}$ | $12.873^{+0.229}_{-0.224}$ | $12.815^{+0.204}_{-0.203}$ | 32.10/40 |
| 11 | X-05-10 | 53311.146 | $0.021^{+0.004}_{-0.001}$ | $0.127^{+0.006}_{-0.016}$ | $149.990^{+1.338}_{-1.329}$ | $3.267^{+0.021}_{-0.021}$ | $12.167^{+0.192}_{-0.189}$ | $12.638^{+0.194}_{-0.194}$ | 23.74/40 |
| 12 | X-05-02 | 53311.306 | $0.021^{+0.014}_{-0.004}$ | $0.126^{+0.002}_{-0.003}$ | $162.910^{+3.033}_{-2.980}$ | $3.041^{+0.053}_{-0.052}$ | $14.133^{+0.613}_{-0.641}$ | $14.016^{+0.550}_{-0.549}$ | 33.27/40 |
| 13 | X-05-04 | 53312.736 | $0.020^{+0.008}_{-0.002}$ | $0.128^{+0.010}_{-0.024}$ | $168.780^{+2.106}_{-2.078}$ | $3.237^{+0.033}_{-0.033}$ | $12.504^{+0.365}_{-0.354}$ | $15.540^{+0.423}_{-0.422}$ | 31.36/40 |
| 14 | X-06-00 | 53314.749 | $0.020^{+0.007}_{-0.002}$ | $0.127^{+0.007}_{-0.022}$ | $171.966^{+2.146}_{-1.900}$ | $3.135^{+0.025}_{-0.032}$ | $13.108^{+0.334}_{-0.325}$ | $15.217^{+0.345}_{-0.344}$ | 18.94/40 |

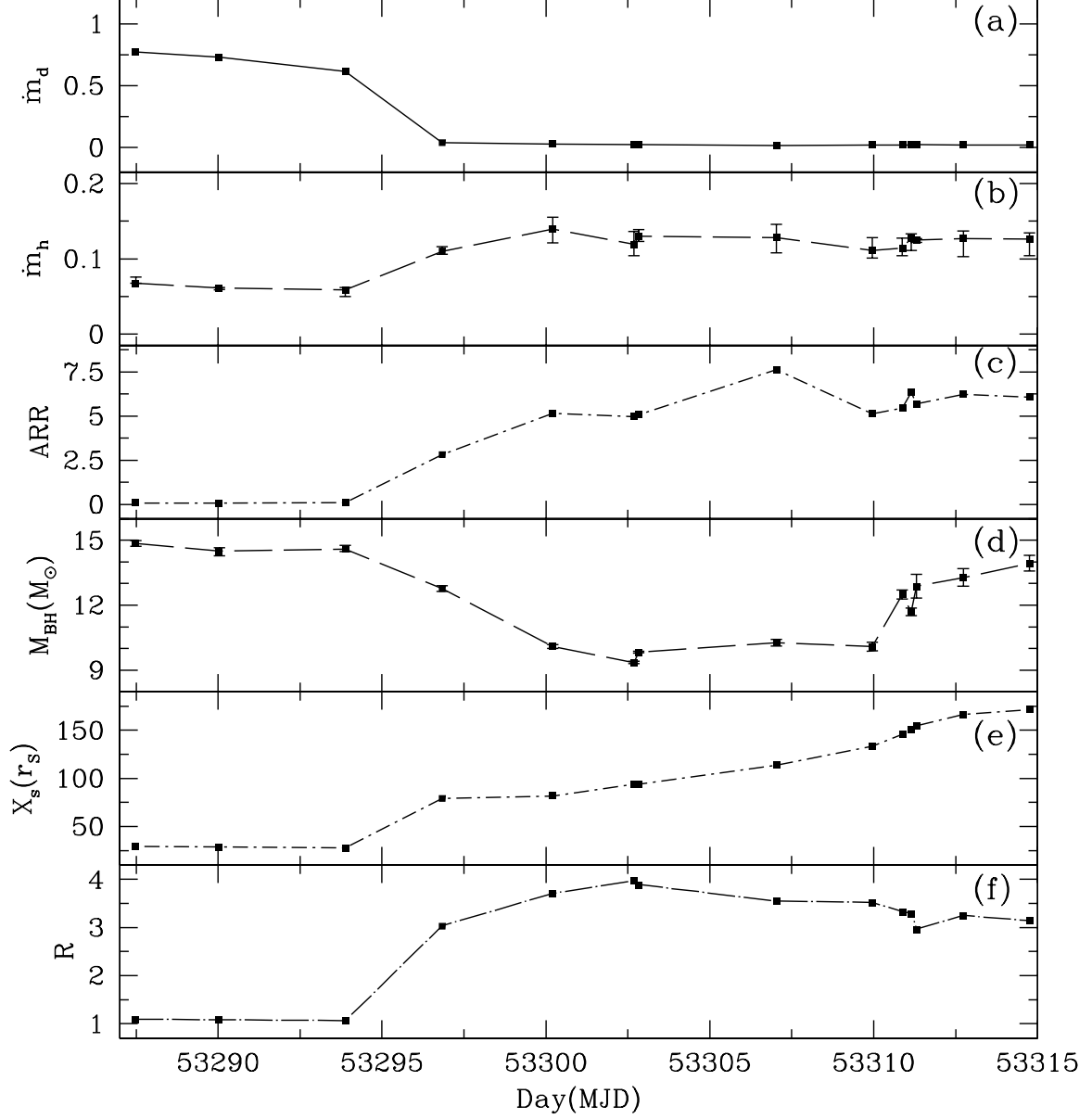


Figure 4.9: Variation of (a) the disc accretion rate \dot{m}_d (in Eddington units), (b) the sub-Keplerian halo accretion rate \dot{m}_h (in Eddington units), (c) the accretion rate ratio, $\text{ARR}(= \dot{m}_h/\dot{m}_d)$, (d) the mass of the black hole (in units of M_{\odot}), (e) the shock location X_s (in units of r_s), (f) the shock strength R , with day (MJD). Variation of all the aforementioned quantities are studied in the 2.5-25 keV energy band keeping the the normalization of the TCAF model fixed to $N = N_{\text{avg}} = 13.65$. We have added error-bars corresponding to Fig. 4.9(b) and Fig. 4.9(d). The remaining error-bars are too inconspicuous to be marked. Taken from Bhattacharjee et al. (2017).

Table 4.2

Table 4.2: TCAF Model Fitted Parameters in 2.5 – 25 keV energy band for normalization, $N = N_{avg} = 13.65$. Here, we list the variations of disc accretion rate (\dot{m}_d) and halo accretion rate (\dot{m}_h) in Eddington units, shock location (X_s) in units of Schwarzschild radius, shock compression ratio (R) and mass of the BHC (M_{BH}) in M_\odot with MJD, along with their errors. The reduced (χ^2) values for each case is also shown in the last column. Taken from Bhattacharjee et al. (2017).

| Obs. | Id. | MJD | $\dot{m}_d (M_{Edd})$ | $\dot{m}_h (M_{Edd})$ | $X_s (r_S)$ | R | $M_{BH} (M_\odot)$ | N | χ^2/dof |
|------|---------|-----------|---------------------------|----------------------------|-----------------------------|---------------------------|----------------------------|-------|--------------|
| 1 | X-02-00 | 53287.484 | $0.771^{+0.065}_{-0.022}$ | $0.068^{+0.008}_{-0.0003}$ | $29.153^{+0.027}_{-0.027}$ | $1.079^{+0.001}_{-0.001}$ | $14.852^{+0.130}_{-0.128}$ | 13.65 | 36.81/41 |
| 2 | X-02-01 | 53290.036 | $0.730^{+0.020}_{-0.019}$ | $0.061^{+0.001}_{-0.002}$ | $28.808^{+0.025}_{-0.025}$ | $1.075^{+0.001}_{-0.001}$ | $14.491^{+0.165}_{-0.216}$ | 13.65 | 44.12/41 |
| 3 | X-03-00 | 53293.882 | $0.615^{+0.050}_{-0.012}$ | $0.059^{+0.003}_{-0.009}$ | $27.768^{+0.032}_{-0.032}$ | $1.054^{+0.001}_{-0.001}$ | $14.594^{+0.167}_{-0.125}$ | 13.65 | 38.71/41 |
| 4 | X-03-10 | 53296.834 | $0.039^{+0.004}_{-0.004}$ | $0.110^{+0.006}_{-0.004}$ | $79.041^{+0.494}_{-0.491}$ | $3.026^{+0.016}_{-0.016}$ | $12.772^{+0.127}_{-0.126}$ | 13.65 | 40.40/41 |
| 5 | X-04-00 | 53300.208 | $0.027^{+0.003}_{-0.003}$ | $0.139^{+0.016}_{-0.018}$ | $81.732^{+1.278}_{-1.260}$ | $3.700^{+0.046}_{-0.046}$ | $10.095^{+0.082}_{-0.081}$ | 13.65 | 41.68/41 |
| 6 | X-04-10 | 53302.689 | $0.024^{+0.002}_{-0.008}$ | $0.119^{+0.017}_{-0.015}$ | $93.727^{+1.872}_{-1.838}$ | $3.963^{+0.034}_{-0.033}$ | $9.356^{+0.061}_{-0.061}$ | 13.65 | 35.63/41 |
| 7 | X-04-20 | 53302.829 | $0.026^{+0.004}_{-0.001}$ | $0.130^{+0.009}_{-0.007}$ | $94.085^{+1.076}_{-1.068}$ | $3.883^{+0.086}_{-0.084}$ | $9.831^{+0.034}_{-0.034}$ | 13.65 | 30.09/41 |
| 8 | X-05-00 | 53307.032 | $0.017^{+0.004}_{-0.001}$ | $0.128^{+0.018}_{-0.020}$ | $113.569^{+0.793}_{-0.788}$ | $3.538^{+0.014}_{-0.028}$ | $10.268^{+0.153}_{-0.151}$ | 13.65 | 31.19/41 |
| 9 | X-05-01 | 53309.956 | $0.022^{+0.004}_{-0.004}$ | $0.111^{+0.017}_{-0.010}$ | $133.302^{+1.573}_{-1.557}$ | $3.510^{+0.032}_{-0.032}$ | $10.082^{+0.204}_{-0.199}$ | 13.65 | 17.51/41 |
| 10 | X-05-03 | 53310.876 | $0.021^{+0.004}_{-0.003}$ | $0.114^{+0.013}_{-0.010}$ | $145.746^{+1.276}_{-1.270}$ | $3.321^{+0.023}_{-0.023}$ | $12.488^{+0.208}_{-0.205}$ | 13.65 | 32.10/41 |
| 11 | X-05-10 | 53311.146 | $0.020^{+0.004}_{-0.001}$ | $0.127^{+0.006}_{-0.016}$ | $150.742^{+1.335}_{-1.326}$ | $3.281^{+0.021}_{-0.021}$ | $11.700^{+0.177}_{-0.174}$ | 13.65 | 23.75/41 |
| 12 | X-05-02 | 53311.306 | $0.022^{+0.001}_{-0.001}$ | $0.125^{+0.002}_{-0.003}$ | $154.643^{+3.178}_{-3.117}$ | $2.957^{+0.050}_{-0.050}$ | $12.867^{+0.562}_{-0.538}$ | 13.65 | 33.28/41 |
| 13 | X-05-04 | 53312.736 | $0.020^{+0.008}_{-0.002}$ | $0.127^{+0.010}_{-0.024}$ | $166.567^{+2.131}_{-2.107}$ | $3.239^{+0.034}_{-0.033}$ | $13.282^{+0.408}_{-0.395}$ | 13.65 | 31.35/41 |
| 14 | X-06-00 | 53314.749 | $0.021^{+0.008}_{-0.002}$ | $0.126^{+0.008}_{-0.022}$ | $171.430^{+2.157}_{-1.788}$ | $3.135^{+0.025}_{-0.032}$ | $13.935^{+0.374}_{-0.364}$ | 13.65 | 18.94/41 |

Table 4.3

Comparison of QPO frequencies obtained from theoretical predictions and actual fits when N is in the range 10 – 20.

| Obs ID. | MJD | $M_{BH} (M_\odot)$ | $X_s (r_S)$ | R | $\nu_{qpo}^{POS} (Hz)$ | $\nu_{qpo}^{PDS} (Hz)$ | $M_{BH}^{POS} (M_\odot)$ |
|----------------|-----------|----------------------------|----------------------------|---------------------------|---------------------------|---------------------------|----------------------------|
| 90115-01-03-10 | 53296.834 | $13.995^{+0.151}_{-0.149}$ | $75.662^{+0.704}_{-0.699}$ | $2.804^{+0.010}_{-0.010}$ | $3.957^{+0.112}_{-0.112}$ | $3.952^{+0.157}_{-0.166}$ | $14.011^{+0.602}_{-0.547}$ |
| 90115-01-04-00 | 53300.208 | $10.476^{+0.091}_{-0.090}$ | $84.784^{+1.263}_{-1.249}$ | $3.717^{+0.046}_{-0.046}$ | $3.359^{+0.145}_{-0.145}$ | $3.358^{+0.208}_{-0.144}$ | $10.479^{+0.487}_{-0.620}$ |

Table 4.3: The spectral parameters from TCAF fits M_{BH} , X_s and R are used in the formula obtained from POS for the determination of QPO frequency. The value is listed as ν_{qpo}^{POS} within errorbars. The mass M_{BH} is then tuned further to reduce the difference between POS prediction and observed QPO ν_{qpo}^{PDS} . The corresponding values is noted as M_{BH}^{POS} . Taken from Bhattacharjee et al. (2017).

Table 4.4

Comparison of QPO frequencies obtained from theoretical predictions and actual fits keeping $N = N_{avg} = 13.65$.

| Obs ID. | MJD | $M_{BH} (M_\odot)$ | $X_s (r_S)$ | R | $\nu_{qpo}^{POS} (Hz)$ | $\nu_{qpo}^{PDS} (Hz)$ | $M_{BH}^{POS} (M_\odot)$ |
|----------------|-----------|----------------------------|----------------------------|---------------------------|---------------------------|---------------------------|----------------------------|
| 90115-01-03-10 | 53296.834 | $12.772^{+0.127}_{-0.126}$ | $79.041^{+0.494}_{-0.491}$ | $3.026^{+0.016}_{-0.016}$ | $3.758^{+0.092}_{-0.092}$ | $3.952^{+0.157}_{-0.166}$ | $12.156^{+0.521}_{-0.475}$ |
| 90115-01-04-00 | 53300.208 | $10.095^{+0.082}_{-0.081}$ | $81.732^{+1.273}_{-1.260}$ | $3.700^{+0.046}_{-0.046}$ | $3.697^{+0.145}_{-0.162}$ | $3.358^{+0.208}_{-0.144}$ | $11.125^{+0.487}_{-0.656}$ |

Table 4.4: Spectral parameters from TCAF fits M_{BH} , X_s and R are used in POS model for the determination of QPO frequency. The value is listed as ν_{qpo}^{POS} within errors bars. The mass M_{BH} is then tuned further to reduce differences between POS prediction and observed QPO ν_{qpo}^{PDS} . The corresponding value is noted as M_{BH}^{POS} . Taken from Bhattacharjee et al. (2017).

declining phase. Hence we concentrate our study only in this end phase as we expect interplay between the two flow components of TCAF models. We successfully addressed the evolution of accretion rates of both disc and halo, shock location (which represents the size of the Compton cloud) and the compression ratio to have a clear understanding of the outburst. It is important to note here that the fits obtained by spectral models, such as *diskbb + power law*, does not provide any clue about the mass of the object, neither does it explain the accretion flow dynamics around the BHC. TCAF solution, on the other hand, gives an independent estimate of M_{BH} from every single observation.

Molla et al. (M16a) obtained the mass of the black hole in the range $11.2_{-1.95}^{+1.66}M_{\odot}$. Further, they estimated the mass of the BH with other methods such as Shaposhnikov & Titarchuk 2007 (ST07) using the Photon Index-QPO frequency correlation technique. The measured mass of the black hole was obtained as $11.61 \pm 0.62M_{\odot}$. Shaposhnikov & Titarchuk (2009, ST09) predicted the mass of the black hole to be $13.3 \pm 3.2M_{\odot}$ using the correlation between their spectral and timing properties while McClintock et al. (2009), estimated the mass $\sim 11.0M_{\odot}$ using their high frequency QPO correlation method. From the model of high frequency QPOs based on the spin of the black hole Pétri (2008) obtained the mass of the BHC in the range of $9 - 13M_{\odot}$. We have obtained the mass of the black hole in the range $10.31M_{\odot} - 14.07M_{\odot}$ which agrees well with these previous measurements.

The PCA spectra of the object clearly show that most of the flux is contributed from the soft photons emitted by the disc. The flux emitted from the disc is $\sim T^4$ and draws its energy from the loss in gravitational potential energy $\sim \frac{GM_{BH}}{r}$. Thus, roughly the spectra obtained by the best fit with TCAF has an intrinsic dependence of T on M_{BH} as $M_{BH} \sim T^4$. The spectra at low energy, where the blackbody radiation from the disc is dominating, is limited by the resolution of RXTE/PCA. Any error in the measurement, combined with the error in the fit parameters which depend on T , leads to a significant proportional error in the determination of M_{BH} . Despite that, the mass is found to lie in a narrow range which conforms and restricts further, the previous findings by M16a and Pétri et al. (2008).

We assumed that the mass, distance and inclination angle of the object are constant such that the projected area of the disc along the line of sight does not change keeping the model normalization more or less unchanged provided the instrument response function and the absorption from intervening medium are determined correctly which may affect Normalization also. Furthermore, we assumed that there was no contribution to X-rays from the jet. However, since mass, distance or inclination angle are not accurately known and the RXTE resolution is low to generate accurate spectra, we allowed to vary both mass and normalization within a narrow range. We also used the average normalization and repeated our analysis. We found reasonably good χ^2 values as evident from Table 4.1 and Table 4.2. The average reduced χ^2 value is $\langle \chi_{red}^2 \rangle = 0.82 \pm 0.20$ for $10 < N < 20$ and $\langle \chi_{red}^2 \rangle = 0.79 \pm 0.19$ for $N = N_{avg} = 13.65$. We believe that unless the system parameters (most importantly, inclination angle for a precessing disc) change, this Normalization may be used to analyze subsequent outbursts.

The low-frequency of QPO derived from the power density spectrum fitted parameters was found to be in agreement with the one obtained from the POS model if the systematic error is considered. The velocity of the shock front v_s using the POS model was found to be similar to those with the previous work by Debnath et al. (2013).

The masses obtained by the POS model for both the cases with free and constant normalization agree with the range ($10.31 M_{\odot} - 14.07 M_{\odot}$) obtained by the spectral fits with a constant, averaged normalization of $N = N_{avg} = 13.65$. The POS model provides a secondary verification to our

method and reflects upon the general consistency of our approach. We thus conclude from our analysis that the mass of the BHC is in the range $10.31 M_{\odot} - 14.07 M_{\odot}$.

TCAF solves the radiative transfer equation for a steady state two component flow to discuss about the spectral properties. The day-to-day evolution of the spectra are, thus, explained in terms of the variation of physical parameters which are used in TCAF. This allows us to have a fresh estimate of the mass of the black hole, independent of any other observations. The POS model predicts values of QPO frequencies from the spectral parameters, and we find that observed QPOs are of similar values. Thus TCAF self-consistently puts spectral and timing properties under a common framework. The derived mass is well within the range estimated by earlier workers using very different observational data, and model.

Chapter 5

TCAF paradigm applied to persistent BHC: Cyg X-1

ABSTRACT

We investigate spectral behavior of the persistent black hole candidate Cygnus X-1 from December 10, 1997 to May 12, 1998 when it was in its persistent hard state. We also study one of the flaring phases of the source, between March 12, 2003 to October 7, 2003 when the object entered into the soft/intermediate state. We use RXTE/PCA archival data and apply the Two-Component Advective Flow (TCAF) solution for the spectral analysis. We classify the spectral states based on the nature of the TCAF model fitted flow parameters, namely, the disc and the halo rates, the location, size and the density of the Compton cloud (produced by the post-shock advective flow which surrounds the standard disc) and the accretion rate ratio (the ratio between the halo rate and the disc rate). This gives us an idea of the underlying accretion flow dynamics for this persistent source and provides us with evolution of the aforementioned accretion flow parameters. This is the first time that explicit flow parameters of Cygnus X-1 are obtained from the spectral analysis. Moreover, since the mass of the black hole is also an input parameter in the TCAF fitting procedure, we obtain a constraint on the mass of the black hole from each of the spectral fits. For Cygnus X-1, our estimated mass appears to be $M_{avg} = 14.57^{+2.14}_{-2.07} M_{\odot}$ which is consistent with previous estimates reported in the literature. Part of this work has been reported in Banerjee et al. (2019). Figure 5.2 has been taken from there.

Introduction

Stellar mass black holes (BH) in a binary system usually exhibit either transient or persistent behavior. Transient sources mostly remain in quiescent states, except during their outbursts when their X-ray luminosity rises by a large factor over a timescale of a few days to months before returning back to its quiescent state. Persistent sources, on the other hand, are generally always active in X-rays. Their companion stars are massive compared to that of transients and they are generally wind accretors. The companion exhibits mass loss of $\sim 10^{-5} - 10^{-7} M_{\odot} yr^{-1}$ in their winds, a fraction of which is accreted by the compact object. Most of the stellar mass black hole candidates (BHCs) observed till date are transients.

Not surprisingly, Cygnus X-1, the first ever stellar-mass black hole candidate to be discovered, turned out to be a persistent source. It is a galactic high mass X-ray binary (HMXRB) with energy flux $\sim 3 \times 10^{-8} \text{ erg cm}^{-2} \text{ s}^{-1}$ in the 1-200 keV energy band, which makes it one of the brightest sources in the sky (Shaposhnikov & Titarchuk 2006). It has an O9.7Iab type star, HDE226868, as the companion (Bolton et al. 1972, Walborn 1973) which loses mass through stellar winds at a rate of $\sim 3 \times 10^{-6} M_{\odot} yr^{-1}$ (Hutchings 1976, Gies et al. 2003, Ziółkowski 2005). Because of its persistence, brightness and proximity Cygnus X-1 is a very important source to study the physics of accretion processes around black holes.

Cygnus X-1 is located in the constellation Cygnus, at R.A. = $19^{\text{h}}58^{\text{m}}21^{\text{s}}.9$, and Dec = $-35^{\circ}12'9''$. The distance and inclination of the source is estimated to be $1.86_{-0.11}^{+0.12}$ kpc and $\theta = 27.1^{\circ} \pm 0.8^{\circ}$ (Reid et al. 2011) respectively. After considerable effort (Bolton 1972, Webster & Murdin 1972, Paczyński 1974, Gies & Bolton 1986, Ninkov et al. 1987, Herrero et al. 1995) over the past few decades, Orosz et al. (2011) constrained the mass of the BHC in Cygnus X-1 to be $M_{BH} = 14.8 \pm 1.0 M_{\odot}$. Apart from dynamical methods, Shaposhnikov & Titarchuk (2007) used the low-frequency QPO and the photon-index correlation method to determine the mass of Cygnus X-1 to be $8.7 \pm 0.8 M_{\odot}$.

Long-term spectral analyses of Cygnus X-1 reveals that the object mainly exhibits two types of spectral states, either a prolonged hard state or an extended period of soft state. Moreover, once or twice a year it undergoes failed transitions, when it attempts to attain a soft-state but falls back to the hard-state after reaching some intermediate state (Grinberg et al. 2013, Grinberg et al. 2014, Shaposhnikov & Titarchuk 2006, Zhang et al. 1997, Cui et al. 1997, 1998 and references therein). Böck et al. (2011) and Grinberg et al. (2014) analyzed all spectral states of Cygnus X-1 using broken power-law models and reported that it does not exhibit the complete ‘q’-shaped track in the Hardness-Intensity Diagram (HID) implying that a systematic state evolution from HS→HIMS→SIMS→SS→SIMS→HIMS→HS, like a typical transient source did not occur. As shown in Grinberg et al. (2014, 2015), timing analysis plays an essential role in determining the states if phenomenological models such as broken power-law are used. However, this does not imply that the underlying physics of accretion in transients and persistents are very much different since the q-diagram is based on emitted radiation bands and not on any specific physical parameters. The supply of matter from the companion and the viscosity of the system ultimately dictates the two mass accretion rates which subsequently determine whether the source would be in hard or soft state. Long term behavior of the two individual accretion rates eventually decide whether the source would be persistent or outbursting. Since phenomenological models cannot reveal the underlying accretion physics and thereby throw light on the intrinsic properties of the accretion flow, we are therefore motivated to fit the spectra using the more physical Two Component Advective Flow (TCAF) model which is based on the basic equations of fluid dynamics and study the evolution of the flow parameters across the states of Cygnus X-1.

In the TCAF paradigm, the Keplerian component of the flow resides in the equatorial plane and accretes in the viscous timescale while the sub-Keplerian component of the flow enveloping the Keplerian disc falls into the black hole in the freefall timescale (Chakrabarti 1989, Chakrabarti 1990, Chakrabarti & Titarchuk 1995, hereafter CT95; Chakrabarti 1996). The multi-colour black-body component of the observed spectrum (Shakura & Sunyaev, 1973) is supposed to be originated from the Keplerian flow. The advective nature of the sub-Keplerian flow enables it to attain supersonic speed far away from the black hole which however, brakes due to rapid strengthening of the centrifugal barrier (centrifugal force $\sim 1/r^3$ as opposed to gravity $\sim 1/r^2$) forming a shock wave and the post-shock flow then enters into the black hole supersonically after crossing a sonic point. Shock heating distends the post-shock flow resulting into the CENTrifugal pressure supported BOundary Layer or CENBOL which plays the role of the ‘Compton cloud’ (Sunyaev & Titarchuk, 1980, 1985). The CENBOL inverse Comptonizes soft X-ray photons from the adjacent Keplerian disc giving rise to the power-law component of the spectrum. The CENBOL changes its shape depending on the relative importance of the Keplerian and the sub-Keplerian accretion rates. Spectral fitting of BHCs with the TCAF model in XSPEC (Arnaud 1996) clearly showed evidence of two types of accretion flows. Subsequent analysis of RXTE data by several observers reveal that such components have indeed been observed (e.g., Soria et al., 2001; Smith et al., 2002; Wu et al., 2002; Cambier & Smith, 2013; Tomsick et al., 2014). More recently, using extensive numerical simulations, Giri, Garain and Chakrabarti (2015 and references therein), have shown that indeed, such a flow is naturally produced by a generic class of vertical viscosity distribution.

In case of High Mass X-Ray Binaries, compact objects with B[e] companion star (MAXI J1836-194, Jana et al. 2016) or binaries with short orbital periods (MAXI J1659-152, SWIFT J1753.5-0127, XTE J1118+480, etc.) the accretion flow is seen to be halo dominated. In these systems, the stellar wind feeds a huge amount of matter in the form of sub-Keplerian halo component, which is responsible for constant supply of hot electrons to the CENBOL. As a result, even in the softer states, when the disc accretion rate reaches a relatively higher value, the soft photons are not able to completely cool down the CENBOL. This constrains the source to never reach a very soft spectral state where the CENBOL is completely quenched. In harder states, the shock location i.e., the outer edge of the CENBOL which is also the inner edge of the Keplerian disc, could remain far away from the horizon, leading to a very low-efficiency thermal blackbody emission from the disc. This is also a natural consequence of the TCAF solution.

In this Chapter, we analyze the spectra of the persistent source Cygnus X-1 using TCAF model, which has recently proved to be very satisfactory in explaining accretion flow properties of a few transient sources (Dutta & Chakrabarti 2010; Debnath et al. 2008, 2013, 2014, 2015a,b, 2017; Nandi et al. 2012; Rao et al. 2013; Mondal et al. 2014, 2016; Jana et al. 2016; Chatterjee et al. 2016; Molla et al. 2016, 2017; Bhattacharjee et al. 2017; Radhika et al. 2016). We fit the spectra of Cygnus X-1 by the TCAF solution based additive table *fits* file in HEASARC’s spectral analysis software package XSPEC and at the same time extract its mass from the fits independently using each observation since it is an input parameter of the TCAF model.

From 1996 (RXTE launch) to 2015, the states of Cygnus X-1 have been different in different major chunks of time periods of observation (Grinberg et al. 2013):

- (a) A characteristic soft state in 1996 (phase I).
- (b) A stable hard state with very brief periods of softening between the end of 1996 to early 1998 (phase II).
- (c) From early 1998 to mid-2006 it exhibited a series of failed state transitions and a prolonged soft state (phase III).

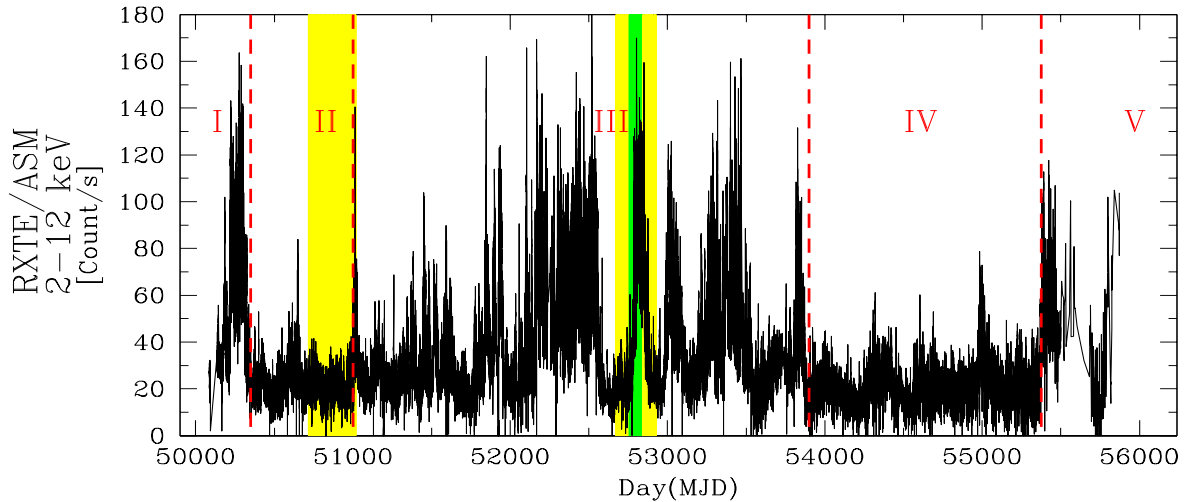


Figure 5.1: RXTE/ASM Light Curve in the 2 to 12 keV energy band illustrating five phases through which the source passed. The shaded region in yellow represents the hard phase of the source analyzed by the TCAF model. The shaded region in yellow and green represents the outburst-like phase of the source analyzed by the TCAF model. The green shaded zone represents the time domain during the outburst phase when the flux increased so much that fits could not be obtained by either *diskbb+powerlaw+Gaussian* or *TCAF+Gaussian* models, while the yellow shaded zone adjacent to the green shaded region represents the rising and declining phases of the outburst which could be analyzed by both the aforementioned models.

(d) A prolonged hard state from mid-2006 to mid-2010 (phase IV).

(e) From mid-2010 to 2014-2015 it exhibited continuous soft states (phase V).

More details on the source behavior can be found in Grinberg et al. (2013) and from more recent works of Tomsick et al. (2014) and Walton et al. (2016).

Here, we choose to analyze data of continuous 150 days of Cygnus X-1 from December 10, 1997 to May 12, 1998 when the object was in the low/hard state (phase II). We also analyze a flaring or quasi-outburst state of Cygnus X-1 lasting for about six months from phase III, starting from March 12, 2003 to October 7, 2003. We use the TCAF solution to extract and analyze the accretion flow parameters, namely, the disc accretion rate, \dot{m}_d , the halo accretion rate, \dot{m}_h , the location and the size of the Compton cloud. This is the first time that these physical parameters and their temporal evolutions are found from the spectral data. Moreover, the spectral analysis also enables us to constrain the mass of the object.

We organize the Chapter in the following way: In §2, we explain the observation and the data analysis procedure implementing HEASARC's HEASoft software package. In §3, we present and discuss the results obtained from the spectral analysis using the Two-Component Advective Flow (TCAF) solution. Finally, in §4, we conclude with a brief summary of our main results and discuss some scope for future work.

Observation and Data Analysis

We analyze the RXTE/PCA archival data of Cygnus X-1 spanning from December 10, 1997 (MJD=50792.297) to May 12, 1998 (MJD=50945.736) which lies in the stable hard phase (phase

II) of the source. We present a total of 22 episodes of data with individual IDs during this period of five months. As the source also exhibits outburst like features, we analyze both the rising and the declining phases during the outburst from March 12, 2003 (MJD=52710.364) to October 7, 2003 (MJD=52919.787). This is because, generally during these two phases of an outburst, rapid changes of the spectral and the timing properties occur. We followed the standard data analysis procedures as in Nandi et al. (2012). HEASARC’s software package HEASoft version HEADAS 6.18 and XSPEC version 12.9.0 were used for the data analysis. We adopted the method applied by Debnath et al. (2015a) and Debnath et al. (2014) for spectral analysis. For RXTE data reduction, we used standard selection criteria for generating goodtime-interval files (see, Nandi et al. 2012 for more details). Standard2 mode Science Data of PCA (FS4a*.gz) with 16s binning were used for spectral analysis. For each data ID, we extracted the spectrum from all the Xenon layers of PCU2 comprising of 128 channels (no grouping was done at this stage). We have taken into account the PCA breakdown (because of the leakage of propane layers of Proportional Counter Units) and dead-time corrections for each extracted data. The SAA data has been taken care of with the incorporation of the *pca_saa_history* file while generating the GTI file to specify the good time interval. We have ignored any data acquired when *time_since_saa* was less than 30 minutes or when elevation is less than 10° or when offset is greater than 0.02. The spectral data (.pha file) was then rebinned for all the 128 channels using the ‘rbnpha’ command. The command “runpcabackest” was used to extract the PCA background spectra by using the latest bright-source background model. The response files were prepared using the task “pcarsp”. Shaposhnikov et al. (2012) and Garcia et al. (2014) emphasized the necessity of incorporating systematic errors in the spectral analysis of PCA data of bright sources. Böck et al. (2011), Grinberg et al. (2013) and Grinberg et al. (2014) used a variable systematic error to analyze their data of Cygnus X-1. We however stick to a more conventional use of a constant systematic error of 1% (Debnath et al. 2014, 2015a,b, 2017; Mondal et al. 2014, 2016; Jana et al. 2016; Chatterjee et al. 2016; Molla et al. 2017; Bhattacharjee et al. 2017), for all energies. A detailed discussion regarding this can be found in §4. The 2.5 to 45.0 keV PCA spectra were background subtracted and fitted with TCAF solution based additive model fits file. The hydrogen column density N_H was kept free roughly in the range $(0.48 - 10.0) \times 10^{22}$ atoms cm^{-2} , as previously shown by Grinberg et al. (2015), in order to obtain the best fits. The absorption model *phabs* was used.

We fit all spectral data using the Two Component Advective Flow (TCAF) solution to obtain various parameters of the accretion flow. In order to fit the spectrum using a TCAF-based model, one needs to provide six input parameters: (a) the disc or the Keplerian accretion rate, \dot{m}_d , in Eddington units, (b) the halo or the sub-Keplerian accretion rate, \dot{m}_h , in Eddington units, (c) the mass of the black hole, M_{BH} , in units of solar mass M_\odot , (d) the location of the shock, X_s , in units of Schwarzschild radius ($r_S = 2GM_{BH}/c^2$), (e) the shock compression ratio, R , and (f) the model normalization, N . However, out of these parameters, mass and normalization could be kept as constant, if they are known. Unlike other models, TCAF model normalization does not generally vary for a particular source observed by a given instrument, since it only depends on intrinsic source parameters: mass, distance and disc inclination angle. Thus essentially TCAF requires only four parameters to fit the spectrum.

In order to fit the data, here we used latest TCAF model fits file (*TACF_v0.3_R4.fits*) as method discussed in DMC15. The model fits file was generated by employing large number ($\sim 10^6$) of theoretical spectra by varying five model input parameters (M_{BH} , \dot{m}_d , \dot{m}_h , X_s , R) in the code used in CT95 (Chakrabarti & Titarchuk 1995). Good fits would automatically yield a constant or nearly constant N which can be used to fit subsequent episodes. The range of input parameters

and the fits file generation procedure is described in detail in DCM14 and DMC15. It successfully fitted the spectral data of several transient BHCs (e.g., H 1743-322, GX 339-4, MAXI J1659-152, MAXI J1836-194, MAXI J1543-564, Swift J1753.5-0127), during their outbursts providing us with a clear picture of the evolution of the Keplerian and sub-Keplerian mass accretion rates, the location and size of the Compton cloud (here, CENBOL) and the strength of the shock, which in conjunction with the size and the accretion rates provides the optical depth of the Compton cloud.

Results

RXTE/ASM one day average light curve in the 2 to 12 keV energy band representing the five phases of evolution of Cygnus X-1 during the RXTE era (1996-2011) are shown in Fig. 1. The yellow shaded regions in phase II and phase III represent the time domain in the hard phase and the flaring phase respectively whose detailed properties are studied by us. The spectra is analyzed with the *TCAF+Gaussian* models. The green shaded region in phase III represents the period during which we did not obtain appropriate fits using *TCAF + Gaussian* model as there was substantial increase of flux during this period.

Spectral Data Fitted by TCAF model during hard phase (phase II of the source activity)

We analyze the data from December 10, 1997 (MJD=50792.297) to May 12, 1998 (MJD=50945.736) which lies within the domain of phase II of the source activity and fit the data using *phabs*(TCAF+Gaussian)* model. In order to obtain the best fit, a Gaussian component (representing the contribution from Iron emission line) is used with energy between 6.2 keV to 6.8 keV. The width of the Gaussian component was allowed to vary in the range 0.001 – 0.8 keV. The normalization of the Gaussian component was allowed to be free, however. It was found that in order to obtain the best fit, the normalization has to be varied between 7.25×10^{-3} to 1.59×10^{-2} during the hard-phase. Table 1 shows all the parameters of the TCAF fits in five month interval during the hard phase. The disc accretion rate \dot{m}_d is found to vary between $0.68\dot{M}_{Edd}$ to $0.75\dot{M}_{Edd}$ during this time period with an average of $\sim 0.72\dot{M}_{Edd}$. The halo accretion rate \dot{m}_h , varies from $1.72\dot{M}_{Edd}$ to $1.84\dot{M}_{Edd}$ with an average of $\sim 1.80\dot{M}_{Edd}$. Since the variation in both the accretion rates is minimal, the accretion rate ratio *ARR* remains roughly constant with slight fluctuations. The average location of the shock X_s is $\sim 72.17r_S$ varying between $70.37r_S$ to $73.35r_S$, while the average strength of the shock R is ~ 1.22 , varying between $R = 1.18$ to $R = 1.25$. It is apparent that all the flow parameters vary within a very narrow range which is characteristic of the persistent hard phase. This is illustrated in Fig. 2(a)-(c), (e)-(f). Since, mass of the black hole M_{BH} is also a parameter of the TCAF model, we automatically obtain a constraint on the mass of the source from each of the spectral fits. During this phase of the source activity, M_{BH} is found to vary in between $\sim 12.50 - 14.82 M_\odot$ with an average value of $M_{avg} = 14.12 M_\odot$. Thus the probable mass of the source during the period of observation turns out to be $14.12^{+0.17}_{-0.36} M_\odot$.

It has been reported previously by Wilms et al. (2006), Zdziarski et al. (2011) and Grinberg et al. (2013) that throughout the five months for which we analyze the data, Cygnus X-1 remains in the “hard-state” with occasional fluctuation in fluxes. Here we reconfirm this result by the spectral analysis with the TCAF solution. During the entire phase, disc rate appears to be high. This is normal in TCAF since the multicolour component comes from a Keplerian disc truncated at $X_s \sim 72R_s$. However, since the wind accretion rate is also high, it is difficult to cool down the

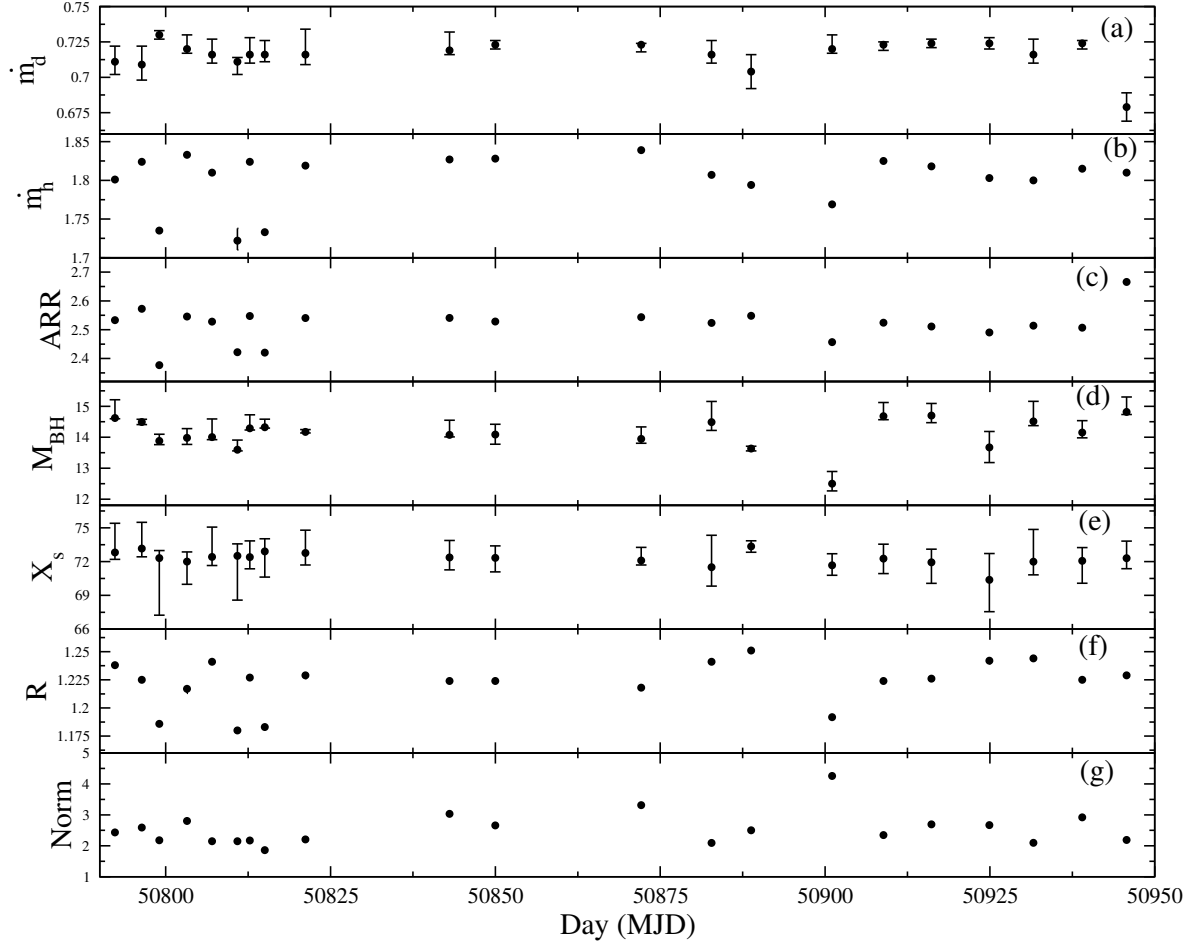


Figure 5.2: Variation of (a) the disc accretion rate \dot{m}_d (in Eddington units), (b) the sub-Keplerian halo accretion rate \dot{m}_h (in Eddington units), (c) the accretion rate ratio (ARR) \dot{m}_h/\dot{m}_d , (d) the mass of the black hole (in units of M_\odot), (e) the shock location X_s (in units of r_S), (f) the shock strength R , and (g) the normalization of the TCAF model, with day (MJD). Variation of all the aforementioned quantities are studied in the 2.5-45.0 keV energy band. Taken from Banerjee et al. (2019).

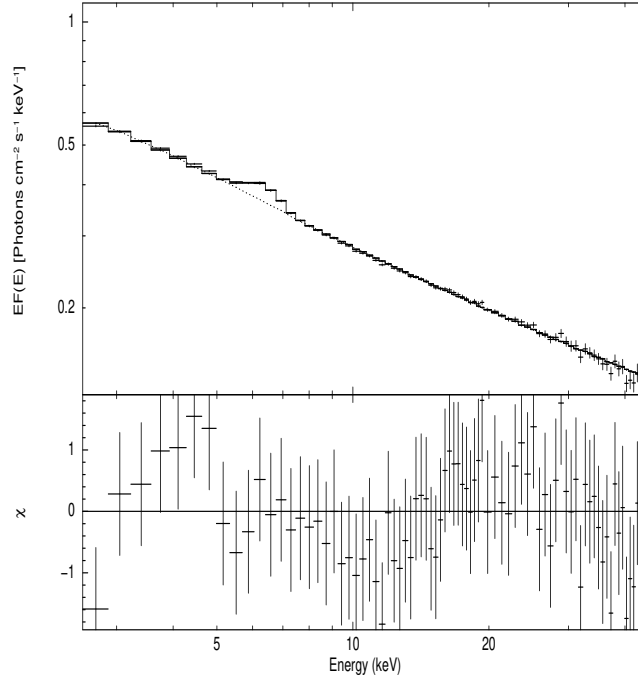


Figure 5.3: Unfolded spectra with residue of observation ID 20175-01-03-00 for energy 2.5-45.0 keV, fitted with $phabs(TCAF+Gaussian)$ models showing the spectrum of a typical hard state.

large ($\sim X_s$) CENBOL and hard-state prevails.

We left the normalization (N) to be free since there are uncertainties in mass, inclination and distance on which it depends. As a result we expect that N should remain constant over the period of observation, unless there is activity in radio indicating possible X-ray emission from the base of the jet or disc precession. Here we obtain N in between 1.86 – 4.26. The model fitted spectrum of a typical hard-state on MJD=50815.031 is illustrated in Fig. 3.

Spectral Data Fitted by TCAF model during the flaring phase (phase III of the source activity)

During phase III, the source exhibited a series of outburst like features with a very prolonged soft state. Here, we examine one such outburst starting from MJD=52710.364 to MJD=52919.787.

We fit the data using $phabs^*(TCAF + Gaussian)$ model as in the previous case. The Gaussian component (representing the iron line) used has energy range of 6.2 keV – 6.8 keV and width range of 0.001 – 0.8keV. The normalization of the Gaussian component was allowed to vary in order to obtain the best fits. The normalization varied between 4.36×10^{-3} and 5.06×10^{-2} . Figure 5.4 illustrates the variation of the TCAF fit parameters with MJD. Depending on the variation of TCAF model fitted flow parameters and ARR, various states, namely, the hard and the intermediate/soft states are marked. Table 2 shows the variation of the accretion flow parameters obtained from TCAF fits during this time domain.

From MJD = 52710.364 to MJD = 52735.224, the object seems to reside in the hard state. During this period the disc accretion rate \dot{m}_d varies between 2.68 to $2.86\dot{M}_{Edd}$ while the halo accretion rate \dot{m}_h varies between 6.25 to $6.29\dot{M}_{Edd}$. The location of the shock X_s ranges from

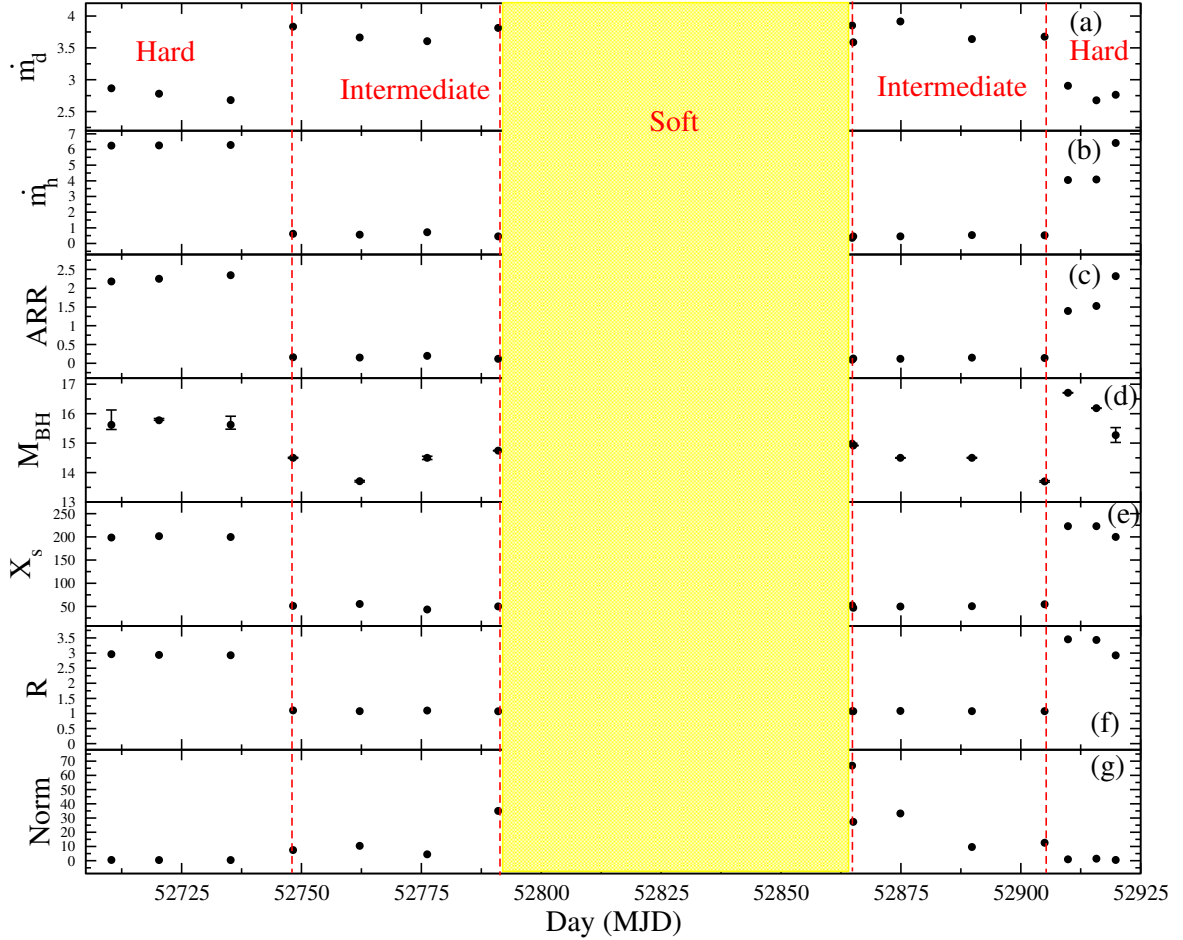


Figure 5.4: Variation of (a) the disc accretion rate \dot{m}_d (in Eddington units), (b) the sub-Keplerian halo accretion rate \dot{m}_h (in Eddington units), (c) the accretion rate ratio (ARR) \dot{m}_h/\dot{m}_d , (d) the mass of the black hole (in units of M_\odot), (e) the shock location X_s (in units of r_S), (f) the shock strength R , and (g) the normalization of the TCAF model, with day (MJD). Variation of all the aforementioned quantities are studied in the 2.5–45.0 keV energy band. The hard and intermediate/soft states are marked. The shaded region represents the time domain during the outburst phase when suitable fits could not be obtained by the *TCAF+Gaussian* model.

198.62 r_S to 201.57 r_S and the shock strength R fluctuates between 2.93 to 2.96. The values of these flow parameters, with high halo rate and low disc rate, large shock location with high compression ratio are all characteristics of a hard state.

The activity of the source during MJD = 52736 to MJD = 52747 is not known and from MJD = 52748.253, the object was found in the intermediate state which is evident from Figs. 4a-c, 4e-f. As the observations were 7-10 days apart, we cannot definitively specify when exactly the state transition took place. The labels ‘hard’, ‘intermediate’ and ‘soft’ in Figure 5.4 are used to show the relative dominance of the two accretion rates, as obtained from the spectral fits. However, they should not be taken as characterization of the spectral states. It was previously reported by Zdziarski et al. (2011) that the soft state for Cygnus X-1, could be similar to “soft-intermediate states” of other LMXBs. Our analysis concerns with the transition from harder to softer (or, vice-versa) transitions, not the absolute classifications of those state. It was already shown by Grinberg et al. (2013, 2014, 2015) that timing analysis is essential for determining the classes and as it has already been done extensively in those works, we refrain from repeating the same analysis.

As mentioned above, from MJD = 52748.253 to MJD = 52791.020 the object seems to have entered a softer state. This is marked as ‘intermediate’ in Fig. 4. Here \dot{m}_d alters between 3.61 \dot{M}_{Edd} to 3.83 \dot{M}_{Edd} while \dot{m}_h ranges from 0.45 \dot{M}_{Edd} to 0.72 \dot{M}_{Edd} . Since the disc rate is greater than the halo rate, the accretion rate ratio ARR = \dot{m}_h/\dot{m}_d shows a sharp dip (Fig. 4c). The shock location X_s moves drastically inward, varying between 43.34 r_S to 55.26 r_S while the average shock strength R drops to ~ 1.09 .

From MJD = 52792 to MJD = 52863 the subsequent increase in the flux is high and *phabs*(TCAF+Gaussian)* model could not give satisfactory fits. These could represent discs away from their equilibrium structure.

The very next observation from where appropriate fits could be obtained is on MJD = 52864.833. From this day to MJD = 52904.977, the behavior of the accretion flow parameters shows that the object was still in the soft/intermediate state, with \dot{m}_d ranging between 3.68 \dot{M}_{Edd} to 3.92 \dot{M}_{Edd} and \dot{m}_h ranging between 0.36 – 0.54 \dot{M}_{Edd} . The average location and strength of the shock in this domain is $X_s \sim 50.90r_S$ and $R \sim 1.08$ respectively.

The data for the next four days were not available and between MJD = 52909.834 to MJD = 52919.787, the object seems to have returned back to its hard state. During this period, \dot{m}_d ranges from 2.68 – 2.91 \dot{M}_{Edd} while \dot{m}_h ranges from 4.05 – 6.41 \dot{M}_{Edd} . This is in concordance with the sharp increase in ARR in Figure 5.4(c). The shock location moves drastically outward with an average $\sim 215.34r_S$ and the shock strength rises steeply, varying between 2.93 – 3.46. There is a gap of five days of data and thus we cannot comment how drastic was the reversal in the behavior of the flow pattern. In Figure 5.5 we plot two spectra fitted by the TCAF model during (a) the hard phase just before the outburst and (b) the soft phase which marks the onset of the outburst. During this entire phase of the source activity, \dot{M}_{BH} is found to vary between $\sim 13.70 - 16.71M_\odot$ with an average value of $15.02^{+0.05}_{-0.09} M_\odot$.

In Fig. 6, we show one specimen contour plot of TCAF fitted model parameters \dot{m}_d and \dot{m}_h for observation ID 60090-01-32-02 (taken from rising phase of the outburst) using default delta fit statistic of 2.3, 4.61 and 9.21 i.e., 68-90-99% confidence levels. As TCAF solution is generated by solving coupled differential equations, \dot{m}_d and \dot{m}_h are closely bound near the minimum chi-square value of the fit. The ARR does not remain constant in both hard and outburst phases showing that \dot{m}_d and \dot{m}_h could be treated as independent rates.

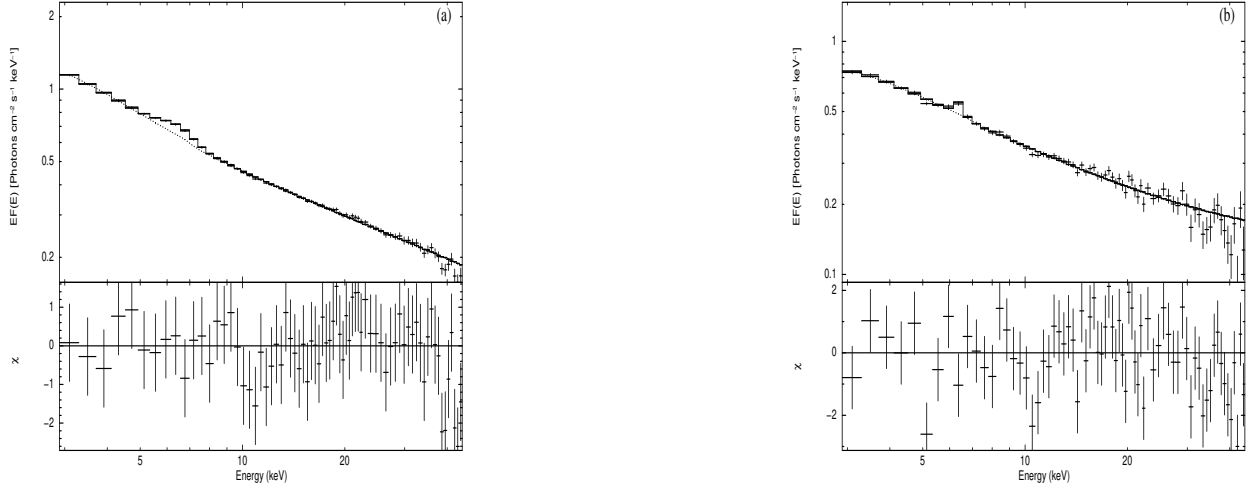


Figure 5.5: Unfolded spectra with residue of two observations (ID: (a) 60090-01-27-01 and (b) 60090-01-32-02 during the hard phase, just before the outburst and the soft phase which marks the onset of the outburst respectively for energy 2.5–45.0 keV, fitted with $phabs(TCAF+Gaussian)$ models.

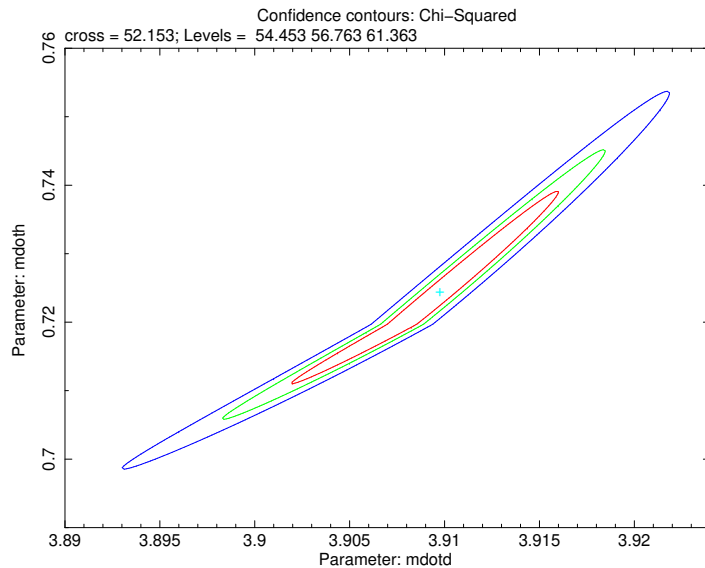


Figure 5.6: Default delta fit statistic of 2.3, 4.61 and 9.21 i.e., 68-90-99 percent confidence contours for the TCAF fitted parameters \dot{m}_d and \dot{m}_h are plotted for observation ID: 60090-01-32-02 during the rising phase of the outburst.

Table 5.1: Variation of the TCAF fit parameters with MJD keeping all the parameters free, in the 2.5-45.0 keV energy range. Duration of the data is from December 10, 1997 to May 12, 1998. Taken from Banerjee et al. (2019).

| <i>Obs</i> | Id | MJD | N_H | \dot{m}_d (M_{Edd}) | \dot{m}_h (M_{Edd}) | M_{BH} (M_{\odot}) | X_s (r_S) | R | N | χ^2/dof |
|------------|----------------|-----------|-------|---|---|--|--|---|---|--------------|
| 1 | 30158-01-01-00 | 50792.297 | 0.462 | 0.711 ^{+0.009} _{-0.011} | 1.801 ^{+0.001} _{-0.001} | 14.623 ^{+0.025} _{-0.587} | 72.818 ^{+0.615} _{-2.593} | 1.238 ^{+0.001} _{-0.002} | 2.433 ^{+1.031} _{-0.031} | 90.25/70 |
| 2 | 30158-01-03-00 | 50796.368 | 0.517 | 0.709 ^{+0.011} _{-0.013} | 1.824 ^{+0.001} _{-0.001} | 14.493 ^{+0.084} _{-0.088} | 73.158 ^{+0.735} _{-2.332} | 1.225 ^{+0.003} _{-0.001} | 2.592 ^{+0.035} _{-0.034} | 79.32/70 |
| 3 | 30158-01-06-00 | 50799.028 | 0.430 | 0.730 ^{+0.003} _{-0.003} | 1.735 ^{+0.003} _{-0.002} | 13.880 ^{+0.119} _{-0.218} | 72.315 ^{+5.073} _{-0.667} | 1.186 ^{+0.001} _{-0.001} | 2.180 ^{+0.021} _{-0.022} | 93.40/70 |
| 4 | 30158-01-08-00 | 50803.229 | 0.552 | 0.720 ^{+0.003} _{-0.010} | 1.833 ^{+0.001} _{-0.002} | 13.979 ^{+1.01} _{-0.299} | 71.999 ^{+2.014} _{-0.986} | 1.217 ^{+0.004} _{-0.001} | 2.803 ^{+0.018} _{-0.028} | 108.36/70 |
| 5 | 30158-01-10-00 | 50807.027 | 0.896 | 0.716 ^{+0.006} _{-0.011} | 1.810 ^{+0.001} _{-0.002} | 14.006 ^{+0.084} _{-0.584} | 72.420 ^{+0.768} _{-2.643} | 1.241 ^{+0.002} _{-0.002} | 2.150 ^{+0.029} _{-0.031} | 87.35/70 |
| 6 | 30161-01-01-00 | 50810.879 | 0.780 | 0.711 ^{+0.009} _{-0.003} | 1.722 ^{+0.012} _{-0.016} | 13.597 ^{+0.037} _{-0.313} | 72.509 ^{+3.927} _{-1.067} | 1.180 ^{+0.001} _{-0.001} | 2.147 ^{+0.021} _{-0.025} | 93.09/70 |
| 7 | 30157-01-04-00 | 50812.763 | 0.758 | 0.716 ^{+0.006} _{-0.012} | 1.824 ^{+0.001} _{-0.001} | 14.290 ^{+0.057} _{-0.436} | 72.396 ^{+1.031} _{-1.450} | 1.227 ^{+0.002} _{-0.002} | 2.171 ^{+0.030} _{-0.031} | 75.29/70 |
| 8 | 20175-01-03-00 | 50815.031 | 0.511 | 0.713 ^{+0.008} _{-0.007} | 1.733 ^{+0.002} _{-0.002} | 14.323 ^{+0.026} _{-0.261} | 72.909 ^{+2.282} _{-1.120} | 1.183 ^{+0.001} _{-0.001} | 1.862 ^{+0.021} _{-0.021} | 51.76/70 |
| 9 | 30157-01-05-00 | 50821.198 | 0.518 | 0.716 ^{+0.007} _{-0.018} | 1.819 ^{+0.001} _{-0.003} | 14.174 ^{+0.035} _{-0.075} | 72.766 ^{+1.066} _{-2.026} | 1.229 ^{+0.003} _{-0.002} | 2.206 ^{+0.047} _{-0.039} | 65.17/70 |
| 10 | 30157-01-08-00 | 50843.049 | 0.540 | 0.719 ^{+0.003} _{-0.013} | 1.827 ^{+0.001} _{-0.002} | 14.077 ^{+0.067} _{-0.472} | 72.071 ^{+1.401} _{-1.209} | 1.224 ^{+0.002} _{-0.002} | 3.034 ^{+0.039} _{-0.143} | 118.01/70 |
| 11 | 30157-01-09-01 | 50849.981 | 0.765 | 0.723 ^{+0.003} _{-0.003} | 1.828 ^{+0.002} _{-0.003} | 14.086 ^{+0.310} _{-0.333} | 72.330 ^{+1.244} _{-1.072} | 1.224 ^{+0.002} _{-0.002} | 2.661 ^{+0.009} _{-0.038} | 92.04/70 |
| 12 | 30157-01-11-00 | 50857.980 | 0.206 | 0.750 ^{+0.002} _{-0.015} | 1.824 ^{+0.001} _{-0.001} | 13.974 ^{+0.01} _{-0.03} | 70.368 ^{+0.63} _{-0.85} | 1.213 ^{+0.001} _{-0.001} | 2.952 ^{+0.049} _{-0.032} | 170.82/70 |
| 13 | 30157-01-12-00 | 50872.114 | 0.655 | 0.723 ^{+0.005} _{-0.001} | 1.839 ^{+0.001} _{-0.003} | 13.945 ^{+0.139} _{-0.390} | 72.100 ^{+1.162} _{-0.85} | 1.218 ^{+0.002} _{-0.001} | 3.313 ^{+0.008} _{-0.025} | 109.70/70 |
| 14 | 30157-01-13-00 | 50882.784 | 0.582 | 0.716 ^{+0.006} _{-0.010} | 1.807 ^{+0.001} _{-0.002} | 14.487 ^{+0.268} _{-0.670} | 71.506 ^{+1.679} _{-2.834} | 1.241 ^{+0.002} _{-0.002} | 2.093 ^{+0.028} _{-0.028} | 85.20/70 |
| 15 | 30157-01-14-00 | 50888.785 | 0.781 | 0.704 ^{+0.012} _{-0.012} | 1.794 ^{+0.001} _{-0.001} | 13.634 ^{+0.074} _{-0.076} | 73.350 ^{+0.490} _{-0.502} | 1.251 ^{+0.002} _{-0.002} | 2.500 ^{+0.035} _{-0.034} | 94.36/70 |
| 16 | 30157-01-16-00 | 50901.071 | 0.896 | 0.720 ^{+0.003} _{-0.010} | 1.769 ^{+0.002} _{-0.003} | 12.499 ^{+0.233} _{-0.295} | 71.671 ^{+0.883} _{-1.027} | 1.192 ^{+0.001} _{-0.001} | 4.256 ^{+0.045} _{-0.043} | 136.98/70 |
| 17 | 30157-01-17-00 | 50908.862 | 0.611 | 0.723 ^{+0.004} _{-0.002} | 1.825 ^{+0.002} _{-0.002} | 14.679 ^{+0.112} _{-0.442} | 72.264 ^{+1.330} _{-1.288} | 1.224 ^{+0.002} _{-0.001} | 2.346 ^{+0.028} _{-0.031} | 92.48/70 |
| 18 | 30157-01-18-00 | 50916.137 | 0.641 | 0.724 ^{+0.003} _{-0.003} | 1.818 ^{+0.002} _{-0.002} | 14.702 ^{+0.232} _{-0.390} | 71.938 ^{+1.868} _{-1.170} | 1.226 ^{+0.002} _{-0.002} | 2.692 ^{+0.037} _{-0.034} | 72.09/70 |
| 19 | 30157-01-19-00 | 50924.929 | 0.488 | 0.724 ^{+0.004} _{-0.004} | 1.803 ^{+0.003} _{-0.002} | 13.671 ^{+0.490} _{-0.514} | 70.379 ^{+2.830} _{-2.344} | 1.242 ^{+0.003} _{-0.002} | 2.671 ^{+0.036} _{-0.038} | 105.15/70 |
| 20 | 30157-01-20-00 | 50931.595 | 0.487 | 0.716 ^{+0.006} _{-0.011} | 1.800 ^{+0.001} _{-0.002} | 14.513 ^{+0.138} _{-0.647} | 71.994 ^{+1.170} _{-2.866} | 1.244 ^{+0.002} _{-0.002} | 2.096 ^{+0.028} _{-0.028} | 90.17/70 |
| 21 | 30157-01-21-00 | 50939.009 | 0.599 | 0.724 ^{+0.004} _{-0.002} | 1.815 ^{+0.002} _{-0.002} | 14.152 ^{+0.175} _{-0.383} | 72.068 ^{+1.985} _{-1.181} | 1.225 ^{+0.002} _{-0.002} | 2.921 ^{+0.043} _{-0.031} | 114.71/70 |
| 22 | 30157-01-22-00 | 50945.736 | 1.143 | 0.679 ^{+0.010} _{-0.010} | 1.810 ^{+0.001} _{-0.001} | 14.817 ^{+0.081} _{-0.484} | 72.303 ^{+0.929} _{-1.519} | 1.229 ^{+0.001} _{-0.002} | 2.188 ^{+0.027} _{-0.028} | 95.22/70 |

Table 5.2: Variation of TCAF fit parameters with MJD keeping all the parameters free, in the 2.5-45.0 keV energy range. Duration of the data is from March 12, 2003 to October 7, 2003.

| <i>Obs</i> | Id | MJD | N_H | \dot{m}_d (M_{Edd}) | \dot{m}_h (M_{Edd}) | M_{BH} (M_{\odot}) | X_s (r_S) | R | N | χ^2/dof |
|------------|----------------|-----------|-------|---|---|--|---|---|--|--------------|
| 1 | 60090-01-27-01 | 52710.364 | 1.315 | 2.864 ^{+0.018} _{-0.015} | 6.248 ^{+0.007} _{-0.007} | 15.622 ^{+0.159} _{-0.501} | 198.620 ^{+3.184} _{-1.212} | 2.963 ^{+0.003} _{-0.004} | 0.561 ^{+0.005} _{-0.006} | 93.040/62 |
| 2 | 60090-01-28-02 | 52720.294 | 1.362 | 2.780 ^{+0.012} _{-0.011} | 6.256 ^{+0.005} _{-0.006} | 15.777 ^{+0.003} _{-0.058} | 201.567 ^{+1.362} _{-0.244} | 2.941 ^{+0.002} _{-0.002} | 0.450 ^{+0.003} _{-0.003} | 98.970/62 |
| 3 | 60090-01-29-03 | 52735.224 | 1.291 | 2.680 ^{+0.014} _{-0.013} | 6.289 ^{+0.008} _{-0.005} | 15.626 ^{+0.152} _{-0.320} | 199.793 ^{+1.904} _{-1.090} | 2.929 ^{+0.001} _{-0.002} | 0.481 ^{+0.002} _{-0.004} | 93.180/62 |
| 4 | 60090-01-30-00 | 52748.253 | 3.506 | 3.833 ^{+0.008} _{-0.013} | 0.618 ^{+0.002} _{-0.018} | 14.502 ^{+0.018} _{-0.018} | 51.079 ^{+0.313} _{-0.127} | 1.100 ^{+0.001} _{-0.001} | 7.487 ^{+0.141} _{-0.132} | 92.040/62 |
| 5 | 60090-01-31-00 | 52762.133 | 2.937 | 3.663 ^{+0.018} _{-0.021} | 0.563 ^{+0.010} _{-0.010} | 13.708 ^{+0.028} _{-0.026} | 55.255 ^{+0.305} _{-0.307} | 1.077 ^{+0.001} _{-0.001} | 10.436 ^{+0.218} _{-0.209} | 81.630/62 |
| 6 | 60090-01-32-02 | 52776.212 | 1.977 | 3.605 ^{+0.014} _{-0.018} | 0.718 ^{+0.014} _{-0.013} | 14.500 ^{+0.056} _{-0.056} | 43.342 ^{+0.212} _{-0.209} | 1.098 ^{+0.001} _{-0.001} | 4.513 ^{+0.071} _{-0.068} | 52.340/62 |
| 7 | 60090-01-31-03 | 52791.020 | 3.024 | 3.813 ^{+0.008} _{-0.005} | 0.454 ^{+0.004} _{-0.004} | 14.745 ^{+0.008} _{-0.009} | 49.975 ^{+0.058} _{-0.069} | 1.072 ^{+0.001} _{-0.001} | 34.965 ^{+0.453} _{-0.448} | 113.14/62 |
| 8 | 60090-01-38-00 | 52864.833 | 4.110 | 3.851 ^{+0.012} _{-0.009} | 0.359 ^{+0.006} _{-0.004} | 14.981 ^{+0.01} _{-0.01} | 52.430 ^{+0.28} _{-0.26} | 1.076 ^{+0.001} _{-0.002} | 66.818 ^{+0.003} _{-0.003} | 94.760/62 |
| 9 | 60090-01-38-02 | 52865.070 | 2.501 | 3.588 ^{+0.015} _{-0.016} | 0.459 ^{+0.005} _{-0.005} | 14.920 ^{+0.011} _{-0.011} | 46.987 ^{+0.109} _{-0.111} | 1.073 ^{+0.001} _{-0.001} | 27.298 ^{+0.367} _{-0.368} | 110.19/62 |
| 10 | 60090-01-39-03 | 52874.899 | 2.992 | 3.915 ^{+0.007} _{-0.007} | 0.459 ^{+0.005} _{-0.005} | 14.500 ^{+0.008} _{-0.008} | 49.912 ^{+0.076} _{-0.078} | 1.085 ^{+0.001} _{-0.001} | 33.193 ^{+0.431} _{-0.430} | 103.42/62 |
| 11 | 60090-01-40-01 | 52889.816 | 2.932 | 3.638 ^{+0.021} _{-0.023} | 0.540 ^{+0.010} _{-0.010} | 14.500 ^{+0.016} _{-0.016} | 50.598 ^{+0.118} _{-0.119} | 1.077 ^{+0.001} _{-0.001} | 9.619 ^{+0.197} _{-0.191} | 53.130/62 |
| 12 | 60090-01-41-00 | 52904.977 | 2.954 | 3.676 ^{+0.015} _{-0.021} | 0.523 ^{+0.006} _{-0.007} | 13.701 ^{+0.027} _{-0.025} | 54.581 ^{+0.229} _{-0.255} | 1.078 ^{+0.001} _{-0.001} | 12.622 ^{+0.249} _{-0.231} | 97.770/62 |
| 13 | 60090-01-53-08 | 52909.834 | 1.526 | 2.905 ^{+0.011} _{-0.013} | 4.050 ^{+0.005} _{-0.005} | 16.708 ^{+0.007} _{-0.007} | 222.939 ^{+0.561} _{-0.448} | 3.457 ^{+0.004} _{-0.004} | 0.969 ^{+0.003} _{-0.004} | 115.07/62 |
| 14 | 60090-01-42-00 | 52915.775 | 1.795 | 2.676 ^{+0.016} _{-0.008} | 4.084 ^{+0.060} _{-0.024} | 16.185 ^{+0.007} _{-0.007} | 223.144 ^{+0.979} _{-1.018} | 3.435 ^{+0.001} _{-0.001} | 1.463 ^{+0.017} _{-0.012} | 102.14/62 |
| 15 | 60090-01-42-04 | 52919.787 | 0.563 | 2.763 ^{+0.011} _{-0.011} | 6.412 ^{+0.004} _{-0.004} | 15.273 ^{+0.249} _{-0.253} | 199.949 ^{+1.849} _{-1.734} | 2.925 ^{+0.002} _{-0.002} | 0.563 ^{+0.003} _{-0.004} | 118.62/62 |

Conclusions

Cygnus X-1 is one of the brightest Galactic black hole X-ray binaries and hence an important source to study the accretion physics around black hole sources. The object belongs to a high mass X-ray binary and thus a predominantly low angular momentum wind fed system. Indeed, in Smith et al. (2002) and Ghosh & Chakrabarti (2016), the presence of a small Keplerian disc in this system has been reported.

The TCAF solution has successfully explained the accretion flow properties of several outbursting/transient BHCs e.g., GRO J1655-40 (Chakrabarti et al., 2005, Debnath et al. 2008), XTE J1550-564 (Chakrabarti et al., 2009), GX 339-4 (Debnath et al., 2010, 2015a; Nandi et al., 2012), GRS 1915+105 (Pal et al. 2011), IGR J17091-3624 (Iyer et al., 2015), MAXI J1543-564 (Chatterjee et al. 2016), MAXI J1836-194 (Jana et al. 2016), H 1743-322 (Debnath et al. 2013, Mondal et al. 2014, Molla et al. 2017, Bhattacharjee et al. 2017) exhibiting reasonable variation of the four flow parameters. Additionally, the mass of the BHC in each of the system has also been estimated. This motivated us to study the spectral behavior of the persistent black hole source Cygnus X-1 using the TCAF solution. Consequently we investigate a persistent/hard period and an outburst-like flare of Cygnus X-1.

Our analysis reveals that during the hard phase, there is very little dynamical evolution of the accretion flow parameters which is characteristic of a persistent source. This in turn, is indicative of the fact that there has been a steady wind accretion from the companion during this period. The minimal evolution of the flow parameters \dot{m}_d , \dot{m}_h , X_s and R obtained from TCAF fits during this period reinforces this fact (see Fig. 3). Substantial activity in radio is suspected in Cygnus X-1, specially during the low/hard phase (Stirling et al. 2001; Gleissner et al. 2004; Fender et al. 2004, 2006; Wilms et al. 2006, 2007; Zdziarski et al. 2011). In presence of such an activity, the base of the jet will also contribute to soft X-ray flux which may be responsible for increasing the average value of χ^2_{Red} of the TCAF fits. On MJD = 50857.980, MJD = 50901.071, MJD = 50843.049, for example, the value of χ^2_{Red} is particularly high. It may be interesting to study the radio-X ray correlations of Cygnus X-1 during these days, which lies beyond the scope of our present work.

During the flaring phase, there is substantial evolution of the flow parameters which is possibly triggered by sudden enhancement of viscosity beyond the critical value (Roy & Chakrabarti, 2017). Viscosity enhances the disc accretion rate reducing the halo rate as the soft state is approached. Soft state stays as long as the viscosity remains high after which the object abruptly returns back to its hard phase.

We note that the average χ^2_{Red} was also on the higher end, $\sim 1.53 \pm 0.32$ during the flaring phase. Indeed, out of 15 observations during this phase, χ^2_{Red} of spectral fits of 9 observations are greater than 1.5. In Jahoda et al. (2006), the authors discuss in detail the presence of line features around ~ 5 keV, ~ 10 keV and large fluctuations of residuals above 20 keV, due to the instrument. In their study, a few standard sources, such as Crab, were considered. After fitting the spectra with power-law, and a Gaussian for the iron line at ~ 6.5 keV, the residue showed similar features to that of ours (most prominently in Fig. 5). The sudden drop of quantum efficiency of the Xenon layers (L-edge) near 5 keV, resulted in line features at 4.78 keV, 5.10 keV, and 5.45 keV. The K-escape line feature around 10 keV was also found. The large fluctuations beyond 20 keV was dealt with and attributed to larger systematic errors (taken up to 2% by them). The low energy fluctuations were due to not using variable absorption models such as ‘varabs’. Jahoda et al. took all these issues into account and rectified the problem by using a variable ISM density of H, He, C, N, O and multiple edge-smearred lines. As the main goal of this Chapter is to study the change of average behavior of the continuum with the accretion flow parameters, we did not venture

into accounting for all the line emissions. The TCAF solution intrinsically takes into account the ‘reflection component’ and is expected to be a better fit to the continuum. We, therefore, ignore the presence of some patterns in the residuals, as long as the reduced χ^2 value is less than 2.0. The study of, or the incorporation of, such features is beyond the scope of this work. The fact that even a constant systematic error of 1% produced reduced $\chi^2 < 2.0$ for both hard and outbursting phases, only testifies to the applicability of TCAF solution.

During both the phases from each spectral fits, we can get an independent estimate of the mass of the object. Combining both the phases, the probable mass of the source ranges from $12.50 - 16.71 M_{\odot}$, such that the average mass turns out to be $14.57^{+2.14}_{-2.07} M_{\odot}$. This is pleasantly in the range estimated from the previous findings. We prefer the lower side than the higher side since the spin of the object has not been taken into account, i.e. the results obtained from the hard state (where the CENBOL is far away from the black hole and hence is less sensitive to the spin) is more trustworthy. In soft states the Keplerian disc moves closer to the black hole and thus the result could be affected by the spin. The normalization of the TCAF model fluctuates very slightly from its average value of 2.56 ± 0.53 , during the low/hard phase as it should be. However, it shows a substantial variation with the onset of the outburst-like phase. This may be due to the fact that the source exhibits radio jets (Stirling et al. 2001; Gleissner et al. 2004; Wilms et al. 2006; Zdziarski et al. 2011) through all spectral states (Zdziarski et al. 2011). Though the correlation between power-law flux in X-ray and the radio flux decreases in the softer states, the behaviour is unlike other transient LMXBs in their soft states (Zdziarski et al. (2011)). It was also reported, in this regard, that the soft state for Cygnus X-1, could be similar to “soft-intermediate states” of other LMXBs. The direct and secondary emissions from the base of the jet may contribute to the X-ray flux affecting the spectrum. At present, the TCAF based model does not include this effect. We expect that once the X-ray emission from the outflow is incorporated in our model we should obtain better fits in such phases.

Chapter 6

Comptonized spectra of a weakly magnetized neutron star (NS)

ABSTRACT

We explore spectral properties of a Two-Component Advective Flow (TCAF) around a neutron star. We compute the effects of thermal Comptonization of soft photons emitted from a Keplerian disc and the boundary layer of the neutron star by the post-shock region of a sub-Keplerian flow, formed due to the centrifugal barrier. The shock location X_s is also the inner edge of the Keplerian disc. We compute a series of realistic spectra assuming a set of electron temperatures of the post-shock region T_{CE} , the temperature of the normal boundary layer (NBOL) T_{NS} of the neutron star and the shock location X_s . These parameters depend on the disc and halo accretion rates (\dot{m}_d and \dot{m}_h , respectively) which control the resultant spectra. We find that the spectrum becomes harder when \dot{m}_h is increased. The spectrum is controlled strongly by T_{NS} due to its proximity to the Comptonizing cloud since photons emitted from the NBOL cool down the post-shock region very effectively. We also show the evidence of spectral hardening as the inclination angle of the disc is increased. Most of these results are reported in Bhattacharjee and Chakrabarti (2017). Figures 6.2, 6.4, 6.7-6.14 have been taken from there.

Simulation Setup

Monte Carlo simulation results of two component advective flows around black holes are present in the literature (Ghosh et al. 2009, 2010, hereafter, GCL09 and GGCL10, respectively). In the present context, in addition to the components used earlier, we must include a boundary layer (NBOL) of the star which will emit a blackbody radiation. In Fig. 6.2, we present the flow configuration of our simulation. We also use a more realistic post-shock region or CENBOL, namely, one that resembles a thick accretion disc (Molteni, Lanzafame & Chakrabarti, 1994). Since we are considering a stationary configuration, to begin with, we use the density and temperature distribution as specified by Chakrabarti (1985) inside a general relativistic model of the thick accretion disc.

The three components of our simulation configuration, namely, the boundary layer of the neutron star (NBOL), the Comptonizing cloud (CENBOL) and the Keplerian disc (KD) are discussed below:

Normal Boundary Layer (NBOL)

It is a thermal blackbody radiation emitting region on the surface of the neutron star, that is symmetrically placed around the equatorial plane between the azimuthal angles $(90^\circ - \theta_*)$ to $(90^\circ + \theta_*)$, where θ_* is an angle which decides the thickness of the boundary layer. The mass of the star is kept constant at $M_{NS} = 1.4 M_\odot$. The radius of the spherical neutron star is taken as $r_{NS} = 3 r_S$, where $r_S = \frac{2GM_{NS}}{c^2}$ is the Schwarzschild radius of the neutron star. Here, c is the speed of light in vacuum. From previous works carried out by IS99 and GS14 the temperature of an accreting neutron star is reported to be around 1.4 keV in the soft states. For our cases, we set the maximum value of accretion rate to one Eddington rate and the corresponding temperature is set to $T_{NS}^{max} = 1.2 \text{ keV}$. An empirical dependence on accretion rates is chosen based on the fact that emitted flux is proportional to the accretion rate, which is formulated as,

$$T_{NS} = T_{NS}^{max} \times (\dot{m}_d + \dot{m}_h)^{1/4} \text{keV}. \quad (6.1)$$

The flux density of photons emitted from the surface, corresponding to temperature T is calculated using (adopted from Garain et al. 2014, hereafter GGC14):

$$n_\gamma = \left[\frac{4\pi}{c^2} \left(\frac{k_b}{h} \right)^3 \times 1.202057 \right] T^3 \text{ cm}^{-2} \text{ s}^{-1}, \quad (6.2)$$

We follow the work of IS99, where it is reported that the angle $\theta_* \rightarrow 90^\circ$, when $\dot{M} \rightarrow \dot{M}_{Edd}$. For our calculations, accretion rates are written in the units of \dot{M}_{Edd} . So, to incorporate such an effect, we assume a simpler variation of θ_* , given by,

$$\theta_* = \sin^{-1}(\dot{m}_d + \dot{m}_h), \quad \text{if } (\dot{m}_d + \dot{m}_h) \leq 1. \quad (6.3)$$

The flux, however, is not a constant w.r.t. θ . It is believed that due to the meridional motion of the flow in the NBOL, radiation reaches a maximum flux near the angle θ_* (IS99). The effect of this is incorporated, at least qualitatively, by using a truncated double Gaussian distribution of photon flux where the peaks are located at θ_P^\pm . We took the 95% of the θ_* as the location of

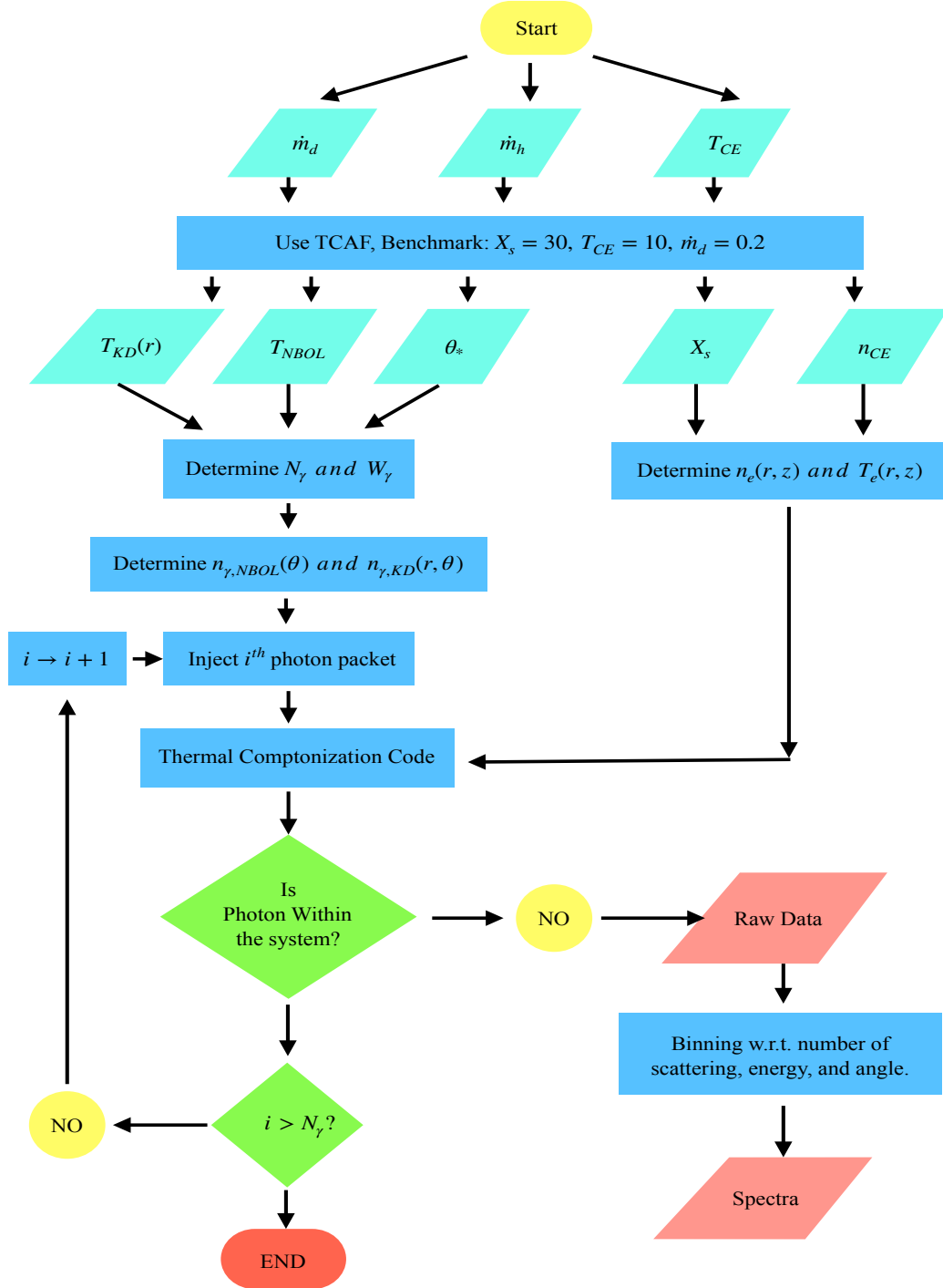


Figure 6.1: A flowchart of the Monte Carlo, thermal Comptonization code, implemented in the TCAF geometry around a neutron star. Here, N_γ and W_γ denote the total number of photon packets and the weightage of packets, respectively. $n_{\gamma, NBOL}(\theta)$ and $n_{\gamma, KD}(r, \theta)$ denote the distribution of number of photons to be injected from the NBOL and KD, respectively. Rest of the notations are kept same as in the text.

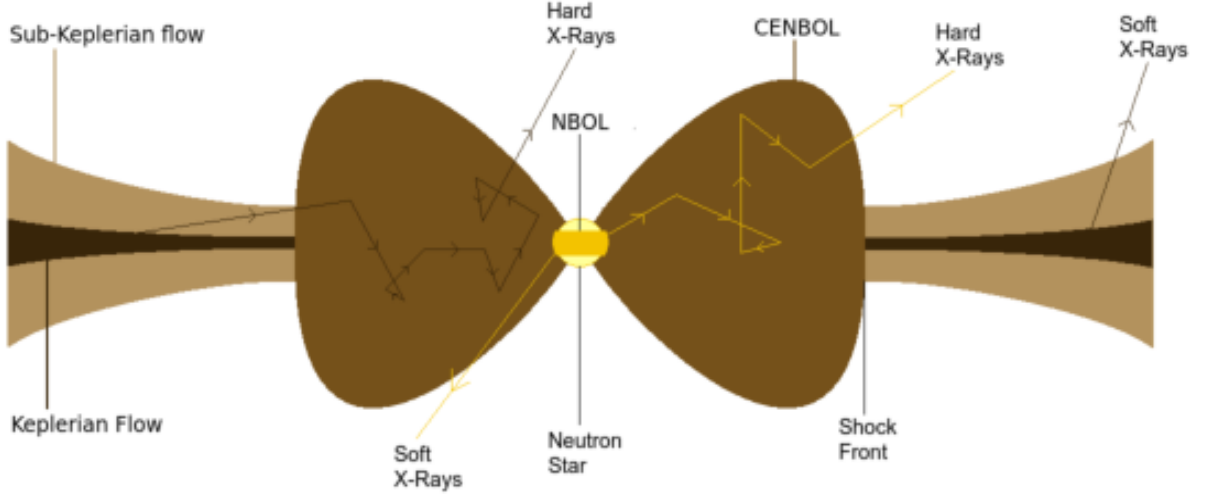


Figure 6.2: A schematic diagram of the Two-component Advective Flow (TCAF) around a neutron star. The Keplerian disc and the boundary layer on the surface of the neutron star (NBOL) emit soft blackbody photons which are scattered by the hot electrons in the centrifugal pressure supported boundary layer or CENBOL. Taken from Bhattacharjee and Chakrabarti (2017).

the peaks, as this is not crucial to the net final spectrum, i.e.,

$$\theta_P^\pm = \left(90^\circ \pm 0.95 \times \theta_* \right). \quad (6.4)$$

The distribution takes the form:

$$f(\theta) = \exp(-(\theta - \theta_P^+)^2) + \exp(-(\theta - \theta_P^-)^2). \quad (6.5)$$

After calculating the total flux from the entire NBOL, we redistributed the photon numbers according to the double Gaussian profile $f(\theta)$ along θ so as to have a realistic injection of photons from the NBOL on to CENBOL.

CENBOL

The centrifugal barrier supported boundary layer is modelled in shape by the equipotential contours of a standard thick disc (Chakrabarti, 1985; Chakrabarti, Jin and Arnett 1987, Ghosh et al. 2009). The analytical forms of potential ϕ , adiabatic constant related to entropy K , density ρ and temperature T_e profiles are given below:

$$\phi = \frac{\lambda^2}{2(r^2 - z^2)} - \frac{1}{2(r - 1)} = \frac{\lambda^2}{2R^2} - \frac{1}{2(\sqrt{R^2 + z^2} - 1)}, \quad (6.6)$$

where λ is the specific angular momentum, R is the cylindrical radius, z is the vertical height, $r = \sqrt{R^2 + z^2}$ is the radial distance and ϕ is the specific potential energy in units of c^2 (GCL09; Chakrabarti 1985).

The entropy ($K(\beta, \mu)$) is defined as (GCL09; Chakrabarti 1985),

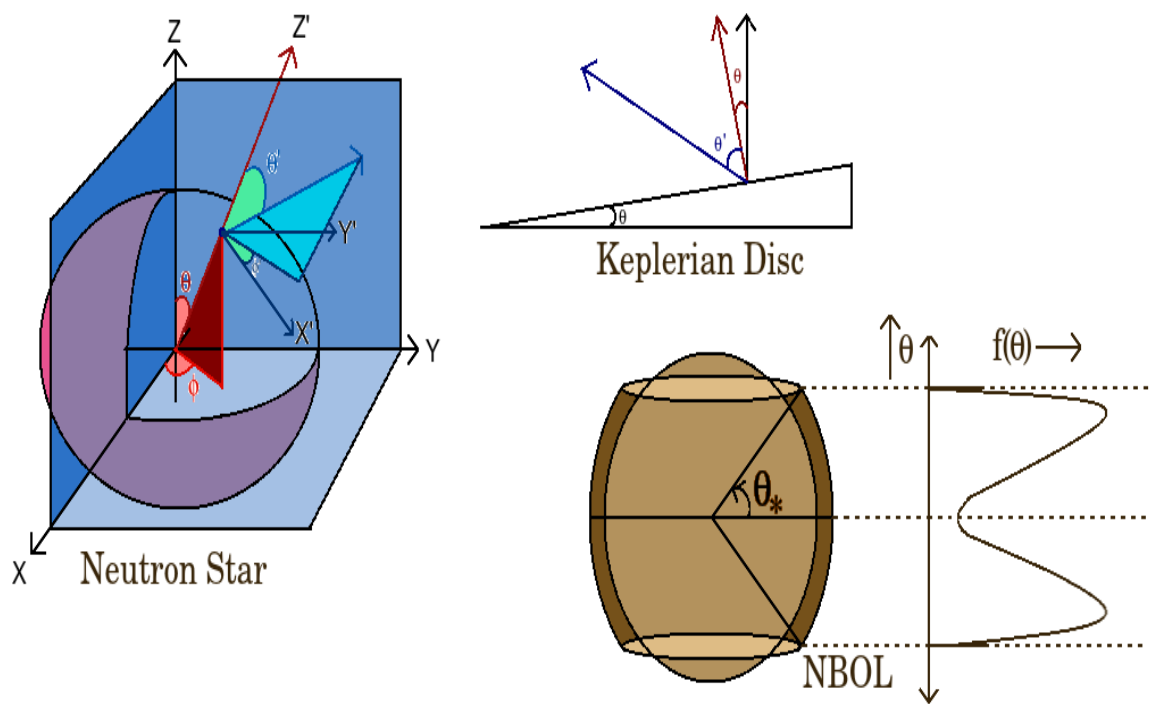


Figure 6.3: A schematic for the NBOL and SS73 disc which supply the seed photons. The local angles are also shown (with primed variables θ' , ϕ' , which are used while injecting photons. The distribution of flux along θ for NBOL has been modelled using a truncated double Gaussian (Inogamov and Sunyaev 1999).

$$K(\beta, \mu) = \left[\frac{3}{a} \frac{1 - \beta}{\beta^4} \frac{(k_b)^4}{(\mu m_p)^4} \right]^{\frac{1}{3}} cm^3 g^{-1/3} s^{-2}, \quad (6.7)$$

where μ is the mean molecular weight, a is the Stefan's radiation density constant, β is the ratio of gas pressure and total pressure, k_b is the Boltzmann constant, m_p is the mass of the proton.

The density ρ is then written as (adapted from GCL09; Chakrabarti 1985),

$$\rho(r, z) = C_\rho \times \left[\frac{\phi(r, z)}{n\gamma K} \right]^n g cm^{-3}, \quad (6.8)$$

where n is the polytropic index, γ is the adiabatic index.

The temperature T_e , can also be written as (adapted from GCL09; Chakrabarti 1985),

$$T_e(r, z) = C_T \times \left[\frac{\beta \mu m_p K}{k_b} \right] \rho^{1/3} K. \quad (6.9)$$

For our calculations, $\lambda = 1.9$, $\beta = 0.5$, $n = 3.0$ and the centre of the thick disc is at $\sim 4.25 r_S$. We did not modify the entropy by tuning β , but kept it constant at 0.5 throughout. Here, C_T is a constant introduced to supply the central temperature as a parameter. In order to obtain the spectra relevant to the observed ones, we restrict the central temperature of the CENBOL to the range obtained so far by previous observational fits (between 3 keV to 25 keV). From the observational and theoretical studies of accretion onto black holes, it is well known that with increasing disc accretion rate, CENBOL would be cooled down and become smaller in size. This is regularly observed in outbursting candidates, such as GRO J1655-40, GX339-4, H1743-322, MAXI J1836-194, MAXI J1543-564 etc. (Debnath et al. 2008, 2010, 2013; Mondal et al. 2014, 2016; Jana et al. 2016; Chatterjee et al. 2016; Molla et al. 2017, 2016). This happens because the photon flux from the disc increases with \dot{m}_d . This soft radiation cools down the CENBOL and the shock condition (balancing of pressure on both sides of the shock) is satisfied at a smaller value of shock location. In order to incorporate this, we use the scaling behaviour of the CENBOL with central temperature. For our case, a reference is set for $\dot{m}_d = 0.2 \dot{M}_{EDD}$, $T_{CE} = 10 keV$, $X_s = 30 r_S$. The density is modified by the constant C_ρ , which is determined self-consistently from the strong shock condition of a hybrid 1.5 dimensional advective flow solution (Chakrabarti 1989). The disc and halo accretion rates (\dot{m}_d and \dot{m}_h , respectively), the shock location (X_s), and the compression ratio (R_{comp}) determine the density at the post-shock region. The pre-shock flow is assumed to have a velocity, $v_R \sim R^{-1/2}$ since the lower angular momentum flow would be quasi-spherical. In the post-shock region, the matter initially slows down and gradually picks up its speed. For a black hole, matter becomes supersonic before crossing the horizon. In case of neutron stars, the hard surface and the flow pressure force the matter to slow down just before reaching the surface.

The parameters we use in our simulations are given in Table 6.1. There are altogether nine cases divided into three groups with different disc accretion rates (\dot{m}_d) and the central temperatures (T_{CE}). Once we normalize the outer edge of the CENBOL at $X_s = 30.0$ for cases C4-C6, the outer edge changes following constant temperature contours and the corresponding X_s are given in the

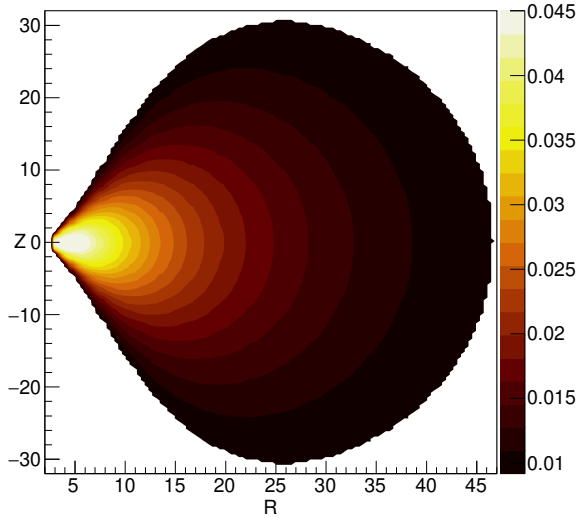


Figure 6.4: The temperature contours used for the simulation (for $\dot{m}_d = 0.1$, $T_{CE} = 25.0$ keV, $X_s = 46.8$ r_s . The temperatures are written in dimensionless unit (kT_e/mc^2). This profile, symmetric w.r.t. z-axis, is used to get the values of temperatures at different points of CENBOL. Taken from Bhattacharjee and Chakrabarti (2017).

Table. For each (\dot{m}_d, T_{CE}) pair, we change the halo rate \dot{m}_h . Since the matter density inside the CENBOL is decided by the sum of the two rates, the number density of electrons at the centre of CENBOL also changes. The values of T_{NS} , θ_* and $T_e(\tau_0)$ are obtained from Eqs. 1, 3, and 13, respectively.

In Fig. 6.4, we present the temperature contours corresponding to C3. The contours show that a CENBOL is essentially a toroidal star with highest density and temperature at the ‘centre’ (which is actually a ring around the neutron star). The vertical colour bar shows the temperatures in dimensionless unit.

For a cylinder of half height h_s and radius X_s , we have the accretion rate \dot{m}_{tot} ,

$$\dot{m}_{tot} = (\dot{m}_d + \dot{m}_h) = 4\pi X_s h_s \rho_+ v_+. \quad (6.10)$$

The density at the equatorial plane of the post-shock flow is written as (from Eq. 6.10),

$$\rho_+ = \frac{(\dot{m}_d + \dot{m}_h) R_{comp}}{4\pi h_s \sqrt{X_s}}. \quad (6.11)$$

In writing Eqs. 6.10 and 6.11, R_{comp} used represents the shock compression ratio. We have assumed a strong shock condition for our calculation and set $R_{comp} = 4$ for that purpose, throughout the simulations. As there is effectively optically thin matter outside CENBOL, we set the density outside to 0 except on the equatorial plane where there is a Keplerian disc.

$$\rho(r, z) = 0, \quad \text{if } \phi(r, z) > \phi(X_s, 0). \quad (6.12)$$

The effective temperature is calculated by transforming from coordinate space to τ space and then

averaging over all values of $T_e(\tau)$. We followed the method of CT95 for this purpose.

$$T_e(\tau_0) = \frac{\int_0^{\tau_0} T_e(\tau) g^2(\tau) (\tau - \tau_0)^2 d\tau}{\int_0^{\tau_0} g^2(\tau) (\tau - \tau_0)^2 d\tau}, \text{ where} \quad (6.13)$$

$$g(\tau) = \left(1 - \frac{3}{2} e^{-(\tau+2)}\right) \cos \frac{\pi}{2} \left(1 - \frac{\tau}{\tau_0}\right) + \frac{3}{2} e^{-(\tau_0+2)}. \quad (6.14)$$

Here, the integration is carried out along the equatorial plane (along R direction).

Keplerian Disc (KD)

A dense region of geometrically thin and optically thick disc extends outward from the outer edge of CENBOL (X_s). The outer edge of the disc is set at $R_{out} = 200 r_s$ for simplicity. The standard Shakura-Sunyaev disc (Shakura and Sunyaev, 1973) is used to determine the flux and height of disc as a function of radial distance in between X_s and R_{out} . This acts as a secondary source of blackbody photons. Here, $dr = 0.5 r_s$, \dot{M}_{17} is the disc accretion rate in the units of $10^{17} \text{ gm s}^{-1}$. The radial distance r is measured in the units of r_s . The injected energy flux is given by (SS73; GCL09),

$$F(r) = 5 \times 10^{26} (M_{NS})^{-2} \dot{M}_{17} (2r)^{-3} \left[1 - \sqrt{\frac{3}{r}}\right] \text{ erg cm}^{-2} \text{ s}^{-1}. \quad (6.15)$$

From which, the effective temperature ($T(r) = (F(r)/\sigma)^{1/4}$) and height of the disc is determined as (adopted from GCL09),

$$T(r) \approx 5 \times 10^7 (M_{NS})^{-1/2} \dot{M}_{17}^{1/4} (2r)^{-3/4} \left[1 - \sqrt{\frac{3}{r}}\right]^{1/4} K, \quad (6.16)$$

$$H(r) = 10^5 \dot{M}_{17} \left[1 - \sqrt{\frac{3}{r}}\right] \text{ cm}. \quad (6.17)$$

For our case, every cylindrical shell between r and $r + \delta r$ of height $H(r)$, emits a total $dN(r)$ number of photons per second (GGC14) from its top and bottom surfaces, where

$$dN(r) \approx 2\pi r \delta r n_\gamma(r). \quad (6.18)$$

For computational purposes, we chose packets of photon instead of individual photons, in such a way that, effective $dN(r) \sim 10^5$, which is required for a good statistics.

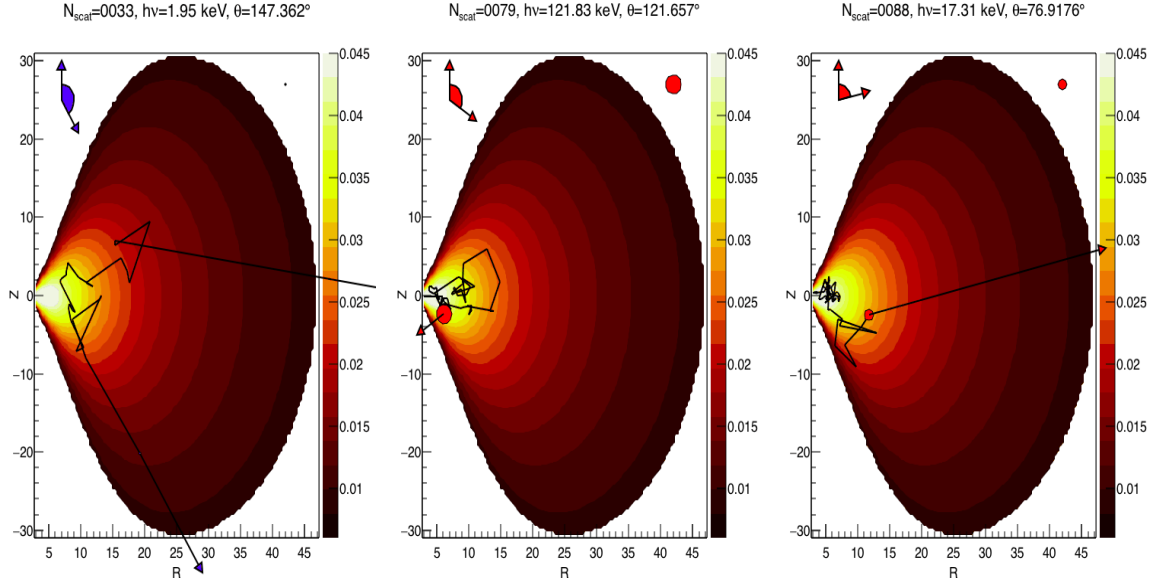


Figure 6.5: Photon scattering being tracked within the particle dynamics of the MC code. The solid lines represent the path of the photons. The arrows represent the direction. The energies and ejection angles are also depicted in the frames. The contours of constant temperature are depicted in the colour-map in the background.

Scattering Process

We adopt the method followed by Pozdnyakov, Sobol, and Sunyaev (1983, hereafter PSS83) to model the thermal Compton scattering process.

Radiative processes

We simulate thermal Compton scattering phenomenon between the soft photons emitted by the Keplerian disc (or, the NBOL, the boundary layer of the neutron star) and the hot electrons in the post-shock region (CENBOL), using a Monte Carlo code. Photons from the Keplerian disc and the boundary layer are modelled using Planck's distribution formula for blackbody radiation. The radial temperature distribution for Keplerian disc $T(r)$ is used as above. For the neutron star, the value (T_{NS}) is kept constant throughout the simulation. In both the cases, the number density of photons ($n_\gamma(E)$) having an energy between E and $E + dE$ is expressed by (PSS83):

$$n_\gamma(E) = \frac{1}{2\zeta(3)} b^3 E^2 (e^{bE} - 1)^{-1}, \quad (6.19)$$

where $b = 1/kT$. Here $T = T(r)$ for KD and $T = T_{NS}$ for NS. The zeta function, $\zeta(3) = \sum_1^\infty l^{-3} = 1.202$.

For every packet of photon, we start the simulation by determining the local normal at the randomly chosen position on the i) NBOL or the ii) Keplerian disc. Then, a random direction (θ_r) is chosen w.r.t. the local normal, with the probability density $\cos(\theta_r)$. We also assign a random critical optical depth τ_c . During the photons' motion, we calculate τ by summing over $d\tau$ to check if it has crossed τ_c or not. Here, $d\tau = \rho_n \sigma dl$ where ρ_n is the number density of electrons and dl is the length traversed. σ is the scattering cross-section, determined using the Klein-Nishina formula,

Table 7.1
List of parameters for the system used in simulation

| ID | \dot{m}_d (\dot{M}_{EDD}) | \dot{m}_h (\dot{M}_{EDD}) | X_s (r_S) | T_{CE} (keV) | n_{ce} ($\times 10^{18}$) | T_{NS} (keV) | θ_* (degrees) | $T_e(\tau_0)$ (keV) |
|----|---------------------------------|---------------------------------|-----------------|----------------|-------------------------------|----------------|----------------------|---------------------|
| C1 | 0.1 | 0.1 | 46.8 | 25.0 | 1.772 | 0.802 | 11.52 | 22.062 |
| C2 | 0.1 | 0.2 | 46.8 | 25.0 | 2.658 | 0.888 | 17.48 | 22.062 |
| C3 | 0.1 | 0.5 | 46.8 | 25.0 | 5.317 | 1.056 | 36.90 | 22.062 |
| C4 | 0.2 | 0.1 | 30.0 | 10.0 | 1.515 | 0.888 | 17.48 | 8.909 |
| C5 | 0.2 | 0.2 | 30.0 | 10.0 | 2.020 | 0.954 | 23.61 | 8.909 |
| C6 | 0.2 | 0.5 | 30.0 | 10.0 | 3.535 | 1.098 | 44.40 | 8.909 |
| C7 | 0.5 | 0.1 | 21.8 | 3.0 | 2.100 | 1.056 | 36.90 | 2.705 |
| C8 | 0.5 | 0.2 | 21.8 | 3.0 | 2.450 | 1.098 | 44.40 | 2.705 |
| C9 | 0.5 | 0.5 | 21.8 | 3.0 | 3.500 | 1.200 | 90.00 | 2.705 |

Table 6.1: Set of parameters chosen for the simulations. Disc accretion rate (\dot{m}_d) and halo accretion rate (\dot{m}_h) are varied independently. Temperatures are from typical observational range and consistent with high disc accretion rates leading to lower temperatures of CENBOL. Shock locations (X_s) are chosen accordingly. Neutron star's (NBOL) temperature (T_{NS}), θ_* and central number density n_{ce} are derived using empirical rules given in the text. Taken from Bhattacharjee and Chakrabarti (2017).

$$\sigma = \frac{2\pi r_e^2}{x} \left[\left(1 - \frac{4}{x} - \frac{8}{x^2} \right) \ln(1+x^2) + \frac{1}{2} + \frac{8}{x} - \frac{1}{2(1+x)^2} \right],$$

where $x = \frac{2E}{mc^2} \gamma \left(1 - \mu \frac{v}{c} \right)$. Here, $r_e = e^2/mc^2$ is the classical electron radius and m is the mass of the electron.

The electrons are assumed to have a relativistic Maxwell-Boltzmann distribution of momentum. If $\mathbf{p} = \gamma m \mathbf{v}$, with $\gamma = (1 - \frac{v^2}{c^2})^{-1/2}$ and $\mu = \hat{\Omega} \cdot \hat{\mathbf{v}}$, the number density of electrons between momentum \mathbf{p} and $\mathbf{p} + d\mathbf{p}$ is given by PSS83,

$$dN(\mathbf{p}) \propto \exp[-(p^2 c^2 + m^2 c^4)^{1/2} / kT_e] d\mathbf{p}. \quad (6.20)$$

Based on the scattering cross-section obtained, the optical depth is calculated. If, $\tau > \tau_c$, we allow the photon to scatter and assign a new direction based on its energy. A new random τ_c is generated and the process is continued till the photon leaves the system under consideration. Details of the procedure is given in PSS83.

We continue the simulations for all the nine cases listed in Table 6.1. The angle θ_* , number density n_{ce} and average temperature $T_e(\tau_0)$ were all derived from other parameters. Inclusion of the compression ratio (R_{comp}) and mass of the star (M_{NS}), would make the number of independent parameters to be seven. For our theoretical investigations in the present Chapter, we did not focus on the reduction of the number of parameters in the present work, but we can further reduce it by deriving CENBOL properties from fundamental equations. We vary \dot{m}_d and \dot{m}_h independently and determine the rest of the parameters either using observational facts or through the formulae derived.

Photoelectric absorption

Photoelectric effect due to gases present in the interstellar media (ISM) is the most significant cause of absorption of photon, in the domain of energy we are considering in this Chapter. Depending on the degree of absorption, the observed spectra can be largely modified between in the range 0.03 – 10 keV (Morrison and McCammon 1983). We have used the standard formula for photoelectric cross-section,

$$\sigma(E) = 4\alpha\sqrt{2}z^5 8\pi \frac{r_e^2}{3} \left[\frac{m_e c^2}{E} \right]^{3.5} \text{ cm}^2. \quad (6.21)$$

An exponential absorption model was used, following the ‘wabs’ model used in XSPEC, which can be written as,

$$M(E) = \exp(-n_H \sigma(E)), \quad (6.22)$$

where n_H is the equivalent column density of hydrogen in ISM along the observational direction.

In Figs. 6.10 to 6.12, the dotted lines show our derived spectra before the interstellar absorption and solid lines show the spectra after absorption. For the cases C1 to C9, $n_H = 4.0 \times 10^{22} \text{ cm}^{-2}$ was chosen for concreteness.

Effects of cooling

We focus on the cases when the CENBOL has temperature up to 25 keV, and the accretion rates are not too high ($\leq \dot{M}_{Edd}$). In the flaring branches, however, the observed spectra shows the Comptonized spectrum extending beyond 200 keV, pointing towards a hotter outer CENBOL. In order to check this effect of cooling we take the case of comparatively hotter central temperature ($T_{CE} = 250 \text{ keV}$), and vary the accretion rates to observe the effects of cooling due to Comptonization. In the scenario when cooling is efficient, the static background temperature distribution should be modelled by the modified temperature, rather than the unmodified thick disc distribution. However, the spectra of those cases are not discussed any more as the Comptonized spectra of the disc is well understood in the cases of black hole under the TCAF paradigm.

First, we project the entire 3D simulation region onto an axisymmetric cylindrical grid, for which the thick disc distributions are used. The number density of electron at each grid location (ir, iz) , which corresponds to the position (R, z) , is given by $n_e(ir, iz)$. Assuming a torus, for axisymmetric system, the total number of electrons within that volume is given by $dN_e(ir, iz)$,

$$dN_e(ir, iz) = 2\pi R n_e(ir, iz) dR dz \quad (6.23)$$

where dR and dz are the grid sizes in R and z directions, respectively.

Depending on the actual photon flux and the number of bundles of photons injected, a weightage can be assigned to each bundle. Let the weightage for i^{th} packet be f_W^i . For a completely relativistic hydrogen plasma, the total thermal energy of all the electrons in the torus with temperature $T_e(ir, iz)$ is given by,

$$3k_B T_e(ir, iz) dN_e(ir, iz) = 6\pi k_B R T_e(ir, iz) n_e(ir, iz) dR dz. \quad (6.24)$$

If the i^{th} packet of photon undergoes Compton scattering at the position (ir, iz) on the grid gaining (or losing) energy ΔE^i , then the final temperature $k_B T'_e(ir, iz)$ after all the photons have left the system, can be written as,

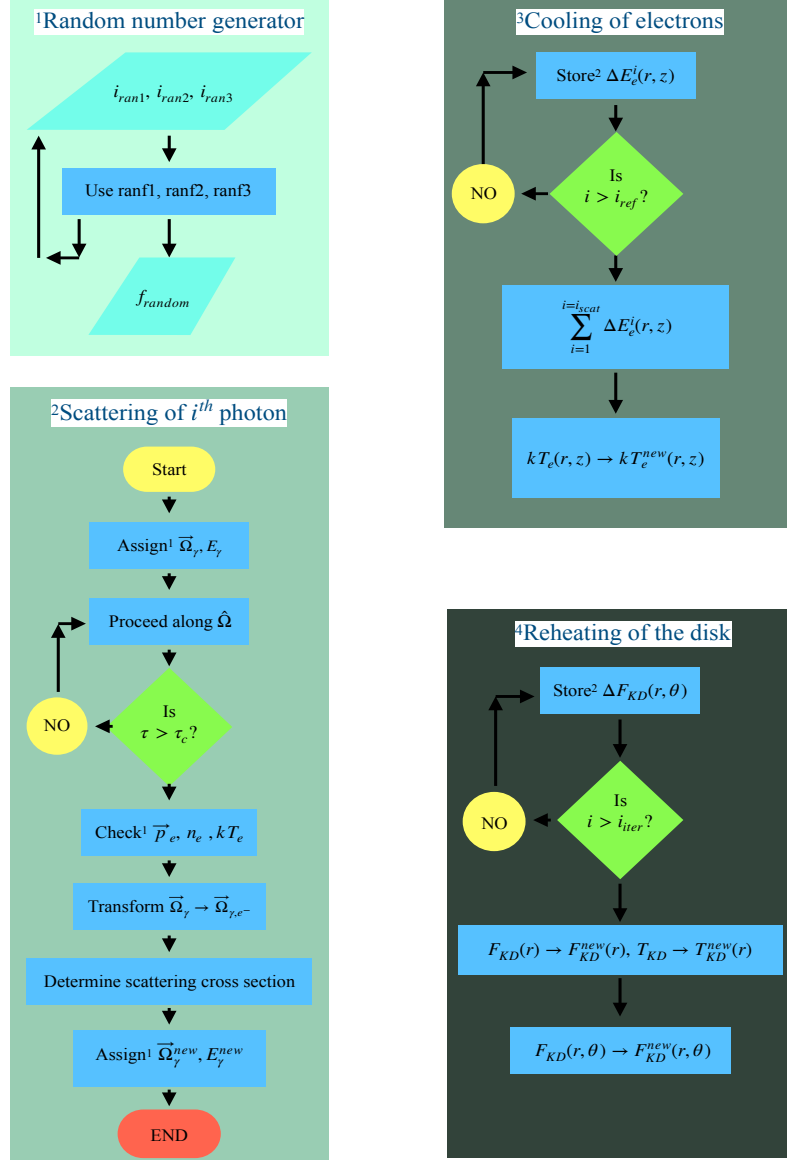


Figure 6.6: Flowcharts for the 1. random number generator routine, 2. thermal Compton scattering process, 2. cooling of CENBOL, 3. thermal reprocessing in the disc. Here, i_{ran1} , i_{ran2} , and i_{ran3} are the odd integer seeds of the random number generator functions $ranf1$, $ranf2$, and $ranf3$. Each call used a seed to return a new seed and a random fraction between 0 and 1. The periodicity of these functions were between 2^{26} to 2^{30} , which is greater than the number of calls in the code for a specific function. Here, we follow the method described in PSS83 for the scattering. A detailed text can also be found in the Thesis of Dr. Himadri Ghosh (2012). i_{ref} is the refresh rate of cooling calculation. Different values were tried, in increasing order, before finding a value beyond which no further accuracy was achieved. We used $i_{ref} = 1000$. Here, $\Delta E_e^i(r, z)$ is the weighed loss of energy at the location (r, z) due to the i th photon, and i_{scat} denotes the number of photons that scattered at (r, z) . $\vec{\Omega}_\gamma$ and $\vec{\Omega}_{\gamma,e^-}$ denote the momentum of the photon in the lab frame and electron's frame, respectively. $F_{KD}(r, \theta)$ represents the distribution of KD flux w.r.t. radial distance on the disc and the inclination angle θ . The *new* superscripts denote the value of a variable after the corresponding process in which it was modified.

$$k_B T'_e(ir, iz) = k_B T_e(ir, iz) - \frac{\sum_{i=1}^{i_{max}} \Delta E^i f_W^i}{3dN_e(ir, iz)} \quad (6.25)$$

where $i_{max} \sim 10^8$.

We divide the CENBOL into two domains of equal optical depth, calculated along the equatorial plane. If the total optical depth of the CENBOL is τ_0 , the region up to $\tau = \tau_0/2$ from the NBOL (or the shock location X_s) is the cloud “visible” to the NBOL (or the Keplerian disc), which would produce effectively the same number of scatterings. We determine the average temperature based on the method specified in eqn. 13, for both the cases, to study the effect of cooling of the CENBOL, by the NBOL and by the disc. This is just to find out the two temperatures in the two halves which Seifina et al. (STF13, STSS15) and Titarchuk et al. (TSS14) found in their work by fitting COMPTB1 and COMPTB2 respectively. The results of this exercise is shown in Fig. 14(a-d) (below).

Results

The photons are collected outside a sphere of radius R_{out} where they leave our system. They are binned according to their energy, angle of observation, the original location of emission (NBOL or KD) and the number of scatterings each of them suffered. We generate the output spectra from these information.

We first report variation of spectra w.r.t. the number of scatterings in CENBOL. A considerable fraction of the seed photons emitted are intercepted by CENBOL. This interception and subsequent Comptonization depend on the density and temperature along the path of the photon. These parameters are however governed by the accretion rates. In case of a black hole, matter is advected in through the event horizon and the efficiency of radiation is around 6%, leading to a large, though notional, upper limit ($\sim 16 \dot{M}_{EDD}$) of the Keplerian disc accretion rate. In the case of a neutron star, the hard surface ensures stopping of the flow at the surface and the radiation decreases the upper limit of maximum acceptable accretion rate. For our calculations, we have strictly kept the upper limit at $1.0 \dot{M}_{EDD}$. The density is, thus, lower than that around a black hole, leading to a lower number of scatterings of the photons emitted by the Keplerian disc. The seed photons emitted by the NBOL, however, are exposed to the densest region of CENBOL first and that leads to a significant number of scattering. As a result, the contribution to hard X-Rays from seed photons that originated from the disc is smaller compared to those emitted from NBOL and the overall spectra, in hard states, is expected to be softer than the hard state spectra of a black hole. The observational differences are reported by Gilfanov (2009). We plot the variation of the combined spectra for the case C3 (from Table 7.1), w.r.t. number of scattering in Fig. 6.7. The binning is done for scattering number 0 (no scattering), 1 – 2, 3 – 6, 7 – 18, 19 – 28, 29 and above. The overall spectra are also drawn. What is clear is that the photons from the Keplerian disc are not scattered much. The lower number of scatterings (including those emitted without scattering) of NBOL photons produced the first hump at around 6 keV while higher number of scatterings which are effectively close to the hot region of CENBOL (i.e., centre), produce the hump at ~ 45 keV.

The spectral properties of any compact object in space, be it a neutron star or a black hole, depend on the inclination angle between the objects line of sight and direction in which the photon is emitted. In presence of an accretion disc which emits photons maximally along the

local normal, the received flux is maximum when the disc is seen end-on and minimum when seen edge-on. In order to check the validity of any spectral model, it has to be compared with observational data and angle dependency of spectra is to be studied to achieve that. We plot the variation of spectra when the photons are binned w.r.t. the average direction of observation, viz., $0^\circ - 30^\circ$, $30^\circ - 60^\circ$, $60^\circ - 90^\circ$. In the system, both the photon sources emit photons symmetrically w.r.t. the equatorial plane or the angle $\theta = 90^\circ$. The structure of CENBOL has the same symmetry as well. As no advection velocity or spin effects are included to derive CENBOL properties, the emergent Comptonized spectra are expected to have the symmetry of the system. Thus in Fig. 6.8, we indicate the spectra of photons along the average bin angle in the bins of the first quadrant only. The peak flux of unscattered spectra from the Keplerian disc decreases with increase of angle θ . In case of the radiation from NBOL, the peak flux direction is decided by the peaks of the double Gaussian distribution of emitted flux used in the simulation (Case C3) are along $\theta_{\bar{p}} = 54.94^\circ$ in the first quadrant. The flux is modulated further due to the interception by CENBOL. The geometry of the post-shock region blocks the escape of unscattered photons emitted at high values of θ . This is reflected in Fig. 6.9(a). The low energy peaks are due to photons emitted from the Keplerian disc and the high energy peaks are formed by photons from NBOL. The scattered photons, however, with the increase of the number of scatterings, lose their initial directional distribution and are re-distributed almost isotropically. Although, the presence of the disc and the neutron star, both of which recapture scattered photons, lowers the number of photons received at around angle $\theta = 90^\circ$. The net flux is highest at $\sim 45^\circ$ since the flux of NBOL is high at $\theta = \theta_{\bar{p}} = 54.94^\circ$ and still has some direct effect. The remnant effect of the double Gaussian enhances the flux along this direction. The Fig. 6.9(b) showcases this.

As shown in the context of black holes (CT95, Ghosh et al. 2009), a rise of halo accretion rate for a given disc accretion rate, makes the spectrum harder. Because of its hard surface, the upper limit of accretion rate for neutron stars is also much lower than that for black holes. This restricts the density of post-shock region leading to relatively softer spectra when compared to the spectra of black holes. Of course, a major factor is the abundance of seed photons from NBOL itself. Figures 6.10, 6.11 and 6.12 show how, in each case, the spectrum is affected by the increase of the halo accretion rate. In order to account for the cooling due to photons emitted by disc, we decreased the temperature of CENBOL self-consistently with the increase of \dot{m}_d (see, Table 6.1). In Fig. 6.12, the spectrum is roughly a superposition of two blackbody emissions in each of the three cases. In Fig. 6.11, the Compton up-scattering slightly modifies the spectra but they still remain in typical soft states. In Fig. 6.10, where $T_{CE} = 25 \text{ keV}$, the spectrum changes from soft to hard with the increase of \dot{m}_h . We take the linear domain of the $\log(\nu F_\nu)$ vs. $\log(E)$ curves plotted in logarithmic scales, if present, and try to fit the data with a power-law having spectral index α ($\nu F_\nu \sim E^{-\alpha}$). The spectral index α , has the values 0.926, 0.357 and -0.239 as \dot{m}_h takes the values 0.1, 0.2 and 0.5, respectively. The indices are calculated from the best fit of the spectra in the energy range 10.0 to 20.0 keV. We have shown the theoretical spectra for cases C1 to C9, in Figs. 6.10, 6.11, and 6.12, with dotted lines and the spectra after absorption through ISM are plotted with solid lines. Cases C1, C4, and C7 are in black, C2, C5, and C8 are in red and C3, C6 and C9 are in blue (online version). Please note that unlike some models (e.g., White et al. 1986, Mitsuda et al. 1989) we do not give emphasis on the NBOL temperature or the decrease of the total luminosity. Rather, our harder states are primarily achieved due to hotter CENBOL with higher advective halo rates.

The absorption due to the presence of interstellar medium modifies the low energy spectra considerably. In the hard states, when the disc accretion rate is low, the multi-colour blackbody

component is hardly observed as a separate peak due to the heavy absorption below 1 keV. This was reflected in the Figs. 6.10 to 6.12. After these considerations, the spectra corresponding to Case C3, looks similar to hard state spectra of neutron stars (see Fig. 6.13, adapted from Gilfanov 2010). The spectrum of neutron stars in hard states is relatively softer than those of black holes, because of the upper bound of maximum accretion rate. The spectra of a number of weakly magnetized accreting stars were chosen to highlight that fact in Fig. 6.13. They also have the characteristic iron line emission around 6.5 keV. Apart from that feature, the observed spectra of neutron stars, as reported in Gilfanov (2010), are similar to our Case C3, which does not include the iron line emission. It can also be concluded that the variation of the parameters of our model, e.g., T_{NS} , T_{CE} , X_s , R_{comp} , \dot{m}_d and \dot{m}_h can reproduce the observed spectra when suitable normalization is used. In this Chapter, we only report the variation of spectra with accretion rates.

To check the variation of the effective geometry of the Compton cloud, CENBOL, we varied the accretion rates and the central temperature T_{CE} of the CENBOL and observed how the Compton scattering changed the temperature profile. For T_{CE} values reported in Table 6.1, the effect was insignificant and are not shown here. But, the cooling mechanism is more prominent when the central temperature is high. To showcase these effects we chose the case where $T_{CE} = 250 \text{ keV}$, $X_s = 46.8 r_S$. We are reporting four cases here where the halo accretion rate is varied from 0.3 to 0.9, as shown in Fig. 14(a) through 10(d). As the accretion rates increase, so does the temperature of the NBOL, the cooling is more efficient. Not only that, the effective temperature closer to NBOL decreases more than the one nearer to the disc, as can be seen from the shifting of the peak towards the disc in the Figure 6.14(a-d). From these Figures, one can see that the effective geometry of the CENBOL is similar to the ones proposed by TSS14 for the flaring branches. The temperature of cloud near the disc are in between $\sim 30 \text{ keV}$ to $\sim 65 \text{ keV}$ for the cases studied here, which are in the same ballpark figure as found from COMPTB model analysis in TSS14 and STSS15.

Thermal reprocessing in the disc

We also studied the reflected flux at the KD (see flowchart, Fig. 6.6). An initial run of the MC code was used to obtain the flux received at different locations of the disc. These fluxes were binned w.r.t r and local angle θ . After a complete run of the code, these fluxes were added to the origin disc flux which modifies the effective temperature (Fig. 6.16). In the 2nd iterative run, this new temperature is used. The flux distribution, however, is assigned based on the angle at which it was received (Fig. 6.15), to take care of reflection. Multiple iteration of this is done till the temperature of CENBOL reached a convergence. The variation of the disc spectra, relative hardening along high inclination, with angle is shown in Fig. 6.17.

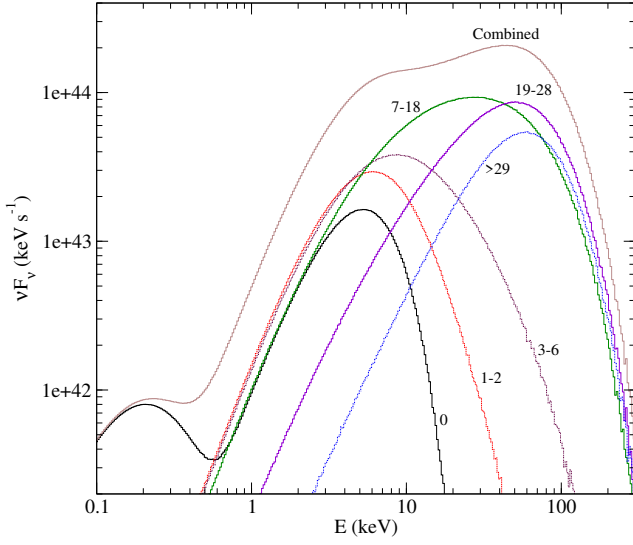


Figure 6.7: Evidence of hardening of spectra with the number of scattering. The seed photons are emitted from the NBOL and Keplerian disc and are Comptonized by CENBOL. Here, halo accretion rate \dot{m}_h is 0.5 and disc accretion rate is \dot{m}_d is 0.1. The photons are binned based on the number of scatterings they underwent before emerging out of the system. The binning was done for 0, 1 – 2, 3 – 6, 7 – 18, 19 – 28, 29 or higher number of scatterings. These numbers are written beside the corresponding curves to give an idea of how variously scattered photons contribute to the spectra. The combined spectrum is also plotted. Taken from Bhattacharjee and Chakrabarti (2017).

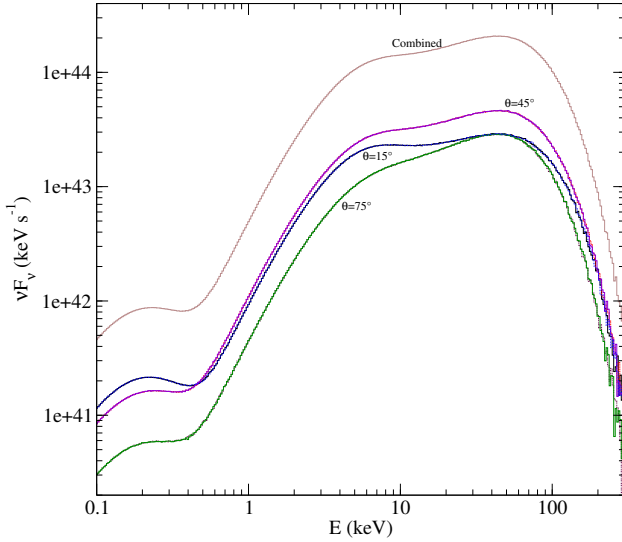


Figure 6.8: Evidence of hardening of spectra with the observing angle. The seed photons are emitted from the NBOL and Keplerian disc and are Comptonized by CENBOL. Here, halo accretion rate \dot{m}_h is 0.5 and disc accretion rate is \dot{m}_d is 0.1. Photons are binned according to the direction of observation. All the angles are measured w.r.t. the rotation axis (z-axis). The number beside each plot shows the corresponding average angle for each bin (in degrees). Taken from Bhattacharjee and Chakrabarti (2017).

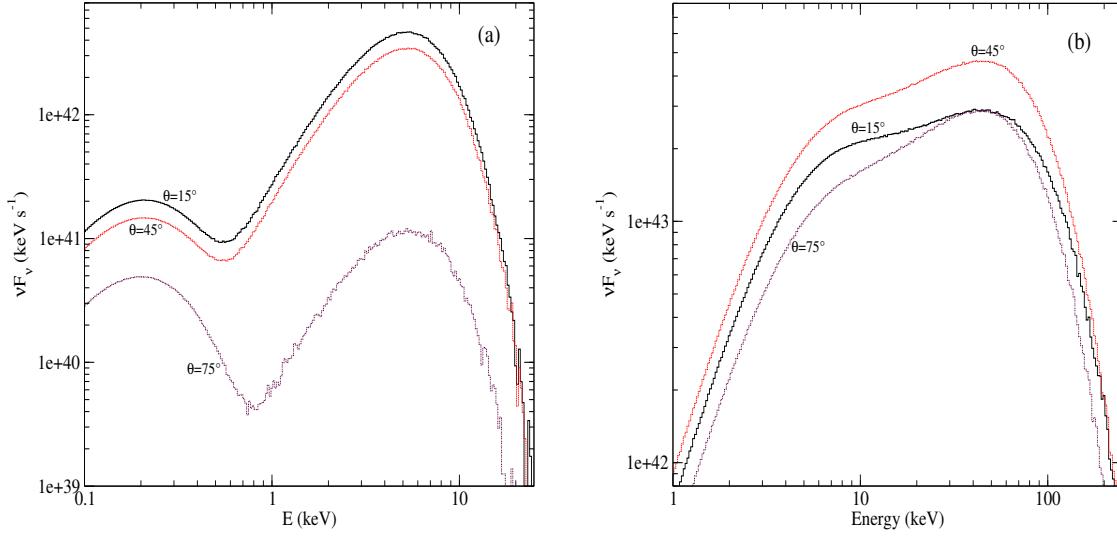


Figure 6.9: Evidence of hardening of spectra with the observing angle. The seed photons are emitted from the NBOL and Keplerian disc and are Comptonized by CENBOL. The flow parameters are for Case C3 of Table 6.1. The photons are binned according to the direction of observation. All the angles are measured w.r.t. the rotation axis (z -axis). The numbers beside each plot shows the corresponding average angle bins (in degrees). In (a), only the photons which escape without being scattered are binned. The angle dependency arises out of the injection direction and geometry of CENBOL. In (b), all the photons that underwent at least one scattering are clubbed together. Taken from Bhattacharjee and Chakrabarti (2017).

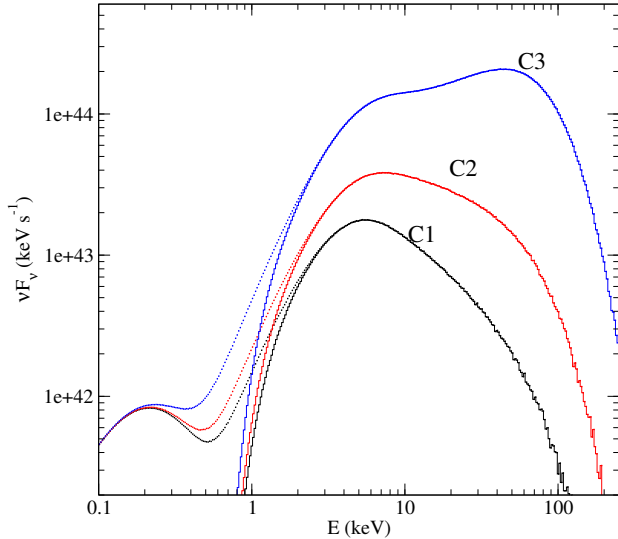


Figure 6.10: The variation of combined spectra from NBOL, KD and the Comptonized photons as \dot{m}_h is varied from 0.1, 0.2 and 0.5. Here, $\dot{m}_d = 0.1$ (Cases C1 to C3). The dotted lines show our computed spectra as are emitted from the disc while the solid lines show our spectra after absorption through ISM as they reach us. Here, we used photoelectric absorption due to hydrogen atoms, with $n_H = 4 \times 10^{22} \text{ cm}^{-2}$. The cases C1, C2 and C3 are shown in black, red and blue, respectively. Taken from Bhattacharjee and Chakrabarti (2017).

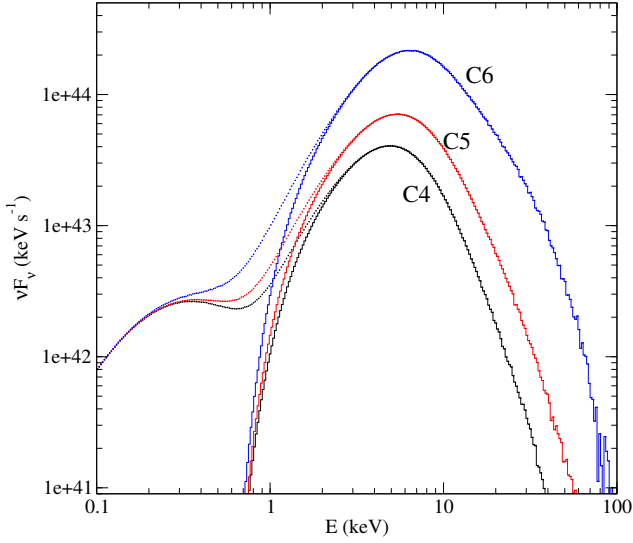


Figure 6.11: Variation of combined spectra from NBOL, KD and the Comptonized photons as \dot{m}_h is varied from 0.1, 0.2 and 0.5. Here, $\dot{m}_d = 0.2$. (Cases C4 to C6). Dotted lines show our computed spectra as are emitted from the disc while the solid lines show our spectra after absorption through ISM as they reach us. Here, we used photoelectric absorption due to hydrogen atoms, with $n_H = 4 \times 10^{22} \text{ cm}^{-2}$. The cases C4, C5 and C6 are shown in black, red and blue, respectively. Taken from Bhattacharjee and Chakrabarti (2017).

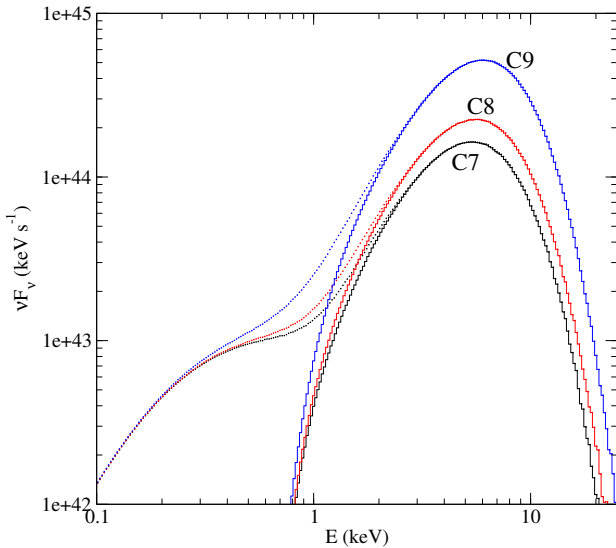


Figure 6.12: Variation of combined spectra from NBOL, KD and the Comptonized photons as \dot{m}_h is varied from 0.1, 0.2 and 0.5. Here, $\dot{m}_d = 0.5$. (Cases C7 to C9). Dotted lines show our computed spectra as are emitted from the disc while the solid lines show our spectra after absorption through ISM as they reach us. Here, we used photoelectric absorption due to hydrogen atoms, with $n_H = 4 \times 10^{22} \text{ cm}^{-2}$. The cases C7, C8 and C9 are shown in black, red and blue, respectively. Taken from Bhattacharjee and Chakrabarti (2017).

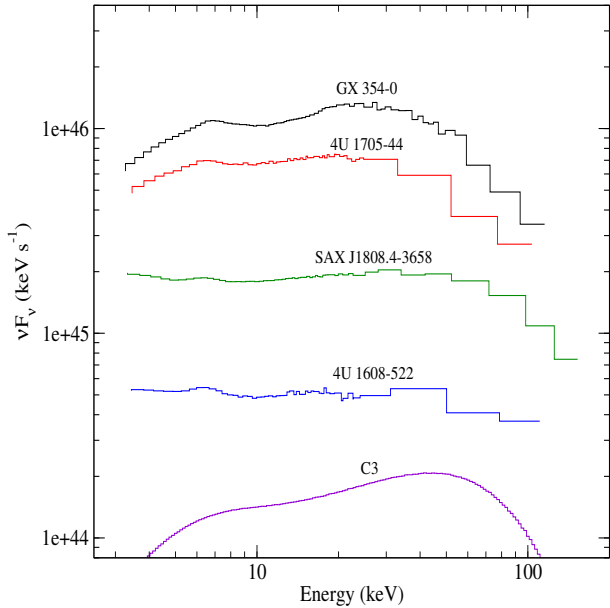


Figure 6.13: The spectra of a few weakly magnetized neutron stars, namely, 4U 1705-44, 4U 1608-522, SAX J1808.4-3658 and GX 354-0. For comparison, we put the spectrum of Case C3 (without the iron line emission) of our simulation to show that we generally reproduce the features. These observed spectra were obtained by RXTE observations and are adapted from Gilfanov (2010). Taken from Bhattacharjee and Chakrabarti (2017).

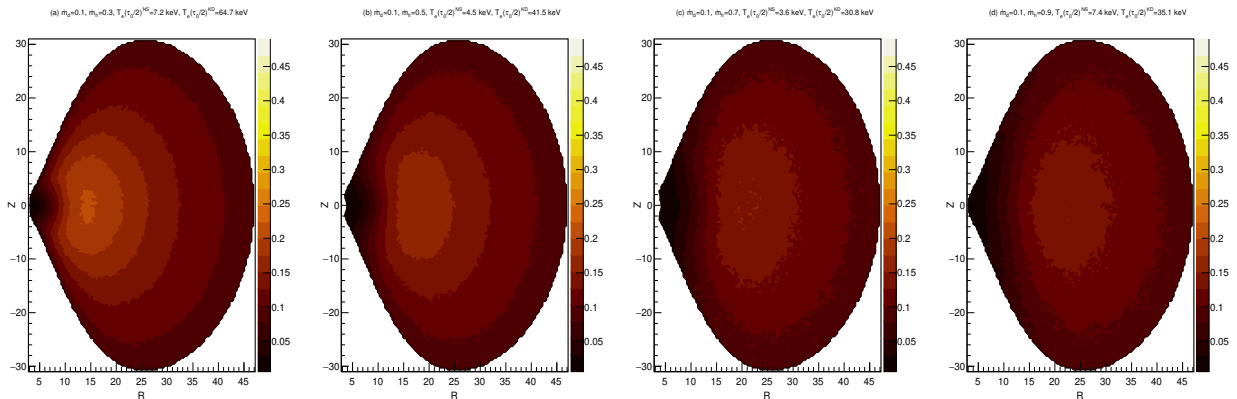


Figure 6.14: The temperature contours after Compton cooling, from the simulation (for initial $T_{CE} = 250.0 \text{ keV}$, $X_s = 46.8 r_S$). The temperatures are written in dimensionless unit (kT_e/mc^2). From left to right, the halo accretion rate is increased from 0.3 to 0.9. For (a) to (c), with the increase of \dot{m}_h , the temperature of CENBOL closer to NBOL, $T_e(\tau_0/2)^{NS}$ decreased from 7.2 keV to 3.6 keV. The temperature of CENBOL closer to disc, $T_e(\tau_0/2)^{KD}$, also decreased from 64.7 keV to 30.8 keV, but remain greater than the corresponding $T_e(\tau_0/2)^{NS}$. In the case (d), where the angle θ_* was $\pi/2$, a large fraction of blackbody photons escaped the system without scattering and hence the effect of cooling, although present, is less than the case (c). The modified contours show the effective region of Compton scattering and are similar to the proposed geometry of TSS14. Taken from Bhattacharjee and Chakrabarti (2017).

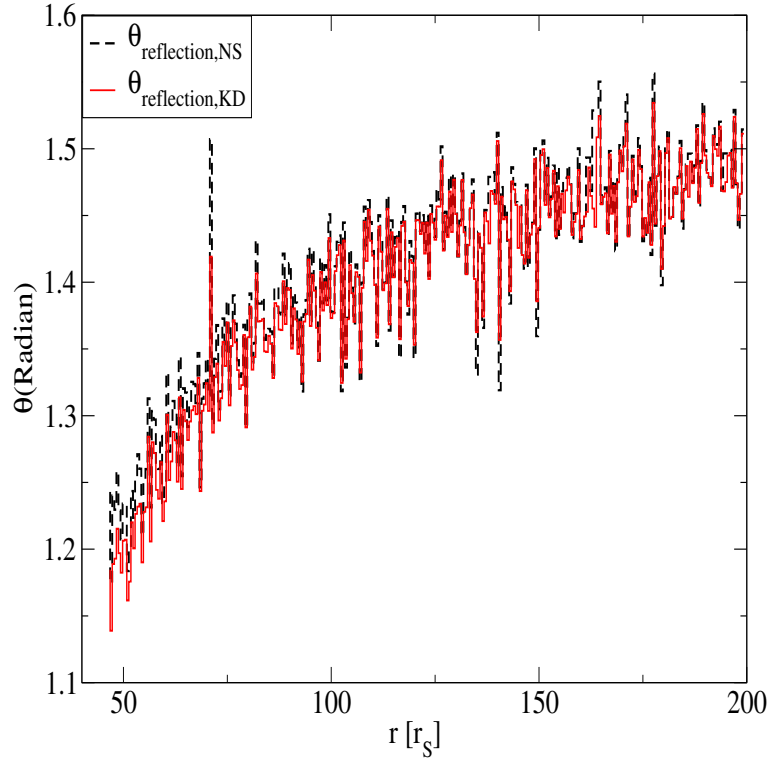


Figure 6.15: Variation of average angle of reemission of reflected flux with the radial distance. The scattering close to CENBOL can produce reflection along smaller value of θ , and the angle increases with distance on the disc. The value saturates towards $\pi/2$ for larger values of r . The photons that originated from NBOL (in black, dashed) and KD (in red, solid), show similar behaviour, which suggest that the scattering in CENBOL removes any history of their previous directions of injections.

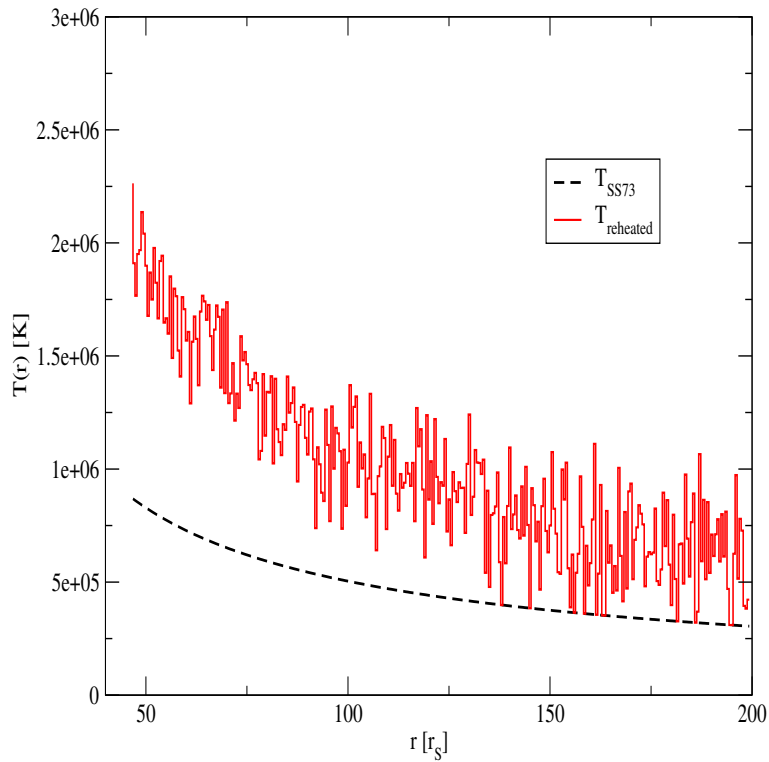


Figure 6.16: Variation of disc temperature (in K), before and after thermal reprocessing, due to the absorption of Comptonized photons. The temperature distribution of the disc changes differentially, based on the received photons, which depend on the distance from CENBOL. In the nearest region, reheating is strong enough to raise the disc temperature 2.5 times the initial SS73 temperature.

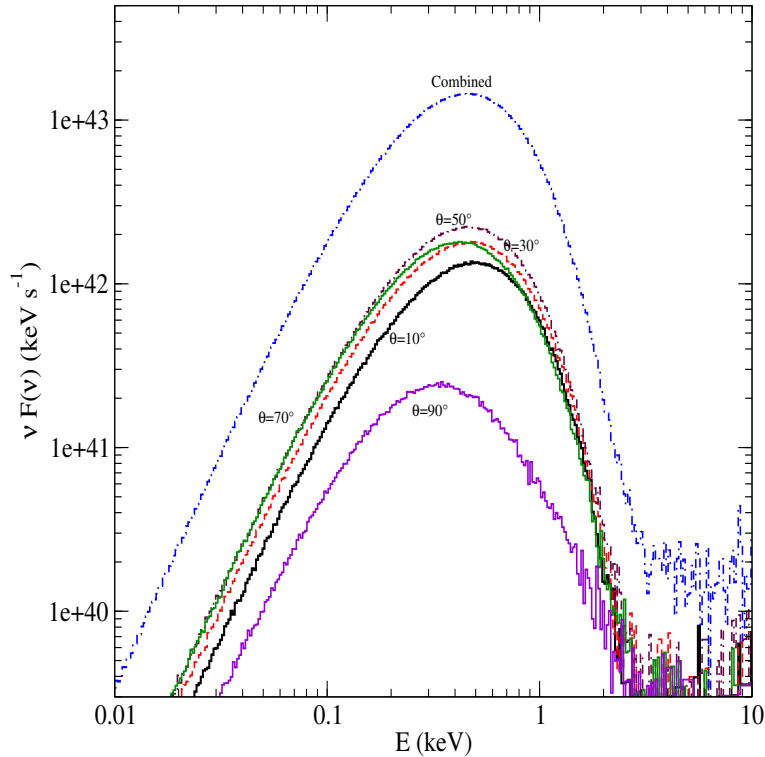


Figure 6.17: Variation of disc spectra with inclination angle θ , when thermal reprocessing is taken into account. The high inclination cases show relative hardening.

Discussions and Conclusions

In the literature, much studies have been done of the advective flows around black holes and their spectral properties. These solutions typically consist of two components, with a Keplerian disc flanked vertically by an advective component. Moreover, the inner part of the advective component forms a centrifugal barrier and the post-barrier region (CENBOL) was found to behave as the Compton cloud producing typically the power-law with exponential cut-off. CT95 has demonstrated that the spectrum changes from soft to hard as the relative importance of accretion rate of the Keplerian component vis-a-vis the accretion rate of the halo is decreased. Since the segregation of the advective flow into a Keplerian and sub-Keplerian components could take place very far out, there is no *a priori* reason why a neutron star accretion flow could not also comprise of the same two types of components, especially that very far away the flow has not knowledge of the nature of the compact object.

In the present Chapter, we used the successful paradigm of TCAF in the context of a weakly magnetized neutron star accretion flow. The flow properties were changed on the neutron star surface due to modification of the inner boundary condition and a blackbody emitting normal boundary layer (NBOL) is created on the neutron star surface, in addition to the CENBOL in TCAF. Due to the extra source of seed photons, the CENBOL became cooler easily and the spectra appeared to be softer for the same input flow parameters. The behaviour of CENBOL is similar to the Compton cloud invoked phenomenologically by Titarchuk et al. (TSS14). In our analysis, we restricted our studies within one Eddington rate. However, the general conclusion that the spectrum is hardened with the increase in halo accretion rate remains valid.

The resulting spectrum has several features arising out of the specific flux emission properties

of the normal boundary layer, namely, NBOL. The radiation dynamics of NBOL with Keplerian disc reveals (IS99) that the maximum flux emitted from the NBOL may not be really along the equatorial plane, but from an angle (θ_*). This, together with the fact a CENBOL intercepts more photons from the NBOL than the Keplerian component, produces double hump patterns in the spectra. Photons from NBOL are inverse Comptonized more efficiently and thus dictate the spectra to a greater extent. We also studied how the spectra would change with the observing angle and found that with increasing inclination angle, the spectra is indeed hardened, a result also valid for black hole accretion (GCL09; GGCL10). However, unlike a black hole accretion, in the present scenario, the radiation could be maximum at an intermediate viewing angle (e.g., ~ 45 in Fig. 4) and not necessarily along the polar axis.

The observed spectra from neutron star candidates, especially those which have weak magnetic fields, are found to have similar shapes as found in the present Chapter thus confirming the general idea that TCAF can be used in the spectral study of neutron stars as well. For instance, the hard spectra of case C3 (Fig. 6.10) are similar to those of several neutron stars (Gilfanov, 2009). Similar results have also been reported by Lin et al. in 2007. Thus the motivation of our exercise to check if the studies of the black hole and neutron star spectra could be carried out under a common framework is well justified.

Chakrabarti (1997) expanded CT95 work on TCAF to establish that the advective component of accretion (the sub-Keplerian halo) is essential to produce the hotter CENBOL. Otherwise, if the transition layer is produced solely from the Keplerian disc and its optical depth and temperature were calculated self-consistently, the Comptonization would be sufficient to cool it down. Otherwise, one can use the latter quantities as free parameters without explicit use of the second component as in Titarchuk et al. (2014) who reproduce the spectra very satisfactorily. In the present Chapter, we kept in mind the inter-relationship among the flow parameters and thus nine cases have been put in three main groups of increasing Keplerian accretion rate. Our NBOL cools the inner CENBOL rapidly. So in a way, the CENBOL behaves like the TL of TSS14.

It has been reported from observations that the photon index of COMPTB model for the νF_ν vs $h\nu$ spectra reaches a saturation value of $\Gamma \sim 2$, for the Comptonized spectra of a neutron star. The spectra from the disc's Comptonized components, however, show no such saturation in general. In ST11, ST12 the spectra was fitted with *Bbody* + *COMPTB* + *Gaussian*, where the Bbody was related to the disc emission. In STF13 two *COMPTB* + *Bbody* components were used, where both the photon indices show stability around the value 2. In TSF13 the cloud temperature was seen to vary from 2.9 keV to 21 keV without any significant change in spectral slope of COMPTB spectra due to NS, but the normalization decreased by a factor of eight. TSS14, STSS15 have shown the saturation of spectral index of COMPTB (for NS only) w.r.t the variation of the temperature of the Compton cloud. The second COMPTB component showed a two-phase behaviour: in HB-NB, the photon index was around 2, but in FB, the photon index decreased and had values $1.3 < \Gamma < 2$. It was stated that the spectrum at the FB is determined by high radiation pressure from the NS surface. Burke et al. (2017) also reported the constancy of Comptonization parameters, which reflects saturation of photon index at around $\Gamma \sim 2$. In all these cases, the illumination factor f , that controls the amount of Comptonization by the Compton cloud, underwent significant changes, which shows that the geometry or the size of the Compton cloud was changing with spectral states. In STS16, it was shown that the second COMPTB component (for the Comptonized spectra of the disc) showed variations around $\Gamma \sim 2$. Γ went below 2 when the disc temperature is reduced from 1.1 keV to 0.8 keV, implying an expansion of Compton cloud. A simultaneous increase of the cloud temperature (of the outer

part) was also observed. These phenomenological results can be very well understood by varying halo accretion rate which appears to be the key controlling factor here. With the increase of \dot{m}_h , more hot electrons are supplied, resulting in the expansion of CENBOL and spectral hardening (CT95, GGC14). We explore the variation of spectra with the halo accretion rate for such cases. The results are consistent with observed results.

The proposed geometry of the Compton cloud in TSS14, for the flaring branch shows a hotter outer TL and a cooler inner TL. When we consider the effects of cooling within the Monte Carlo simulation and modify the temperature of the CENBOL, a similar profile is obtained, as shown in Fig. 10(a-d). The peak of the distribution shifts towards the disc as accretion rate is increased, for a given initial set of temperature and shock location. The temperatures obtained by us are also consistent with the observed values as reported in TSS14 and STSS15.

Recently, the TCAF solution has been used to fit spectra of several black hole candidates and at the same time to extract physical flow properties and the mass of the compact object (Molla et al. 2017, 2016, Bhattacharjee et al. 2017 and references therein). In near future, we plan to extract physical flow parameters onto neutron stars as well. Similarly, we are also extending the time-dependent studies of TCAF flow with radiative transfer in order to understand real reason for the high and low-frequency quasi-periodic oscillations in neutron star systems. In a future work, we will compare the spectral fits using our model and fits obtained using COMPTB model.

Chapter 7

Simulation of Inviscid flows around NS which include Shock Waves

ABSTRACT

We carry out the first robust numerical simulation of accretion flows on a weakly magnetized neutron star using Smoothed Particle Hydrodynamics (SPH). Unlike the case of black holes where the lack of a hard surface allows matter to advect in supersonically, for neutron stars, however, the presence of a hard surface requires matter to be at rest on the surface, forcing the flow to be subsonic. Though this is the only fundamental difference between the two cases, this has profound effects on the spectral and timing properties on the respective flows. In presence of Keplerian and sub-Keplerian matter, as in Two Component Advective Flow (TCAF) paradigm, the Keplerian disc will behave in the same way as a normal standard disc, while the low viscosity sub-Keplerian flow will additionally create a normal boundary layer (or, NBOL) right on the star surface other than the centrifugal pressure supported boundary layer (or, CENBOL) as is also present in a black hole accretion. Both of these density jumps could give rise to standing or oscillating shock fronts. During a hard spectral state, the incoming flow has a negligible viscosity causing more sub-Keplerian component as compared to the Keplerian disc component. We show that our simulation of flows with a cooling and a negligible viscosity produces precisely two shocks and a strong supersonic wind from these boundary layers. We find that the specific angular momentum of matter dictates the locations and the nature of oscillations of these shocks. For low angular momentum flows, the radial oscillation appears to be preferred. For flows with higher angular momentum, the vertical oscillation appears to become dominant. In all the cases, asymmetries w.r.t. the $Z=0$ plane are seen and instabilities set in due to the interaction of inflow and outgoing strong winds. Our results capture both the low and high-frequency quasi-periodic oscillations observed in the power density spectra without invoking magnetic fields or any precession mechanism. Most importantly, these solutions directly corroborate observed features of the wind dominated high-mass X-ray binaries, such as Cir X-1. These results are reported in Bhattacharjee and Chakrabarti (2019). Figures 7.3-7.6 have been taken from that paper.

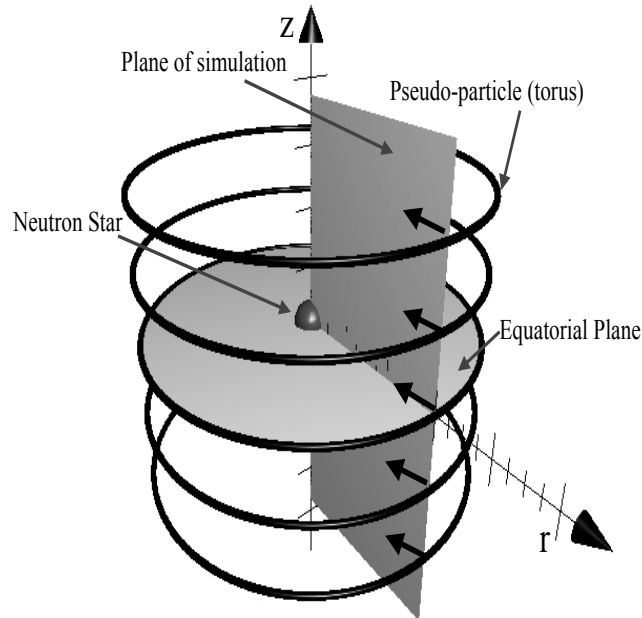


Figure 7.1: A schematic of the simulation setup for the SPH code. The tori represent the toroidal pseudo-particles, being injected into the axisymmetric system (depicted by the plane of simulation), around the neutron star.

Method

The Smoothed Particle Hydrodynamics (SPH) method was introduced by Monaghan in 1992. It has since been used in many astrophysical systems, including the simulation of accreting matter around black holes to simulate accretion in 1D (Chakrabarti & Molteni 1993, hereafter CM93); 2D flows (Molteni, Lanzafame & Chakrabarti 1994, hereafter MLC94); viscous Keplerian discs (Chakrabarti & Molteni 1995, hereafter CM95); resonance oscillation of shocks due to cooling in 2D (MSC96); comparative study of shocked advective flows using SPH and TVD schemes (Molteni, Ryu & Chakrabarti 1996, hereafter MRC96); thick accretion discs (Lanzafame, Molteni & Chakrabarti 1998, hereafter LMC98); bending instability of an accretion disc (Molteni et al. 2001a, hereafter M01a; Molteni et al. 2001b, hereafter M01b); interaction of accretion shocks with winds (Acharyya, Chakrabarti & Molteni 2002, hereafter ACM02); and effect of cooling on the time dependent behavior of accretion flows (Chakrabarti, Acharyya & Molteni 2004, hereafter CAM04).

We base our studies of accretion onto neutron star mostly on MSC96, though we modify the SPH algorithm to suit our need to handle both hot and cold particles in the code.

Model Equations

We consider a rotating, axisymmetric, inviscid flow around a neutron star (see Fig 7.1, for the schematic of setup). We consider the magnetic field to be negligible and ignore its effects completely. The gravitational force due to the compact object was modelled using the pseudo-Newtonian potential of Paczynski and Wiita (1980). The matter density (ρ), isotropic pressure (P) and the internal energy (e) of the flow are related to each other through $P = \rho e(\gamma - 1)$. The adiabatic index $\gamma = 4/3$, is kept constant throughout our simulations. We used a single-temperature model for the electrons and protons. The specific angular momentum λ is varied from case to case but it is constant everywhere in a simulation setup, as the flow is purely inviscid. Furthermore, the SPH code uses toroidal particles and thus it strictly preserves λ . The hydrodynamic code uses dimensionless quantities for computation. However, the cooling mechanisms require physical units (cgs is used here). For that purpose, all the relevant quantities are non-dimensionalized using their corresponding reference values. We use density of injected particles of the flow at the outer edge $\rho_{ref} = \rho_0$, the speed of light $v_{ref} = c$, and the Schwarzschild radius $x_{ref} = r_S = 2GM_{NS}/c^2$ of the neutron star mass M_{NS} , as the reference density, velocity, and distance, respectively. From that we can derive the units of time $t_{ref} = x_{ref}/v_{ref} = r_S/c$, specific angular momentum $\lambda_{ref} = x_{ref}v_{ref} = cr_S$, mass $M_{ref} = \rho_{ref}x_{ref}^3 = \rho_{ref}r_S^3$, and mass accretion rate $\dot{M}_{ref} = \rho_{ref}x_{ref}^3/t_{ref} = \rho_{ref}r_S^3c$.

We are providing the Lagrangian formulae for the two-dimensional fluid dynamics equations for Smoothed Particle Hydrodynamics (SPH) in cylindrical coordinates, below.

The conservation of mass is given as (LMC98)

$$\frac{D\rho}{Dt} = -\rho\vec{\nabla} \cdot \vec{v} \quad (7.1)$$

(here, D/Dt is the comoving derivative).

The conservation of momentum is given by (LMC98, dropping the viscous terms from Eq. 2)

$$\frac{D\vec{v}}{Dt} = -\frac{1}{\rho}\vec{\nabla}P + \vec{g} + \frac{\lambda^2}{r^3}\hat{r} \quad (7.2)$$

where, \hat{r} is the radial direction vector and

$$\vec{g} = -\frac{1-\mathcal{C}}{2(R-1)^2}\frac{\vec{R}}{R}, \quad (7.3)$$

$$g_r = -\frac{1-\mathcal{C}}{2(R-1)^2}\frac{r}{R}, \quad (7.4)$$

$$g_z = -\frac{1-\mathcal{C}}{2(R-1)^2}\frac{z}{R}. \quad (7.5)$$

Here, $\vec{R} = r\hat{r} + z\hat{z}$, $R = \sqrt{r^2 + z^2}$, and \mathcal{C} is the radiative pressure term arising out of the blackbody emission from the surface of the star. We have assumed the term to be isotropic for our simulations.

To achieve a better accuracy, we use a form of energy conservation where the sum of kinetic and thermal energies are used instead of only thermal energy (Monaghan 1985). Then, the energy conservation can be written as (following Eq. 9c of MSC96 and Eq. 11 of LMC98)

$$\frac{D}{Dt} \left(e + \frac{1}{2} \vec{v}^2 \right) = -\frac{P}{\rho} \vec{\nabla} \cdot \vec{v} + \vec{v} \cdot \left(\frac{D\vec{v}}{Dt} \right) - \zeta_{1/2} \rho e^\alpha \quad (7.6)$$

Here, $\zeta_{1/2}$ is the non-dimensional bremsstrahlung loss coefficient, as defined in MSC96,

$$\zeta_{1/2} = \frac{j \rho_{ref} x_{ref} T_{ref}^{1/2}}{c^3 m_p^2} \quad (7.7)$$

and

$$T_{ref} = \frac{c^2 m_p \mu (\gamma - 1)}{k} \quad (7.8)$$

where $\mu = 0.5$ and $j = 1.4 \times 10^{-27}$ cgs unit for ionized hydrogen (Allen 1973), m_p is the mass of the proton, and k is the Boltzmann constant. The subscript 1/2 to ζ signifies the use of a cooling law $\Lambda = \zeta_{1/2} \rho^2 e^\alpha$ with a constant $\zeta_{1/2}$ which is identical to the bremsstrahlung case ($\alpha = 0.5$).

SPH: Implementation of the cooling law

We use the method described in detail by MSC96, while making changes to match the notations used so far. We have assumed the flow to be axisymmetric and thus, all the equations are written for cylindrical geometry. The interpolating kernel W which is a function of cylindrical radial coordinate \vec{R} and k th particle of mass m_k as (MSC96)

$$m_k = 2\pi \rho_k r_k \Delta \vec{R}_k. \quad (7.9)$$

Any smooth function $A(\vec{R}_i)$ at position \vec{R}_i can be defined as (MSC96),

$$\begin{aligned} A(\vec{R}_i) &= \int A(\vec{R}) W(\vec{R} - \vec{R}_i; h) \frac{2\pi \rho r}{2\pi \rho r} d\vec{R}_k \\ &\approx \sum_k \frac{m_k}{2\pi \rho_k r_k} A(\vec{R}_k) W(\vec{R}_k - \vec{R}_i; h), \end{aligned} \quad (7.10)$$

where h is the particle size. This simplifies the expression of the conservation laws and quantities that can be computed easily. As an example, the density at position can be simplified to

$$\rho(\vec{R}_i) \approx \sum_k \frac{m_k}{r_k} W(\vec{R}_k - \vec{R}_i; h), \quad (7.11)$$

which satisfies the continuity equation in cylindrical coordinates (MSC96).

The equations of motion to be solved using SPH reduces to three separate ones. The radial component of momentum equation,

$$\left(\frac{Dv_r}{Dt} \right)_i = \sum_k \frac{m_k}{r_k} \left(\frac{P_i}{\rho_i^2} + \frac{P_k}{\rho_k^2} + \Pi_{ik} \right) \frac{\partial W_{ik}}{\partial r_i} + \frac{\lambda^2}{r_i^3} - \frac{1 - \mathcal{C}}{2(R_i - 1)^2} \frac{r_i}{R_i}, \quad (7.12)$$

the vertical component of the momentum equation,

$$\left(\frac{Dv_z}{Dt} \right)_i = \sum_k \frac{m_k}{r_k} \left(\frac{P_i}{\rho_i^2} + \frac{P_k}{\rho_k^2} + \Pi_{ik} \right) \frac{\partial W_{ik}}{\partial z_i} - \frac{1 - \mathcal{C}}{2(R_i - 1)^2} \frac{z_i}{R_i}, \quad (7.13)$$



Figure 7.2: A flowchart of the Smoothed Particle Hydrodynamics code used for time-dependent simulations around neutron stars. Here, α_{vis} and α_{cool} are the α -viscosity and cooling (power-law) index, respectively. In this Chapter, $\alpha_{vis} = 0$. $\Delta_{i,j}$ is the separation between the i th and j th particle, and $\Delta_{crit} = 0.1h$, is the critical separation, below which particles were merged. t_{run} is the runtime of simulation, and Δt is the time-step of evolution. $v_0, a_0, \rho, \lambda_{inj}$, are the injected values of velocity, sound speed, density and specific angular momentum, respectively, at the equatorial plane [following Hybrid Model by Chakrabarti (1989; 1990)].

and the specific energy equation which can be written as,

$$\left(\frac{D(e + \bar{v}^2/2)}{Dt}\right)_i = \sum_k \frac{m_k}{r_k} \left(\frac{P_i}{\rho_i^2} + \frac{P_k}{\rho_k^2} + \Pi_{ik}\right) - \frac{\Lambda_i}{\rho_i} + \vec{v}_i \cdot \left(\frac{D\vec{v}}{Dt}\right)_i. \quad (7.14)$$

where, $\Lambda_i = \zeta_{1/2} \rho_i^2 (e_i)^\alpha$ is the cooling term.

The kinematic dissipation is mimicked using artificial viscosities (MSC96),

$$\begin{aligned} \Pi_{ij} &= \frac{\alpha_v \mu_{ij} \bar{c}_{ij} + \beta \mu_{ij}^2}{\bar{\rho}_{ij}}, \\ \mu_{ij} &= \frac{r_i v_{ri} - r_j v_{rj}}{r_i (l_{ij}^2 + \eta_{ij}^2)} + \frac{(v_{zi} - v_{zj})(z_i - z_j)}{(l_{ij}^2 + \eta_{ij}^2)}, \\ l_{ij}^2 &= (r_i - r_j)^2 + (z_i - z_j)^2, \quad \eta_{ij} = \eta = 0.1h^2. \end{aligned}$$

where, α_v and β are the artificial viscosity coefficients.

The Equations (7.12-7.14) have been adopted from MSC96 and LMC98, with the introduction of the term \mathcal{C} . It is to be noted that the kinematic viscosity modifies the energy significantly but does not modify the angular momentum beyond 0.05% of the initial value. Thus, our simulations are effectively reproducing the flow with almost constant angular momentum. The abbreviations for density $\bar{\rho}_{ij}$ and sound speed \bar{a}_{ij} are taken from Monaghan (1992):

$$\bar{\rho}_{ij} = \frac{\rho_i + \rho_j}{2}, \quad \bar{a}_{ij} = \frac{a_i + a_j}{2}.$$

Conservation of angular momentum

We have used the following equation (LMC98 and MSC96) for the conservation of angular momentum,

$$\left(\frac{Dv_\phi}{Dt}\right)_i = -\left(\frac{v_\phi v_r}{r}\right)_i + \frac{1}{\rho_i} \left[\frac{1}{r^2} \frac{\partial}{\partial r} (r^3 \mu_{ij} \frac{\partial}{\partial r} \left(\frac{v_\phi}{r}\right)) \right]_i, \quad (7.15)$$

where, μ_{ij} is the kinematic viscosity. The terms α_v and β control the amount of μ_{ij} necessary to reduce oscillations in shock transitions. However, the *2nd term* \ll *1st term* on the right hand side and made no significant contribution. We determined the value of $\lambda_i = r_i (v_\phi)_i$ for each particle and use in the Equation 7.12. It was observed that for all the cases we have tried, the determined angular momentum was almost constant and equal to the injected values up to an error of 0.05%. The average value over all particles deviated even less from the injected value, e.g. for C1 $\lambda_{avg} = 1.800001$, matching the injected value up to 5 decimal places. This numerical error is due to the fluctuation of the values of $(v_\phi)_i$ and $(v_r)_i$. Thus the obtained values of λ_i are effectively equal to the λ of the injected particles, which is obtained as a natural consequence of the conservation of angular momentum throughout the flow. As the flow is always sub-Keplerian, even at the surface of the star, it can continue to the inner boundary. A part of the flow is absorbed into the star beyond $R = R_{NS}$ where the rotational velocity matches with that of the star and the surplus rotational kinetic energy is released through $\Delta\mathcal{E}(t)$ (see Boundary Conditions). As an example, the rate of transport of angular momentum onto the star for C1, i.e. the spin-up torque $N \approx \dot{M}_{accer} \lambda$ was such that the spin-up rate $\dot{\nu} = N/2\pi I$ was roughly around $5 \times 10^{-14} \text{ Hz s}^{-1}$, where, the moment of inertia $I \approx 0.4 M_{NS} R_{NS}^2$. Thus any change of the spin of the star due to this feedback effect can be safely ignored for the purpose of calculations for the runtimes we have chosen.

Boundary Conditions

For our simulations, the pseudo-particles (or just ‘particles’ used in the text) are injected from $r_{inj} = 30r_S$ with the same specific energy and specific angular momentum. The flow is assumed to be in vertical equilibrium when injected. The particles are tracked as long as they are within $r < r_{inj}$ and $R < R_{out}$, where, $R_{out} = 35r_S$. The choice of R_{out} was made so as to minimize the computational time taken to track isolated particles moving far away from the inflow region. We have also checked our simulations for a rectangular simulation box, but no significant changes were observed. For *C1*, injection velocity at equatorial plane with $v = 0.1202$ and sound speed $a = 0.0586$ was done which are appropriate for the transonic branch. Similarly, for cases *C2* to *C5*, to ensure injection with the same total energy and Mach number, we had to choose $v = 0.1211$ and $a = 0.0590$. In order to implement a reflection boundary condition at the inner boundary of $R_i < R_{NS} + h$ we used a reflective condition for the velocity component v_R . A no-slip condition is used for the azimuthal component where the v_ϕ of the flow is matched with the angular velocity of the star ($\omega_{NS}R_{ns}$) at the surface. For our calculations, $\omega_{NS} = 142Hz$. For the v_θ component, a sliding or slipping boundary condition is used, where the flow maintains its v_θ value at the surface. Along with the cooling criteria, these conditions allow matter to settle down on the surface of the star and also allow meridional motion from the equatorial region towards the poles (and vice-versa). However, if the flow reaches $R_i = R_{NS}$, it is immediately absorbed and all the thermal and kinetic energy of the particle is assumed to be released as a blackbody radiation. In the present simulations we did not study the secondary emission due to Comptonization of seed photons which could be originated from bremsstrahlung or blackbody radiation. We, however, included the effects of radiation pressure on the hydrodynamics through the quantity \mathcal{C} . We report the cases where the temperature is self-consistently modified by taking into account additional flux arising out of energy of the accreted particles. The initial surface temperature T_{NS}^0 of the neutron star was kept constant for all cases (*C1* to *C5*) at $T_{NS}^0 = 0.0 \text{ keV}$. The term \mathcal{C} is controlled by the total energy dumped by the particles at the surface of the star ($\Delta\mathcal{E}$) and it given by,

$$\mathcal{C}(t) = \frac{T_{NS}^4(t)\sigma_{bb}R_{NS}^2m_p}{c\sigma_T}, \text{ where } T_{NS}(t) = \left((T_{NS}^0)^4 + \frac{\Delta\mathcal{E}(t)}{\sigma_{bb}4\pi R_{NS}^2 dt} \right)^{0.25}. \quad (7.16)$$

Here, σ_{bb} is the Stefan-Boltzmann constant, m_p is the mass of proton, σ_T is the Thompson scattering cross-section.

Coalescing of Particles

One of the major issues with the previous version of the code was that it did not dynamically evolve when the particles came very close to each other ($R_{ij} < h$) and the corresponding timescale became very small. This problem is even more acute in our case as particles tend to aggregate at the surface of the star. In the original code, within 150 time steps the value of $dt < 0.0002$ and effectively stopped the evolution. A simple absorption condition at the boundary did not solve the problem as the aggregates grew beyond the surface’s immediate vicinity. To circumvent this, we implemented a 2-particle coalescing scheme (adopted from Vacondio et al. 2013) when the inter-particle distance $R_{ij} < 0.1h$.

After each time step, we check for neighbours using a *linked – list* algorithm. The neighbour list of a particle i is then searched for all such neighbours j , for which $R_{ij} < 0.1h$. The minimum of such R_{ij} values and the corresponding (i, j) pair is selected. If such pairs are found, a list of such pairs is made and the following scheme is applied to coalesce particle-pairs (i, j) .

Table 7.1: Parameters for the simulations and centroid frequencies (in Hz) found in the PDS of bremsstrahlung loss. Taken from Bhattacharjee and Chakrabarti (2019).

| ID | \dot{m}_h (\dot{M}_{EDD}) | λ (r_{Sc}) | R_{NS} (r_S) | α | ν_{LF1}, Q_{LF1} | ν_{LF2}, Q_{LF2} | ν_{hHz}, Q_{hHz} | ν_l, Q_l | ν_u, Q_u |
|----|---------------------------------|------------------------|--------------------|----------|----------------------|----------------------|----------------------|--------------|--------------|
| C1 | 0.094 | 1.8 | 3.0 | 0.5 | - | - | 128.88, 17.82 | 213.31, 3.17 | - |
| C2 | 0.094 | 1.7 | 3.0 | 0.5 | - | - | 102.22, 3.91 | 425.40, 5.61 | 633.78, 1.77 |
| C3 | 0.188 | 1.7 | 3.0 | 0.5 | - | - | 115.55, 5.02 | 486.08, 2.49 | 742.73, 1.48 |
| C4 | 0.094 | 1.7 | 3.0 | 0.6 | 41.62, 1.30 | 94.41, 4.66 | 137.58, 5.78 | 434.97, 4.96 | 599.23, 3.51 |
| C5 | 0.094 | 1.7 | 4.0 | 0.5 | 36.36, 2.91 | 77.55, 3.14 | 196.11, 18.06 | 465.70, 5.11 | 654.67, 3.51 |

To conserve the total mass:

$$m_k = m_i + m_j, k = \min(i, j). \quad (7.17)$$

We preserve the total momenta, by using:

$$\vec{v}_k = \frac{m_i \vec{v}_i + m_j \vec{v}_j}{m_i + m_j}. \quad (7.18)$$

We also preserve the total thermal energy, by using:

$$e_k = \frac{m_i e_i + m_j e_j}{m_i + m_j}. \quad (7.19)$$

The new location of the particle is determined by,

$$\vec{R}_k = \frac{m_i \vec{R}_i + m_j \vec{R}_j}{m_i + m_j}. \quad (7.20)$$

After going through the list of all such pairs, a standard re-indexing is done for all the particles still left in the system. As a result, the average number of particles present in the simulation stayed between ~ 14000 and ~ 16000 for $C1$ and between ~ 11500 and ~ 13000 for $C2 - C5$.

Timing Analysis

We computed the total emitted energy due to bremsstrahlung $\mathcal{E}(t)$ by integrating the emission per unit mass (Λ_i/ρ_i) over the particles existing in the simulation (n),

$$\mathcal{E}(t) = \sum_{i=1}^{i=n} \Lambda_i m_i / \rho_i. \quad (7.21)$$

As a consequence the densest and hottest regions contributed more to the time variation of the bremsstrahlung loss. In order to probe the hydrodynamic characteristics of CENBOL and NBOL, the emitted energy was plotted against time to generate the lightcurve. To extract periodic features, we used NASA's FTOOLS package to create the fast Fourier transformed Power Density Spectra (PDS) from the lightcurves. Data was gathered after every 10^{-5} s to generate the lightcurve. We used POWSPEC command, with a rebinning factor of -1.05 for all the cases to generate the PDS. Any oscillatory signature (such as a Quasi Periodic Oscillation or a peaked

noise) is reflected as a peak in the PDS. We report only those 5 cases (see, Table 7.1.) where significant variations of QPOs are observed. To avoid the effects of the transient phase, we only used data collected from 0.05 s to 0.3286 s . A Lorentzian profile is used to fit a QPO in the PDS. We determined the centroid frequencies, full-width half maxima and rms power up to 90% confidence level. While fitting the QPOs with Lorentzians, we only fitted the fundamental frequency of a type of QPO, when the harmonic is overlapping with another fundamental frequency. In case of such an overlap we take the best statistical fit (one peak or a mean position as the case demanded). When no such overlap occurs, and the harmonic feature is significant, the corresponding Lorentzian is fitted (Table 7.1).

Results

We studied multiple cases (see, Table 7.1) by varying the specific angular momentum (λ), radius of the star (R_{NS}), accretion rate (\dot{m} , alternatively used as the halo accretion rate \dot{m}_h), cooling index (α), one at a time, to study the effects in accretion and outflow.

We first discuss a typical scenario in detail to highlight the hydrodynamical aspects of the flow.

Case C1: In order to demonstrate the hydrodynamic properties, we first focus on case C1. The initial simulation parameters are mentioned in the Table 7.1. The simulation was run for 32860 time steps ($t = 0.3286s$), which is equivalent to 200 dynamical time steps at $30 r_S$. The cooling process was switched on after ($t \sim 0.0083s$). The system settled into a steadily oscillating state after a brief transient phase (up to $t \sim 0.0500s$). Indeed, the temperature of NBOL was found to fluctuate around 0.15keV even though initially its value was chosen to be $\sim 0.0keV$. Fig. 7.3(a) shows the variation of NBOL temperature during our simulation. This would induce fluctuations of the NBOL height as well. Details of the behaviour of NBOL is kept out of the current Chapter and some part of it has been discussed in the next Chapter. In this case, we studied PDS of the mass outflow through the upper quadrant. The hHz frequency corresponding to vertical oscillation was found at $\nu_{hHz} = 127.22 Hz$, with a harmonic at $\nu_{hHz} = 254.40 Hz$. For black holes, Molteni et al. 2001 found such oscillations due to bending instabilities in the flow. When scaled for the mass of the neutron star (here, assumed to be $M_{NS} = 1.0M_{\odot}$ for computational purposes), the frequency range comes out as 20-300 Hz. Thus, we can clearly identify the oscillations in the lightcurve as well as the mass outflow due to such instabilities, which is also reflected in Fig. 7.4(c-d).

In Fig. 7.3(b), the velocity in $r-z$ plane is plotted for all the particles. The Mach Numbers are shown in the colour gradient. Multiple turbulent cells are seen to be formed due to the interaction of wind and accreting matter. The formation of outflow, in both upper and lower quadrants, from the post-shock region of CENBOL is also captured. In the lower quadrant, a portion of the outflow falls back on to the inflow after failing to reach escape velocity.

In Fig. 7.3(c), the variation of the rate of transfer of angular momentum (N , see sect. 3.3) with time is plotted for accretion (black) and outflows (red). Given the specific angular momentum of the flow remains almost constant, the variation of the transfer rate with time depends on the mass flow rate in accretion and outflow, respectively. As the flow is always sub-Keplerian, the solution allows the matter to fall onto the star and transfer the angular momentum on the surface of the star. However, the spin-up torque (N) plotted in Fig. 7.3(c) was such that it corresponded to a spin-up rate of $\sim 5.0 \times 10^{-14} Hz s^{-1}$. The value agrees well with observational results and predictions from other models (Bildsten 1998; Revnivtsev & Mereghetti, 2015; Sanna et al. 2017;

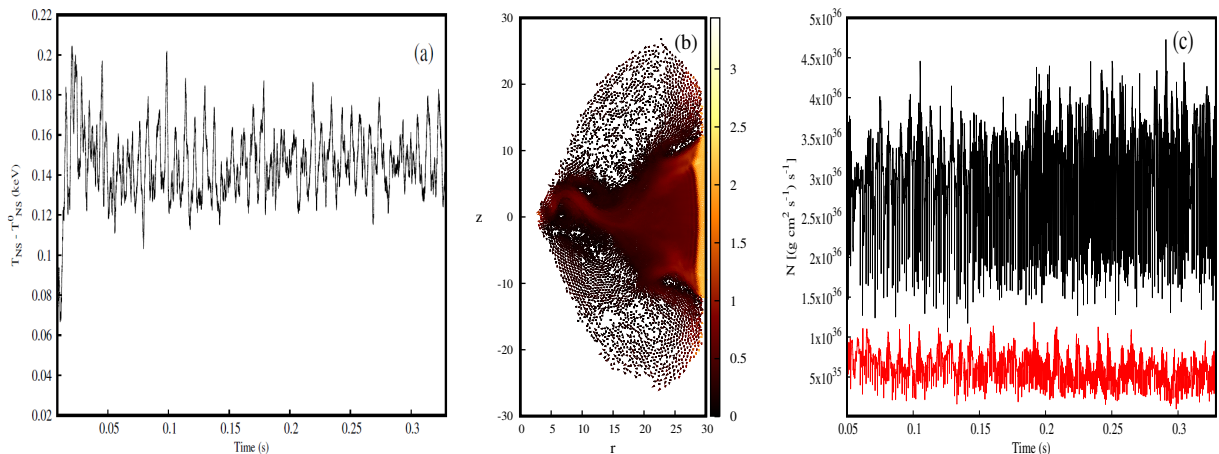


Figure 7.3: (a) The variation of T_{NS} with time (s), (b) the velocity vector $v_r \hat{r} + v_z \hat{z}$ (arrow heads) with the Mach number in the colour bar, for the flow configuration $C1$ at time $t = 0.2690s$, (c) variation of the rate of transfer of angular momenta (N) onto the surface of the star (black) and in the outflows (red) with time (s). Taken from Bhattacharjee and Chakrabarti (2019).

Bhattacharyya & Chakrabarty, 2017; Gügercinoglu & Alpar, 2017; Ertan 2018). The rest of the angular momentum is carried out by the outflows in both quadrants.

In Fig. 7.4(a), we show the density contours [$\log(\rho/\rho_0)$]. The temperature contours (logarithmic scale) are plotted in Fig. 7.4(b). The contours of constant Mach number for accreting matter, at time $t = 0.2690s$, is shown in Fig. 7.4(c). Fig. 7.4(d) shows the Mach number contours for the same case $C1$, at time $t = 0.2528s$. The flow puffs up after the centrifugal shock (CENBOL) and acts as the base of the outflowing matter. Matter nearest to the star are observed to be hottest and densest. A dense and hot outflow is seen to emerge from within the CENBOL region. The Mach number contours show that the flow has time-dependent asymmetric distribution about $z = 0$ plane. For $C1$, the high angular momentum creates the outer shock at around $26 r_S$ on the equatorial plane. The subsonic flow beyond the shock surface slowly becomes supersonic near the inner boundary of the star and finally settles on the surface through a strong shock. Notice that the Mach number contours near the edge of the star are supersonic and no subsonic contours are plotted. This is due to the fact that in the plotted case, the shock surface was very close to the boundary and the subsonic pseudo particles were absorbed at the surface, before being written out, within the code.

Case C2: When λ is reduced from 1.8 to 1.7, it reduces the asymmetry around $z = 0$ plane (Fig. 7.5a). The shock near the star becomes more prominent and the outflow profile changes. For $C1$, most of the outflow is generated from the immediate vicinity of the post-shock region of CENBOL. We plot the ratio of mass outflow to the mass accreted onto the star in unit time (denoted by $\dot{M}_{out}/\dot{M}_{accr} = M_{out}/M_{accr}$) for both $C1$ and $C2$ in Fig. 7.5(c). Apart from the initial higher values for $C1$, the ratio is comparable. However, the particle coalescing scheme merges the particles in higher density region, which reduces the number of particles in the simulation. The inset panel of Fig. 7.5(c) shows the same comparison in terms of the ratio of number of particles outflow to the number of accreted particles in unit time (denoted by $\dot{n}_{out}/\dot{n}_{accr} = n_{out}/n_{accr}$). The lower value for $C2$ further affirms the fact that bulk of the outflow is generated near the NBOL for $C2$. The outflow in Fig. 7.5(a) also undergoes a shock transition before becoming transonic again. In Fig. 7.6 (c), we plot the PDS of bremsstrahlung loss for the case $C3$. As λ

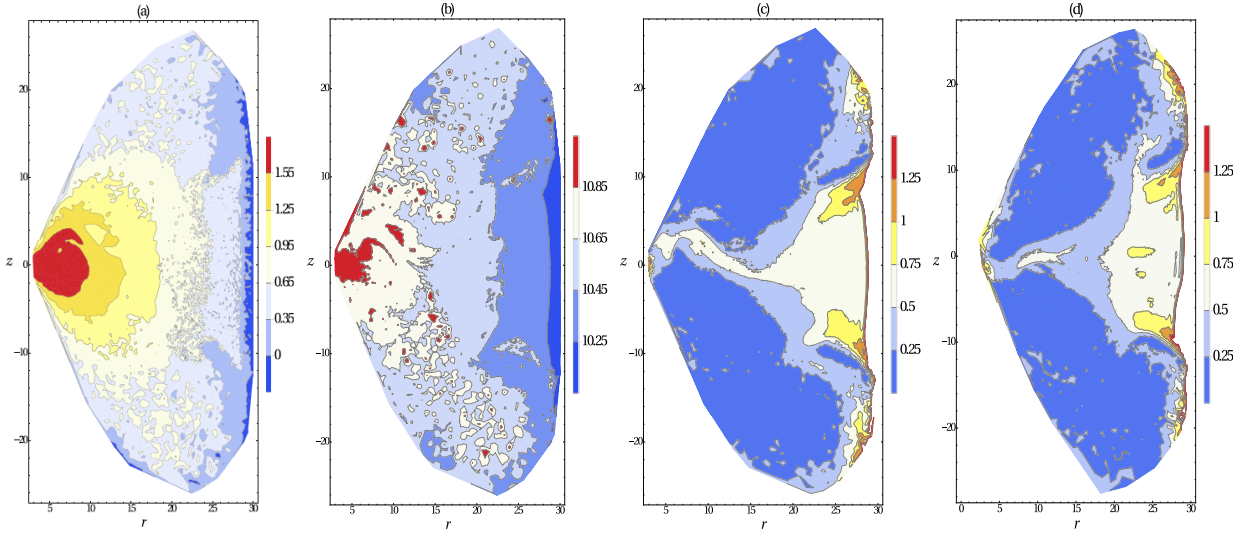


Figure 7.4: The flow configuration for the case *C1*: (a) $\log(\rho/\rho_0)$, (b) \log of temperature in K , (c) Mach number contours for accreting inviscid flow, at $t = 0.269s$ and (d) at $t = 0.2528s$. Both the density and temperature change by an order of magnitude in the inner part of CENBOL, as compared to the outer part. The flow configuration in (c) shows only the pre-shock region of the secondary shock (NBOL) at the boundary. However, in (d), we see that the shock has formed at $\sim 5 r_S$, and a shock in outflow forms at very close to the surface of the star. The outflow (in both (c) and (d)) becomes supersonic near the outer edge of the simulation boundary. Taken from Bhattacharjee and Chakrabarti (2019).

was decreased from 1.8 to 1.7, the centrifugal pressure dominated force is decreased. However, the flow was injected with the same total energy as that of case C1 which resulted in a higher radial velocity. This increases the ram pressure of the flow and prompts the resonance oscillation to take place at a smaller radius. The resulting oscillations are also seen to be dominated by the radial motion as compared to the vertical motion. The CENBOL moves closer to the star surface. The hecto-Hz QPO is still present and observed at $\nu_{hHz} = 102.22 Hz$. We also observe the twin kHz QPOs between $400 Hz$ and $700 Hz$. The centroid frequencies of the lower and upper kHz QPOs are at $\nu_l = 425.40 Hz$ and $\nu_u = 633.78 Hz$, respectively.

Case C3: In Fig. 7.6 (d), we plot the PDS of bremsstrahlung loss for C3. As \dot{m}_h was increased from 0.094 to 0.188, the effective radiative cooling due to the bremsstrahlung process is increased (higher ρ). The decrease in cooling timescale, prompts the resonance oscillation to take place at a smaller radius. This brings the NBOL closer to the surface. The hecto-Hz QPO is also observed at $\nu_{hHz} = 115.55 Hz$. Both the lower and upper kHz QPOs show an increase in centroid frequency (compared to C2) at $\nu_l = 486.08 Hz$ and $\nu_u = 742.73 Hz$, respectively.

Case C4: As α was increased from 0.5 to 0.6, the effective radiative cooling due to the bremsstrahlung process decreased (lower Λ). The increase in cooling timescale, prompts the resonance oscillation to take place at a larger radius. This pushes the NBOL away from the surface. The PDS of bremsstrahlung loss for the case C4 is shown in Fig. 7.6(e). The low-frequency QPOs are observed at $\nu_{LF1} = 41.62 Hz$ and at $\nu_{LF2} = 94.41 Hz$. The hecto-Hz QPO is also observed at $\nu_{hHz} = 137.58 Hz$. Both the lower and upper kHz QPOs are also observed at $\nu_l = 434.97 Hz$ and $\nu_u = 599.23 Hz$, respectively.

Case C5: In this case, as R_{NS} was increased from $3 r_S$ to $4 r_S$, the effective radiative pressure

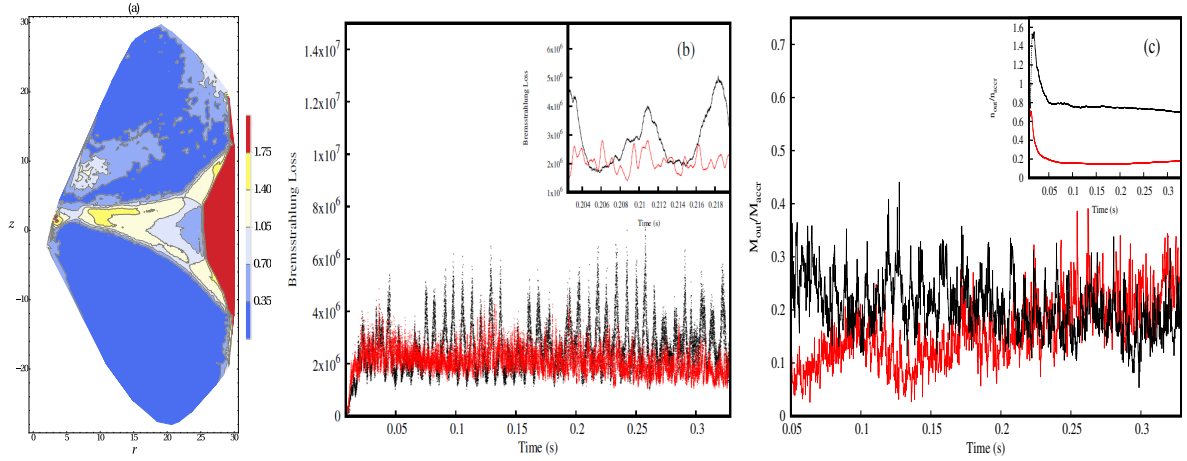


Figure 7.5: (a) Contours of constant Mach Number for the case $C2$, at time $t = 0.269s$. The outer shock forms closer to the star at ($\sim 25 r_S$). The inner shock is formed at $\sim 5 r_S$. The shock in outflow is diffused as compared to $C1$ and is formed between $\sim 10 - 15 r_S$. The outflow became transonic near the outer edge. In (b), we show the lightcurves of the total bremsstrahlung loss from the system for cases $C1$ (black) and $C2$ (red). Both the lightcurves show periodic behavior with distinctly different frequencies. In (c), the ratio M_{out}/M_{accr} ($= \dot{M}_{out}/\dot{M}_{accr}$) for both $C1$ (black) and $C2$ (red) is plotted. The inset of (c) shows the n_{out}/n_{accr} ratio ($= \dot{n}_{out}/\dot{n}_{accr}$), which shows more particles were coalesced near the NS boundary and the outflow generated from the regions closer to the NS surface had a low n_{out}/n_{accr} value despite having comparable M_{out}/M_{accr} . Taken from Bhattacharjee and Chakrabarti (2019).

due to the blackbody emission from the surface of the star decreased (lower \mathcal{C}). This aided the gravitational force in bringing both the shocks closer to the surface. The reduction of the outer edge of CENBOL increased the centroid frequency, above $10 Hz$, corresponding to the low-frequency QPO $\nu_{LF1} = 36.36 Hz$ and its harmonic $\nu_{LF2} = 77.55 Hz$, making them detectable (Fig. 7.6(f)). The hecto-Hz QPO is also observed at $\nu_{hHz} = 196.11 Hz$. Both the lower and upper kHz QPOs are also observed at $\nu_l = 465.70 Hz$ and $\nu_u = 654.67 Hz$, respectively.

Conclusions

In this Chapter, we have made an effort to understand the dynamics of an inviscid, rotating, geometrically thick and optically thin flow around a weakly magnetic neutron star using smoothed particle hydrodynamics. We add modified bremsstrahlung cooling so as to particularly study the timing properties of the centrifugally driven shocks (CENBOL) as well as the density jump (normal boundary layer or NBOL) formed on the star surface due to sudden arrest of matter. Such simulations were done for black holes earlier (MLC94, MSC96, MRC96, M01a, M01b, ACM02, CAM04, GC13, GGC14, Deb et al. 2017) and oscillations of the CENBOL were found in radial and vertical directions. These oscillations were then identified with the low frequency QPOs observed in black hole candidates.

In presence of a hard boundary on the neutron star surface, we expect another oscillation of higher frequency and well as others due to non-linear interactions of the flows. Our present simulations indeed show complex timing properties of the radiation as well as the flow dynamics. For this, we chose the flow to have an accretion rate (\dot{m}_h) below the Eddington limit for all the

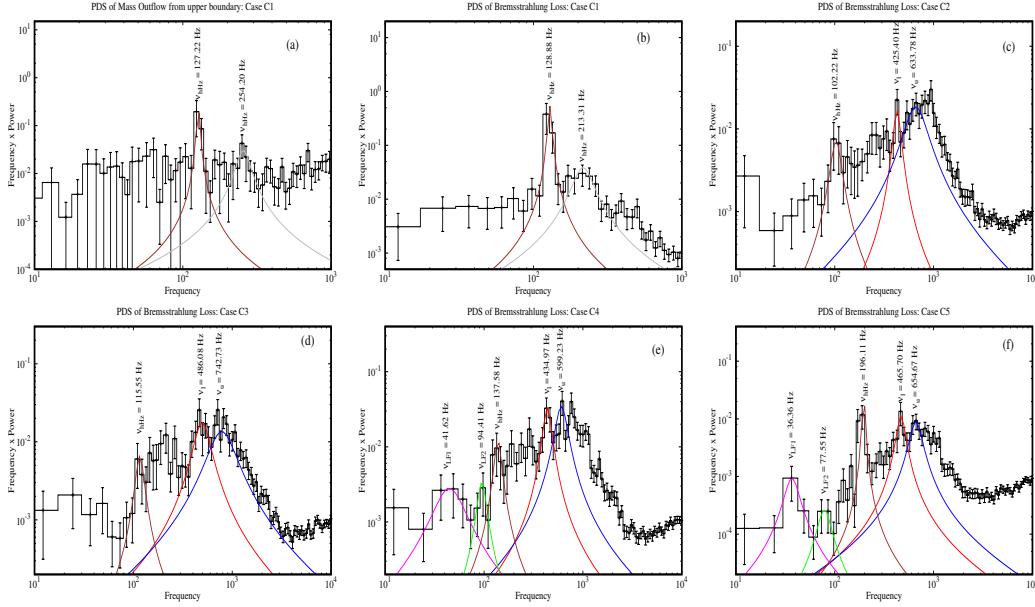


Figure 7.6: (a) Power Density Spectrum ($frequency \times Power$ vs $frequency$) of the mass outflow from upper quadrant of the simulation setup, for case C1. A clear QPO at ~ 127 Hz with a harmonic at ~ 254 Hz is observed. (b) A similar QPO feature at ~ 129 Hz was found in the corresponding lightcurve of the bremsstrahlung loss. (c) PDS of bremsstrahlung loss for C2, (d) for C3, (e) for C4 are also shown. The clear harmonics of the k Hz QPOs and the influences of those in the power spectra have been ignored while fitting separate peaks (b-e). In (f), for case C5, only the 2nd harmonic of ν_{LF} is shown. For that, five distinct peaks have been fitted with Lorentzian profiles, having centroid frequencies at 36.36 Hz (magenta, ν_{LF1}), 77.55 Hz (green, ν_{LF2}), 196.11 Hz (brown, ν_{hHz}), 465.70 Hz (red, ν_l), and 654.67 Hz (blue, ν_u) which are also plotted. Taken from Bhattacharjee and Chakrabarti (2019).

cases we studied. The cooling rate exponent α was varied from 0.5 (bremsstrahlung) to 0.6 to observe the effects of the strength of cooling on the oscillation of shocks. The specific angular momentum λ was chosen based on the recent study by Deb et al. (2017) where an onset of vertical oscillation was seen between the two values chosen here. The variation of the radius of the neutron star had a more complex effect as it controlled the influence of radiation pressure on the hydrodynamics through the parameter \mathcal{C} when a self-consistent variation is chosen. It is also to be noted that for the timescales of the simulations C1 to C5, the mass and momentum deposited on the star were negligible compared to the star's mass and spin. This accumulation of mass and momentum would become significant for timescales of the order of years or more, which is outside the purview of this paper. However, the energy release at the surface was found to be significant, resulting in a measurable change of T_{NS} .

We show, among other things, that the simulations produce both low and high-frequency QPOs and the oscillations last during the whole simulation period (more than 200 dynamical timescales measured at the injected flow radius, i.e., $30 r_S$). This suggests that the QPOs are formed due to a part of the flow dynamics and not a transient effect as inferred by Barret and Olive (2005). We measure the QPO frequencies and find that both the centroid frequency and Q factors match well with observed results of neutron stars such as GX17+2, 4U 1728-34 and Cir X-1. We believe that the advective flow suggested in the literature while explaining the behavior of the source Cir

X-1 (Boutloukos et al. 2006), is precisely our dynamic transonic solution. We showed that the presence of angular momentum itself can generate multiple modes of oscillation in CENBOL and NBOL, manifesting in QPOs in the PDS, in presence of cooling. In Fig. 7.3(b), 7.3(c-d), 7.3(a), we see different types of shocks are being formed. The outer shock was found to be vertical near the equatorial plane and oblique away from the plane, very similar to what was seen for simulations around black holes (MLC94). The bending instabilities reported in M01a, are also found here and correspond to the hecto-Hz oscillations found in the PDS.

So far, in the literature, a model which appears to be capable of phenomenologically addressing both timing and spectral properties is the transition layer (TL) model of TLM98 who assumed the disc to be Keplerian to begin with. The viscosity was also assumed to be high enough to redistribute angular momentum to maintain a Keplerian distribution. The QPOs are then explained as the oscillation of the TL at different orbital frequencies. The COMPTT and COMPTB models, used for spectral analysis of accreting NSs, used an extended TL. Many NS LMXBs are studied using the COMPTB framework, such as 4U 1728-34 (Seifina et al. 2011), GX 3+1 (Seifina and Titarchuk 2012), GX 339+0 (Seifina et al. 2013), 4U 1820-30 (Titarchuk et al. 2013), Scorpius X-1 (Titarchuk et al. 2014), 4U 1705-44 (Seifina et al. 2015) etc. The HMXB 4U 1700-37 has also been examined, recently, using the same model (Seifina et al. 2016). This model, in general, required two COMPTB components. The one corresponding to a cloud closer to the Keplerian disc typically had higher temperature and the one closer to the star had a relatively lower temperature (see, works cited above). The one corresponding to Comptonization of NS surface photons, showed a saturation in COMPTB model's spectral index (Farinelli and Titarchuk, 2011). This index is, however, different from the spectral index found by fitting the power-law component of the spectrum, which can have a continuous range of values depending on the halo and disc accretion rates (BC17). However, since the source of high viscosity required to sustain a complete Keplerian distribution remains elusive, the physical processes to create two Compton clouds out of a Keplerian disc is also not demonstrated, we preferred to start with a sub-Keplerian inviscid advective flow onto a neutron star which is a general configuration. In presence of higher turbulent viscosities this flow will become a Keplerian disc as in the case of black hole accretion by simply redistributing angular momentum (Chakrabarti, 1990, 1996, Chakrabarti 2017), and thus in softer states the flow would resemble a configuration similar to the TLM98 model. In general, the flow should have both the sub-Keplerian and Keplerian components (CT95; Chakrabarti 2017). It is to be noted that the infall timescale from CT95 (and subsequent work in the TCAF paradigm) has the same $r^{3/2}$ dependence with the radial distance r and differ from Keplerian orbital time scale by a factor of $R_{comp}/2\pi$, where R_{comp} is the compression ratio of the shock. This suggests that the TCAF scenario, in principle, would produce the same numerical values of frequencies for all such sources, even when the viscosity is low enough to form a TL and flow is not-Keplerian to begin with. The pre-shock and post-shock regions of NBOL are orders of magnitude denser than those of CENBOL and contribute to higher frequency oscillations as well. In the TCAF scenario, the presence of NS surface aids the inner shock formation (NBOL) apart from the CENBOL surface formed even in black hole accretion.

We found that the ratio ν_u/ν_l varied from 1.38 to 1.53 and the ratio ν_l/ν_{hHz} varied from 1.66 to 4.20 in our simulations. The Q factors of lower kHz QPOs were always found to be greater than the Q factor of the upper one. This agrees well with observational results (Barret et al. 2005). In our cases, the separation $\delta\nu$ between ν_u and ν_l increased with accretion rate, which is similar to the results of Cir X-1 (Boutloukos et al. 2006). In fact, the values of Table 7.1, when scaled with the mass of Cir X-1, lies in the same ball park figure as that found in observation.

In passing, we may mention that our simulation clearly demonstrated that the advective flows onto a non-magnetic neutron star can create a stable configuration. The flow with a sub-Keplerian specific angular momentum had at least two density jumps in accretion and shocks were also found in the outflows. In presence of cooling, the shocks underwent oscillations in both radial and vertical directions and were manifested as QPOs in the PDS of bremsstrahlung loss from the system. We also find that the shock location, and hence the QPO frequencies depend on many parameters of the flow, viz, the specific angular momentum λ , the accretion rate \dot{m}_h , the radius of the star R_{NS} and the strength of cooling α , which we studied here.

Chapter 8

Simulation of Viscous flows around NS

ABSTRACT

We use Smoothed Particle Hydrodynamics to study viscous accretion flows around a weakly magnetic neutron star. We show the formation of multiple “boundary” layers in presence of both cooling and viscosity. We find that with the introduction of a small viscosity in a sub-Keplerian flow, much like the wind accretion in HMXBs such as Cir X-1, only a single Normal Boundary Layer (NBOL) forms to adjust the rotational velocity component. With the increase of viscosity, the region extends radially and beyond some critical value, a RAdiative KEplerian Disc/layer (RAKED) forms between the sub-Keplerian flow and the NBOL. When viscosity is increased further only NBOL and RAKED remain. In all such cases, the CENtrifugal pressure dominated BOundary Layer (CENBOL) is formed, away from the star, as in the case of black holes. This is the first self-consistent study where such a transition from sub-Keplerian flows has been reported for neutron stars. We also identify the connection between accretion and ejection of matter, following the Two-Component Advective Flow for black holes, for neutron stars. The results are crucial in the understanding of the formation of discs, boundary layers and outflows in wind dominated neutron star systems. These findings have been reported in Bhattacharjee and Chakrabarti (2019). Fig. 8.1 has been taken from there.

In the present Chapter, we focus on the effects of the introduction of viscosity and its gradual enhancement on the flow configuration from a theoretical point-of-view. We note the similarities and differences with the cases of Paper I. We study the formation of discs, boundary layers in the inflow. We also note the changes in the pattern of ejection of matter from the equatorial plane as compared to that in inviscid flows studied in Paper I.

Method

We use the SPH code used in Paper I to solve for the conservation of mass, momentum and energy. All the equations, notations and boundary conditions (inner and outer) are kept the same. We add the α -viscosity prescription for the system following LMC98, which modifies the following.

1. Conservation of azimuthal component of the momentum:

$$\left(\frac{Dv_\phi}{Dt}\right) = -\left(\frac{v_\phi v_r}{r}\right) + \frac{1}{\rho} \left[\frac{1}{r^2} \frac{\partial}{\partial r} (r^2 \tau_{r\phi}) \right], \quad (8.1)$$

where, $\tau_{r\phi} = \mu r \frac{\partial \Omega}{\partial r}$, $\Omega = \frac{v_\phi}{r}$. Here, we use the standard Shakura-Sunyaev turbulent viscosity (Shakura & Sunyaev 1973) $\mu = \alpha \rho a Z_{disc}$, where Z_{disc} is the vertical thickness of the flow as obtained from the vertical equilibrium condition and is given by $Z_{disc}^2 = \frac{2}{\gamma} a r (r-1)^2$ (Chakrabarti 1989, 1990; LMC98).

2. Conservation of energy (viscous heating term added)

$$\frac{D}{Dt} \left(e + \frac{1}{2} \vec{v}^2 \right) = -\frac{P}{\rho} \vec{\nabla} \cdot \vec{v} + \vec{v} \cdot \left(\frac{D\vec{v}}{Dt} \right) - \zeta_{1/2} \rho e^\alpha + \frac{\mu}{\rho} \left[r \frac{\partial \Omega}{\partial r} \right]^2 \quad (8.2)$$

Equations 8.1 and 8.2 are identical to the Eq. 15 and 6 of Paper I, apart from the last terms which introduce the viscous effects in the flow (in Paper I, μ was 0). The flow was injected from $r_{inj} = 30r_S$ with $v = 0.1211$, $a = 0.0590$ and $\lambda_{inj} = 1.7$ (similar to case C2 of Paper I).

Results

We increased the viscosity parameter from 0.075 (C1) to 0.15 (C2) to 0.3 (C3) and kept injected $\lambda_{inj} = 1.7$ (see, Table 8.1). We also define the RAdiative KEplerian Disc (RAKED) as the equivalent of a standard Keplerian Disc following the prescription of Chakrabarti & Sahu 1997 (hereafter, CS97), when the effect of the radiative pressure term due to the emission from NBOL is included. If the average repulsive radiative force is $F_{rad} = \frac{\langle C \rangle}{2(R-1)^2}$, then the effective gravitational force reduces to $F_g = \frac{1-\langle C \rangle}{2(R-1)^2}$ (CS97, Paper I).

Case C1: In presence of lower viscosity ($\alpha = 0.075$), the sub-Keplerian flow adjusted its angular momentum very close to R_{NS} . The layer where most of this transition took place was the previously identified Normal Boundary Layer (NBOL). In a very small region ($5 - 7 r_S$), a RAdiative KEplerian Disc appears and disappears from time to time. Figure 8.1(h) shows one such instance when the RAKED is formed. Rest of the outer flow remained sub-Keplerian. This is similar to the cases reported in Paper I. We also see that the turbulent nature of the inner flow, which shows multiple bending instabilities, is very similar to the cases reported in Paper I. Furthermore, matter is ejected from both CENBOL and NBOL in the upper quadrant and only from CENBOL in the lower quadrant. The outflowing matter from NBOL undergoes multiple shock transitions (one before merging with CENBOL-outflow, one after), before becoming transonic near the outer edge. A part of the ejected matter falls back to CENBOL and another

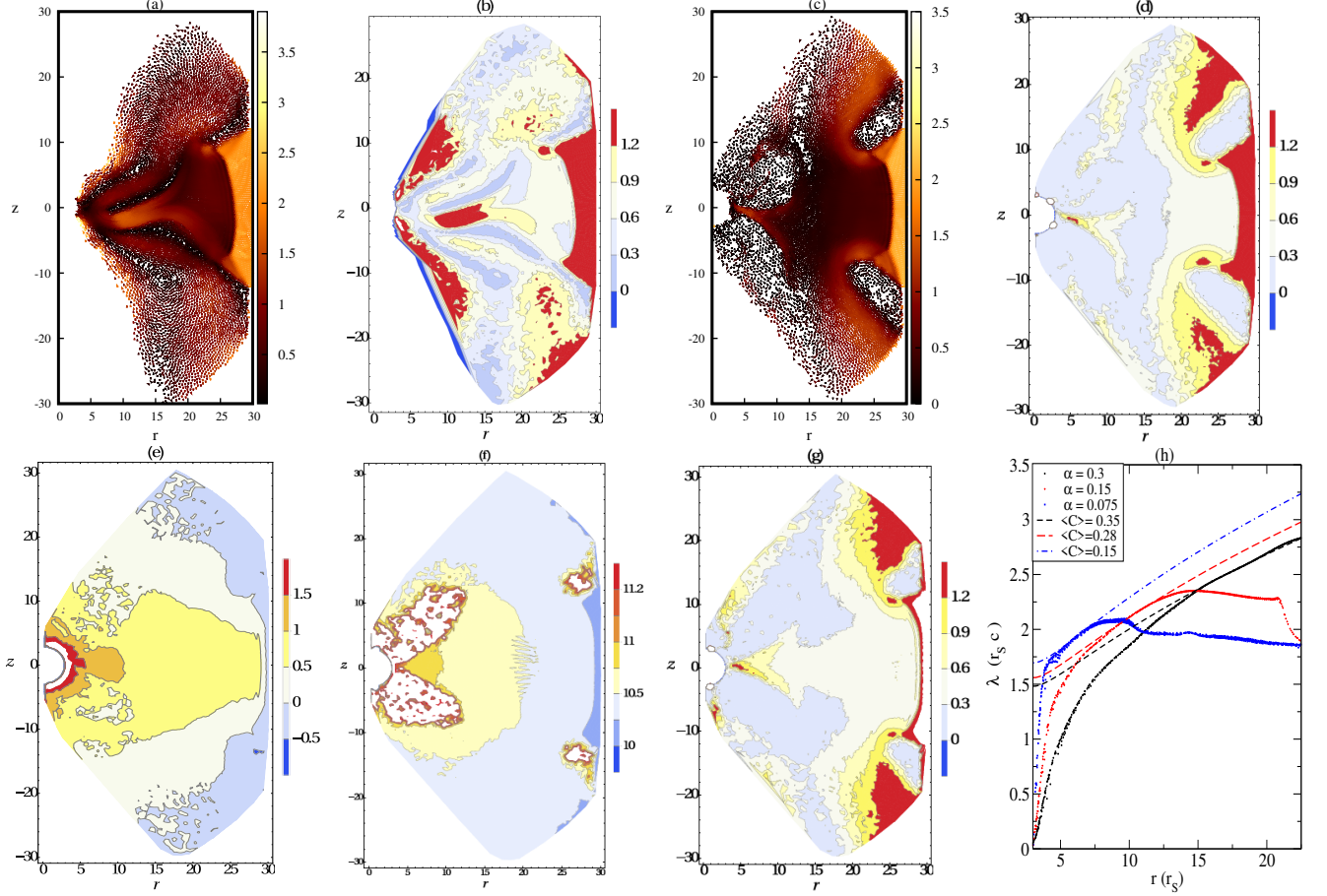


Figure 8.1: (a) Velocity vector $v_r \hat{r} + v_z \hat{z}$ (arrow heads) with Mach number in the colour bar, for the flow configuration $C1$ at time $t = 0.2800s$ and (b) corresponding contours of constant Mach number range showing the outer and inner shocks. (c) Velocity vector $v_r \hat{r} + v_z \hat{z}$ (arrow heads) with Mach number in the colour bar, for the flow configuration $C2$ at time $t = 0.1400s$ and (d) corresponding contours of constant Mach number range showing the outer and inner shocks. (e) Contours of constant $\log(\rho/\rho_0)$ range for case $C3$ at time $t = 0.0400s$ and (f) Corresponding contours of constant temperature range in K (log scale) and (g) Corresponding Mach number range contours. (h) Formation of different regions in inflow for various α , at a time $t = 0.016s$. Dashed curves are the theoretical distribution with $\frac{\sqrt{1-\langle C \rangle} r^{1/2}}{\sqrt{2(1-1/r)}}$ shape, while the dotted curves are as obtained from the simulations. Clear indication of RAKED formation is seen.

| Case | α | $\langle C \rangle$ | NBOL (r_S) | RAKED (r_S) | SK (r_S) | $R_{CE,O}$ (r_S) |
|------|----------|---------------------|-----------------|-----------------|------------------|----------------------|
| C1 | 0.075 | 0.15 | $R_{NS} - 5.0$ | $5.0 - 7.5$ | $7.5 - R_{out}$ | 17.5 |
| C2 | 0.15 | 0.28 | $R_{NS} - 8.5$ | $8.5 - 12.0$ | $12.0 - R_{out}$ | 21.0 |
| C3 | 0.3 | 0.35 | $R_{NS} - 14.5$ | $14.5 - 23.5$ | - | 27.5 |

Table 8.1: Different regions of the inflow for different values of α , at $t = 0.016$ s, for $-0.5 < z < 0.5$. Here, $R_{CE,O}$ is the outer boundary of CENBOL or the outer shock location.

part is accreted onto the NS through more radial shocks. This fallback onto the star is primarily achieved due to the lowered angular momentum near the surface.

Case C2: When the viscosity parameter is increased from 0.075 to 0.15, the size of the NBOL is increased from $\sim 2r_S$ to $\sim 5.5r_S$. The size of RAKED is also increased from $\sim 2.5r_S$ in C1 to $\sim 3.5r_S$ here, though it has relatively weaker oscillations. The outer part of the flow remained sub-Keplerian throughout the simulation. This case is of particular interest as all the layers are present simultaneously. When the velocity vectors and Mach numbers are compared with those in C1, we notice that the flow has become more stable due to introduction of viscosity and consequent decrease of specific angular momentum in the inner regions. The outer shock is moved at a larger distance from the star boundary. The NBOL did not eject any matter due to the lack of centrifugal drive by low angular momentum and only the CENBOL ejected matter. A part of the outflowing matter is seen to move towards the NS surface transonically. The flow interacts with a larger area on the NS surface due to the further reduction of angular momentum near the star. The inner shock moves closer to the NS and is narrower.

Case C3: Further increase of viscosity parameter from 0.15 to 0.3 leads to increase of NBOL size to $\sim 11.5r_S$. Furthermore, the RAKED kept growing in size as its outer boundary started to increase with time. The inner edge of RAKED (outer edge of NBOL) remained fairly constant. We also show the density, temperature and Mach number contours of this case at time $t = 0.04s$, in Figs. 8.1(e), 8.1(f) and 8.1(g), respectively. Both the density jumps near CENBOL and NBOL are distinctly seen in 1(e) and 1(g). We also notice that matter is ejected from near the the outer shock. The temperature distribution of the flow also captures the shock transition. In addition to those, further hotter and clumpy regions are seen near the NBOL where the inflow and outflows mix. In this case, the shock is pushed to the outer boundary very quickly and matter is ejected in both quadrants from CENBOL. NBOL is almost symmetric about $z = 0$ and did not produce any outflow. Fallback of some matter onto the star could be seen.

The λ vs r curve is drawn in Fig. 8.1(h) to show the region where RAKED is formed. The dashed curves are theoretical shapes $\lambda = \frac{\sqrt{1-\langle C \rangle} r^{1/2}}{\sqrt{2(1-1/r)}}$ while the dotted curves are as obtained from simulations. The values of $\langle C \rangle$ increased with the increase of α , suggesting that more energetic matter (due to viscous heating) makes its way to the NS surface and raised the radiative pressure exerted on the inflowing matter.

Conclusions

In this Chapter, we report the formation of a normal boundary layer and a radiative Keplerian disc out of a sub-Keplerian injected flow around a weakly magnetic neutron star. To our knowledge, this is the first detailed study of viscous flows around a weakly magnetized neutron star. We carried out a qualitative study of the behaviour of three regions formed in the inflowing matter

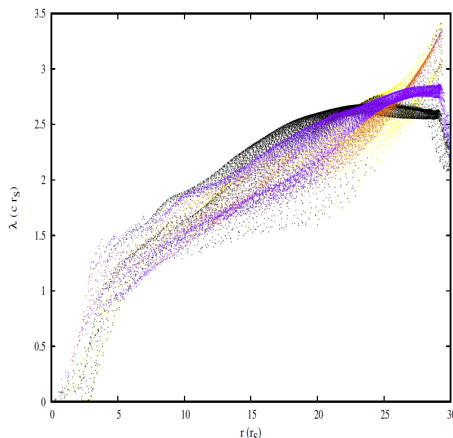


Figure 8.2: Variation of specific angular momentum of pseudo particles with radial distance when the spin of neutron star is changed from 0.0042 to 0.42 in dimensionless units. The black (inflow) and yellow (outflow) points represent the former case whereas purple (inflow) and orange (outflow) points represent the latter case.

as the flow viscosity is gradually increased. When viscosity is low, resembling an inviscid flow, matter adjusts its angular momenta only very close to the NS surface and forms the NBOL out of the sub-Keplerian flow. RAKED is transient in nature for these cases. We believe this happens in HMXBs, such as, Cir X-1. We notice that two regions, one on the inner edge of CENBOL and the other near NBOL, eject matter along the z -direction. A part of these two matter merge and a part actually falls back to these regions. For higher viscosity, the RAKED is formed in between NBOL and the sub-Keplerian flow. Here, the RAKED is small and steadily oscillate. These would be the most general type of inflow in presence of viscosity. We also notice that the redistribution of angular momentum helps in ejecting more matter out of the equatorial plane, even more compared to inviscid cases. For even higher viscosity, a clear RAKED is formed and increased in size towards larger radial distance. This suggests that these cases are possible in the super-critical range of viscosity. Within 25 dynamical timescales at $30r_S$, the RAKED reached the outer edge. The redistributed angular momentum also leads to an even higher ejection of matter from the disc. The added viscosity appears to make the flow more stable and the vertical oscillations become negligible.

In Paper I, the simulations were carried out for more than 200 dynamical timescales measured at the injected flow radius, i.e., $30 r_S$, which was around $0.33s$. In this Chapter, we carried out simulations of $C1$ and $C2$ till the same timescales as the solutions appear to be free from boundary effects during this time. The flow configurations plotted in Figs. 8.1(a-d) are taken from that duration to showcase some typical features. For the case $C3$, the outer shock reached the outer boundary soon after $0.04s$, and we only comment on the solutions prior to that time to avoid effects which could be artefacts of simulations. The flow configuration we discuss is at $t = 0.04s$. The λ vs r plot was made at a much shorter time ($0.016s$) to capture the effects of viscosity away from the outer boundary.

We also chose the simulation box to be the same as that of Paper I for a proper comparison. The system can be studied for a larger radial distances, which can be used to determine the critical viscosity α_c where the entire inflow, apart from NBOL, becomes a RAKED out of a sub-Keplerian matter flowing in. The study of the system on a larger vertical scales will enable us in tracking

the ejected matter better. Whether the outflowing matter falls back onto the inflow, escapes, or catches up with a previous shock, can also be investigated by such a study on larger length-scales. Both of these cases would require the system to be studied for a much larger timescale and would require a robust computational setup and longer runtime. These are beyond the scope of the present work.

Chapter 9

Generalized flows around neutron stars

ABSTRACT

In this Chapter, we show that a TCAF geometry is formed out of a sub-Keplerian flow, in presence of strong cooling and viscosity. This structure remains as long as the viscosity remains active. The flow configuration changes back to the sub-Keplerian flow, after the viscosity is turned off. This shows that TCAF is formed around NSs, suggesting it to be a generalized solution for BHs and NSs. We also construct a new TCAF-based spectral model, with the introduction of 3 more physical parameters, which is capable of fitting spectral data of multiple types of spectral states and generate the Colour-Colour diagrams which are similar to the ones observed for Atoll and Z sources. Part of this work has been reported in Bhattacharjee and Chakrabarti (2019). Fig. 9.2 and 9.4 have been taken from there.

Flow configuration with a vertical viscosity gradient and strong cooling

We introduce the viscous term in the conservation equations following the method of LMC98 and introduce the viscosity gradient prescription of Giri and Chakrabarti 2013. Along with that, we calculated the optical depth from top and bottom of the simulation box. For regions in the pre-shock domain where the optical depth was greater than a critical value, we used blackbody cooling laws; for regions with sub-critical optical depths bremsstrahlung was used. A similar method for one quadrant was used in GC13.

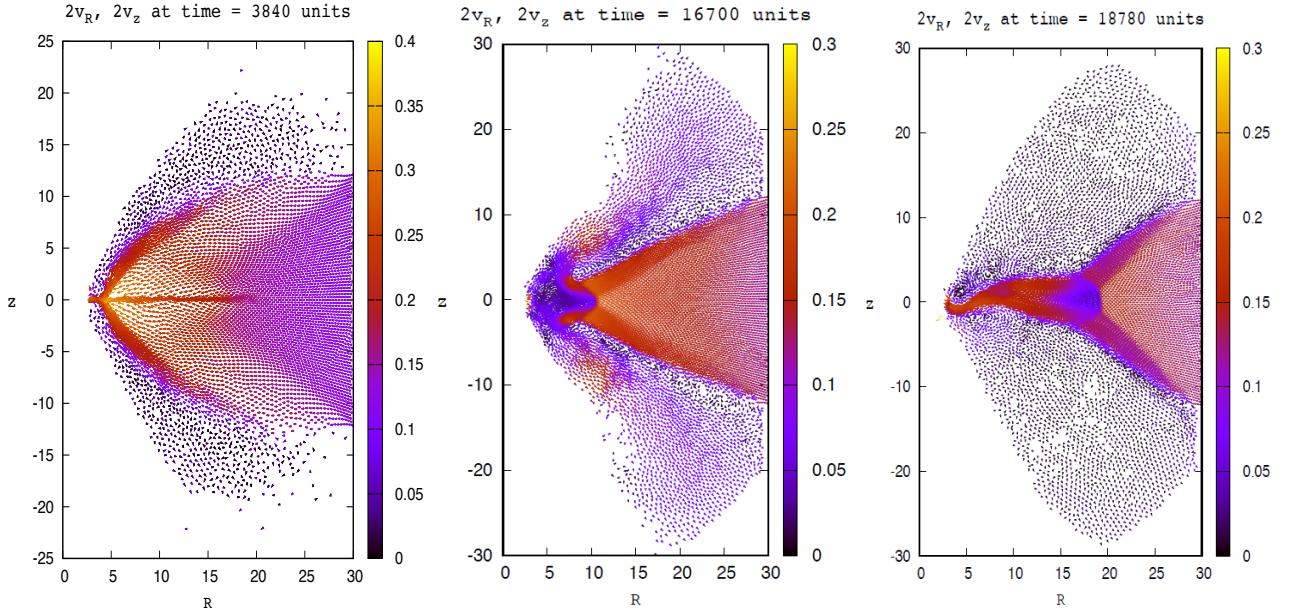


Figure 9.1: The velocity vectors and Mach number (in colour bar) for accreting flow, at different times (in simulation time steps) mentioned in the panels. In Panel 1: a disc-like component is created along the equatorial plane in presence of strong cooling and viscosity with vertical gradient. In Panel 2: Viscosity is turned off and the disc is seen to be dissipated away as outflowing matter. In Panel 3: the flow goes back to the typical configuration of an inviscid flow. In all panels, the time units of simulation are given on top.

A unified spectral model for BHs and NSs

In the above case we clearly see the formation of TCAF around NSs. A TCAF based spectral model for the neutron stars to satisfactorily explain the observed spectral variations is therefore essential. Here we show that additional three physical parameters to existing TCAF solution hitherto applicable only for black holes, one can fit the spectra of accreting neutron stars and reproduce intricate features of two broad classes of sources (van der Klis 1989), viz., Z and Atoll. We include soft photons from both the Keplerian disc and the normal boundary layer of the star and compute the combined Comptonized spectra (see Fig. 9.2 for the schematic and 9.3 for the method). Existing models used multiple phenomenological parameters to fit the spectra and provided limited insight into the physical processes and the variation of the geometry of the accretion flow (Bhattacharjee 2018). However, TCAF-based model maintains its robust geometrical config-

uration away from the compact objects while accommodating boundary layer(s) in the accreting matter around both the black holes and neutron stars. To our knowledge, ours is the first physical model which tries to unify the accretion flow solutions in presence of these compact objects.

We use the following parameters in the spectral code TCAF Around Neutron Stars or TANS (Figure 9.2):

1. \dot{m}_d : disc (or Keplerian) accretion rate (in \dot{M}_{Edd}),
2. \dot{m}_h : halo (or sub-Keplerian) accretion rate (in \dot{M}_{Edd}),
3. X_s : location of the outer shock (=truncation radius of the disc) (in r_S),
4. R_{comp} : compression ratio of the outer shock,
5. T_{NBOL} : temperature of the Normal BOUNDary Layer or NBOL (in keV),
6. f_{CB} : fraction of NBOL photons intercepted by CENBOL (and vice-versa),
7. f_{ic} : transparency factor of the inner cloud. If the optical depth of the entire CENBOL is τ_0 , inner cloud transparent to the star till $\tau = f_{ic}\tau_0$.

Here \dot{M}_{Edd} is the Eddington rate for the NS and $r_S = 2GM_{NS}/c^2$, is its Schwarzschild radius. For the present version of the code we kept the mass of the star constant at $M_{NS} = 1.4M_\odot$. A single suitable normalization (N) is required to match observed spectra with the theoretical one across spectral states.

In Fig. 9.2, we show schematically how the seed soft photons from the NBOL and the KD are Comptonized by CENBOL electrons and are emitted to the observers. Apart from the four TCAF parameters, namely the rates of the halo and the disc, shock strength and location, meanings of three more parameters needed for a NS spectral fit are shown. Also shown are the four contributors of the final spectrum. In Panel 1 of Fig. 9.4, we give examples of our computation of a few typical spectra of the generalized flow configuration TANS as the parameters are varied in order to impress that our model is capable of reproducing observed spectra in Horizontal Branch (HB), Normal Branch (NB; Bottom Normal Branch: bot NB), and Flaring Branch (Bottom: bot FB; Middle: mid FB; Top: top FB). The computational parameters for all the cases are listed in Table 9.1. In Panel 2 of Fig. 9.4 we show that the Island Branch (IS), Lower Left Banana Branch (LLB), Lower Banana Branch (LB), and Upper Banana Branch (UB) spectra can be generated by our model as well. In Panel 3 of Fig. 9.4 we present colour-colour diagrams of the same cases to show that the track characteristics of the transitions observed in Z and atoll sources can also be reproduced by us. In Panel 4, we attempt to fit manually a few observed spectra (marked in the Figure caption) in the 3.0 - 60.0 keV energy range without adding the absorption properties at low energies. We obtained reasonable agreement between the theoretical and the observed spectra, especially in the 5.0 - 60.0 keV range.

In this Chapter, we presented examples of applications of the spectral model TANS for accreting NSs. We showed that with only seven independent parameters, we can reproduce spectra of all the observed states and also generate the tracks for the transitions between different branches of Z and Atoll sources. Though our code is yet to be integrated with a spectral fit software, we find encouraging signs that observed spectra of several sources could be fitted manually with reasonable accuracy with these seven parameter model alone. In all the cases we do not change the normalization as our spectra from theoretical consideration with self-consistent Comptonization and reflection are generated as a whole across the states and the normalization is needed only to scale these theoretical spectra with the observed spectra. We also report three manually fitted spectra of an IS, a LB and a HB spectrum of two different objects to impress that excellent fits are possible. The deviations of the fits at lower energies are primarily due to non-inclusion of absorption due to the inter-stellar medium ($< 5keV$). A detailed study of dependences of the flow

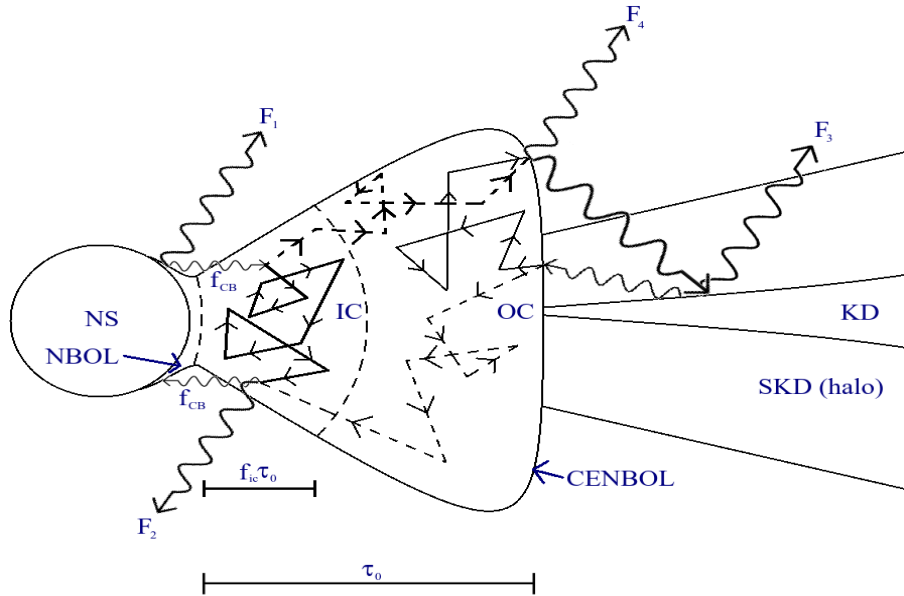


Figure 9.2: A schematic of the TANS model. Expected TCAF configuration around a Neutron star. The two components, namely, Keplerian Disc (KD) and sub-Keplerian or halo (SKD), are marked. The CENTrifugal pressure dominated BOUNDary Layer (CENBOL), which is the truncation radius of KD, serves as the Comptonizing region. The subsonic post-shock matter inside CENBOL hits the NS surface after passing through the inner shock which is the outer edge of the Normal BOUNDary Layer (NBOL). Seed photons from KD and NBOL are intercepted by CENBOL and are reprocessed to higher energy which reach the observers either directly or after getting reflected by the KD. NBOL and KD typically interacts with different regions, namely the Inner Cloud (IC) and the Outer Cloud (OC) respectively, of CENBOL due to proximity effects and the separation is characterized by a parameter f_{ic} . Fraction of photons received by CENBOL from NBOL and vice-versa is determined by f_{CB} . The final spectrum is obtained by combining the four fluxes: F_1 , F_2 , F_3 , and F_4 .

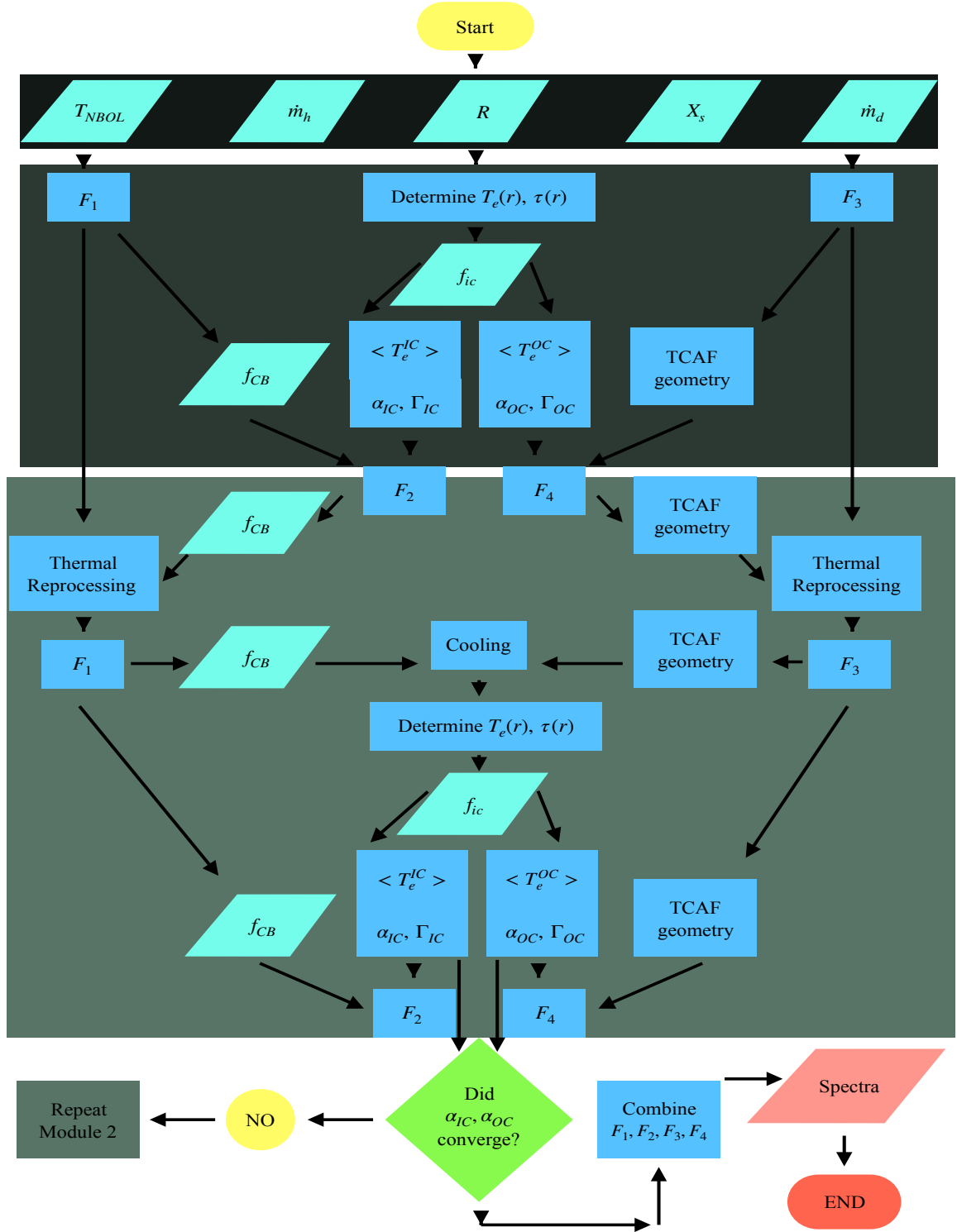


Figure 9.3: A flowchart of the working of the TANS model for NS spectra. Here, $T_e(r)$ and $\tau(r)$ are the distribution of electron temperature and optical depth with radial distance, respectively. $\langle T_e^{IC} \rangle$ and $\langle T_e^{OC} \rangle$ denote the average effective temperature of the inner and outer clouds, respectively. In the same order, α_{IC} and α_{OC} , denote the spectral slopes of Comptonized component of the inner and outer cloud. The corresponding Comptonizing efficiencies are denoted by Γ_{IC} and Γ_{OC} , respectively. Rest of the symbols have the same meanings as in the text.

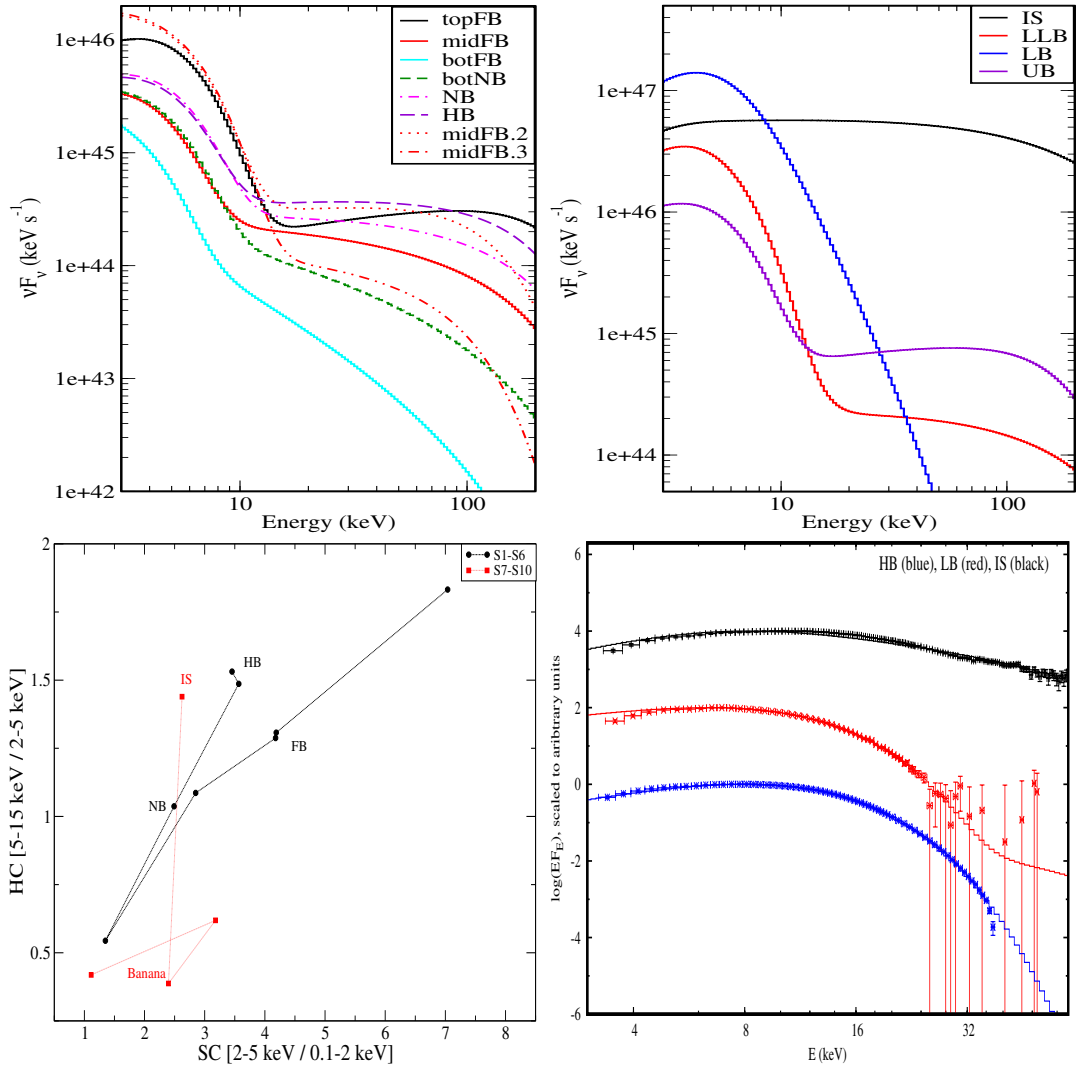


Figure 9.4: Examples of variations of spectra, colour-colour diagram as the flow parameters are varied (Table 9.1). Comparison with observed X-ray spectra of Sco X-1 and 4U 1705-44. Panel 1: Model-generated spectra of $HB \rightarrow NB \rightarrow FB$ transitions in 3.0-200.0 keV energy range. Panel 2: Model generated spectra of $IS \rightarrow LLB \rightarrow LB \rightarrow UB$ transitions in the same energy range. Normalization (N) is kept fixed. Panel 3: Hard Colour (HC) vs. Soft Colour (SC) plots for the simulated spectra which follow typical tracks characteristics of the transitions found in Z and Atoll sources (see, Fig. 1, Panel 2 and Fig. 3, Panel 3 of van der Klis 1989). Both HC and SC were scaled by a multiplicative factor of 5 for S1 to S5 to show variations in the same plot. It can be seen by comparing S5 and S6 with S5.2 and S5.3, that the parameters reported here have a complex effect and in no way uniquely represent a particular state in spectra or the Colour-Colour Diagram. Panel 4: RXTE/PCA spectra for the observation IDs: 20053-01-01-00 (blue, HB, Sco X-1), 40034-01-09-00 (black, IS, 4U 1705-44), and 40034-01-02-09 (red, LB, 4U 1705-44) have been plotted in 3.0-60.0 keV energy range, with error-bars. The standard product data from PCU2 were used here. The corresponding solid lines show the model generated spectra to indicate fits of varied spectra are possible by changing only a few flow parameters. The data and model spectra agree well above 5 keV. Below 5 keV, the deviation is due to non-inclusion of absorption.

| Source | Obs ID/Class | \dot{m}_d | \dot{m}_h | X_s | T_{NBOL} | f_{ic} | f_{CB} |
|------------|---------------------|-------------|-------------|-------|------------|----------|----------|
| Sco X-1 | 20053-01-01-00 (HB) | 1.5 | 1.0 | 10.0 | 2.10 | 0.65 | 0.325 |
| 4U 1705-44 | 40034-01-09-00 (IS) | 0.5 | 2.5 | 15.0 | 0.60 | 0.925 | 0.950 |
| 4U 1705-44 | 40034-01-02-09 (LB) | 1.5 | 2.5 | 15.0 | 1.80 | 0.25 | 0.425 |
| S1 | HB | 1.5 | 2.0 | 15.0 | 0.60 | 0.10 | 0.500 |
| S2 | NB | 1.5 | 1.5 | 15.0 | 0.60 | 0.10 | 0.500 |
| S3 | bot NB | 2.0 | 1.0 | 15.0 | 0.60 | 0.50 | 0.500 |
| S4 | bot FB | 2.5 | 0.5 | 15.0 | 0.60 | 0.50 | 0.250 |
| S5 | mid FB | 1.5 | 1.5 | 15.0 | 0.60 | 0.25 | 0.250 |
| S5.2 | mid FB | 1.5 | 2.5 | 30.0 | 1.00 | 0.25 | 0.250 |
| S5.3 | mid FB | 1.5 | 2.5 | 30.0 | 1.00 | 0.10 | 0.125 |
| S6 | top FB | 0.5 | 2.5 | 15.0 | 1.00 | 0.05 | 0.125 |
| S7 | IS | 0.5 | 0.5 | 45.0 | 0.20 | 0.95 | 0.500 |
| S8 | LLB | 1.0 | 1.5 | 15.0 | 1.00 | 0.25 | 0.125 |
| S9 | LB | 0.5 | 0.5 | 30.0 | 0.60 | 0.95 | 0.500 |
| S10 | UB | 2.0 | 2.5 | 15.0 | 1.00 | 0.05 | 0.125 |

Table 9.1: A set of spectral model parameters for different states for Z and atoll type variations in Colour-Colour Diagram (CCD).

parameters is being carried out along with the creation of an additive table model for use within XSPEC. This will be reported elsewhere.

Chapter 10

Summary

Fulfillment of objectives

1. The summaries of works in Chapter 2 show that there does exist a steady state configuration of accreting matter around a black hole: the Two-Component Advective Flow solution which is most general and is relevant for spectral and timing study.
2. The analysis of Chapters 4 and 5 shows our successful implementation of TCAF solution for black holes where it explained the spectral and timing properties self-consistently and also provided a well-constrained estimates of the masses of the compact objects. This shows how TCAF simultaneously explains the spectral and timing properties.
3. The discussions of Chapter 6 show that TCAF, combined with NBOL, explains the spectral features of neutron stars when thermal Comptonization is used. State transition properties are addressed and origin of the geometry of some phenomenological models are also suggested. In Chapter 7, we investigated the inviscid flows with cooling to show that for the wind dominated systems, such as Cir X-1, our solutions are capable of reproducing the observational frequencies of LF, hecto-Hz and kHz QPOs. In Chapter 8, we include viscosity and show that the boundary layer forms even when we start with a sub-Keplerian flow when the viscosity is high. These three Chapters, along with the summaries of works in Chapter 3, show that the TCAF formalism can be applied to the cases of neutron stars, with certain modifications.
4. In Chapter 9, we studied the flows with cooling and viscosity where a two-component (disk and halo) flow is disaggregated from the sub-Keplerian flow. In our simulations we ignored the effects of magnetic fields, which is the case for weakly magnetized neutron stars. We also construct a new spectral model namely, TANS, which is based on the TCAF, which requires three additional physical parameters to produce different types of observed spectra for NSs. These new parameters are based on the inferences of the previous Chapters. This suggests that there can be a generalized solution applicable for black holes and neutron stars.

Since the nature of the companion remains generally similar irrespective of whether the compact object is a BH or an NS, it is natural that we use the TCAF solution for the NSs as well, specifically when the magnetic field is not very strong. As suggested in Chakrabarti 2017, the presence of strong magnetic field will modify the flow configuration from standard TCAF and matter would eventually accrete along the field lines onto the poles, in extreme cases. But, the two

components, Keplerian and sub-Keplerian, of accretion would still extend to the magnetosphere, making the flow more complex than what is typically considered in the literature so far.

In general, the spectral and timing properties of black holes and neutron stars, both from theoretical and observational perspectives, reveal that the Two-Component Advective Flow is at the core of the most general accretion flow configuration, though details may vary depending on presence or absence of magnetic fields, winds, jets etc.

Future Plans

Study of X-ray Binaries

Black Holes

Study of spectral and timing properties of multiple transient (MAXI J1535-571, H1743-322 etc.), persistent (Cygnus X-1) and class variable sources (GRS 1915+105) using TCAF solution. Large scale survey of LMXBs and HMXBs would be helpful in extracting features of accretion flows around black holes.

Neutron Stars

Studying weakly magnetic neutron stars with the TANS model. Astrosat and NASA archival data of sources such as 4U 1705-44, Sco X-1, 4U 1728-34, GX 3+1, GX 340+0, 4U 1820-30, GX 17+2, 4U 1700-37 can be utilized to check the properties of accretion around NSs.

Numerical Simulation

Study of Outflows

Both BHs and NSs have angular momentum driven ejection of matter. The entrainment, collimation, fallback of such matter with the variation of thermal energy, viscosity and angular momentum can be studied with a larger simulation box. I plan on using the SPH code to study these effects. Effects of momentum deposition of photons are to be made after the initial studies.

Formation of TCAF around NS

A detailed study of sub-Keplerian flows in presence of differential cooling and viscosity gradient is to be conducted. The initial cases show the formation of TCAF. I want to find the critical viscosity both in absence and presence of cooling which can then be compared to the cases of BHs. For these studies a larger simulation box and a longer runtime would be required.

Transient Behaviour

A time and radius dependent viscosity is to be added to simulate a realistic outburst scenario for BHs and NSs. A timing study can also show the variation of QPOs with accretion rate during an outburst.

Effects of Radiation

The effects of radiation on the hydrodynamics of the flow can be studied within the MC code. A coupled MCSPH code can be used to effectively simulate time-dependent spectral variations. This would require parallelization using MPI to perform faster.

Boundary Layer

A detailed study of NBOL in sub-Keplerian and Keplerian flows is required. I want to include blackbody radiation to capture the compactness of the layer and study the dynamics in high time resolution to capture the meridional motion along the surface.

Model Development

Additive Table model for TANS in XSPEC

I want to create a local table model corresponding to TANS. A pre-compiled .out file and an additive table model file are to be created using the 'ftpcl' subroutines. This will help in fitting X-ray data of NSs.

Line emission in TCAF

I want to include the effects of line emissions present in the X-ray SEDs of BHs due to presence of Iron. This would require either a Laor type injected photon flux distribution alongside diskbb or a chemical reaction code which would determine the iron line emission from abundances. The combined model can be compared with reflection models like xillver or relxill. This might require inclusion of spin of BH.

Bibliography

- [1] Abramowicz, M. A., Czerny, B., Lasota, J. P., & Szuszkiewicz, E. 1988, *The Astrophysical Journal*, 332, 646.
- [2] Abramowicz, M. A., & Chakrabarti, S. K. 1990, *The Astrophysical Journal*, 350, 281.
- [3] Acharya, K., Chakrabarti, S. K., & Molteni, D. 2002, *Journal of Astrophysics and Astronomy*, 23, 155.
- [4] Allen, C. W. 1973, London: University of London,.
- [5] Arnaud, K. A. 1996, *Astronomical Data Analysis Software and Systems V*, 101, 17.
- [6] Axford, W. I., & Newman, R. C. 1967, *The Astrophysical Journal*, 147, 230.
- [7] Baade, W., & Minkowski, R. 1954, *The Astrophysical Journal*, 119, 215.
- [8] Banerjee, A., Bhattacharjee, A., & Chakrabarti, S. K. 2019, arXiv e-prints, arXiv:1905.01538.
- [9] Banerjee, I., Bhattacharjee, A., Banerjee, A., Debnath, D., & Chakrabarti, S. K. 2019, arXiv e-prints, arXiv:1904.11644.
- [10] Bardeen, J. M., & Petterson, J. A. 1975, *The Astrophysical Journal*, 195, L65.
- [11] Bardeen, J. M. 1970, *Nature*, 226, 64.
- [12] Barnothy, J.M., and Barnothy. M.F., *Astron. J. Suppl. Ser.* 73 164 (1968)
- [13] Barret, D., Kluźniak, W., Olive, J. F., Paltani, S., & Skinner, G. K. 2005, *Monthly Notices of the Royal Astronomical Society*, 357, 1288.
- [14] Barret, D. 2001, *Advances in Space Research*, 28, 307.
- [15] Barret, D., Olive, J.-F., & Miller, M. C. 2005, *Monthly Notices of the Royal Astronomical Society*, 361, 855.
- [16] Barret, D., & Olive, J.-F. 2002, *The Astrophysical Journal*, 576, 391.
- [17] Begelman, M. C. 1978, *Astronomy and Astrophysics*, 70, 583.
- [18] Belloni et al., *Astron. Astrophys.* 355 271 (2000)
- [19] Belloni, T., Méndez, M., & Homan, J. 2005, *Astronomy and Astrophysics*, 437, 209.
- [20] Belloni, T., Psaltis, D., & van der Klis, M. 2002, *The Astrophysical Journal*, 572, 392.
- [21] Bhattacharjee, A., & Chakrabarti, S. K. 2017, *Monthly Notices of the Royal Astronomical Society*, 472, 1361.
- [22] Bhattacharjee, A. 2018, *Astrophysics and Space Science Proceedings*, 53, 93.
- [23] Bhattacharjee, A., & Chakrabarti, S. K. 2019, *The Astrophysical Journal*, 873, 119.
- [24] Bhattacharjee, A., Banerjee, I., Banerjee, A., Debnath, D., & Chakrabarti, S. K. 2017, *Monthly Notices of the Royal Astronomical Society*, 466, 1372.
- [25] Bhattacharyya, S., & Chakrabarty, D. 2017, *The Astrophysical Journal*, 835, 4.

- [26] Bildsten, L. 1998, American Institute of Physics Conference Series, 431, 299.
- [27] Biermann, L., Zs. f. Ap. 29 274 (1951); Zs. F. Naturf. 7a 127 (1952)
- [28] Blandford, R., and Eichler, D., Physics Reports 154 1 (1987)
- [29] Blandford, R. D., & McKee, C. F. 1982, The Astrophysical Journal, 255, 419.
- [30] Blumenthal, G. R., & Mathews, W. G. 1976, The Astrophysical Journal, 203, 714.
- [31] Bolton, C. T. 1972, Nature, 235, 271.
- [32] Bondi, H., Mon. Not. R. Astron. Soc. 112 195 (1952)
- [33] Borozdin, K., Revnivtsev, M., Trudolyubov, S., Shrader, C., & Titarchuk, L. 1999, The Astrophysical Journal, 517, 367.
- [34] Boutloukos, S., van der Klis, M., Altamirano, D., et al. 2006, The Astrophysical Journal, 653, 1435.
- [35] Burke, M. J., Gilfanov, M., & Sunyaev, R. 2017, Monthly Notices of the Royal Astronomical Society, 466, 194.
- [36] Cambier, H. J., & Smith, D. M. 2013, The Astrophysical Journal, 767, 46.
- [37] Capitanio, F., Ubertini, P., Bazzano, A., et al. 2005, The Astrophysical Journal, 622, 503.
- [38] Capitanio, F., Belloni, T., Del Santo, M., & Ubertini, P. 2009, Monthly Notices of the Royal Astronomical Society, 398, 1194.
- [39] Casella, P., Belloni, T., & Stella, L. 2006, Astronomy and Astrophysics, 446, 579.
- [40] Chakrabarti, S. K., Acharyya, K., & Molteni, D. 2004, Astronomy and Astrophysics, 421, 1.
- [41] Chakrabarti, S. K., Debnath, D., Nandi, A., & Pal, P. S. 2008, Astronomy and Astrophysics, 489, L41.
- [42] Chakrabarti, S.K., and Nandi, A., Ind. J. Phys. 75B 1 (2000)
- [43] Chakrabarti, S.K., in High Energy Gamma Ray Astronomy (eds) F A Aharonian and H V?olk p. 831 (2001)
- [44] Chakrabarti, S.K., AIP Conf. Proc. of 4th Gamow Int. Conf. on Astrophys. & Cosm. After Gamow 1206 244 (2010)
- [45] Chakrabarti, S.K., Manickam, S.G., Nandi, A., and Rao A.R., in Proceedings of IXth Marcel Grossmann Meeting (Ed) Remo Ruffini (Singapore: World Scientific)
- [46] Chakrabarti, S.K., Astrophys. and Sp. Sc. 297 131 (2005)
- [47] Chakrabarti, S.K., Frontiers in Astrophysics, Eds S. K. Chakrabarti 14 (astro-ph/0402562) (2004)
- [48] Chakrabarti. S.K., Astron. and Astrophys. 351 185 (1999)
- [49] Chakrabarti, S.K., *Theory of Transonic Astrophysical Flows* (1990)
- [50] Chakrabarti, S. K. 1986, The Astrophysical Journal, 303, 582.
- [51] Chakrabarti, S. K. 1985, The Astrophysical Journal, 288, 1.
- [52] Chakrabarti, S.K., and Khanna, R., Mon. Not. R. Astron. Soc. 256 300 (1992)
- [53] Chakrabarti, S.K., and Lu, J.F., (Unpublished, 1993)
- [54] Chakrabarti, S. K., Nandi, A., Chatterjee, A. K., Choudhury, A. K., & Chatterjee, U. 2005, Astronomy and Astrophysics, 431, 825.
- [55] Chakrabarti, S. K., & Sahu, S. A. 1997, Astronomy and Astrophysics, 323, 382.

- [56] Chakrabarti, S., & Titarchuk, L. G. 1995, *The Astrophysical Journal*, 455, 623.
- [57] Chakrabarti, S. K. 1989, *Journal of Astrophysics and Astronomy*, 10, 261.
- [58] Chakrabarti, S. K. 1993, *The Astrophysical Journal*, 411, 610.
- [59] Chakrabarti, S. K., & Mondal, S. 2006, *Monthly Notices of the Royal Astronomical Society*, 369, 976.
- [60] Chakrabarti, S. K., & Molteni, D. 1995, *Monthly Notices of the Royal Astronomical Society*, 272, 80.
- [61] Chakrabarti, S. K. 1988, *The Astrophysical Journal*, 324, 391.
- [62] Chakrabarti, S. K., Jin, L., & Arnett, W. D. 1987, *The Astrophysical Journal*, 313, 674.
- [63] Chakrabarti, S. K., & Wiita, P. J. 1993, *The Astrophysical Journal*, 411, 602.
- [64] Chakrabarti, S. K., & Manickam, S. G. 2000, *The Astrophysical Journal*, 531, L41.
- [65] Chakrabarti, S. K. 1995, *Seventeenth Texas Symposium on Relativistic Astrophysics and Cosmology*, 759, 546.
- [66] Chakrabarti, S. K. 2016, arXiv e-prints, arXiv:1604.05955.
- [67] Chakrabarti, S. K. 1989, *Monthly Notices of the Royal Astronomical Society*, 240, 7.
- [68] Chakrabarti, S. K., Dutta, B. G., & Pal, P. S. 2009, *Monthly Notices of the Royal Astronomical Society*, 394, 1463.
- [69] Chakrabarti, S. K., Nandi, A., Debnath, D., Sarkar, R., & Datta, B. G. 2005, arXiv e-prints, astro-ph/0508024.
- [70] Chakrabarti, S. K. 1999, *Astronomy and Astrophysics*, 351, 185.
- [71] Chakrabarti, S. K., & Molteni, D. 1993, *The Astrophysical Journal*, 417, 671.
- [72] Chakrabarti, S. K. 1990, *Theory of Transonic Astrophysical Flows*. Edited by CHAKRABARTI SANDIP K. Published by World Scientific Publishing Co. Pte. Ltd.,
- [73] Chakrabarti, S. K., & Wiita, P. J. 1994, *The Astrophysical Journal*, 434, 518.
- [74] Chakrabarti, S. K., & Wiita, P. J. 1992, *The Astrophysical Journal*, 387, L21.
- [75] Chakrabarti, S. K. 1997, *The Astrophysical Journal*, 484, 313.
- [76] Chakrabarti, S. K., Mondal, S., & Debnath, D. 2015, *Monthly Notices of the Royal Astronomical Society*, 452, 3451.
- [77] Chakrabarti, S. K., Nandi, A., Manickam, S. G., Mandal, S., & Rao, A. R. 2002, *The Astrophysical Journal*, 579, L21.
- [78] Chakrabarti, S. K., Pal, S., Nandi, A., Anandarao, B. G., & Mondal, S. 2003, *The Astrophysical Journal*, 595, L45.
- [79] Chakrabarti, S. K. 1995, *The Astrophysical Journal*, 441, 576.
- [80] Chakrabarti, S. K. 1990, *Monthly Notices of the Royal Astronomical Society*, 243, 610.
- [81] Chakrabarti, S. K. 1989, *The Astrophysical Journal*, 347, 365.
- [82] Chakrabarti, S. K. 1996, *The Astrophysical Journal*, 464, 664.
- [83] Chakrabarti, S. K. 1996, *The Astrophysical Journal*, 471, 237.
- [84] Chang, K. M., & Ostriker, J. P. 1985, *The Astrophysical Journal*, 288, 428.
- [85] Chatterjee, D., Debnath, D., Jana, A., & Chakrabarti, S. K. 2019, *Astrophysics and Space Science*, 364, 14.

- [86] Chatterjee, D., Debnath, D., Chakrabarti, S. K., Mondal, S., & Jana, A. 2016, *The Astrophysical Journal*, 827, 88.
- [87] Chen, X., & Taam, R. E. 1993, *The Astrophysical Journal*, 412, 254.
- [88] Coleman, H.H., and Shields, G.A., *Astrophys. J.* 363 415 (1990) [246] J F Kartje and Ko?nigl *Astrophys. J.* 375 69 (1991)
- [89] Colpi, M., Maraschi, L., & Treves, A. 1984, *The Astrophysical Journal*, 280, 319.
- [90] Cooke, B. A., Levine, A. M., Lang, F. L., Primini, F. A., & Lewin, W. H. G. 1984, *The Astrophysical Journal*, 285, 258.
- [91] Coriat, M., Corbel, S., Prat, L., et al. 2011, *Monthly Notices of the Royal Astronomical Society*, 414, 677.
- [92] Cox, J. P. 1981, *The Astrophysical Journal*, 247, 1070.
- [93] Cui, W., Heindl, W. A., Rothschild, R. E., et al. 1997, *The Astrophysical Journal*, 474, L57.
- [94] Cui, W., Ebisawa, K., Dotani, T., & Kubota, A. 1998, *The Astrophysical Journal*, 493, L75.
- [95] Cunningham, C. T. 1975, *The Astrophysical Journal*, 202, 788.
- [96] Deb, A., Giri, K., & Chakrabarti, S. K. 2017, *Monthly Notices of the Royal Astronomical Society*, 472, 1259.
- [97] Deb, A., Giri, K., & Chakrabarti, S. K. 2016, *Monthly Notices of the Royal Astronomical Society*, 462, 3502.
- [98] Debnath, D., Chakrabarti, S. K., & Nandi, A. 2010, *Astronomy and Astrophysics*, 520, A98.
- [99] Debnath, D., Chakrabarti, S. K., & Mondal, S. 2014, *Monthly Notices of the Royal Astronomical Society*, 440, L121.
- [100] Debnath, D., Chakrabarti, S. K., Nandi, A., & Mandal, S. 2008, *Bulletin of the Astronomical Society of India*, 36, 151.
- [101] Debnath, D., Molla, A. A., Chakrabarti, S. K., & Mondal, S. 2015, *The Astrophysical Journal*, 803, 59.
- [102] Debnath, D., Chakrabarti, S. K., & Nandi, A. 2013, *Advances in Space Research*, 52, 2143.
- [103] Debnath, D., Mondal, S., & Chakrabarti, S. K. 2015, *Monthly Notices of the Royal Astronomical Society*, 447, 1984.
- [104] Debnath, D., Jana, A., Chakrabarti, S. K., Chatterjee, D., & Mondal, S. 2017, *The Astrophysical Journal*, 850, 92.
- [105] Di Salvo, T., & Stella, L. 2002, arXiv e-prints, astro-ph/0207219.
- [106] Dieters, S. W., & van der Klis, M. 2000, *Monthly Notices of the Royal Astronomical Society*, 311, 201.
- [107] Di Matteo, T., and Psaltis, D., *Astrophys. J.* 526 101 (1999)
- [108] Doerr, T., Riffert, H., Staubert, R., & Ruder, H. 1996, *Astronomy and Astrophysics*, 311, 69.
- [109] Dopita, M. A., Koratkar, A. P., Allen, M. G., et al. 1997, *The Astrophysical Journal*, 490, 202.
- [110] Doxsey, R., Bradt, H., Fabbiano, G., et al. 1977, *International Astronomical Union Circular*, 3113, 2.
- [111] Dutta, B. G., & Chakrabarti, S. K. 2010, *Monthly Notices of the Royal Astronomical Society*, 404, 2136.

- [112] Eardley, D. M., & Lightman, A. P. 1975, *The Astrophysical Journal*, 200, 187.
- [113] Eardley, D. M., Lightman, A. P., & Shapiro, S. L. 1975, *The Astrophysical Journal*, 199, L153.
- [114] Elsner, R. F., & Lamb, F. K. 1977, *The Astrophysical Journal*, 215, 897.
- [115] Emelyanov, A. N., Aleksandrovich, N. L., & Sunyaev, R. A. 2000, *Astronomy Letters*, 26, 297.
- [116] Ertan, Ü. 2018, *Monthly Notices of the Royal Astronomical Society*, 479, L12.
- [117] Farinelli, R., & Titarchuk, L. 2011, *Astronomy and Astrophysics*, 525, A102.
- [118] Farinelli, R., Titarchuk, L., Paizis, A., & Frontera, F. 2008, *The Astrophysical Journal*, 680, 602.
- [119] Flammang, R.A., *Mon. Not. R. Astron. Soc.* 199 833 (1982)
- [120] Galeev, A. A., Rosner, R., & Vaiana, G. S. 1979, *The Astrophysical Journal*, 229, 318.
- [121] Garain, S. K., Ghosh, H., & Chakrabarti, S. K. 2014, *Monthly Notices of the Royal Astronomical Society*, 437, 1329.
- [122] Garcia, M. R., McClintock, J. E., Narayan, R., et al. 2001, *The Astrophysical Journal*, 553, L47.
- [123] Ghez, A. M., Klein, B. L., Morris, M., & Becklin, E. E. 1999, *Observational Evidence for the Black Holes in the Universe*, 234, 265.
- [124] Ghosh, A., & Chakrabarti, S. K. 2016, *Astrophysics and Space Science*, 361, 310.
- [125] Ghosh, H., *MONTE CARLO SIMULATIONS OF THE ADVECTIVE INFLOW AND OUTFLOW AROUND A BLACK HOLE*, PhD Thesis, (2012)
- [126] Ghosh, A., & Chakrabarti, S. K. 2018, *Monthly Notices of the Royal Astronomical Society*, 479, 1210.
- [127] Ghosh, H., Garain, S. K., Giri, K., & Chakrabarti, S. K. 2011, *Monthly Notices of the Royal Astronomical Society*, 416, 959.
- [128] Ghosh, H., Chakrabarti, S. K., & Laurent, P. 2009, *International Journal of Modern Physics D*, 18, 1693.
- [129] Ghosh, H., Garain, S. K., Chakrabarti, S. K., & Laurent, P. 2010, *International Journal of Modern Physics D*, 19, 607.
- [130] Ghosh, P., Lamb, F. K., & Pethick, C. J. 1977, *The Astrophysical Journal*, 217, 578.
- [131] Ghosh, P., & Lamb, F. K. 1979, *The Astrophysical Journal*, 232, 259.
- [132] Ghosh, P., & Lamb, F. K. 1979, *The Astrophysical Journal*, 234, 296.
- [133] Giacconi, R., Kellogg, E., Gorenstein, P., Gursky, H., & Tananbaum, H. 1971, *The Astrophysical Journal*, 165, L27.
- [134] Giacconi, R., Gursky, H., Paolini, F. R., & Rossi, B. B. 1962, *Physical Review Letters*, 9, 439.
- [135] Giacconi, R., Gursky, H., Paolini F., and Rossi, B., *Phys. Rev.lets* 9 439 (1962); Giacconi, R., Gursky, H., and Waters, J.R., *Nature* 207 572 (1965); Gursky, H., Giacconi, R., Gorenstein, P., Waters, J.R., Oda, M., Bradt, H., Garmire, G., and Sreekantan, B.V., *Astrophys. J.* 144 1249 (1966)
- [136] Gies, D. R., & Bolton, C. T. 1986, *The Astrophysical Journal*, 304, 371.
- [137] Gilfanov, M. 2010, *Lecture Notes in Physics*, Berlin Springer Verlag, 794, 17.

- [138] Gilfanov, M. R., & Sunyaev, R. A. 2014, *Physics Uspekhi*, 57, 377-388.
- [139] Giri, K., *Numerical Simulation of Viscous Accretion Flows Around Black Holes Which Include Shocks*, PhD Thesis, (2014).
- [140] Giri, K., Garain, S. K., & Chakrabarti, S. K. 2015, *Monthly Notices of the Royal Astronomical Society*, 448, 3221.
- [141] Giri, K., & Chakrabarti, S. K. 2013, *Monthly Notices of the Royal Astronomical Society*, 430, 2836.
- [142] Gleissner, T., Wilms, J., Pooley, G. G., et al. 2004, *Astronomy and Astrophysics*, 425, 1061.
- [143] Grinberg, V., Hell, N., Pottschmidt, K., et al. 2013, *Astronomy and Astrophysics*, 554, A88.
- [144] Grinberg, V., Leutenegger, M. A., Hell, N., et al. 2015, *Astronomy and Astrophysics*, 576, A117.
- [145] Gursky, H., Bradt, H., Doxsey, R., et al. 1978, *The Astrophysical Journal*, 223, 973.
- [146] Gügercinoğlu, E., & Alpar, M. A. 2017, *Monthly Notices of the Royal Astronomical Society*, 471, 4827.
- [147] Haardt, F., & Maraschi, L. 1993, *The Astrophysical Journal*, 413, 507.
- [148] Hazard, C., Mackay, M.B., and Shimmins, A.J., *Nature* 197 1037 (1963)
- [149] Hewish, A., Bell, S.J., Pilkington, J.D.H., Scott, P.F., and Collins, R.A., *Nature* 217 709 (1968)
- [150] Herrero, A., Kudritzki, R. P., Gabler, R., Vilchez, J. M., & Gabler, A. 1995, *Astronomy and Astrophysics*, 297, 556.
- [151] Holzer, T. E., & Axford, W. I. 1970, *Annual Review of Astronomy and Astrophysics*, 8, 31.
- [152] Hoshi, R., and Inoue, H., *Publ. Astron. Soc. Japan* 40 42 (1988)
- [153] Hoyle, F., and Lyttleton, R.A., *Proc. Camb. Phil. Soc.* 35 405 (1939)
- [154] Hoyle, F., & Burbidge, G. R. 1966, *The Astrophysical Journal*, 144, 534.
- [155] Ichimaru, S. 1977, *The Astrophysical Journal*, 214, 840.
- [156] Inogamov, N. A., & Sunyaev, R. A. 1999, *Astronomy Letters*, 25, 269.
- [157] Ipser, J. R., & Price, R. H. 1982, *The Astrophysical Journal*, 255, 654.
- [158] Iyer, N., Nandi, A., & Mandal, S. 2015, *The Astrophysical Journal*, 807, 108.
- [159] Jana, A., Debnath, D., Chakrabarti, S. K., Mondal, S., & Molla, A. A. 2016, *The Astrophysical Journal*, 819, 107.
- [160] Jennison, R. C., & Das Gupta, M. K. 1953, *Nature*, 172, 996.
- [161] Jonker, P. G., Wijnands, R., van der Klis, M., et al. 1998, *The Astrophysical Journal*, 499, L191.
- [162] Jonker, P. G., van der Klis, M., Wijnands, R., et al. 2000, *The Astrophysical Journal*, 537, 374.
- [163] Kaluzienski, L. J., & Holt, S. S. 1977, *International Astronomical Union Circular*, 3099, 3.
- [164] Kato, S., *Mon. Not. R. Astron. Soc.* 185 629 (1978)
- [165] Kozłowski, M., Jaroszynski, M., and Abramowicz, M.A., *Acta Astron.* 63 209 (1978)
- [166] Kato, S., Honma, F., & Matsumoto, R. 1988, *Publications of the Astronomical Society of Japan*, 40, 709.
- [167] Katz, J. I. 1976, *The Astrophysical Journal*, 206, 910.

- [168] Kazanas, D., & Ellison, D. C. 1986, *The Astrophysical Journal*, 304, 178.
- [169] Kerr, R.P., *Phys. Rev Let.* 11 522 (1963)
- [170] Konigl, A. 1989, *The Astrophysical Journal*, 342, 208.
- [171] Lamb, F. K., Shibazaki, N., Alpar, M. A., & Shaham, J. 1985, *Nature*, 317, 681.
- [172] Lanzafame, G., Molteni, D., & Chakrabarti, S. K. 1998, *Monthly Notices of the Royal Astronomical Society*, 299, 799.
- [173] Lightman, A. P., & Eardley, D. M. 1974, *The Astrophysical Journal*, 187, L1.
- [174] Lin, D. N. C., & Shields, G. A. 1986, *The Astrophysical Journal*, 305, 28.
- [175] Lin, D., Remillard, R. A., & Homan, J. 2007, *The Astrophysical Journal*, 667, 1073.
- [176] Livio, M., & Shaviv, G. 1981, *The Astrophysical Journal*, 244, 290.
- [177] Lu, J.-F., Yu, K. N., Yuan, F., & Young, E. C. M. 1997, *Astronomy and Astrophysics*, 321, 665.
- [178] Lu, J.-F., Gu, W.-M., & Yuan, F. 1999, *The Astrophysical Journal*, 523, 340.
- [179] Luminet, J.-P. 1979, *Astronomy and Astrophysics*, 75, 228.
- [180] Luo, C., & Liang, E. P. 1998, *The Astrophysical Journal*, 498, 307.
- [181] Lynden-Bell, D. 1978, *Physica Scripta*, 17, 185.
- [182] Lynden-Bell, D. 1969, *Nature*, 223, 690.
- [183] Malkan, M.M., *Astrophys. J.* 268 582 (1983)
- [184] Malkan, M. A., & Sargent, W. L. W. 1982, *The Astrophysical Journal*, 254, 22.
- [185] Mandal, S., & Chakrabarti, S. K. 2008, *The Astrophysical Journal*, 689, L17.
- [186] Maraschi, L., Treves, A., & Roasio, R. 1982, *The Astrophysical Journal*, 253, 312.
- [187] Maraschi, L., Reina, C., & Treves, A. 1976, *The Astrophysical Journal*, 206, 295.
- [188] Markwardt, C. B., & Swank, J. H. 2003, *The Astronomer's Telegram*, 133, 1.
- [189] Mauche, C. W. 2002, *The Astrophysical Journal*, 580, 423.
- [190] McClintock, J. E., & Remillard, R. A. 2006, *Compact stellar X-ray sources*, 39, 157.
- [191] McClintock, J. E., Remillard, R. A., Rupen, M. P., et al. 2009, *The Astrophysical Journal*, 698, 1398.
- [192] Meszaros, P. 1975, *Astronomy and Astrophysics*, 44, 59.
- [193] Michel, F. C. 1972, *Astrophysics and Space Science*, 15, 153.
- [194] Miller-Jones, J. C. A., Sivakoff, G. R., Altamirano, D., et al. 2012, *Monthly Notices of the Royal Astronomical Society*, 421, 468.
- [195] Mirabel, I. F., & Rodríguez, L. F. 1994, *Nature*, 371, 46.
- [196] Mitsuda, K., Inoue, H., Koyama, K., et al. 1984, *Publications of the Astronomical Society of Japan*, 36, 741.
- [197] Mitsuda, K., Inoue, H., Nakamura, N., & Tanaka, Y. 1989, *Publications of the Astronomical Society of Japan*, 41, 97.
- [198] Molla, A. A., Chakrabarti, S. K., Debnath, D., & Mondal, S. 2017, *The Astrophysical Journal*, 834, 88.
- [199] Molla, A. A., Debnath, D., Chakrabarti, S. K., Mondal, S., & Jana, A. 2016, *Monthly Notices of the Royal Astronomical Society*, 460, 3163.

- [200] Molteni, D., Acharya, K., Kuznetsov, O., Bisikalo, D., & Chakrabarti, S. K. 2001, *The Astrophysical Journal*, 563, L57.
- [201] Molteni, D., Ryu, D., & Chakrabarti, S. K. 1996, *The Astrophysical Journal*, 470, 460.
- [202] Molteni, D., Sponholz, H., & Chakrabarti, S. K. 1996, *The Astrophysical Journal*, 457, 805.
- [203] Molteni, D., Lanzafame, G., & Chakrabarti, S. K. 1994, *The Astrophysical Journal*, 425, 161.
- [204] Monaghan, J. J. 1985, *Computer Physics Reports*, 3, 71.
- [205] Monaghan, J. J. 1992, *Annual Review of Astronomy and Astrophysics*, 30, 543.
- [206] Moncrief, V. 1980, *The Astrophysical Journal*, 235, 1038.
- [207] Mondal, S., Chakrabarti, S. K., & Debnath, D. 2015, *The Astrophysical Journal*, 798, 57.
- [208] Mondal, S., & Chakrabarti, S. K. 2013, *Monthly Notices of the Royal Astronomical Society*, 431, 2716.
- [209] Mondal, S., Debnath, D., & Chakrabarti, S. K. 2014, *The Astrophysical Journal*, 786, 4.
- [210] Mondal, S., Chakrabarti, S. K., & Debnath, D. 2016, *Astrophysics and Space Science*, 361, 309.
- [211] Morrison, R., & McCammon, D. 1983, *The Astrophysical Journal*, 270, 119.
- [212] Motta, S. E., Rouco Escorial, A., Kuulkers, E., Muñoz-Darias, T., & Sanna, A. 2017, *Monthly Notices of the Royal Astronomical Society*, 468, 2311.
- [213] Munro, M. P., Remillard, R. A., & Chakrabarty, D. 2002, *The Astrophysical Journal*, 568, L35.
- [214] Méndez, M., van der Klis, M., Wijnands, R., et al. 1998, *The Astrophysical Journal*, 505, L23.
- [215] Méndez, M., van der Klis, M., van Paradijs, J., et al. 1997, *The Astrophysical Journal*, 485, L37.
- [216] Méndez, M. 2006, *Monthly Notices of the Royal Astronomical Society*, 371, 1925.
- [217] Méndez, M., & van der Klis, M. 1999, *The Astrophysical Journal*, 517, L51.
- [218] Nandi, A., Debnath, D., Mandal, S., & Chakrabarti, S. K. 2012, *Astronomy and Astrophysics*, 542, A56.
- [219] Nandi, A., Manickam, S.G., Rao, A.R., and Chakrabarti, S.K., *MNRAS* 324 267 (2001)
- [220] Nandi, A., Manickam, S.G., and Chakrabarti, S.K., *Ind. J. Phys.* 74B 331 (2000)
- [221] Narayan, R., & Yi, I. 1994, *The Astrophysical Journal*, 428, L13.
- [222] Ninkov, Z., Walker, G. A. H., & Yang, S. 1987, *The Astrophysical Journal*, 321, 425.
- [223] Novikov, I.D., and Thorne, K.S., in: *Black Holes* (eds.) C. DeWitt and B. DeWitt (Gordon and Breach: New York) (1973)
- [224] Nowak, M. A., & Wagoner, R. V. 1991, *The Astrophysical Journal*, 378, 656.
- [225] Odaka, H., Khangulyan, D., Tanaka, Y. T., et al. 2014, *The Astrophysical Journal*, 780, 38.
- [226] Odaka, H., Khangulyan, D., Tanaka, Y. T., et al. 2013, *The Astrophysical Journal*, 767, 70.
- [227] Orosz, J. A., McClintock, J. E., Aufdenberg, J. P., et al. 2011, *The Astrophysical Journal*, 742, 84.
- [228] Ostriker, J.P., *Nature* 217 1222 (1968)
- [229] Ostriker, J. 1968, *Nature*, 217, 1227.

- [230] Paczynski, B. 1974, *Astronomy and Astrophysics*, 34, 161.
- [231] Paczynski, B. 1987, *Nature*, 327, 303.
- [232] Paczyński, B., & Wiita, P. J. 1980, *Astronomy and Astrophysics*, 500, 203.
- [233] Paizis, A., Farinelli, R., Titarchuk, L., et al. 2006, *Astronomy and Astrophysics*, 459, 187.
- [234] Pal, P. S., Chakrabarti, S. K., & Nandi, A. 2011, *International Journal of Modern Physics D*, 20, 2281.
- [235] Park, M.-G., & Ostriker, J. P. 2001, *The Astrophysical Journal*, 549, 100.
- [236] Parker, E. N. 1958, *The Astrophysical Journal*, 128, 664.
- [237] Parmar, A. N., Kuulkers, E., Oosterbroek, T., et al. 2003, *Astronomy and Astrophysics*, 411, L421.
- [238] Payne, D.G., and Blandford, R.D., *Mon. Not. R. Astron. Soc.* 196 781 (1981)
- [239] Pneuman, G. W. 1966, *The Astrophysical Journal*, 145, 242.
- [240] Popham, R., & Sunyaev, R. 2001, *The Astrophysical Journal*, 547, 355.
- [241] Pozdnyakov, L. A., Sobol, I. M., & Syunyaev, R. A. 1983, *Astrophysics and Space Physics Reviews*, 2, 189.
- [242] Priedhorsky, W., Hasinger, G., Lewin, W. H. G., et al. 1986, *The Astrophysical Journal*, 306, L91.
- [243] Pringle, J. E., & Rees, M. J. 1972, *Astronomy and Astrophysics*, 21, 1.
- [244] Pringle, J., *Mon. Not. R. Astron. Soc.* 177 65 (1976)
- [245] Psaltis, D., Belloni, T., & van der Klis, M. 1999, *The Astrophysical Journal*, 520, 262.
- [246] Pétri, J. 2008, *Astrophysics and Space Science*, 318, 181.
- [247] Rees, M.J., Begelman, M.C., Blandford, R.B., and Phinney, E.S., *Nature* 295 17 (1982)
- [248] Rees, M.J., *Ann. Rev. Astron. Astrophys.* 22 471 (1984)
- [249] Reid, M. J., McClintock, J. E., Narayan, R., et al. 2011, *The Astrophysical Journal*, 742, 83.
- [250] Remillard, R. A., & McClintock, J. E. 2006, *Annual Review of Astronomy and Astrophysics*, 44, 49.
- [251] Revnivtsev, M., & Mereghetti, S. 2015, *Space Science Reviews*, 191, 293.
- [252] Reynolds, C. S., Young, A. J., Begelman, M. C., & Fabian, A. C. 1999, *The Astrophysical Journal*, 514, 164.
- [253] Reynolds, S. P. 1999, *Astrophysical Letters and Communications*, 38, 425.
- [254] Robinson, I., Schild, A., and Schucking, E.L., *Quasi-stellar Sources and Gravitational Collapse* (Chicago: The Univ. of Chicago Press) (1965)
- [255] Rybicki, G.B., and Lightman, A.P., *Radiative Processes in Astrophysics* (1979) (RL 79).
- [256] Ryu, D., in *Observational Evidence for Black Holes in the Universe*, (ed.) S K Chakrabarti (Dordrecht: Kluwer Academic Publishers) p 73 (1998)
- [257] Ryu, D., Chakrabarti, S. K., & Molteni, D. 1997, *The Astrophysical Journal*, 474, 378.
- [258] Salpeter, E. E. 1964, *The Astrophysical Journal*, 140, 796.
- [259] Sanna, A., Riggio, A., Burderi, L., et al. 2017, *Monthly Notices of the Royal Astronomical Society*, 469, 2.
- [260] Scharlemann, E. T. 1981, *The Astrophysical Journal*, 246, L15.

- [261] Schmidt, M. 1963, *Nature*, 197, 1040.
- [262] Schreier, E., Gursky, H., Kellogg, E., Tananbaum, H., & Giacconi, R. 1971, *The Astrophysical Journal*, 170, L21.
- [263] Seifina, E., & Titarchuk, L. 2012, *The Astrophysical Journal*, 747, 99.
- [264] Seifina, E., & Titarchuk, L. 2011, *The Astrophysical Journal*, 738, 128.
- [265] Seifina, E., Titarchuk, L., & Shaposhnikov, N. 2016, *The Astrophysical Journal*, 821, 23.
- [266] Seifina, E., Titarchuk, L., & Frontera, F. 2013, *The Astrophysical Journal*, 766, 63.
- [267] Seifina, E., Titarchuk, L., Shrader, C., & Shaposhnikov, N. 2015, *The Astrophysical Journal*, 808, 142.
- [268] Seon, K.-I., Choi, C.-S., Nam, U.-W., & Min, K.-W. 1994, *Journal of Korean Astronomical Society*, 27, 45.
- [269] Shakura, N. I., & Sunyaev, R. A. 1973, *Astronomy and Astrophysics*, 500, 33.
- [270] Shang, J.-R., Debnath, D., Chatterjee, D., et al. 2019, *The Astrophysical Journal*, 875, 4.
- [271] Shapiro, S. L., & Salpeter, E. E. 1975, *The Astrophysical Journal*, 198, 671.
- [272] Shapiro, S. L., & Teukolsky, S. A. 1983, *A Wiley-Interscience Publication*.
- [273] Shapiro, S. L. 1973, *The Astrophysical Journal*, 185, 69.
- [274] Shapiro, S. L. 1973, *The Astrophysical Journal*, 180, 531.
- [275] Shaposhnikov, N., & Titarchuk, L. 2007, *The Astrophysical Journal*, 663, 445.
- [276] Shaposhnikov, N., & Titarchuk, L. 2009, *The Astrophysical Journal*, 699, 453.
- [277] Shaposhnikov, N. 2010, *The Astronomer's Telegram*, 2857, 1.
- [278] Shimura, T., & Takahara, F. 1995, *The Astrophysical Journal*, 445, 780.
- [279] Smith, D. M., Heindl, W. A., Markwardt, C. B., & Swank, J. H. 2001, *The Astrophysical Journal*, 554, L41.
- [280] Smith, D. M., Heindl, W. A., & Swank, J. H. 2002, *The Astrophysical Journal*, 569, 362.
- [281] Soria, R., Kinwah, W., Hannikainen, D., McCollough, M., & Hunstead, R. 2001, *X-ray Emission from Accretion onto Black Holes*, 65.
- [282] Steeghs, D., Miller, J. M., Kaplan, D., & Rupen, M. 2003, *The Astronomer's Telegram*, 146, 1.
- [283] Steiner, J. F., McClintock, J. E., & Reid, M. J. 2012, *The Astrophysical Journal*, 745, L7.
- [284] Strohmayer, T. E., Zhang, W., Swank, J. H., et al. 1996, *The Astrophysical Journal*, 469, L9.
- [285] Sun, W.-H., & Malkan, M. A. 1989, *The Astrophysical Journal*, 346, 68.
- [286] Sunyaev, R. A., & Titarchuk, L. G. 1985, *Astronomy and Astrophysics*, 143, 374.
- [287] Sunyaev, R. A., & Titarchuk, L. G. 1980, *Astronomy and Astrophysics*, 500, 167.
- [288] Sunyaev, R. A., & Truemper, J. 1979, *Nature*, 279, 506.
- [289] Thorne, K. S., Flammang, R. A., & Zytlow, A. N. 1981, *Monthly Notices of the Royal Astronomical Society*, 194, 475.
- [290] Thorne, K. S. 1974, *The Astrophysical Journal*, 191, 507.
- [291] Titarchuk, L., Seifina, E., & Frontera, F. 2013, *The Astrophysical Journal*, 767, 160.
- [292] Titarchuk, L., Seifina, E., & Shrader, C. 2014, *The Astrophysical Journal*, 789, 98.
- [293] Titarchuk, L., Osherovich, V., & Kuznetsov, S. 1999, *The Astrophysical Journal*, 525, L129.

- [294] Titarchuk, L., Lapidus, I., & Muslimov, A. 1998, *The Astrophysical Journal*, 499, 315.
- [295] Titarchuk, L., & Osherovich, V. 1999, *The Astrophysical Journal*, 518, L95.
- [296] Tomsick, J. A., Yamaoka, K., Corbel, S., et al. 2014, *The Astrophysical Journal*, 791, 70.
- [297] Tomsick, J. A., Nowak, M. A., Parker, M., et al. 2014, *The Astrophysical Journal*, 780, 78.
- [298] Vacondio, R., Rogers, B. D., Stansby, P. K., Mignosa, P., & Feldman, J. 2013, *Computer Methods in Applied Mechanics and Engineering*, 256, 132.
- [299] van der Klis, M. 1989, *Two Topics in X-Ray Astronomy, Volume 1: X Ray Binaries. Volume 2: AGN and the X Ray Background*, 1, 203.
- [300] van der Klis, M., Hasinger, G., Damen, E., et al. 1990, *The Astrophysical Journal*, 360, L19.
- [301] van der Klis, M., Jansen, F., van Paradijs, J., et al. 1985, *Nature*, 316, 225.
- [302] van der Klis, M., Wijnands, R. A. D., Horne, K., & Chen, W. 1997, *The Astrophysical Journal*, 481, L97.
- [303] van Doesburgh, M., & van der Klis, M. 2017, *Monthly Notices of the Royal Astronomical Society*, 465, 3581.
- [304] Vikhlinin, A., Churazov, E., Gilfanov, M., et al. 1994, *The Astrophysical Journal*, 424, 395.
- [305] Wandel, A., & Petrosian, V. 1988, *The Astrophysical Journal*, 329, L11.
- [306] Wang, J., Chang, H.-K., & Liu, C.-Y. 2012, *Astronomy and Astrophysics*, 547, A74.
- [307] Wang, J. 2016, *International Journal of Astronomy and Astrophysics*, 6, 82.
- [308] Wheeler, J., *Am. Scientist* 56 1 (1968)
- [309] White, N. E., & Marshall, F. E. 1984, *The Astrophysical Journal*, 281, 354.
- [310] White, N. E., Peacock, A., Hasinger, G., et al. 1986, *Monthly Notices of the Royal Astronomical Society*, 218, 129.
- [311] Wijnands, R., van der Klis, M., Homan, J., et al. 2003, *Nature*, 424, 44.
- [312] Wijnands, R., Homan, J., van der Klis, M., et al. 1997, *The Astrophysical Journal*, 490, L157.
- [313] Wijnands, R., Méndez, M., van der Klis, M., et al. 1998, *The Astrophysical Journal*, 504, L35.
- [314] Wijnands, R., Homan, J., van der Klis, M., et al. 1998, *The Astrophysical Journal*, 493, L87.
- [315] Wilson, J., *Astrophys. J.* 187 575 (1974)
- [316] Wilson, J. R. 1972, *The Astrophysical Journal*, 173, 431.
- [317] Wu, K., Soria, R., Campbell-Wilson, D., et al. 2002, *The Astrophysical Journal*, 565, 1161.
- [318] Wyller, A., *Nature* 226 64 (1970)
- [319] Yahel, R. Z., & Brinkmann, W. 1981, *The Astrophysical Journal*, 244, L7.
- [320] Yu, W., van der Klis, M., & Jonker, P. G. 2001, *The Astrophysical Journal*, 559, L29.
- [321] Zdziarski, A. A., Lubiński, P., Gilfanov, M., & Revnivtsev, M. 2003, *Monthly Notices of the Royal Astronomical Society*, 342, 355.
- [322] Zeldovich, Y. B., & Guseynov, O. H. 1966, *The Astrophysical Journal*, 144, 840.
- [323] Zhang, S. N., Cui, W., Harmon, B. A., et al. 1997, *The Astrophysical Journal*, 477, L95.

Appendix A

Geometrical Aspects of a Black Hole

General relativistic form

For any matter of mass m , to escape from the gravitational pull of a massive object of M and radius R , the kinetic energy must be greater than or equal to the potential energy, i.e:

$$\frac{1}{2}mv_e^2 \geq \frac{GMm}{R},$$

where $v_e = \text{Escape velocity}$.

As the radius of the object decreases, the escape velocity increases. If the radius is small enough to make $v_e = c$, even light can not escape the object from within the radius R . In case of a black hole, this is seen and the corresponding hypersurface, where escape velocity is equal to the speed of light, is called the “event horizon”.

Hence, we have for a spherical object of mass M , the event horizon is at,

$$r_g = \frac{2GM}{c^2}. \quad (\text{A.1})$$

The geometry of any region in space is defined by the metric in that region. The metric acts like a “measuring stick” of sorts and manifests the nature of space-time around the said point. The strong gravity changes the Minkowski metric. Depending on the mass, spin and charge of black hole, the metric attains different forms. For a non-rotating black hole with no charge, the Schwarzschild metric gives the correct solution of gravitational fields:

$$ds^2 = \left(1 - \frac{2GM}{c^2 r}\right) c^2 dt^2 - \frac{dr^2}{\left(1 - \frac{2GM}{c^2 r}\right)} - r^2(d\theta^2 + \sin^2\theta d\phi^2). \quad (\text{A.2})$$

The metric reaches a singularity as $r \rightarrow \frac{2GM}{c^2}$. At this value of radius,

$$g_{00} = \left(1 - \frac{2GM}{c^2 r}\right) \rightarrow 0,$$
$$g_{11} = -\frac{1}{\left(1 - \frac{2GM}{c^2 r}\right)} \rightarrow \infty.$$

This radial value, r_g is defined as the Schwarzschild radius or gravitational radius of mass M . Once compressed to a smaller radius than r_g , by means of some astrophysical process, the gravitational collapse is inevitable for a spherical star. The amount of compression a star undergoes when it becomes a black hole can be understood with a small information: If a black hole forms from a star of 1 solar mass, r_g for that would be only $\sim 3\text{km}$.

Pseudo-Newtonian form

The metric determines the potential near and around a black hole. For a Schwarzschild black hole, when $r \gg r_g$, the Newtonian potential suffices to account for the gravitational field. When matter comes close to event horizon, i.e., $r \sim r_g$, the general relativistic effects become dominant and need to be taken into account. Whereas a fully general relativistic approach is accurate, it is at times very complex and can be avoided by using a so-called pseudo potential which produces similar effects as that of a GR potential.

One such potential for the non-rotating black holes was proposed by Paczyński and Wiita in 1980. The pseudo-Newtonian potential can be written as:

$$\Phi = -\frac{GM}{r - \frac{2GM}{c^2}}. \quad (\text{A.3})$$

The GR approach, after some mathematical manipulation leads to an effective potential V_{eff} given by,

$$V_{eff} = \left[(1 - 2/r)(1 + l^2/r^2) \right]^{1/2}, \quad (\text{A.4})$$

where $l = \textit{specific angular momentum}$ and we have chosen $G = M = c = 1$.

The modified pseudo-Newtonian potential with a rest mass term can be written as,

$$V_{Newt}^{PW}(r) = 1 + \Phi_{PW} + \frac{l^2}{2r^2}, \quad (\text{A.5})$$

where $\Phi_{PW} = -\frac{1}{r-2}$.

The marginally stable orbit ($r = r_{ms}$) for both the cases, is found to be at $r = 6$, with Keplerian angular momentum $l = 2\sqrt{3}$. The binding energies (energy released at the marginally stable orbit, before matter enters black hole) are 5.72% and 6.25% for the GR and PW cases, respectively. This leads to the conclusion that pseudo-Newtonian potential is a very good approximation of GR effects and thus this is a widely used model potential.

Appendix B

Fluid dynamical aspects of an accretion flow

Governing equations

We follow the prescriptions given in Landau and Lifshitz (1959) and the modifications noted in Giri 2015 (PhD Thesis) for the description of fluid dynamical aspects of accreting matter. If the mean free path of gaseous particles, is very small compared to the accretion flow length scale, the gas can be assumed to be a continuum of fluid with density ρ and velocity \vec{v} .

Conservation of Mass

The conservation of mass for a fluid with density $\rho(r)$ and velocity $\vec{v}(r)$, at each point of space, is given by the continuity equation,

$$\frac{\partial \rho}{\partial t} + \vec{\nabla} \cdot (\rho \vec{v}) = 0. \quad (\text{B.1})$$

Conservation of Momentum

The Navier-Stokes equation gives the conservation of momentum for a fluid in motion.

$$\frac{\partial \vec{v}}{\partial t} + (\vec{v} \cdot \vec{\nabla}) \vec{v} = -\frac{1}{\rho} \vec{\nabla} P + \vec{f}_{external}. \quad (\text{B.2})$$

where P is the gas pressure due to thermal motion, $\vec{f}_{external}$ is the external force, such as gravity, viscous drag, body forces etc.

Conservation of Energy

The conservation of energy takes into account the mechanical energies and thermal heating or cooling effects, and one of the forms of which is given by,

$$\frac{\partial}{\partial t} \left(\frac{1}{2} \rho v^2 + \rho \mathcal{E} \right) + \vec{\nabla} \cdot \left[\left(\frac{1}{2} \rho v^2 + \rho \mathcal{E} + P \right) \vec{v} \right] = \vec{f} \cdot \vec{v} - \vec{\nabla} \cdot \vec{F}_{rad} - \vec{\nabla} \cdot \vec{q}, \quad (\text{B.3})$$

where the terms ρv^2 and $\rho \mathcal{E}$ measure the kinetic energy density and internal energy density respectively. In the right hand side, \vec{F}_{rad} represents the radiative flux vector and \vec{q} denotes the

conductive heat flux. In general, \vec{q} estimates the rate of transport of thermal energy inside the gas due to random motions.

Shocks

A shock is a place where certain jumps in thermodynamic variables, such as the pressure and temperature take place in a flow. In terms of Mach number of the flow ($M(r) = \frac{v(r)}{a(r)}$), a shock is a discontinuous jump in the value of Mach number from supersonic ($M > 1$) to subsonic ($M < 1$) branch of solution of the flow. Depending on the quantities which are preserved at the shock front, they can be divided into the following categories.

Rankine-Hugoniot Shocks, Isentropic Compression Waves and Isothermal Shocks

We define the specific energy, entropy and temperature as $(\mathcal{E}_-, \mathcal{E}_+), (s_-, s_+), (T_-, T_+)$. Here, ‘-’ and ‘+’ subscripts denote the variables in the pre-shock and post-shock regions, respectively.

For a Rankine-Hugoniot shock, without dissipation [from Abramowicz and Chakrabarti (1990) and Chakrabarti (1990)]:

$$\mathcal{E}_- = \mathcal{E}_+, s_- \neq s_+, T_- \neq T_+. \quad (\text{B.4})$$

For isentropic shocks, where, energy is dissipated in the form of radiation from the shock front, we have [Abramowicz and Chakrabarti (1990) and Chakrabarti (1990)],

$$\mathcal{E}_- \neq \mathcal{E}_+, s_- = s_+, T_- \neq T_+. \quad (\text{B.5})$$

For isothermal shocks, where cooling timescale is short enough to bring the gas back to its original temperature after the heating up process at the shock front, we have [from Abramowicz and Chakrabarti (1990) and Chakrabarti (1990)],

$$\mathcal{E}_- \neq \mathcal{E}_+, s_- \neq s_+, T_- = T_+. \quad (\text{B.6})$$

Appendix C

Radiative Processes

All the information about a black hole is attained from the radiation emitted by the accreting matter. But which radiations are important and which must be incorporated in solving the equation of motion for the accreting matter, varies. It is finally a matter of energy scales and time scales. The physical variables of the flow, such as density, temperature and pressure, determine the total energy radiated and the cooling timescales of different radiations. If these match with the other dynamical timescales under considerations, they are important. Given below are some of the local and non-local radiative processes which become dominant in different domains (Rybicki and Lightman 1979).

Thermal Emission

a) Blackbody radiation: Blackbody radiation comes out from a system which is in thermodynamic equilibrium. Once the radiation enters into the system, it does not emit from it unless an equilibrium is established. The photons have to scatter a large number of times with the gas particle to attain the temperature of the system. If optical depth is $\tau > 1$, this condition is satisfied and a blackbody spectrum is produced. The intensity of the blackbody photons emitted from a system characterized by the temperature T is given by the Planck's Law,

$$B_\nu(T) = \frac{2h\nu^3/c^2}{e^{h\nu/kT} - 1}. \quad (\text{C.1})$$

b) Bremsstrahlung: Bremsstrahlung or *free-free emission* is the radiation emitted due to the acceleration of a charged particle in the Coulomb field of another particle. We consider thermal distribution of electron velocities, i.e.,:

$$dP = \sqrt{\left(\frac{m_e}{2\pi k_b T}\right)^3} 4\pi v^2 \exp\left(-\frac{m_e v^2}{2k_b T}\right) dv, \quad (\text{C.2})$$

where

$m_e = \text{mass of an electron},$

$dP = \text{probability of finding an electron having a velocity between } v \text{ and } v + dv.$

Using Equation (C.2) we arrive at the expression for energy dissipated per unit volume per unit time, or the *volume emissivity* (Λ_{brew}):

$$\Lambda_{brew} = 1.43 \times 10^{-27} N_e N_i Z^2 T^{1/2} g_f \text{ erg cm}^{-3} \text{ s}^{-1}.$$

where

$$\begin{aligned}
& N_e = \text{Number density of electrons}, N_i = \text{Number density of ions}, \\
& Z = \text{Atomic number of the matter forming the gas}, T = \text{Temperate of the plasma}, \\
& g_f = \text{Gaunt factor}. \text{ Here, } g_f \text{ is a slowly varying function of frequency taken} = 1. \\
& \text{For Hydrogen plasma, } Z = 1. \\
& N_e Z = \frac{\rho}{m_p + m_e} \approx \frac{\rho}{m_p}.
\end{aligned}$$

A radiation process similar to that of Bremsstrahlung, but with a much stronger dependance on temperature T , can be achieved by increasing the index from $1/2$ to a higher value. Typically, the dependance is taken as a *power-law*, $\Lambda \sim T^\beta$, hence the cooling is termed as *Power-law cooling* (Giri, Garain and Chakrabarti 2014). Here, we take $\beta = 1$.

$$\Lambda_{pow} = 1.43 \times 10^{-27} N_e N_i Z^2 T g_f \text{ erg cm}^{-3} \text{ s}^{-1}.$$

c) Thermal Comptonization: Scattering of a photon by an electron is known as Comptonization (i.e., Compton scattering). A significant part of the energy is transferred from one to the another. When electron gains energy from the photon, it is called the Compton scattering, whereas, when the reverse process occurs, i.e., photon gains energy from the electrons, it is called the inverse-Compton scattering. When the energy of incoming and outgoing photon are the same, a special case, it is called Thompson scattering. In astrophysics, photons are energized by the second process when they enter into a hot plasma or electron gas, i.e., by inverse-Comptonization, and by the term Comptonization, we generally mean this process.

When the photon has a long wavelength (i.e., photon energy $h\nu \ll m_e c^2 = 511 \text{keV}$), the scattering is closely elastic. It is called Thomson scattering. Electrons oscillate in the electric field of the wave, radiating the scattered wave as it does so. The scattering cross-section is $\sigma_T = \frac{8\pi r_e^2}{3}$, where r_e is the classical radius of the electron. But, when quantum effects enter, one considers Comptonization process. Let us assume that a photon of energy $E = h\nu$ and momentum $E \frac{\vec{\Omega}}{c}$ is scattered by an electron of energy $\gamma m_e c^2$ and momentum $\vec{p} = \gamma m_e \vec{v}$, with $\gamma = \left(1 - \frac{v^2}{c^2}\right)^{-1/2}$. After scattering the photon has energy $E' = h\nu'$ and momentum $E' \frac{\vec{\Omega}'}{c}$. Defining $\mu = \vec{\Omega} \cdot \vec{v}$, $\mu' = \vec{\Omega}' \cdot \vec{v}$ and scattering angle $\alpha = \cos^{-1}(\vec{\Omega} \cdot \vec{\Omega}')$, we find that,

$$\frac{\nu'}{\nu} = \frac{1 - \mu v/c}{1 - \frac{\mu' v}{c} + \frac{h\nu}{\gamma m_e c^2 (1 - \cos\alpha)}}. \quad (\text{C.3})$$

If the electron is at rest ($v = 0$), then,

$$\frac{\nu'}{\nu} = \frac{1}{1 + \frac{h\nu}{m_e c^2 (1 - \cos\alpha)}}. \quad (\text{C.4})$$

The scattering cross-section is given by the Klein-Nishina formula (Poznyakov, Sobol & Sunyaev 1983),

$$\sigma = \frac{2\pi r_e^2}{x} \left[\left(1 - \frac{4}{x} - \frac{8}{x^2}\right) \ln(1+x) + \frac{1}{2} + \frac{8}{x} - \frac{1}{2(1+x)^2} \right]. \quad (\text{C.5})$$

where x is given by,

$$x = \frac{2E}{m_e c^2} \gamma \left(1 - \frac{\mu v}{c}\right). \quad (\text{C.6})$$

Here, $r_e = \frac{e^2}{m_e c^2}$ is the classical electron radius and m_e is the mass of the electron.

As mentioned earlier, in Comptonization, energy of photon decreases, i.e., $\delta\nu < 0$. However, when we consider the scattering of a photon by a moving electron and the electron has a sufficient kinetic energy compared to the photon energy, an inverse-Comptonization occurs. This is also called Compton up-scattering, as the energy of photon goes up. Also, in astrophysics, we have to consider the scattering of isotropic distribution of photons with isotropic distribution of electrons. For non-relativistic electrons in thermal equilibrium at temperature T , the expression for the energy transfer per scattering is given by (Rybicki and Lightman 1979),

$$\frac{(\Delta h\nu)_{NR}}{h\nu} = \frac{4kT - h\nu}{m_e c^2}. \quad (C.7)$$

If the electrons have a temperature high enough so that $4kT > h\nu$, the photons gain energy, while at a low electron temperature it is the other way around. In any case, the fractional energy gain is very small, so that many scatterings are required for a significant effect, leading to diffusion of the energy in phase space. Hence, the emitted spectrum depends upon the factor $y = \tau_{es}(\Delta h\nu)_{NR}/h\nu$, where τ_{es} is the electron scattering optical depth. For relativistic distribution of electron velocities, higher order terms of $\frac{kT}{m_e c^2}$ have to be taken into account.

Non-thermal Emission

Non-thermal radiations are emitted when the emitter particles are not in thermal equilibrium, i.e., not Maxwellian. Photons do not interact with the electrons completely since the matter is advected rapidly. Non-thermal emission is very important in any environment where there are high energy particles.

a) *Cyclotron radiation*: This is basically the bremsstrahlung process due to the presence of a magnetic field. If an electron gas is permeated by a magnetic field, the electrons will be forced to gyrate about the field lines, and the radiation that is emitted as a result of this acceleration is known as the Cyclotron radiation, provided the electrons are moving at non-relativistic speeds. The radiation is emitted at the gyro-frequency, which is proportional to the magnetic field strength, \vec{B} , and is given by, $\vec{\omega}_c = \frac{e\vec{B}}{m_e}$. The radiation emitted is linearly polarized when viewed perpendicular to the direction of the field lines, and circularly polarized when viewed end-on. In this particular type of emission process, unless the field strength (\vec{B}) is large, the acceleration is not particularly large, nor is the intensity which depends on the square of the acceleration.

b) *Synchrotron Radiation*: For relativistic distribution of velocities, the cyclotron radiation is not-symmetric w.r.t. the direction of motion of the electrons (or the corresponding accelerated particles), and called *synchrotron radiation*. The value of γ dictates the degree of asymmetry. The emitted power is confined mostly within the cone of half vertical angle θ which for large γ value, is given by,

$$\theta \sim \frac{1}{\gamma}.$$

The effect is seen in the spectrum of the radiation. When integrated over all frequency range, the volume emissivity (Λ_{sync}) (Shapiro and Teukolsky 1983) is found to be:

$$\Lambda_{sync} = \frac{16}{3} \frac{e^2}{c} \left(\frac{eB}{m_e c} \right)^2 \left(\frac{k_b T}{m_e c^2} \right)^2 N_e \text{ erg cm}^{-3} \text{ s}^{-1},$$

where $B = \text{Magnetic field intensity}$,
 $e = \text{charge of electron} = 4.8 \times 10^{-10} \text{ esu}$.

c) Non-thermal Comptonization: We considered the scattering of photons with electrons in thermal equilibrium. However, electrons may be energized at the shock front by the shock acceleration process (Blandford & Eichler 1987; Chakrabarti 1996) very close to the black hole, where their kinetic energy become very high. These highly energetic electrons are called non-thermal electrons and with the presence of these, the process of Comptonization will be modified with respect to the thermal case. The process is self-similar and this leads to the formation of a power law spectrum of high energy tail above the thermal cut-off. This high-energy tail is simply the characteristic of the superposition of the individual electron spectra of non-thermal electrons which have optical depth (τ) $\ll 1$. Therefore, the spectral shape depends on the energy index p of the power-law like, with an spectral index $s = \frac{1}{2}(p - 1)$.

Appendix D

Numerical and visualization tools

Data visualization techniques

Data visualization is one of the most important aspects of organizing, analyzing and interpreting observed and simulated data. Depending on the system and data at hand, a varied range of ways can be used to look into the raw data, for various purposes. For example, the lightcurves generated from cooling within the SPH code can provide an insight onto the dynamics of densest and hottest regions on an average. However, a 2D contour plot of the density or temperature of the same system lends a better perspective on that. A continuous movie of such plots captures the time-dependent variations of the system in even more details. We have used multiple techniques, based on the pros and cons associated with their usage for a particular task. The observational data was analyzed and have been represented, mostly, here with the QDP software inbuilt NASA's HEASOFT package. For simulated datasets we used the following visualization softwares, a brief summary of which is given below.

SuperMongo

SuperMongo (SM) is a plotting programme written by Robert Lupton (rhl@astro.princeton.edu) and Patricia Monger (monger@mcmaster.ca). It is useful for 1D graphic rendering and creating high resolution plots, with texts, which are small in size. Plots for Chapter 4 are created using SM. Disadvantages are: lack of support community, non-intuitive macros, only text-user-interface and lack of 3D rendering.

GnuPlot

GNUPLOT is a open source software, used most often for the rendering of the plots included in the work. We have used GNUPLOT version 5.0 patchlevel 3 (both on linux and Mac OS) for initial plots. The user-friendly interface, intuitive syntax, demo and support files' availability online, made this software an essential part of the visualization process. The 3D rendering and contour plotting capabilities are also easily modified interactively. Shell scripts were also used in combination with Gnuplot to render videos of time-dependent simulations. It is also highly customizable to the needed resolution but leads to an increase of file size and lag in startup time. Another disadvantage is the plotting of contour maps using PM3D when the datapoints are not on a regular mesh or grid. For Chapter 7 and 8, where the SPH scheme was applied, the particles were spread in a non-uniform (mesh-free) way over the 2D plane of simulation. GnuPlot failed to interpolate the data in between the points and extrapolated false data despite not having any

points in some regions. Any effort in increasing the number of interpolation points lead to slower rendering but did not yield any significant gain in terms of accuracy in regions where points were sparse.

XmGrace

In terms of portability, XmGrace is the most effective plotting tool, which has been used here. We have used Grace-5.1.25 for Linux to generate the plots of Chapters 5 (variation of parameters), 6 (spectra), 8(λ vs r) and 9 (spectra, colour-colour diagrams). Grace allow the loading of data files (single column or block data) into the plot itself and thus provides post-processing of data better than any listed here. Mostly 2D plots are rendered within the graphical interface which provide numerous data handling options. There are only three major drawbacks: 1. No shell compatible interface, could not be used within a script; 2. No 3D rendering, 3. No ‘undo’ option.

ROOT

ROOT is a modular scientific software toolkit, developed by the ROOT team at CERN, mainly written in C++. It is an extremely useful tool for processing large amount of data, conducting large scale simulations and visualization of processed data. It is a open source software and version 6.06/04 (Linux; release date 03 May, 2016) has been used by us for data visualization. For data written in a regular grid in 2D, very high quality and low space consuming contour plots can be generated by ROOT. This has been used in the Chapters 6 for rendering the contours of equal temperatures and densities for the CENBOL. Both interactive and command line tools are available as interfaces. The canvases can be used to plot multiple types of plots (arrow, line and contours) on top of each other. Dynamic videos of scattering processes were also generated using this tool. The command line interface allow for creation of shell scripts to be written and helps in execution of repeatative visualization of similar data structures. The drawback, however, is the non-intuitive syntax and dependency on C++ language. Those who are not used to C++, would face a steeper learning curve. Another negative aspect is the management of non-uniform points in 2D. The rendering was spotty with unwanted inter- and extra-polations in blank spaces.

MATHEMATICA

Wolfram Mathematica is undoubtably the strongest tool used for the works included in my work. It is the most well-documented and robust modern technical computational tool used here. The possibilities of the software go way beyond the graphics rendering. We have used MATHEMATICA version 10 for Linux to generate the contour plots of the SPH simulations. It handled the pseudo-particle better than the rest for 3D plots and contours. The interface allows simultaneous computation and graphical rendering. It is also available as a command line tool, allowing for shell scripts to use it in combination with other tasks. Only issue was the large size of plots of high resolution.

Computational setups and techniques

As our work revolved around data, observed or simulated, computational tools had a major role in determining the problem solving time, detail and at times the prioritization of a certain aspect of problem. We have used FORTRAN 77 as the basis of our numerical codes. Bash scripts are also used in combination with the fortran codes for running multiple repeatative cases or variations.

At the moment the codes are all written for serial processing. We used IFORT v18.0.1 (release date 20171018) compiler for the latest version of codes. This provided better handling of double precision floating points, faster runtimes, better optimization schemes, vast array of predefined subroutines and a robust debugging system, compared to GFORTRAN or F77 compiler.

Code testing platforms

All the codes were primarily written on a Ubuntu 16.04 LTS machine with an 8-core Intel Core-i7 CPU having 12GB of RAM. This setup is provided by the S. N. Bose National Centre for Basic Sciences. For minor modifications and plotting purposes a Macbook Air with Mac OS Mojave, with a 4-core Intel Core-i5 CPU having 4 GB of RAM was used.

Performance statistics

There are three types of numerical simulations that were carried out for the works included here: MC, SPH, TANS (radiative transfer). The MC code is a fully 3D code which handles particle dynamics upto any required precision. The number of photon packets that were injected for NBOL were $\sim 10^7$ whereas for the disc it was $\sim 10^8$ in total. For such a case, the spectral generation would take from 7.5 to 12 days, depending on the accretion rates (which controlled the optical depth) in the i7 machine.

The SPH simulations took about 2.5-3 days to run on the same machine for a runtime of 32,000 timesteps. The TANS code converged within 10 sec to 3 minutes, depending on the parameters.

Usage of clusters

For serial job executions, two clusters were used at S. N. Bose National Centre for Basic Sciences: Photon and Phonon. Both had the same configurations. Each is a Computation Cluster for Serial Computing. User can submit serial jobs in this cluster. There are 7 compute nodes having 12 CPU cores and 24 GB of RAM each. 2 Intel Xeon E5650 (2.67 GHz), 6 Core CPUs are used in the cluster. Total 7 nodes are kept active at a time. There was a limit of maximum 10 jobs per account during the work period. The MC code was mostly run on the cluster for the works included in Chapter 6. Intel Fortran Compiler (IFORT V11.0) is available on these clusters, which has fewer features and slower speed compared to the one installed in the desktop. This lead to a 2-2.5 times longer runtime for similar numerical simulations.